Magnetohydrodynamic Wave Behaviour in the Vicinity of Proper and Improper Magnetic Null Points

Jonathan Ormston Thurgood

PhD

2013

Magnetohydrodynamic Wave Behaviour in the Vicinity of Proper and Improper Magnetic Null Points

Jonathan Ormston Thurgood

A thesis submitted in partial fulfilment of the requirements of the University of Northumbria at Newcastle for the degree of Doctor of Philosophy

Research undertaken in the Department of Mathematics and Information Sciences

November 2013

Abstract

Context: Both MHD waves and magnetic null points are prevalent in many astrophysical plasmas, including the solar corona, and as such their interaction is inevitable. Current theory implicates coronal null points as locations of localised heating events due to MHD waves propagating in their vicinity. However, previous work on the topic of wave-null interactions has almost exclusively been based on treatments of two-dimensional (2D) magnetic null point models. The surrounding magnetic field configuration of three-dimensional (3D) magnetic null points is, topologically, significantly different. Since MHD wave behaviour is highly dependent on the magnetic structure of the medium in which it propagates, it is not clear whether these existing 2D results apply to realistic magnetic null points, which are necessarily 3D.

Aims: To investigate the nature of MHD wave propagation about 3D null points, with a specific interest in their transient behaviour and interaction with other modes of oscillation. This thesis evaluates the extent to which 2D theory carries over to the 3D case, and determines whether realistic 3D null points are also likely locations for localised heating events.

Methods: This thesis primarily considers simulations of wave propagation in the vicinity of 3D null points by numerically solving the MHD equations using the LARE3D code. The isolation of different modes of oscillation in the vicinity of 3D null points is facilitated by the construction of a special fieldline and flux-based coordinate system. The coordinate system permits the introduction of pure-mode waves in driving conditions, and the tracking of subsequent excitation of different modes of oscillation.

Results: It is found at $\beta = 0$ potential 3D null points that the linear, transient behaviour of the different modes are as follows: (i) Fast waves propagate according to the Alfvén-speed profile along and across the fieldlines, refracting and accumulating at the null point where ohmic heating occurs; (ii) Alfvén waves, which are necessarily torsional, are confined to fieldlines which diverge on the approach to the null, thus pulses exhibit a 'spreading' effect (dilation) and typically accumulate near the fan plane. Different degrees of fieldline eccentricity at the null simply alter the rate of refraction/dilation, i.e. the qualitative behaviour of waves is the same for proper and improper null points. These modes are found to be linearly decoupled in all cases considered, although there is some evidence for nonlinear Alfvén to fast mode conversion due to the action of the ponderomotive force. In a treatment of the ponderomotive force, it is found that in general inhomogeneous MHD Alfvén waves sustain longitudinal and transverse compressive daughter disturbances, and that excitation of magnetoacoustic modes can occur as they undergo dispersion or phase mixing.

Conclusions: The main results from existing 2D work do indeed carry over to 3D magnetic null points and so this thesis concludes that 3D nulls are likely locations for preferential heating in the corona by interaction with MHD waves.

Declaration

I, Jonathan Thurgood, hereby certify that this thesis is a faithful record of the original research carried out during my PhD project and is solely my own work. I also confirm that, where appropriate, the opinions, contributions and ideas of others have been fully acknowledged and that none of the contents have been submitted as part of any previous application for any other award.

Any ethical clearance for the research presented in this thesis has been approved. Approval has been sought and granted by the University Ethics Committee on 15^{th} December 2010.

This thesis contains 39,946 words.

Name: Jonathan Thurgood **Signature:**..... **Date:** .....

Acknowledgements

First and foremost, I would like to express my sincerest gratitude to my supervisor, Dr James McLaughlin, who has always made time for me despite being incredibly busy. James not only has been an excellent scientific guide but also a good professional role model. I am also grateful for his keen editors eye, which has prevented my repeated misspellings of dependant dependent making it to press. I could not have asked for a better supervisor.

And then, in no particular order I would like to thank:

- My parents, Alan and Susan, and my brother Alexander for their sustained enthusiasm and support over the last three years. In particular, for the Sunday lunches (thanks mum!), the on-the-fly beers (thanks Dad!) and the sly trips to the climbing wall when I was meant to be doing science (thanks Alex!)
- Katie. Over the past 2+ years you've become my best friend, and I don't know how I would have got through the stressful periods without you. I can only thank the fates that I wasn't pig-headed enough to go stick to my vow at the start of my PhD (to stay away from distracting girls!) I cannot wait to get a real job so we can go on the big adventure you deserve, what do you say to Thailand 2014?
- Daisy. Please don't eat this manuscript.
- Everyone in the maths department at Northumbria, and the students of Pandon F7, for making it such a pleasant working environment.
- The instructors and fellow students at Team Phoenix Martial Arts. It has been an excellent outlet over the past three years, and been just as big a part in keeping me sane the other people acknowledged here. In particular, thanks to my flatmate-come-sparring partner Jamie Brown for taking my occasional bouts of 'over-enthusiasm' in good humour.

Finally, I would like to thank both the Royal Astronomical Society (RAS) and the Institute of Mathematics and its Applications (IMA) for their generous support in funding my conference attendance over the past 3 years, and thanks to Northumbria University for my scholarship.

Publications

The research presented in this thesis has also been published in the following peer-reviewed journals:

'Linear and nonlinear MHD mode coupling of the fast magnetoacoustic wave about a 3D magnetic null point'

Thurgood & McLaughlin (2012), Astronomy & Astrophysics, 545, A9

'On Ponderomotive Effects Induced by Alfvén Waves in Inhomogeneous 2.5D MHD Plasmas'

Thurgood & McLaughlin (2013a), Solar Physics, 288, 205-222

'Nonlinear Alfvén Wave Dynamics at a 2D Magnetic Null point: Ponderomotive Force'

Thurgood & McLaughlin (2013b), Astronomy & Astrophysics, 555, A86

'3D Alfvén wave behaviour around proper and improper magnetic null points'

Thurgood & McLaughlin (2013c), Astronomy & Astrophysics, 558, A127

Contents

List of Figures

Chapter 1

Introduction

An alleged scientific discovery has no merit unless it can be explained to a barmaid.

— Ernest Rutherford (1871 - 1937)

1.1 Motivation

This thesis details the results of an investigation into the behaviour of magnetohydrodynamic (MHD) waves in the vicinity of fully 3D magnetic null points, and considers the implications of the results for the physics of the solar corona. In the corona, the prevalence and importance of MHD wave behaviour is well established, with current satellite imaging revealing oscillatory behaviour at MHD scales throughout the solar atmosphere. Likewise, magnetic null points are thought to be abundant in the solar atmosphere and are a crucial component of many theoretical models for solar processes (playing, for example, a central role in most magnetic reconnection mechanisms). Given the ubiquity of MHD waves and the prevalence of magnetic null points in the corona, the interaction between waves and null points is inevitable.

There exists a large body of literature on wave-null theory. In it, the vicinity of coronal null points are implicated as locations of preferential and localised heating, mode-conversion and reconnection due to passing MHD waves. However, this research is almost exclusively based on 2D treatments. As singular points, realistic null points are intrinsically 3D, and as we will see, the surrounding fieldline geometry is very much different to that of a 2D null point (which physically, in 3D, could only represent the topologically unstable infinite null line). Since 2D and 3D null point configurations are topologically distinct, it is unclear to what extent 2D theory carries over to the more physical 3D case, and whether these results hold at all.

In the concluding remarks of a recent review of wave-null theory (McLaughlin et al. 2011b), the authors stressed that, in light of the above, the nature of MHD wave behaviour at 3D nulls was an important outstanding question which should be addressed. As the 2D theory suggests that wave-null interaction is a fundamental plasma process with important consequences for coronal physics, it is crucial to determine whether this is the case for realistic 3D nulls. Specifically; at the beginning of this PhD/thesis it was unclear how the waves will propagate at fully 3D null points, whether the 3D nature facilitates geometric coupling between differing modes of oscillation, and whether the 3D nulls are sufficiently inhomogeneous to facilitate nonlinear mode conversion. By the end of this thesis, we will have answers to these questions.

The introduction chapter is structured as follows. In the next subsection, the solar atmosphere is discussed. Subsequently, in Section 1.3, we outline the magnetohydrodynamical framework which underpins the research presented in this thesis. Then, we discuss the fundamentals of MHD wave theory in Section 1.4 and the prevalence and structure of magnetic null points in Section 1.5. Finally, in Section 1.6 we discuss the numerical scheme used.

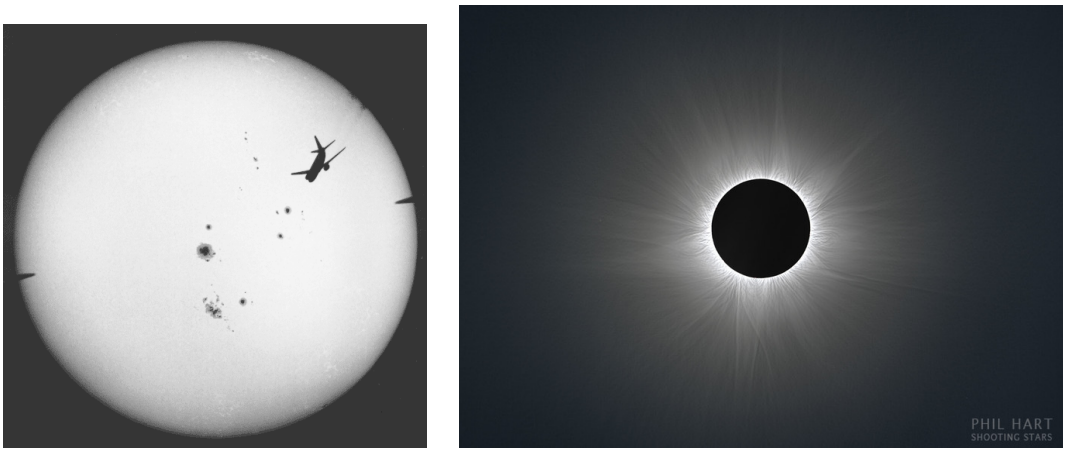

Figure 1.1: The Sun in visible light. *Left*: A simple photograph of the Sun, taken on July 25^{th} 1991 by the Ellerman telescope at Mt. Wilson Observatory (© UCLA). Sunspots (and an airliner!) are clearly visible. *Right*: A photograph taken in Queensland during the November 2012 total solar eclipse (© Phil Hart photography). During such events, the moon acts as a natural coronagraph and blocks the bright photosphere.

1.2 The Solar Atmosphere

In visible light, it appears that the Sun has a well-defined surface, with no apparent atmosphere (Figure 1.1, left). It appears mostly smooth and uniform, barring the presence of very large, dark features (*sunspots*) which can be observed to emerge, move and eventually disappear. This ostensibly 'hard' surface (*photosphere*) is somewhat of an illusion. Essentially a ball of gas, the Sun does not have a physical surface surrounded by a well-defined, finite atmosphere in the same sense as here on Earth. Rather, the Sun extends throughout the whole solar system, with its gases becoming increasingly tenuous and rarefied. In a sense, we on Earth exist within the solar atmosphere, as do all bodies within the solar system. This apparent surface is the manifestation of the interface between the outermost layer of the Sun where the gas is opaque, beyond which further regions are transparent. When a solar eclipse occurs, the moon perfectly occults this surface, blocking its light, and reveals the presence of a more tenuous 'outer atmosphere' which extends out into the solar system (Figure 1.1, right).

At around a few hundred kilometres thick and with an effective temperature of around $5780K$ and a mass density of about $2 \times 10^4 \,\mathrm{kg\,m^{-3}}$, the photosphere is a thin region which separates the solar interior (where the gases are dense, and gravitational, convective and radiative processes dominate) and the more diffuse exterior, where magnetism (generated by interior dynamo processes) is comparatively much more important. The *chromosphere* sits immediately above the photosphere, where temperature steadily rises and density falls over the course of a few hundred kilometres. At an altitude of around 2200km, the atmosphere undergoes a sharp jump in temperature, which increases by many orders of magnitude. This *transition region* separates the chromosphere from

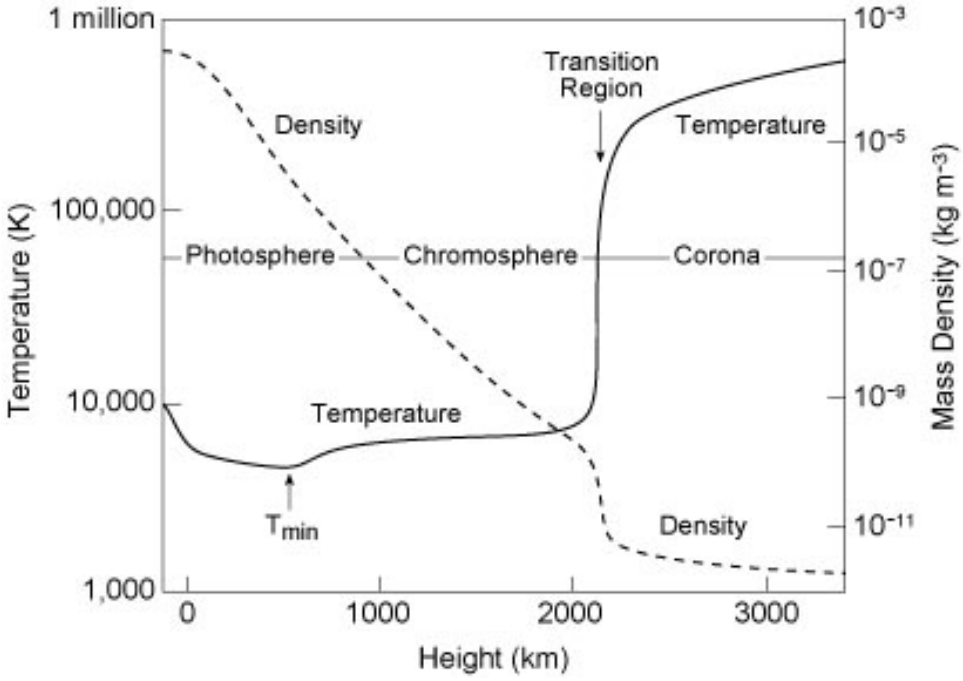

Figure 1.2: The change in temperature and mass density at different altitudes in the solar atmosphere (from Lang 2001).

the *solar corona*, with high temperatures ranging from hundreds-of-thousands to a few million degrees Kelvin.

The corona is a highly variable, structured and dynamic layer of the atmosphere, where the material is extremely diffuse and fully ionised due to the high temperatures. When observed in various wavelengths (corresponding to different temperature bands) we find a host of coronal features. The most iconic is arcades of *coronal loops* (Figure 1.3). Typically anchored in photospheric sunspots, these features are bundles of closed magnetic fieldlines that have erupted from the solar surface and subsequently filled with plasma. Thus, in a sense they are magnetic fieldlines made visible. Aside from the loops, we observe a myriad of coronal structures and phenomena, including more violent events such as *solar flares* and *coronal mass ejections*.

One key motivation for studying the physics of the solar atmosphere is to address the so-called *coronal heating problem*, a long-outstanding question in astrophysics. Why does the temperature increase, rather than decrease, with altitude? Why is the corona so much hotter than the photosphere? Currently, there are two popular mechanisms thought likely to contribute to coronal heating; magnetic reconnection and wave heating. As the work in this thesis concerns the behaviour of waves around nulls (which is associated with reconnection), our results not only contribute to the specific question of how waves and nulls interact, but also contribute (in a broad sense) to our understanding of the coronal heating problem.

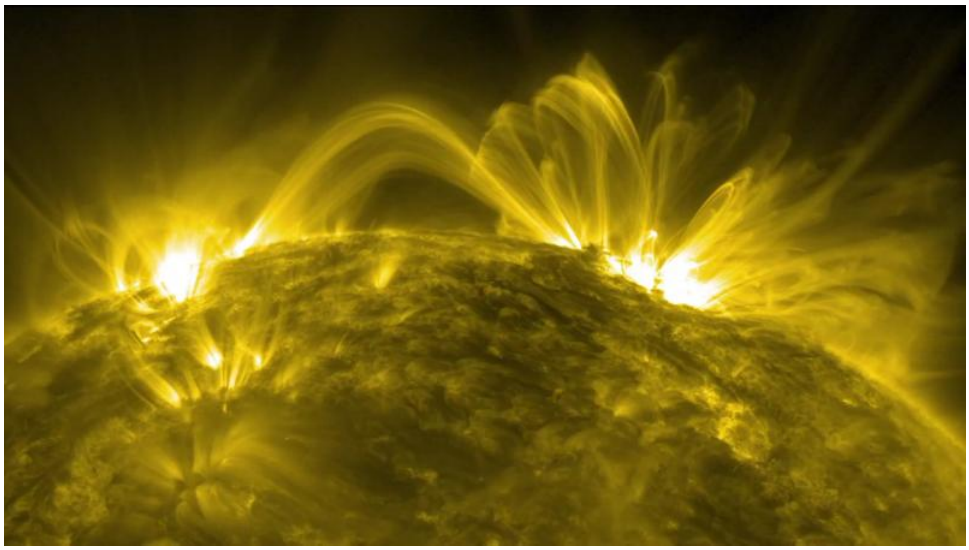

Figure 1.3: The solar corona observed in 171 Å by the Atmospheric Imaging Assembly (AIA) aboard the Solar Dynamics Observatory (SDO) on the 12^{th} July 2012.

1.3 Magnetohydrodynamics

The study of electrically conducting, macroscopic fluids is known as *magnetohydrodynamics* (MHD), a field which exists on the interface between continuum mechanics and electromagnetism. Since examples of electrically conducting fluids are abundant (including plasmas, liquid metals, salt water and electrolytes), MHD is a widely applied and important discipline. Compared to other classical theories MHD is relatively young, having rapidly developed over the last 70-or-so years. Much of this development has been motivated by its huge bearing on theoretical astrophysics (plasmas are estimated to account for over 99% of ordinary matter in the visible universe, Gurnett & Battarcharjee 2005), and also its applicability to plasma-confinement issues for controlled thermonuclear fusion. In solar physics, MHD models are widely applicable and produce plausible results. In this thesis, the applicability of single fluid MHD is assumed. In practice, this means that we consider plasmas where:

- characteristic speeds are much less than the speed of light,
- characteristic time scales are larger than the plasma period, gyroperiod and the collisional time scale,
- characteristic spatial scales are longer than the mean free path,

which is usually appropriate in the corona. Formal discussions regarding the applicability of single-fluid MHD to plasma phenomena may be found in, e.g., Boyd & Sanderson (2003), Goedbloed and Poedts (2004), and Schnack (2009).

1.3.1 MHD Equations

The MHD equations corresponding to an inviscid, resistive MHD medium are:

Equation of Motion

$$\rho\left[\frac{\partial \mathbf{v}}{\partial t} + (\mathbf{v}\cdot\nabla)\,\mathbf{v}\right] = -\nabla p + \mathbf{j}\times\mathbf{B} + \rho\mathbf{g} \quad , \tag{1.1}$$

Mass Conservation

$$\frac{\partial \rho}{\partial t} + \nabla\cdot(\rho\mathbf{v}) = 0 \quad , \tag{1.2}$$

Adiabatic Energy Equation

$$\frac{\partial p}{\partial t} + \mathbf{v}\cdot\nabla p = -\gamma p \nabla\cdot\mathbf{v} \quad , \tag{1.3}$$

Ideal Gas Law

$$p = \frac{R}{\hat{\mu}}\rho T \quad , \tag{1.4}$$

Ampére's Law

$$\mu\mathbf{j} = \nabla\times\mathbf{B} \quad , \tag{1.5}$$

Solenodial Condition

$$\nabla\cdot\mathbf{B} = 0 \quad , \tag{1.6}$$

Faraday's Law

$$\frac{\partial \mathbf{B}}{\partial t} = -\nabla\times\mathbf{E} \quad , \tag{1.7}$$

Ohm's Law

$$\frac{\mathbf{j}}{\hat{\sigma}} = \mathbf{E} + \mathbf{v}\times\mathbf{B} \quad , \tag{1.8}$$

where $\mathbf{v}$ is fluid velocity, ρ is density, p is pressure, $\mathbf{B}$ is the magnetic induction (often refereed to as magnetic field), $\mathbf{E}$ is electric field, $\mathbf{g}$ is gravitational acceleration, $\mathbf{j}$ is the electric current density, T is the temperature, μ is the magnetic permeability, R is the universal gas constant, $\hat{\mu}$ is the mean atomic weight (average mass per particle in units of mass of a proton), $\hat{\sigma}$ is electric

conductivity and γ is the ratio of specific heats.

These governing equations can be derived in two ways. One way is to postulate that a conducting fluid, when interacting with an electromagnetic field, must be governed by both the equations of fluid dynamics and the equations of electromagnetism, appropriately coupled. Alternatively, one constructs an appropriate statistical, kinetic description of the medium, then derives the fluid equations by taking moments of the Boltzman equation. Both approaches are presented in great detail in the textbook of Goedbloed & Poedts (2004). It is readily apparent to those familiar with electromagnetism and fluid dynamics that equations (1.1–1.8) are essentially a union of the Navier-Stokes equations and Maxwell's Equations.

1.3.2 Induction Equation

In solar MHD, it is usual to eliminate the electric field $\mathbf{E}$ and the electric current density $\mathbf{j}$ and choose to work with $\mathbf{B}$ and $\mathbf{v}$. Using equations (1.5) and (1.8) the variable $\mathbf{E}$ is removed from equation (1.7), yielding:

$$\frac{\partial \mathbf{B}}{\partial t} = -\nabla \times \left(-\mathbf{v} \times \mathbf{B} + \frac{\nabla \times \mathbf{B}}{\mu \hat{\sigma}} \right) . \tag{1.9}$$

Denoting the resistivity $\eta = (\mu\hat{\sigma})^{-1}$ (assumed constant in this thesis), and employing the vector calculus identity $\nabla \times (\nabla \times \mathbf{B}) = \nabla (\nabla \cdot \mathbf{B}) - \nabla^2 \mathbf{B}$ (also noting that $\nabla \cdot \mathbf{B} = 0$), equation (1.9) can be expressed as

$$\frac{\partial \mathbf{B}}{\partial t} = \nabla \times (\mathbf{v} \times \mathbf{B}) + \eta \nabla^2 \mathbf{B} . \tag{1.10}$$

which is known as the induction equation. The $\nabla \times (\mathbf{v} \times \mathbf{B})$ term is associated with advection of magnetic induction and the $\eta \nabla^2 \mathbf{B}$ term is associated with magnetic diffusivity.

1.3.3 Resistive and Ideal MHD

We can evaluate the relative importance of the advection and diffusion terms in the induction equation by considering the magnetic Reynolds number

$$R_m = \frac{L\bar{v}}{\eta} \tag{1.11}$$

where L is a typical length scale for the plasma, $\bar{v}$ is a typical plasma velocity and η is the magnetic diffusivity. Typically, in the solar atmosphere we consider large length and velocity scales and thus R_m is usually large. In this thesis, we assume that $R_m \gg 1$ and thus the induction equation simplifies to

$$\frac{\partial \mathbf{B}}{\partial t} = \nabla \times (\mathbf{v} \times \mathbf{B}) \ .$$

This $\eta = 0$ approximation corresponds to the case of a perfectly conducting medium, otherwise known as ideal MHD (when the diffusion term is also considered, the regime is referred to as resistive MHD). In ideal MHD, Alfvén's frozen-flux theorem (Alfvén 1942) applies; which stipulates that the magnetic fieldlines and fluid move in unison (i.e., fieldlines correspond to a particular fluid element) and that the fieldlines are frozen into the plasma (for the proof, see, e.g., Schnack 2009).

1.3.4 Scale Height Argument

The scale height H_0 is defined as

$$H_0 = \frac{p_0}{\rho_0 \, g} \ ,$$

where p_0 and ρ_0 are the typical pressure and density of the system (see, e.g., Priest 1982). The scale height indicates how quickly the variables change under the effect of gravity. When modelling systems that have typical length scales that are much less than this measure, $L \ll H_0$ we may neglect gravitational forces. In this thesis, all the problems considered will ignore gravitational effects.

1.3.5 The magnetic field in MHD

In MHD, the magnetic field acts as a source of anisotropy and inhomogeneity in the medium, unlike in fluid dynamics which usually deals with isotropic, homogeneous media. As we will see later, magnetic topology can vary in complexity, ranging from fairly simple, curvilinear features to highly complicated configurations, namely the magnetic null points considered in this thesis. The solar atmosphere is clearly highly structured by the magnetic fields, as evident in observations such as Figure 1.3, where the coronal loops are in a sense 'fieldlines made visible'. In the corona the magnetic field acts to exert forces, store and release energy, whilst providing structure and stability. The central role played by the magnetic field and forces in MHD is reflected in the convention of favouring treatments with $\mathbf{B}$ as the primary variable, as opposed to $\mathbf{E}$ (as is more typical in the theory of electromagnetism).

Lorentz Force

Conducting fluids experience a volumetric force due to the action of electromagnetic fields on their constituent charges known as the *Lorentz force*. Exploiting Ampere's law (1.5), it may be expressed purely in terms of magnetic induction

$$\mathbf{F} = \mathbf{j} \times \mathbf{B} = \frac{1}{\mu} (\nabla \times \mathbf{B}) \times \mathbf{B} \tag{1.12}$$

$$= \frac{1}{\mu} (\mathbf{B} \cdot \nabla) \mathbf{B} - \nabla \left(\frac{\mathbf{B} \cdot \mathbf{B}}{2\mu} \right) \tag{1.13}$$

Equation (1.13) indicates that the force can be considered to comprise of an elastic component and a pressure gradient component. The magnetic tension $(\mathbf{B} \cdot \nabla)\mathbf{B}$ acts to straighten magnetic field-lines, and the magnetic pressure gradient $\nabla (\mathbf{B} \cdot \mathbf{B})$ acts to evenly distribute magnetic induction throughout the medium.

The Lorentz force does not act along the magnetic field ($\mathbf{F} \cdot \mathbf{B} = 0$) as the magnetic pressure gradient and magnetic tension along the field always cancel. The perpendicular action of the Lorentz force contributes to the anisotropic nature of MHD. Later in this thesis, the distinction between motions longitudinal and transverse to the field, and the underlying driving/restoring forces, will be particularly important.

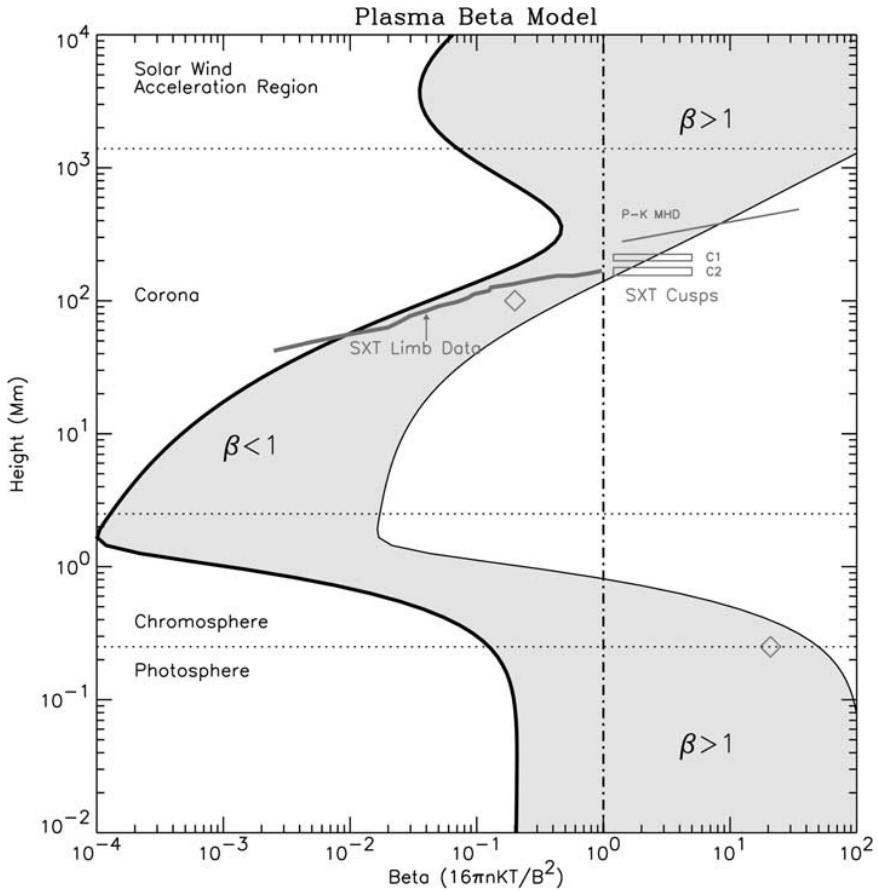

Figure 1.4: Estimates of plasma-β ranges in a solar atmosphere (Gary 2001). The values (shaded region) are obtained between assumed field strengths of 2500 G (left) and 100 G (right).

Plasma-β

For a given MHD scenario, the plasma-β provides a measure of the relative importance of thermodynamic and electromagnetic forces on the fluid motion. It is defined as

$$\beta = \frac{\text{gas pressure}}{\text{magnetic pressure}} = \frac{p_0}{B_0^2/2\mu}. \tag{1.14}$$

Where $\beta \ll 1$, magnetism is dominant, whereas at higher values it is less important. In the limits, $\beta = 0$ describes a magnetic-only regime (a 'cold plasma') whereas $\beta = \infty$ describes a hydrodynamic medium. Figure 1.4 illustrates how the plasma-β varies through different regions of the solar atmosphere. Often, it is appropriate to use a zero-β approximation in the mathematical treatment of small-β plasmas, neglecting gas-pressure and simplifying the equations. From Figure 1.4, we see that in much of the chromosphere and corona $\beta \ll 1$.

1.4 MHD Waves

In the past few decades, an abundance of observational data from solar instruments including *SOHO* (e.g. Ofman et al. 1997; DeForest & Gurman 1998), *TRACE* (e.g. Nakariakov et al. 1999; De Moortel et al. 2000), *Hinode* (e.g. Ofman & Wang 2008), *SDO* (e.g. Morton et al. 2012) and recently *Hi-C* (Morton & McLaughlin 2013) has unequivocally confirmed the existence of MHD wave motions in the coronal plasma. Here, we discuss the properties and basic theory of MHD waves.

1.4.1 Properties of MHD Waves

MHD wave behaviour is richer than hydrodynamics due to the inclusion of the Lorentz force. Magnetic tension provides an elastic restoring force, which sustains transverse disturbances along the magnetic field in much the same way as a wave on a string. Such disturbances propagate with the characteristic speed

$$c_A = \frac{B}{\sqrt{\mu\rho}} \tag{1.15}$$

where c_A is known as the Alfvén speed. The magnetic pressure gradient facilitates longitudinal wave motions at the same speed. Gas-pressure disturbances propagate at the sound speed

$$c_S = \sqrt{\frac{\gamma p}{\rho}} \quad . \tag{1.16}$$

The interaction between these different forces results in a variety of differing modes of oscillation. In general there are three such modes; the Alfvén mode, the fast magnetoacoustic mode, and the slow magnetoacoustic mode. Each mode is in differing ways anisotropic and propagates at its own characteristic speed. The magnetoacoustic waves arise from the interaction of the magnetic and gas forces, resulting in the (relatively) higher frequency fast mode and the lower frequency slow mode. The Alfvén wave, named for Hannes Alfvén following his 1942 paper, is purely tension-driven and incompressive. The specific properties of these modes, and whether they couple and interact, varies according to various factors including;

- The value of β, which can be expressed in terms of characteristic speeds as $\beta = \frac{2}{\gamma}\left(\frac{c_S}{c_A}\right)^2$
- The geometry and structuring of the medium. For example, for embedded magnetic structures the waves are manifest as body-waves which are evanescent outside the structure (e.g., the kink and sausage waves described by Edwin & Roberts 1983), and surface modes occur on the interface (e.g. Goossens et al. 2012). Addionally, modes may be coupled through

Mode of Oscillation	plasma-$\beta \gg 1$ (high-β)	plasma$-\beta \ll 1$ (low-β)
Alfvén	Transverse wave propagating along fieldlines at speed c_A	
Fast Magnetoacoustic	Behaves like sound wave, propagating roughly isotropically at speed $\approx c_S$	Propagates roughly isotropically, travelling along and across fieldlines at speed $\approx c_A$
Slow Magnetoacoustic	Highly anisotropic, guided along $\mathbf{B}$ at speed $\approx c_A$	Highly anisotropic, guided along $\mathbf{B}$ at speed $\approx c_S$

Table 1.1: Properties of MHD waves depending on the plasma$-\beta$.

processes such as resonant absorption (e.g. Goosens et al. 2011). In regions of cross-field inhomogeneity, phase mixing phenomena can alter and enhance the dissipative properties of MHD waves (e.g. Heyvaerts & Priest 1983).

- The nonlinearity of the regime. Where amplitudes are high and nonlinear terms are important, wave modes can be coupled (e.g., Nakariakov et al. 1997, Thurgood & McLaughlin 2013a) and shocks can develop (e.g. Friedrichs 1957).

Mathematical analysis of tractable 2.5D [1] cases with uniform magnetic field and homogeneous density profiles gives an insight into the general properties of these waves (see Section 1.4.2). The general properties of the differing modes is summarised for the two β-limits in Table 1.1. Typically, the behaviour of waves in more complicated media are understood and interpreted in terms of nomenclature and properties originating in idealistic models.

1.4.2 Waves in Linear, Homogeneous and Ideal 2.5D MHD

We wish to consider the case of MHD waves propagating through a homogeneous, flow-free background medium which contains a unidirectional field of uniform strength that arbitrarily runs

[1] In the context of this thesis, '2.5D' refers to an analysis where variables are considered to change only in two dimensions, but perturbations are permitted in all three dimensions. See e.g. the analysis in Section 1.4.2.

in the $\hat{\mathbf{y}}$-direction. The equilibrium fluid variables are

$$\mathbf{v}_0 = \mathbf{0}\,, \qquad \mathbf{B}_0 = B_0\hat{\mathbf{y}}\,, \qquad \nabla p_0 = \nabla\rho_0 = \mathbf{0}\,. \tag{1.17}$$

Note that this corresponds to a force-free equilibrium (as opposed to force-balance), as gas pressure gradients are zero and the field is potential, and thus exerts no Lorentz force.

We begin by linearising equations (1.1), (1.2), (1.3) and (1.10) (with $\eta = 0$) by considering finite-amplitude perturbations of the form $\mathbf{B} = \mathbf{B}_0 + \varepsilon\mathbf{b}(\mathbf{r},t)$, $\mathbf{v} = \mathbf{0} + \varepsilon\mathbf{v}_1(\mathbf{r},t)$, $\rho = \rho_0 + \varepsilon\rho_1(\mathbf{r},t)$, and $p = p_0 + \varepsilon p_1(\mathbf{r},t)$. The amplitude of the perturbation is considered small ($0 < \varepsilon \ll 1$) and thus we neglect terms of $\mathcal{O}(\varepsilon^2)$ and higher in the following analysis. The resulting linearised ideal MHD equations are

$$\rho_0\frac{\partial\mathbf{v}_1}{\partial t} = -\nabla p_1 + \frac{1}{\mu}(\nabla\times\mathbf{b})\times\mathbf{B}_0\,, \tag{1.18}$$

$$\frac{\partial\mathbf{b}}{\partial t} = \nabla\times(\mathbf{v}_1\times\mathbf{B}_0)\,, \tag{1.19}$$

$$\frac{\partial\rho_1}{\partial t} = -\nabla\cdot(\rho_0\mathbf{v}_1)\,, \tag{1.20}$$

$$\frac{\partial p_1}{\partial t} = -\gamma p_0\,(\nabla\cdot\mathbf{v}_1)\,. \tag{1.21}$$

Taking the time-derivative of (1.18) and introducing (1.19) and (1.21), for the equilibrium (1.17) and recognising the sound and Alfvén speeds yields

$$\frac{\partial^2\mathbf{v}_1}{\partial t^2} = c_S^2\nabla(\nabla\cdot\mathbf{v}_1) - c_A^2\{\nabla\times[\nabla\times(\mathbf{v}_1\times\hat{\mathbf{y}})]\}\times\hat{\mathbf{y}}\,. \tag{1.22}$$

We now decompose the wave equation (1.22) into its xyz-components such that $\mathbf{v}_1 = (v_x, v_y, v_z)$, and simplify to a 2.5D case by permitting perturbations in the z-direction, but imposing the condition that they must be translationally invariant, i.e. $\partial/\partial z = 0$ throughout. This yields

$$\frac{\partial^2 v_x}{\partial t^2} = c_S^2\frac{\partial}{\partial x}\left(\frac{\partial v_x}{\partial x} + \frac{\partial v_y}{\partial y}\right) + c_A^2\left(\frac{\partial^2}{\partial x^2} + \frac{\partial^2}{\partial y^2}\right)v_x \tag{1.23}$$

$$\frac{\partial^2 v_y}{\partial t^2} = c_S^2\frac{\partial}{\partial y}\left(\frac{\partial v_x}{\partial x} + \frac{\partial v_y}{\partial y}\right) \tag{1.24}$$

$$\frac{\partial^2 v_z}{\partial t^2} = c_A^2\frac{\partial^2 v_z}{\partial y^2} \tag{1.25}$$

Plane wave solutions such that

$$\mathbf{v}_1(\mathbf{r},t) = \mathbf{v}_1\exp\left[i(\mathbf{k}\cdot\mathbf{r} - \omega t)\right] \tag{1.26}$$

where ω is the frequency and $\mathbf{k} = (k_x, k_y, k_z)$ is the wavevector (with total wave number $k^2 =$

$k_x^2 + k_y^2 + k_z^2$) are now calculated. This sets the derivative operators $\partial/\partial x = ik_x$, $\partial/\partial y = ik_y$ and $\partial/\partial t = -i\omega$. The plane wave solution to the set of wave equations now reduces to a set of simultaneous equations which are (in matrix form)

$$\begin{bmatrix} \omega^2 - k^2 c_A^2 - k_x^2 c_S^2 & -k_x k_y c_S^2 & 0 \\ -k_x k_y c_S^2 & \omega^2 - k_y^2 c_S^2 & 0 \\ 0 & 0 & \omega^2 - k_y^2 c_A^2 \end{bmatrix} \begin{bmatrix} v_x \\ v_y \\ v_z \end{bmatrix} = \begin{bmatrix} 0 \\ 0 \\ 0 \end{bmatrix} \tag{1.27}$$

to which non-trivial solutions may be found where the determinant is zero. The solution

$$\left(\omega^2 - k_y^2\, v_A^2\right)\left[\omega^4 - \omega^2\left(c_S^2 + v_A^2\right)k^2 + k^2\, k_y^2\, c_S^2\, v_A^2\right] = 0\,, \tag{1.28}$$

is the dispersion relationship for MHD waves in the medium described, where its roots correspond to the different MHD modes. Noting that k_y is the wavevector component along the equilibrium magnetic field and recognising that it can be expressed as $k_y = k\cos\theta$ where θ is the angle the wavevector makes with $\mathbf{B}_0 = B_0\hat{\mathbf{y}}$, the roots are as follows:

$$\frac{\omega^2}{k^2} = c_A^2\cos^2\theta\,, \tag{1.29}$$

$$\frac{\omega^2}{k^2} = \frac{1}{2}\left(c_A^2 + c_S^2\right) \pm \frac{1}{2}\sqrt{\left(c_A^2 + c_S^2\right)^2 - 4c_S^2 c_A^2\cos^2\theta}\,. \tag{1.30}$$

First, let us discuss equation (1.30), which corresponds to magnetoacoustic waves which come about due to interaction of both gas-pressure gradients and the Lorentz force (as evidenced by the dependence on both c_S and c_A). The higher-frequency solution of (1.30) corresponds to the fast magnetoacoustic wave, whereas the lower-frequency solution corresponds to the slow magnetoacoustic waves. Respectively, they can be thought of as due to the constructive and destructive interference between the gas and magnetic restoring forces. In Figure 1.5, which shows phase-speed for the different MHD modes according to the direction of propagation relative to the equilibrium magnetic field, we can see that both of these modes are anisotropic. The fast wave can propagate along magnetic fieldlines at the Alfvén speed and across magnetic fieldlines at the fast speed $c_F^2 = c_S^2 + c_A^2$, whereas the slow wave can only propagate along the field at the sound speed.

Equation (1.29) corresponds to the Alfvén wave, which propagates only along the fieldlines at the Alfvén speed, and cannot cross magnetic fieldlines. We see from the dispersion relationship that it is independent of sound-speed, and is thus exclusively a magnetically-driven wave. If, in the derivation of equation (1.25), one tracks the contribution of magnetic tension and magnetic pressure, we see that the Alfvén wave is exclusively driven by magnetic tension, and is thus a

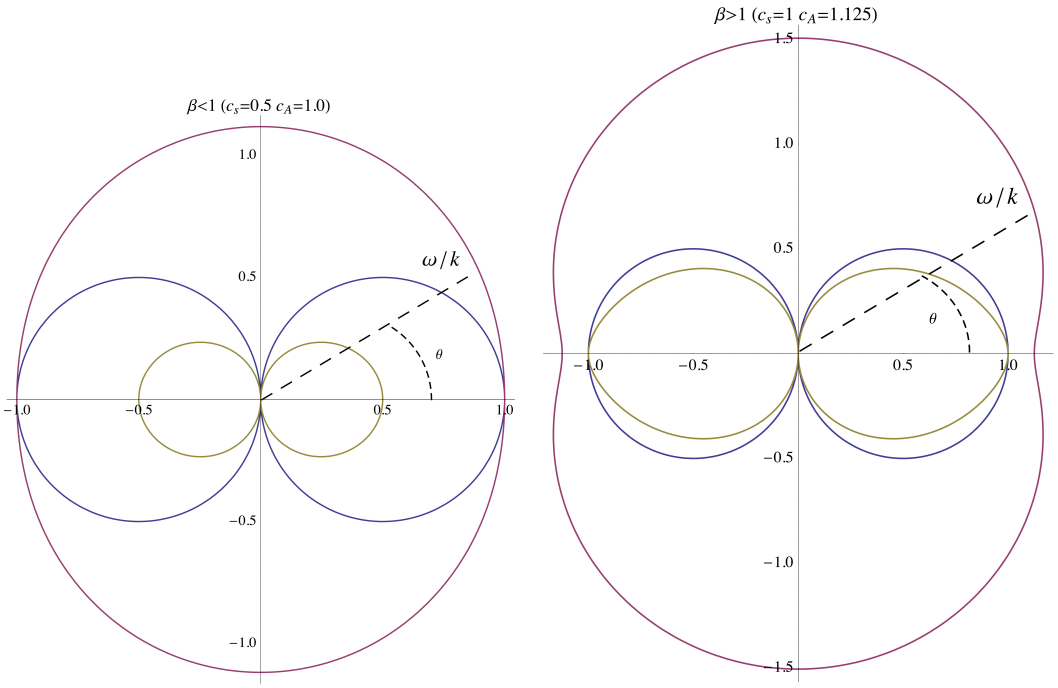

Figure 1.5: Polar plot showing how the phase-speeds of MHD waves vary according to the direction of propagation relative to the background magnetic field. The purple, blue and green plots correspond to the fast, Alfvén and slow magnetoacoustic waves respectively.

purely transverse wave. Therein lies an important distinction between MHD and fluid dynamics; Schnack (2009) defines a fluid as

> A fluid is a substance that resists an applied compressive stress, but continually deforms, or flows, under an applied shear stress, regardless of the magnitude of the applied stress.

However, we see that when fluids are electrically conducting that magnetic tension acts to resist such shearing motions, resulting in an elastic restoring force which drives the Alfvén wave. Thus, the Alfvén wave is an incompressible, purely shear magnetic wave.

The attenuation of a linear MHD wave is primarily due to viscous and resistive dissipation, which deposits wave energy as viscous and ohmic heating. The single-fluid viscous force is of the form (Priest 1982, Aschwanden 2004 and Goedbloed & Poedts 2004)

$$\mathbf{F}_{\text{visc.}} = \nu\rho\left[\nabla^2\mathbf{v} + \frac{1}{3}\nabla\left(\nabla\cdot\mathbf{v}\right)\right] \tag{1.31}$$

where ν is the kinematic viscosity coefficient, $\nabla^2\mathbf{v}$ is dynamic (shear) viscosity and $\nabla\left(\nabla\cdot\mathbf{v}\right)$ is bulk viscosity. For an Alfvén wave (polarised in the direction $\hat{\mathbf{z}}$ as in the preceding analysis, i.e.

associated with v_z and b_z) we can approximate the viscous damping time as

$$\frac{v_z}{\tau_{\text{visc.}}} \approx \frac{D\mathbf{v}}{Dt} \cdot \hat{\mathbf{z}} \approx \frac{\mathbf{F}_{\text{visc.}}}{\rho} \cdot \hat{\mathbf{z}} \longrightarrow \tau_{\text{visc.}} \approx \frac{v_z}{\nu \left[\nabla^2 \mathbf{v} + \frac{1}{3}\nabla\left(\nabla \cdot \mathbf{v}\right)\right]} \cdot \hat{\mathbf{z}} \quad . \tag{1.32}$$

Similarly, we can approximate the resistive damping times from the induction equation (equation 1.10, with the diffusivity term only)

$$\frac{b_z}{\tau_{\text{res.}}} \approx \frac{\partial \mathbf{B}}{\partial t} \cdot \hat{\mathbf{z}} \approx \eta \nabla^2 \mathbf{B} \cdot \hat{\mathbf{z}} \longrightarrow \tau_{\text{res.}} \approx \frac{b_z}{\eta \nabla^2 \mathbf{B}} \cdot \hat{\mathbf{z}} \quad . \tag{1.33}$$

Noting the incompressibility ($\nabla \cdot \mathbf{v} = 0$), we find that these resistive time scales are

$$\tau_{\text{visc.}} \approx \frac{v_z}{\nu \left[\left(\frac{\partial^2}{\partial x^2} + \frac{\partial^2}{\partial y^2}\right) v_z\right]} \tag{1.34}$$

$$\tau_{\text{res.}} \approx \frac{b_z}{\eta \left[\left(\frac{\partial^2}{\partial x^2} + \frac{\partial^2}{\partial y^2}\right) b_z\right]} \tag{1.35}$$

Since typical coronal values of ν and η are small, to efficiently dissipate energy the Alfvén wave must possess large gradients (or, these parameters must somehow be anomalously large). Therefore, a typical 'text-book characterisation' of the purely magnetic Alfvén wave is that of a wave that can efficiently transport energy (from, say, the photosphere to the corona) but cannot readily dissipate said energy (to, say, thermal energy to heat the corona). Given the possible role played by these waves in coronal heating and solar wind acceleration, there is interest in exploring ancillary processes which allow Alfvén waves to deposit energy more readily. Examples could include direct mechanisms which cause Alfvén waves to develop large gradients, such as phase mixing (a process whereby strong transverse gradients develop due to propagation through an inhomogeneous background, see e.g. Heyvaerts & Priest 1983), or due to the 'null-point trapping' effect we will encounter in the coming chapters. Alternatively, efficient dissipation can be achieved through other indirect mechanisms such as mode-conversion processes which allow the wave to change to a compressive mode which is more dissipative due to bulk viscosity.

Finally, it is interesting to note that this 'text-book picture' of the Alfvén wave as a poor dissapator may prove to be somewhat misleading. Many studies indicate a prevalence of plasma inhomogeneity in the solar atmosphere, which appear to be consistent with the conditions required to facilitate the aforementioned processes. For instance, Hahn & Savin (2013) recently found that non-thermal velocities[2] measured along off-limb solar polar plumes (open-field magnetic structures) fall short of the expected trend for undamped Alfvén waves with increasing altitude, and interpreted this data as evidence of Alfvén wave damping at sufficiently low altitudes to permit

[2] which are thought to be a spectroscopic signature of Alfvén waves, although other mass motions of the line of sight could contribute.

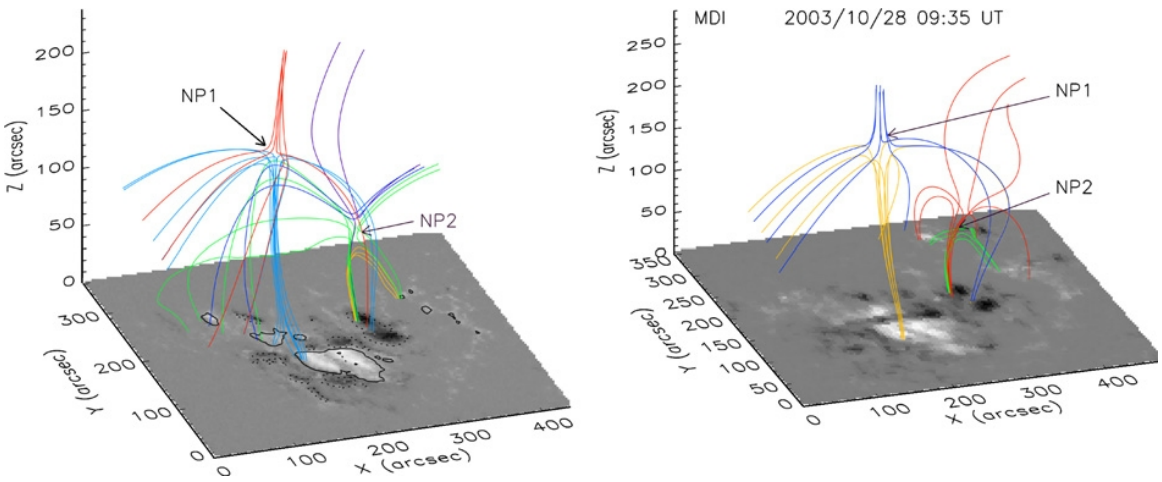

Figure 1.6: Field extrapolations from active region magnetograms indicate the presence of nulls in the large scale magnetic structure above the region, Schmieder et al. (2007)

energy contributions to coronal heating and solar wind acceleration.

1.5 Magnetic Null Points

Magnetic null points are special topological locations where magnetic induction drops off to be zero. Null points naturally occur wherever there are multiple sources of magnetic flux. In the solar atmosphere many isolated sources of flux emerge through the photospheric surface, and as such null points are expected to be present in the solar atmosphere. Direct observations of solar magnetic null points are elusive, although compelling indirect evidence for their existence can be inferred from photospheric magnetograms, where various field-extrapolation schemes result in topologies containing null points (see, e.g., Brown & Priest 2001, Beveridge et al. 2002, and Figure 1.6). Three papers have considered the prevalence of null points in the solar atmosphere. Close et al. (2004) and Régnier et al. (2008) considered potential field extrapolations of (different) magnetogram data and found 1.7×10^{-3} and 6.7×10^{-3} null points per square megameter respectively. Longcope and Parnell (2009) examined the Fourier spectra of 562 magnetograms and estimated $3.1\times10^{-3}\pm3.0\times10^{-4}$ nulls per square megameter. McLaughlin et al. (2011b) point out that, if these results are multiplied by the surface area of the sun, approximately $10,000-40,000$ null points exist in the (quiet) solar corona, and thus are relatively common features.

Null points are categorised according to the topology of the local magnetic field configuration, of which many fieldline geometries are possible (cf. the field around the different nulls in Figure 1.6). The different classifications of null point have been catalogued by Parnell et al. (1996). The authors begin by considering that near the null point (which in this thesis is arbitrarily located at

the origin), the field can be expressed in the form

$$\mathbf{B} = \mathbf{M} \cdot \mathbf{r} \tag{1.36}$$

where $\mathbf{r}$ is a position vector and the Jacobian matrix $\mathbf{M}$ approximates the local linear structure such that $M_{ij} = \partial B_i / \partial x_j$ as per Taylor series linearisation (thus the field decreases linearly on the approach to these null points). By analysing the different possible forms of $\mathbf{M}$, given that its eigenvalues may be interpreted in terms of current and flux, they determine the possible basic structure of nulls. In the following sections, we do not repeat their analysis, but outline the key points and discuss the properties of these different nulls.

1.5.1 2D Magnetic Null Points

In both 2D and 3D, an important distinction between different classes of null point is the distinction between those which are locally current free (*potential*) or current containing (*nonpotential*). Considering a 2D null which lies in the xy-plane, the current

$$\mathbf{j} = \frac{1}{\mu} \nabla \times \mathbf{B} = (0, 0, M_{21} - M_{12}) \tag{1.37}$$

is composed of the off-diagonal terms which do not cancel. The potential part of the field is described by the diagonal terms (which are constrained by the solenoidal condition such that $M_{11} = -M_{22}$), and parts of the off-diagonal terms which do cancel. We define $M_{11} = p$, and $M_{12} = \frac{1}{2}(q - j_z)$ and $M_{21} = \frac{1}{2}(q + j_z)$ so as to separate the potential and nonpotential off-diagonal components, thus the Jacobian is

$$\mathbf{M} = \begin{pmatrix} p & \frac{1}{2}(q - j_z) \\ \frac{1}{2}(q + j_z) & -p \end{pmatrix} \tag{1.38}$$

which has the eigenvectors

$$\lambda = \pm \frac{1}{2} \sqrt{4p^2 + q^2 - j_z^2} = \pm \frac{1}{2} \sqrt{j_{\mathrm{T}}^2 - j_z^2} \,. \tag{1.39}$$

Provided that the current j_z does not equal or exceed the threshold current $j_T = \sqrt{4p^2 + q^2}$, the eigenvalues are real, equal in magnitude and of opposite sign. By constructing the magnetic flux function ($\mathbf{A}$ such that $\mathbf{B} = \nabla \times \mathbf{A}$) we can determine the field-line structure of $\mathbf{B}$, as contours of $\mathbf{A}$ trace fieldlines. In such cases ($j_z < j_T$) the field is of the form of a hyperbolic fixed point (*X-point/type*), which is typical of 2D dynamical systems characterised by such eigenvectors (see e.g. Strogatz 1994).

For $j_z = 0$, the only potential configuration permitted in 2D, with appropriate choice of coordinate system the Jacobian can be rotated to further simpify. Using 2D Cartesian coordinates, the local magnetic field about the 2D null is therefore

$$\mathbf{B} = y\hat{\mathbf{x}} + x\hat{\mathbf{y}}\,, \tag{1.40}$$

or some rotation or translation thereof. The fieldlines are rectangular hyperbola and its separatrices (fieldlines which separate distinct topological regions, here the lines $x = y$ and $x = -y$) intersect at an angle of $\pi/2$, as shown in Figure 1.7a.

In the case of nonpotential nulls, provided the total current does not exceed the threshold current j_T ($0 < j_z < j_T$), the null remains hyperbolic but, as current increases, the angle between separatrices changes; such a null is shown Figure 1.7b. The angle is

$$\tan^{-1}\left(\frac{\sqrt{j_T^2 - |\mathbf{j}|^2}}{|\mathbf{j}|}\right) \quad ,$$

and thus, as $|\mathbf{j}| \to 0$ the fieldlines tend to the rectangular hyperbolic form with perpendicular separatrices, and as current increases the separatrices close up. At the threshold current itself, the eigenvalues become real, equal and zero-valued. Here, the two separatrices degenerate into one and the 'null-point' becomes a topologically unstable null line which acts as a separatrix between two regions of antiparallel, unidirectional field (Figure 1.7c).

Beyond the threshold current, eigenvalues become complex conjugates and so the null becomes a so-called O-type null (Figure 1.7d). This field-configuration is characterised by a null-point surrounded by circular fieldlines. Later, when discussing 2D wave-null theory, we confine our discussion to the X-type nulls as these $|\mathbf{j}| \geq j_T$ nulls are beyond the scope of our study (the $|\mathbf{j}| = j_T$ case does not correspond to a *point*, and the O-type null has no 3D analogue).

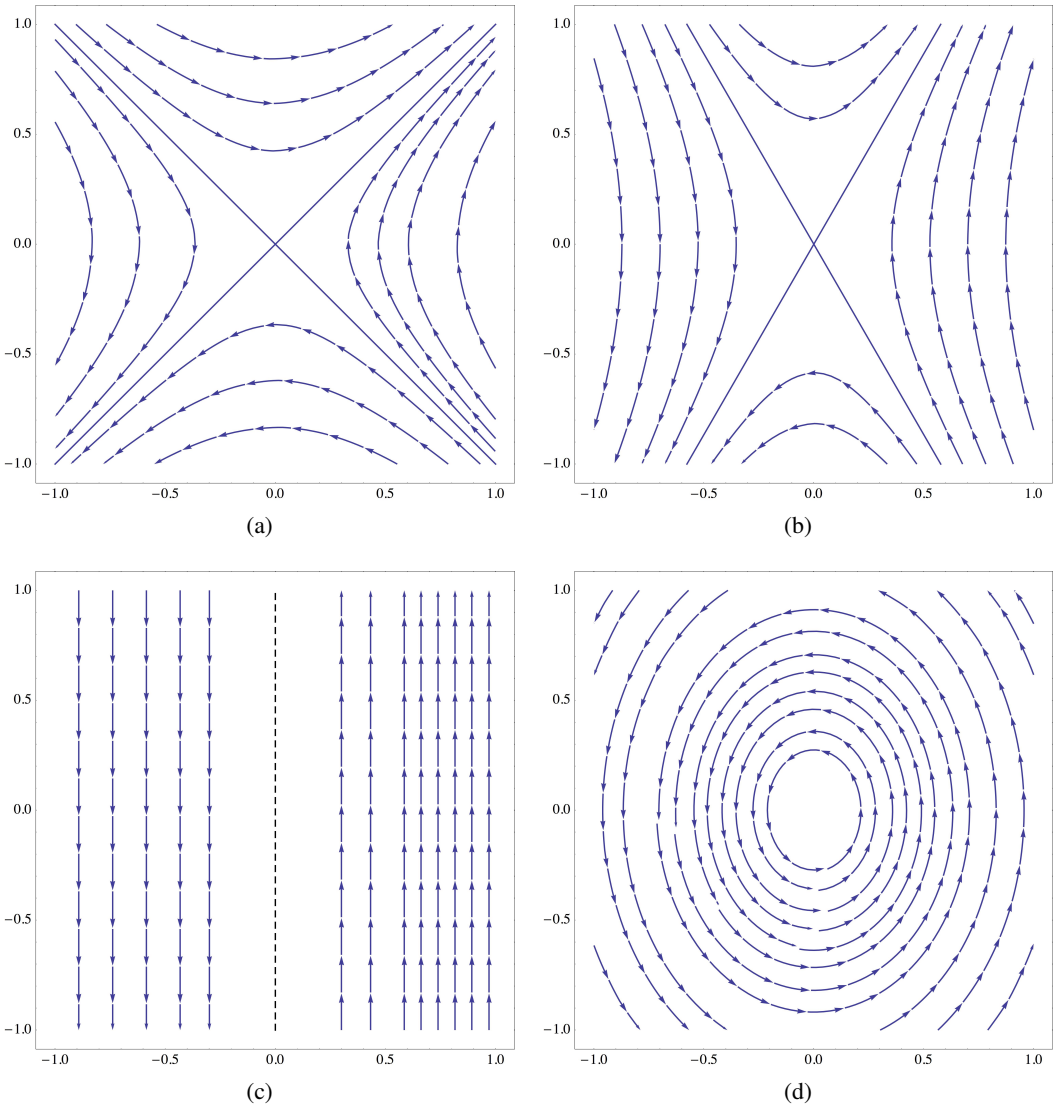

Figure 1.7: 2D field configurations about null points; (a) potential X-point; (b) nonpotential X-point; (c) nonpotential null line; (b) nonpotential O-point;

1.5.2 3D Magnetic Null Points

Following Equation (1.5) and Parnell et al. (1996), linear 3D Magnetic Null Points are described by a 3×3 matrix $\mathbf{M}$, with associated eigenvalues λ_1, λ_2, λ_3 and eigenvectors $\mathbf{x}_1$, $\mathbf{x}_2$, $\mathbf{x}_3$. We can describe a magnetic fieldline in terms of some position vector $\mathbf{r} = (x, y, z)^{\mathrm{T}}$ dependent on an arbitrary parameter k such that

$$\frac{d\mathbf{r}}{dk} = \mathbf{M} \cdot \mathbf{r} = \mathbf{B}\,. \tag{1.41}$$

If we make the substitution $\mathbf{r}(k) = \mathbf{P}\mathbf{u}(k)$ where $\mathbf{P}$ is the matrix of eigenvectors of $\mathbf{M}$ we can attempt to diagonalise

$$\frac{d\mathbf{u}}{dk} = \mathbf{P}^{-1}\mathbf{M}\mathbf{P}\mathbf{u}. \tag{1.42}$$

If $\mathbf{M}$ is diagonalisable to, say, $\mathbf{\Lambda}$, solutions are simply $\mathbf{u} = \exp(\mathbf{\Lambda}k)$ where $\mathbf{A}$ is a diagonal matrix of constants. This implies that

$$\mathbf{r}(k) = Ae^{\lambda_1 k}\mathbf{x}_1 + Be^{\lambda_2 k}\mathbf{x}_2 + Ce^{\lambda_3 k}\mathbf{x}_3\,. \tag{1.43}$$

Alternatively, if $\mathbf{M}$ is not diagonalisable (two repeated eigenvalues) it can be reduced to Jordan normal form which gives solutions

$$\mathbf{r}(k) = (A + Bk)e^{\lambda_1 k}\mathbf{x}_1 + Be^{\lambda_2 k}\mathbf{x}_2^* + Ce^{-2\lambda_3 k}\mathbf{x}_3\,. \tag{1.44}$$

which is also found in terms of eigenvalues, eigenvectors and a Jordan basis vector. By considering specific forms of $\mathbf{M}$, we can trace fieldlines from equations (1.43) or (1.44) to determine the fieldline structure.

Priest & Titov (1996) identified two key topological features present near any (potential and non-potential) 3D null point: the *spine* line and the *fan* plane. The spine is a isolated fieldline that approaches, or leaves, the null point. The fan plane is a separatrix surface which consists of fieldlines which are confined to the plane and point towards or away from the null point. In this thesis, as per Parnell et al. (1996) and without loss of generality, we restrict our attention to *positive* 3D null points, where the spine line approaches the null, and the fieldlines in the fan plane point out from the null.

In the case of positive nulls, fieldlines generally approach the null initially running parallel to the spine and leave the null parallel to the fieldlines in the fan plane. Thus, we investigate the qualitative behaviour of different parameters by considering equations (1.43) or (1.44) in the limits $k \to -\infty$ and $k \to +\infty$. Due to the solenoidal condition, the trace of $\mathbf{M}$ is zero and thus the eigenvalues must sum to zero, i.e., there one eigenvalue with sign opposite to that of the real parts

of the other eigenvalues. For equation (1.43) if we, say, choose real eigenvalues $\lambda_1, \lambda_2 > 0$,$\lambda_3 < 0$ and trace back along fieldlines to $k \to -\infty$ then

$$\mathbf{r}(k) \to Ce^{-2\lambda_3 k}\mathbf{x}_3 \tag{1.45}$$

and we find that all of the field lines that head in towards the null are initially parallel to the eigenvector $\mathbf{x}_3$. If we trace these real eigenvalues away from the null at $k \to \infty$ we find

$$\mathbf{r}(k) \to Ae^{\lambda_1 k}\mathbf{x}_1 + Be^{\lambda_2 k}\mathbf{x}_2\,, \tag{1.46}$$

i.e., as fieldlines depart from the null they tend to run radially outwards parallel to the plane defined by the eigenvectors $\mathbf{x}_1$ and $\mathbf{x}_2$. Thus, for diagonalisable $\mathbf{M}$ we find the spine lies along the eigenvalue $\mathbf{x}_3$ and the fan plane is defined by $\mathbf{x}_1$ and $\mathbf{x}_2$.

Alternatively, for diagonalisable $\mathbf{M}$ we may have two complex and one real eigenvalue, say $\lambda_1, \lambda_2 = \eta \pm i\nu$ and $\lambda_3 = -2\eta$ with corresponding eigenvectors $\mathbf{x}_1, \mathbf{x}_2 = (\mathbf{x}'_1 \pm i\mathbf{x}'_2)/2$ then equation (1.43) may be rewritten as (following Parnell et al. 1996)

$$\mathbf{r}(k) = e^{\eta k}R\cos(\Theta + \nu)k\mathbf{x}'_1 - e^{\eta k}R\cos(\Theta + \nu)k\mathbf{x}'_2 + Ce^{-2\lambda_3 k}\mathbf{x}_3 \tag{1.47}$$

where A and B have been absorbed into new constants R and Θ. Again taking $\lambda_3 > 0$ ($\nu < 0$), and tracing backwards ($k \to -\infty$) we find

$$\mathbf{r}(k) \to Ce^{-2\lambda_3 k}\mathbf{x}_3, \tag{1.48}$$

and tracing forwards ($k \to \infty$)

$$\mathbf{r}(k) = e^{\eta k}R\cos(\Theta + \nu)k\mathbf{x}'_1 - e^{\eta k}R\cos(\Theta + \nu)k\mathbf{x}'_2 \tag{1.49}$$

Thus, once again we find that the spine is defined by $\mathbf{x}_3$, and the fan plane is defined by by $\mathbf{x}_1$ and $\mathbf{x}_2$, although in this case the fieldlines spiral outward. Repeating the process for the non-dimensionalisable form of $\mathbf{M}$ yields similar results, and thus we find generally that the spine lies along the single eigenvector which is of opposite sign to the real parts of the other two which define the fan plane. For negative results, the same qualitative behaviour holds although the spine is now associated with $k \to +\infty$ and the fan with $k \to -\infty$ (due to the reversal of fieldline direction).

To trace the fieldlines in a more specific way, it is useful to determine the form of $\mathbf{M}$ in terms of

the least possible parameters without loss of generality. Parnell et al. (1996) find

$$\mathbf{M} = \begin{pmatrix} 1 & \frac{1}{2}(q - j_{\parallel}) & 0 \\ \frac{1}{2}(q + j_{\parallel}) & p & 0 \\ 0 & j_{\perp} & -(p+1) \end{pmatrix} \tag{1.50}$$

which is obtained by choosing a local orthogonal coordinate system such that the spine is always directed along the z-axis (i.e., $\mathbf{x}_3$ in the above sense is in the z-direction), rotating such that the current perpendicular to the spine lies in the x-direction, and rescaling. The potential part of the field is determined by p and q and the nonpotential part is defined by the current

$$\mathbf{j} = \frac{1}{\mu}\left[j_{\perp}, 0, j_{\parallel}\right] \tag{1.51}$$

Given this form of $\mathbf{M}$, Parnell et al. (1996) catalogue the different possible forms of linear nulls by considering different parameter configurations. For the remainder of the section we not repeat this process but rather summarise the key results.

In the case of potential nulls, where $\mathbf{j} = \mathbf{0}$, there is an extra degree of freedom on $\mathbf{M}$ which allows a further rotation to remove q. Thus, in Cartesian coordinates, 3D potential nulls take the form:

$$\mathbf{B} = \left[x, \epsilon y, -(\epsilon + 1)\, z\right] \tag{1.52}$$

where we have replaced the parameter p with ϵ (for consistency with existing 3D wave-nullpoint literature), which is related to the eccentricity of the magnetic fieldlines, controlling the direction in which they predominantly align. Values of $\epsilon > 0$ yield a positive null. For equation (1.52): the null point itself (i.e. $\mathbf{B} = \mathbf{0}$) occurs at the origin; the spine line occurs along $x = y = 0$; and the fan plane lies in $z = 0$ and contains only radial fieldlines.

For potential nulls the eccentricity parameter ϵ alters the field topology as follows:

- For $\epsilon = 1$, the magnetic null point has azimuthal symmetry about its spine, with no prefered direction for fieldlines, and is known as a *proper* null.

- Null points which deviate from this cylindrical symmetry are known as *improper* nulls. For $0 < \epsilon < 1$ the fieldlines curve to run parallel to the x-axis, and for $\epsilon \geq 1$ curve to run parallel to the y-axis.

- For $\epsilon = 0$, we recover the simple 2D null point in the $xz-$plane, with an infinite null line running through $x = z = 0$ (e.g., cf. Figure 1.7a).

Examples of proper ($\epsilon = 1$) and improper ($\epsilon = 0.5$) 3D potential nulls are shown in Figure 1.8.

For non potential nulls, where $\mathbf{j} \neq \mathbf{0}$, there is greater variability in the possible null point configurations. As in the potential case, the parameters p and q (viz. ϵ) control the preferred direction of the fieldlines in the fan plane. A non-zero perpendicular current ($j_\perp \neq 0$) leads to a skewness of the spine and fan plane, which are no longer perpendicular. The parallel current has a somewhat more complicated role. Where $j_\parallel$ is below a defined threshold current (a function of the eccentricity parameters p, q or ϵ), the eigenvalues remain distinct and real, and consequently the parallel current simply introduces a further degree of fieldline eccentricity. When it is increased to match the threshold current ($j_\parallel = j_T$), provided $j_T \neq 0$ and $p \neq 0$ (viz. $\epsilon \neq 0$, i.e., we have true 3D nulls and not planar arrays of 2D nulls), two eigenvalues become equal and a *critical spiral* null is formed. The fieldlines in the fan plane are of a spiralling nature, but infinitely far from the null they still align with a predominant, radial direction. Beyond the threshold current, two of the eigenvectors become complex conjugates and permit a variety of spiral fieldlines in the fan plane, classes of null which could broadly be considered to be spiral nulls. Examples of skewed and spiral 3D nonpotential nulls are shown in Figure 1.9.

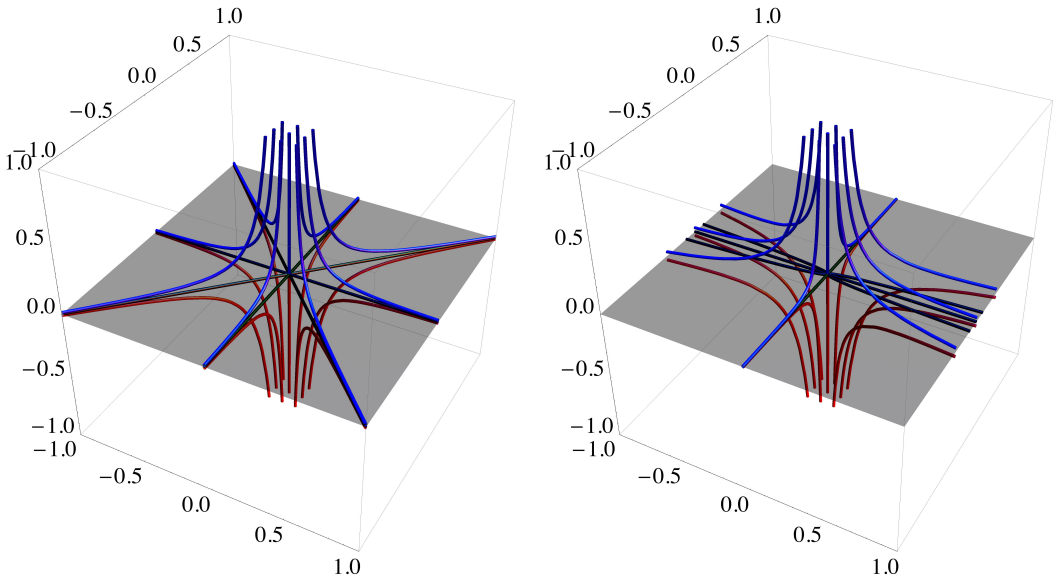

Figure 1.8: Potential Null Configurations: (a) the $\epsilon = 1$, azimuthally-symmetric proper null point. (b): fieldlines for the $\epsilon = 0.5$ improper null point (note the loss of rotational symmetry). Blue fieldlines originate from $z > 0$, red from $z < 0$ and the black fieldlines originate at the null and lie in the fan plane, shaded grey.

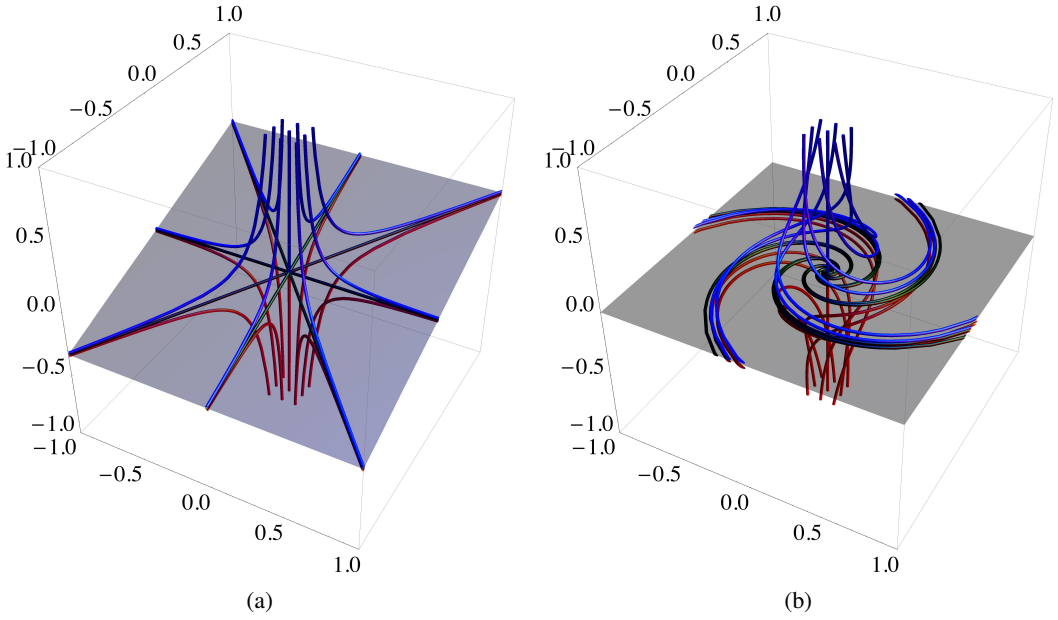

Figure 1.9: Nonpotential Null Configurations: (a) a skewed null with $\epsilon = 1$, $j_\perp = 1$, $j_\parallel = 0$; (b) a spiral null with $\epsilon = 1$, $j_\perp = 0$, $j_\parallel = 4$. Blue fieldlines originate from $z > 0$, red from $z < 0$ and the black fieldlines originate at the null and lie in the fan plane, shaded grey.

1.6 Numerical Simulations with LARE

In this thesis, we use numerical solutions of the MHD equations to simulate the behaviour of MHD waves in the vicinity of null points. This is achieved through the use of the LARE2D and LARE3D codes, written by Arber et al. (2001), which are freely distributed on CCPForge.

LARE solves the fully nonlinear MHD equations using a Lagrangian-Euleurian remap scheme. Lagrangian numerical schemes utilise a grid that is transported with the fluid, as opposed to the simpler case of considering fluid flow past a fixed grid (an Eulerian scheme). Succinctly, Lagrangian schemes theoretically give an advantage in that resolution becomes concentrated where it is needed, giving better accuracy for a given computing budget, however in practice often the grid will become contorted and fail, particularly in the presence of shocks and vortices. LARE combines the two approaches by advancing the code using a Lagrangian solver, then subsequently remapping the code onto the original Eulerian grid before the next step. As such, it is related to so-called ALE numerical schemes used in hydrodynamics (see the review by Benson 1992).

The code has been extensively tested and is in a mature stage of development. Widely-used by the Solar computational MHD community, key features are that LARE:

- Solves the fully nonlinear MHD equations in differential form for variable viscosity and resistivity plasmas, for different equations of state.
- Enforces and conserves the $\nabla \cdot \mathbf{B} = 0$ condition by use of Evans & Hawley (1988) constrained transport.
- Conserves momentum and kinetic energy to machine-precision by exploiting the conservation of mass in the Lagrangian step.
- Accurately 'captures' shocks and avoids Gibb's overshoot phenomenon through an implementation of artificial viscosity at shocks. Tests comparing to other shock codes (Riemann solvers) show good accuracy and quicker calculation.
- Gives accurate results even in low-β plasmas. Alternative conservative schemes determine pressure by subtracting magnetic and kinetic energy, both large terms, from total energy, which creates problems accurately calculating thermal pressure is small. Arber et al. (2001) calculate that for a typical solar value of $\beta = 10^{-3}$ such alternative schemes give a 200% error in calculating pressure and temperature.
- Allows for easy addition of 'extra physics', which are added to the Lagrangian step only (the remap is purely geometrical).

Chapter 2

Thesis Overview

2.1 MHD Waves at Magnetic Null Points

Over the past few decades, high-resolution and high-cadence instruments aboard satellites such as *SOHO*, *TRACE*, *Hinode* and *SDO* have revealed that waves and oscillations are abundant throughout the coronal plasma and are present in most, if not all, of its structures (see reviews by, e.g., De Moortel 2005; Nakariakov & Verwichte 2005; Ruderman & Erdélyi 2009; Goosens et al. 2011; and references therein). MHD wave theory suggests that the plasma potentially supports a wide variety of distinct classes of wave motions, including the Alfvén wave, and fast and slow magnetoacoustic waves. However, the applicability and appropriateness of such classifications has recently provoked intense discussion, for instance reports of observed Alfvén waves in the corona (e.g., Tomcyzyk et al. 2007; De Pontieu et al. 2007) have been contested by, e.g., Erdélyi & Fedun (2007) and Van Doorsselaere et al. (2008), and have generated further discussion regarding the correct classification of MHD waves (e.g., Goossens et al. 2009; 2011; 2012).

The 'classic' terminology of MHD waves originates in the analysis of modes supported by magnetically-unidirectional, homogeneous plasmas of infinite extent which consider plane wave solutions (as per section 1.4.2). Here, three distinct modes are permitted, the Alfvén mode, and the fast and slow magnetoacoustic, and their behaviour and nature is well understood. For a low-β plasma, it is found that the Alfvén wave is a transverse, purely-magnetic wave, propagating at the Alfvén speed, guided by the magnetic field. The fast magnetoacoustic wave is found to propagate roughly isotropically at the fast speed ($c_F = \sqrt{c_A^2 + c_S^2}$, $c_F \approx c_A$ where $\beta \ll 1$), and can travel along and across magnetic fieldlines. The slow magnetoacoustic wave propagates longitudinally along the magnetic fieldlines, roughly at the sound speed (when $\beta \ll 1$).

However in the solar corona, effects including gravitational stratification, inhomogeneous den-

sity profiles and multiple-source magnetic field geometries call into question whether these three, classical modes are still valid. The departure to inhomogeneity typically introduces a variety of phenomena such as resonant absorption (in the corona see, e.g., Ionson 1978; 1982; 1983; Hollweg 1981; Ruderman & Roberts 2002) and phase mixing (e.g. Heyvaerts & Priest 1983), each of which blur the distinction between these separate modes (see also, e.g., Bogdan et al. 2003; McDougall & Hood 2007; Sousa & Cunha 2008; Cally & Hansen 2011; Hansen & Cally 2012).

Typically theorists preserve the concept of the three MHD modes and introduce the concept of conversion and coupling between the constituent modes as waves encounter certain inhomogeneous features. However, as highlighted by Goossens et al. (2009; 2011; 2012), we must take care to understand that realistic plasmas, strictly speaking, do not necessarily support the three 'classic' wave modes but rather that a propagating MHD pulse encounters situations in which it assumes transient properties that qualitatively correspond to one (or more) of the homogeneous modes.

As such, it is unclear whether or not the classic MHD modes exist in the solar atmosphere as discrete entities or if such mode separation requires specific geometries. For example, as discussed by Parker (1991), the existence of true Alfvén waves as per Alfvén (1942) is dependent upon special magnetic geometries which contain invariant directions. Despite this uncertainty, a theoretical framework which involves them conceptually is not necessarily obsolete. Mode interpretation and analysis that relates MHD wave behaviour in inhomogeneous, realistic plasmas to the comparatively simple, classic waves still has the potential to be a useful framework.

In this thesis, we are primarily interested in the behaviour of MHD waves in the vicinity of the 3D *magnetic null point* (section 1.5.2). Null points are topological features of coronal magnetic fields, predicted by magnetic field extrapolations such as Brown & Priest (2001) and Beveridge et al. (2002). At these magnetic null points, the magnetic induction is zero. Hence, approaching a magnetic null point, the coronal plasma is highly inhomogenous. In the solar atmosphere, null points have been identified as playing key roles in many processes, for example; in CMEs (in the *magnetic breakout model*, e.g. Antiochos 1998; Antiochos et al. 1999), magnetic reconnection (e.g. Priest & Forbes 2000; Pontin 2012) and oscillatory reconnection (reconnection driven by wave-null interactions, see McLaughlin et al. 2009; McLaughlin et al. 2012) all of which are thought to play a role in coronal heating. As both waves and null points are ubiquitous in the corona (Close et al. 2004, Longcope & Parnell 2009 and Régnier et al. 2008 give a rough estimates of $1.0 - 4.0 \times 10^4$ null points) wave-null interactions are inevitable and thus are arguably a fundamental plasma process in the solar atmosphere. Hence, this thesis is specifically concerned with the extension of classic MHD wave theory about null points, which in a broader sense contributes to both the theory of MHD wave behaviour in inhomogeneous media and the understanding of fundamental aspects of coronal physics.

MHD wave behaviour in the neighbourhood of magnetic null points have been extensively studied in 2D models. Bulanov & Syrovatskii (1980) performed the first investigation of MHD behaviour about a 2D null and noted that in a 2D geometry the motions governing the Alfvén mode and the fast magnetoacoustic modes are decoupled, permitting analysis that considers the modes separately.[1] By finding solutions for azimuthally symmetric harmonic fast waves (in the 2D sense of a polar coordinate system) bounded by a line-tied, circular boundary at some arbitrary radius from the null point, they found that the fast wave propagates towards the null point. In their solution for Alfvén waves, they find that they propagate along magnetic fieldlines at the local Alfvén speed, and that, due to the inhomogeneity of the Alfvén speed, that such waves accumulate along the separatricies with exponentially increasing gradients. This paper was the first indicator of the key propagation features for each mode at null points, specifically that fast waves are attracted to the null and that Alfvén waves accumulate along separatricies. However, the assumed symmetries left the question as to whether these where general results (e.g., the fast wave could only propagate towards or away from the null point, and further the outer boundary would reflect it back towards the null) and, as we will see, obscured other transient aspects of the wave propagation. Work in this (2D) azimuthal symmetry was continued with a focus on the diffusive properties of the waves in their regions of accumulation, and their role in driving null point collapses (and hence reconnection) by authors such as Craig & McClymont (1991;1993), Craig & Watson (1992), and Hassam (1992). As this thesis is primarily concerned with the transient aspects of MHD waves at null points, which are in-line with Bulanov & Syrovatskii (1980) these studies are not further detailed in this section, although more comparative information can be found in the review paper by McLaughlin et al. (2011b).

The restrictions of (2D) azimuthal symmetry were first relaxed by Ofman et al. (1993), who numerically recovered the same resistive scaling laws as previous authors but also showed that the choice of boundary condition had a strong influence on the solutions. This was re-enforced by Steinolfson et al. (1995) who experimented with both rigid and open boundary conditions to find that fast-wave driven fast reconnection events reported by Craig & McClymont (1991;1993) do not occur for open boundaries. Hassam & Lambert (1996) reconsidered the behaviour of the Alfvén wave and stressed a difference between two types of Alfvén wave behaviour at 2D nulls. They found that, as per Bulanov & Syrovatskii (1980), Alfvén waves are confined to their initial fieldlines. Because of this, only perturbations which initially straddle the separatricies truly accumulate along them - other Alfvén wave perturbations will leave the system, developing strong transverse gradients and eventually become damped by phase-mixing.

The first papers to shift focus more to the transient aspects of fast and Alfvén wave propagation in various 2D null point geometries within a $\beta = 0$ plasma were presented in a series of papers by McLaughlin & Hood (2004; 2005; 2006a). Again, these authors found the two modes decoupled

[1] Note that, as we will see, this decoupling is a feature of any 2D MHD model (in the sense that there is a direction that is ignorable in terms of equilibria and perturbations).

and identified key propagation features for each mode. It was found that the fast wave propagates isotropically (at the same characteristic speed both across and along magnetic fieldlines), with behaviour dictated by the Alfvén-speed profile, propagating from regions of high-to-low Alfvén speed resulting in a refraction effect which focuses the wave energy into the null point. Meanwhile, the Alfvén wave is confined to follow magnetic fieldlines, thus leading the wave energy to accumulate along the separatrices. Due to the resulting current build-up in these regions, these papers concluded that magnetic null points and separatricies are likely locations for localised heating events in the corona. $\beta \neq 0$ and nonlinear behaviour has also been investigated by McLaughlin & Hood (2006b) and McLaughlin et al. (2009) respectively. A comprehensive overview of the 2D null point literature is given in the review paper of McLaughlin et al. (2011b).

Of course, 2D models only give an initial grounding in the physics of realistic null points and for a full understanding we must turn to 3D models (as singularities, null points are inescapably 3D and any 2D X-point configuration in fact only captures the physics of a *null line* of infinite extent). It is not clear to what extent the characteristics and behaviour of waves about 2D null points transfer to the fully 3D case, and surprisingly few papers have been written that address MHD wave behaviour about a fully 3D null point. Most papers have focused on the dynamics of current accumulation over time (in an attempt to locate regions where reconnection is most likely to occur) rather than focus on the transient propagation features of the individual modes.

Galsgaard et al. (2003) consider a proper, $\beta = 0$ null point subject to twisting motions at the boundaries. The imposed driving condition introduces a wave which is generated about the spine and eventually accumulates on the *fan* (perhaps analogous to Alfvén waves behaviour around 2D null points). In addition, they observe a small amount of current accumulation at the null itself, which they suggest is due to nonlinear generation of a fast wave. No linear coupling between wave modes is observed, and in their linear analysis they find that the wave equations for the fast and Alfvén modes decouple. However, this is not surprising since their proper 3D null has azimuthal symmetry, and so the system is arguably 2.5D, not fully 3D.

Pontin & Galsgaard (2007), Pontin et al. (2007) and Galsgaard & Pontin (2011a; 2011b) performed numerical simulations in which the spine and fan of a proper 3D null point are subjected to rotational and shear perturbations. They found that rotations of the fan plane lead to current density accumulation about the spine, and rotations about the spine lead to current sheets in the fan plane. In addition, shearing perturbations lead to 3D localised current sheets focused at the null point itself. Again, this is in good agreement with what we may expect for MHD wave behaviour from the 2D studies, i.e. current accumulation at specific, predictable parts of the magnetic topology.

The first study of MHD wave behaviour in the neighbourhood of a fully 3D null point (i.e., without azimuthal symmetry) was investigated analytically by McLaughlin et al. (2008). These authors

examine the fast and Alfvén waves about both proper and improper null points. The authors utilise the WKB approximation to determine the transient properties of the modes in a linear, $\beta = 0$ plasma regime. Their findings strongly suggest that the features of MHD waves about 3D nulls are not that different to the 2D results: the fast wave propagates across magnetic fieldlines according to the Alfvén-speed profile and the Alfvén wave is confined to magnetic fieldlines, leading to the waves accumulating in specific, predictable topological regions of the null point. However, their implementation of the WKB method is unable to address the question of whether modes couple in the fully 3D geometry, and ignores nonlinear effects, since their first-order WKB solution implicitly precludes these possibilities and constrains the waves to see the magnetic field as locally uniform.

Thus, as it stands the question of what is the true behaviour of MHD waves in the neighbourhood of fully 3D magnetic null points remains unanswered. Specifically, *can we understand and predict the the propagation and evolution of each MHD wave? Additionally, what is the nature of mode-coupling or conversion due to the magnetic geometry and/or due to nonlinear effects*?

2.2 Aim of this Thesis

In this thesis we will construct and evaluate MHD models of wave propagation at 3D null points of varying eccentricity to address the following questions;

- What are the key, transient features of different MHD waves in the vicinity of 3D nulls?
- What role does fieldline eccentricity play? How does transient wave behaviour differ between the azimuthally symmetric proper nulls and asymmetric improper nulls?
- What role does the inhomogeneity of the magnetic topology play? Do the waves correspond to their homogeneous, unidirectional field counterparts? What is the nature of their coupling?

At the outset, it is unclear as to how appropriate the large body of 2D wave-null literature will be for describing the physics of more realistic 3D null points. Although both 2D and 3D null points are similar in that they are both singular regions of zero magnetic field, the local magnetic structures about the two are topologically distinct. The ultimate aim of this thesis is to understand the fundamental aspects of wave-null interaction in 3D geometries, thus answering the question *to what extent does the 2D theory carry over to 3D?*

2.3 Thesis Outline

This thesis presents the results of research investigating how MHD waves propagate about 3D magnetic null points, in both linear and nonlinear MHD regimes. As the investigation progressed it became clear that, due to the inhomogeneity at null points, a better understanding of the fundamental aspects of nonlinear waves propagating in inhomogeneous regions was required. As such, not all chapters directly address the issue of waves at 3D nulls, but do contribute to our eventual understanding of the wave-null system. The chapters are arranged in accordance with the order in which the research was carried out, to better tell the story. Each chapter is based on a self-contained, peer-reviewed publication.

- Chapter 3 begins the investigation. A method for isolating different modes of oscillation around fully 3D null points is developed, and subsequently we investigate the behaviour of fast magnetoacoustic waves in the vicinity of proper and improper 3D, $\beta = 0$ potential magnetic null points.
- In Chapter 4 we detour from the wave-null system to consider how the nonlinear Lorentz force (or *ponderomotive force*) affects wave behaviour in general inhomogeneous MHD systems. In particular, we are interested in the possibility of nonlinear mode coupling and excitation, and the circumstances in which such effects may be expected.
- Chapter 5 considers the previously unexplored case of how the Alfvén wave behaves at 2D null points in a nonlinear MHD regime. Using our insights from the previous chapter, we consider the possibility of mode conversion at the null point.
- Chapter 6 considers the behaviour of Alfvén waves in the vicinity of the same proper and improper, $\beta = 0$ null points as Chapter 3, using the same methods for isolating different modes of oscillation.

Finally, Chapter 7 summarises the results of the preceding chapters, drawing overall conclusions. It also discusses the necessary direction of future research in wave-null interactions, accounting for the new results presented in this thesis. Appendices follow, with Appendix A supporting Chapter 3, Appendices B, C and D supporting Chapter 4, and Appendix E detailing preliminary results discussed in Chapter 7.2.

Chapter 3

Fast magnetoacoustic wave behaviour about 3D magnetic null points

The following chapter details research first reported in:

'Linear and nonlinear MHD mode coupling of the fast magnetoacoustic wave about a 3D magnetic null point' — Thurgood & McLaughlin, *Astronomy & Astrophysics*, **545**, A9, 2012

3.1 Introduction

In this chapter, we seek to investigate the extent to which key features of 2D fast wave propagation carries over to the 3D case, and also look for evidence of interaction between differing wave modes; namely mode-coupling and/or mode conversion through either geometric and/or nonlinear effects. Although we wish to understand the behaviour of fast waves about potential 3D null points in the most general terms possible, analytical progress is unlikely when considering a completely general null point. Thus, we consider the behaviour of the fast wave in the vicinity of nulls with specific values of the eccentricity parameter ϵ via numerical simulation so as to capture the range of topologies possible. Primarily, we consider two nulls; the azimuthally symmetric, $\epsilon = 1$ proper null; and an improper null defined by $\epsilon = 0.5$ where fieldlines are predominantly aligned parallel to the $x-$axis (i.e. we consider the nulls shown in Figure 1.8). By comparing the results for differing ϵ, we address the question of how MHD wave behaviour alters with the field eccentricity.

The chapter is structured as follows: Section 3.2 outlines the specifics of the model and is subdivided into sections on the mathematical model (Section 3.2.1), the method for isolating individual wave modes (Section 3.2.2), the specifics of the numerical solution (Section 3.2.4) and a brief

outline of the supporting WKB solution (Section 3.2.5). Sections 3.4 and 3.3.1 present the results of the simulations for the proper and improper radial null points respectively, and the conclusions are presented in Section 3.5.

3.2 Mathematical Model

3.2.1 Governing MHD Equations

The three-dimensional, nonlinear, ideal, adiabatic MHD equations are solved numerically for a $\beta = 0$ plasma. Note that, although in most of the solar corona the plasma-β is low, ($\beta \ll 1$, Gary 2001) and so the $\beta = 0$ approximation is typically taken as valid, at magnetic null points $\beta \to \infty$ no matter how small the plasma pressure. Here, we are specifically concerned with addressing whether the 3D magnetic field about realistic null points introduces behaviour absent in previous 2D models. Hence, in this study we utilise the $\beta = 0$ approximation intentionally to prohibit the introduction of the slow mode and restrict our attention to the behaviour of fast magnetoacoustic wave and its interplay with the Alfvén mode, on the understanding that the results presented are a first step towards understanding how waves behave at realistic null points in the corona; which are both 3D and must have $\beta \neq 0$ (see section 7.2 for further discussion).

Thus, the governing equations are as follows:

$$\begin{aligned} \rho\left[\frac{\partial \mathbf{v}}{\partial t} + (\mathbf{v}\cdot\nabla)\mathbf{v}\right] &= \left(\frac{\nabla\times\mathbf{B}}{\mu}\right)\times\mathbf{B} \quad , \\ \frac{\partial \mathbf{B}}{\partial t} &= \nabla\times(\mathbf{v}\times\mathbf{B}) \quad , \\ \frac{\partial \rho}{\partial t} &= -\nabla\cdot(\rho\mathbf{v}) \quad , \\ \frac{\partial p}{\partial t} &= -\mathbf{v}\cdot\nabla p - \gamma p\nabla\cdot\mathbf{v} \quad . \end{aligned} \tag{3.1}$$

Here, standard MHD notation applies: $\mathbf{v}$ is plasma velocity, p is plasma/thermal pressure, ρ is density, $\mathbf{B}$ is the magnetic field/induction, $\gamma = 5/3$ is the adiabatic index, and μ is the magnetic permeability.

We consider an equilibrium state of $\rho = \rho_0$, $p = p_0$ (where ρ_0 and p_0 are constants), $\mathbf{v} = \mathbf{0}$ and equilibrium magnetic field $\mathbf{B} = \mathbf{B}_0(\mathbf{r})$. Finite, small perturbations of amplitude $\varepsilon \ll 1$ are considered in the form $\rho = \rho_0 + \varepsilon\rho_1(\mathbf{r},t)$, $p = p_0 + \varepsilon p_1(\mathbf{r},t)$, $\mathbf{v} = \mathbf{0} + \varepsilon\mathbf{v}(\mathbf{r},t)$ and $\mathbf{B} = \mathbf{B}_0 + \varepsilon\mathbf{b}(\mathbf{r},t)$ and a subsequent nondimensionalisation using the substitution $\mathbf{v} = \overline{v}\mathbf{v}^*$,$\nabla = \nabla^*/L$, $\mathbf{B}_0 = B_0\mathbf{B}_0^*$, $\mathbf{b} = B_0\mathbf{b}^*$, $\mathbf{t} = \overline{t}\mathbf{t}^*$, $p_1 = p_0 p_1^*$ and $\rho_1 = \rho_0\rho_1^*$ is performed, with the additional choices $\overline{v} = L/\overline{t}$ and $\overline{v} = B_0/\sqrt{\mu\rho_0}$. The resulting nondimensionalised, governing equations of

the perturbed system are:

$$\begin{aligned}
\frac{\partial \mathbf{v}}{\partial t} &= (\nabla \times \mathbf{b}) \times \mathbf{B}_0 + \mathbf{N}_1 \\
\frac{\partial \mathbf{b}}{\partial t} &= \nabla \times (\mathbf{v} \times \mathbf{B}_0) + \mathbf{N}_2 \\
\frac{\partial \rho_1}{\partial t} &= -\nabla \cdot \mathbf{v} + N_3 \\
\frac{\partial p_1}{\partial t} &= -\gamma \nabla \cdot \mathbf{v} + N_4 \\
\mathbf{N}_1 &= (\nabla \times \mathbf{b}) \times \mathbf{b} - \rho_1 \frac{\partial \mathbf{v}}{\partial t} - (\mathbf{v} \cdot \nabla)\, \mathbf{v} \\
\mathbf{N}_2 &= \nabla \times (\mathbf{v} \times \mathbf{b}) \\
N_3 &= -\nabla \cdot (\rho_1 \mathbf{v}) \\
N_4 &= \mathbf{v} \cdot (\nabla p_1) - \gamma p_1 (\nabla \cdot \mathbf{v})
\end{aligned} \tag{3.2}$$

where terms $\mathbf{N}_i$ are the nonlinear components correct to $\mathcal{O}(\varepsilon^2)$. The star indices have been dropped, henceforth all equations are presented in a nondimensional form. The equations are merged into one governing PDE:

$$\begin{aligned}
\frac{\partial^2 \mathbf{v}}{\partial t^2} &= \{\nabla \times [\nabla \times (\mathbf{v} \times \mathbf{B}_0)]\} \times \mathbf{B}_0 + \mathbf{N} \\
\mathbf{N} &= \{\nabla \times [\nabla \times (\mathbf{v} \times \mathbf{b})]\} \times \mathbf{B}_0 \\
&\quad + \{\nabla \times [\nabla \times (\mathbf{v} \times \mathbf{b})]\} \times \mathbf{b} + (\nabla \times \mathbf{b}) \times [\nabla \times (\mathbf{v} \times \mathbf{B}_0)] \\
&\quad + (\nabla \cdot \mathbf{v} - \mathbf{v} \cdot \nabla)\, (\nabla \times \mathbf{b}) \times \mathbf{B}_0 \\
&\quad - \rho_1 \{\nabla \times [\nabla \times (\mathbf{v} \times \mathbf{B}_0)]\} \times \mathbf{B}_0 \\
&\quad - [(\nabla \times \mathbf{b}) \times \mathbf{B}_0 \cdot \nabla]\, \mathbf{v}
\end{aligned} \tag{3.3}$$

The first term dominates the linear regime of $\mathcal{O}(\varepsilon)$ and the terms $\mathbf{N}$ represent nonlinear terms of $\mathcal{O}(\varepsilon^2)$.

This study utilises numerical solutions of the full nonlinear MHD equations (3.1), using the numerical method detailed in Section 3.2.4 (LARE3D). In conjunction, analytical treatment of wave equation (3.3) derived via second-order perturbation theory is used to create a special coordinate system that will isolate and identify individual wave modes (Section 3.2.2), create a WKB approximation (Section 3.2.5) and to seek analytical confirmation of observed phenomena in the numerical simulations where possible.

3.2.2 Isolating MHD modes

This chapter investigates the transient MHD mode behaviour about a general 3D null point as well as the possible mode coupling/conversion that may occur. To do so, it is necessary to construct a system that allows individual, pure MHD wave modes to be generated, identified and tracked. In turn, such distinction requires a clear definition of the possible modes that can occur.

As outlined in Section 2.1, the concept and terminology of the three classes of MHD wave (Alfvén, fast and slow) that originated within a homogeneous MHD plasma description still remains valid and useful in describing inhomogeneous media, although distinguishing between the individual modes can become increasingly difficult depending upon the exact nature of the inhomogeneity. The $\beta = 0$, uniform density, 3D magnetic null points under consideration in this paper are specific examples of plasma inhomogeneity, namely that of a nonuniform magnetic topology. Hence, the behaviour of the two linear waves sustainable here (Alfvén and fast) is solely due to the Lorentz force, and as such we find that the most appropriate and useful definitions of, and distinctions between, the two modes are purely in these terms.

The nondimensionalised Lorentz force:

$$\mathbf{F} = (\nabla \times \mathbf{B}) \times \mathbf{B} = (\mathbf{B} \cdot \nabla)\,\mathbf{B} - \nabla\left(\frac{\mathbf{B} \cdot \mathbf{B}}{2}\right) \tag{3.4}$$

is the sole driving force in our $\beta = 0$ system, and is denoted $\mathbf{F}$. The first term of the right hand side of the equation (3.4) can be interpreted as magnetic tension, and the second term is a gradient in magnetic pressure. We note that the force has no term parallel to the magnetic induction ($\mathbf{F} \cdot \mathbf{B} = 0$) and it follows that no $\beta = 0$ MHD wave can be driven by or associated with perturbations in this direction, *i.e.* they are all perpendicular perturbations relative to total magnetic field. Thus, in $\beta = 0$, we define our two waves as follows:

1) The Alfvén wave is driven only by magnetic tension. This results in a wave that propagates anisotropically as a transverse wave, confined to and guided along the magnetic fieldlines.

2) The fast magnetoacoustic wave is driven both by magnetic tension and magnetic-pressure gradients. It propagates isotropically via a mixture of transverse and longitudinal motions (due to both magnetic tension and magnetic-pressure gradient respectively).

These definitions are used for the specific purpose of creating a set of orthogonal polarisation vectors that can be used to distinguish between these two modes (a special 'coordinate system'). Note that this will not be valid along the spine or along the fan plane, as here the waves are degenerate: at these locations both the fast wave and Alfvén wave propagate only as transverse, tension-driven waves. Elsewhere, such a system can be obtained by exploiting a mathematically-invariant direction.

For instance, if we consider initial perturbations to the equilibrium magnetic field ($\mathbf{B}_0$) across an invariant direction denoted $\hat{\mathbf{e}}_i$, then due to $\partial/\partial\hat{\mathbf{e}}_i = 0$, the magnetic-pressure gradient is eliminated. As such, this direction is inextricably linked with the Alfvén mode as per our definition, i.e. perturbations in this direction can give rise to waves driven only by magnetic tension that propagate as transverse waves along magnetic field lines. The existence of an invariant direction is just as much a physical requirement for the existence of true, tension-only Alfvén waves as it is a convenient mathematical method for isolating them. Various authors have stated that in the absence of such an invariant coordinate, only the magnetoacoustic waves can exist, and hence only certain special topologies permit the Alfvén mode (see, e.g., Parker 1991; Van Doorsselaere et al. 2008; Goossens et al. 2011).

Alternatively, we can consider perturbations in a direction that is perpendicular to both $\mathbf{B}_0$ and $\hat{\mathbf{e}}_i$. Here both magnetic pressure and magnetic tension can be present and thus we assume this direction is associated with the fast mode as per our definition. That is to say, both magnetic tension and magnetic-pressure gradients sustain an isotropic wave that propagates via longitudinal and transverse motions.

To reiterate: in this chapter we aim to construct a system of orthogonal polarisation vectors, for the potential 3D null, of the form $\hat{\mathbf{B}}_0$, $\hat{\mathbf{e}}_i$ and $\hat{\mathbf{e}}_i \times \hat{\mathbf{B}}_0$, such that motions in the $\hat{\mathbf{e}}_i$-direction correspond to the Alfvén mode and that motions in the $\hat{\mathbf{e}}_i \times \hat{\mathbf{B}}_0$-direction correspond to fast mode.

Similar approaches have been previously utilised in various 2D MHD models, an example of which is the coordinate system used by McLaughlin & Hood (2004; 2005; 2006a) to drive pure fast and Alfvén modes at a 2D X-point. In fact, the essence of any 2D mathematical model is to impose translational invariance, thus facilitating the creation of such a coordinate system. However, for an apparently fully 3D null point ($\epsilon \neq 0, \epsilon \neq 1$), there is no obvious invariance and, unlike 2D models, there is no clear way to discern which of the directions perpendicular to $\mathbf{B}_0$ would be associated with unique MHD wave modes.

We look for clues in the proper ($\epsilon = 1$) null case, where the equilibrium has obvious azimuthal symmetry. Considering the proper null point in cylindrical polar coordinates (r, θ, z) and taking $\partial/\partial\theta = 0$ reduces the problem to 2.5D. We first seek to find a set of polarisation vectors which correspond to unique wave modes in this specific case, then look for a more generalised system (of which this would be a specific case) that would work with any potential 3D null point.

The equilibrium magnetic field with $\epsilon = 1$ rephrased in cylindrical polars is $\mathbf{B}_0 = [r, 0, -2z]$ where $r^2 = x^2 + y^2$. By our definition, the Alfvén wave is associated with invariant directions, such as $\hat{\boldsymbol{\theta}}$. Thus, it follows that the fast wave is associated with the direction that completes the orthogonal set, i.e. $\hat{\boldsymbol{\theta}} \times \mathbf{B}_0$. Considering the linear components of the wave equation (3.3) parallel to the orthogonal vectors $\hat{\boldsymbol{\theta}}$, $\mathbf{B}_0$ and $\hat{\boldsymbol{\theta}} \times \mathbf{B}_0$, in cylindrical polars for $\epsilon = 1$ leads to three decoupled wave equations governing the linear Alfvén, fast and slow (absent) mode respectively:

$$\begin{aligned}
\frac{\partial^2 \mathbf{v}}{\partial t^2} \cdot \hat{\boldsymbol{\theta}} &= \left[-1 + r\frac{\partial}{\partial r} + r^2\frac{\partial^2}{\partial r^2} + 4z\frac{\partial}{\partial z} + 4z^2\frac{\partial^2}{\partial z^2}\right. \\
&\quad \left. -4rz\frac{\partial^2}{\partial r \partial z}\right] v_\theta \\
\frac{\partial^2 \mathbf{v}}{\partial t^2} \cdot \left(\hat{\boldsymbol{\theta}} \times \mathbf{B}_0\right) &= -\left(r^2 + 4z^2\right)\left[\left(4\frac{\partial}{\partial z} + 2z\frac{\partial^2}{\partial z^2} - \frac{2z}{r^2} + \frac{2z}{r}\frac{\partial}{\partial r}\right.\right. \\
&\quad \left.\left. + 2z\frac{\partial^2}{\partial r^2}\right) v_r + \left(3\frac{\partial}{\partial r} + r\frac{\partial^2}{\partial r^2} + r\frac{\partial^2}{\partial z^2}\right) v_z\right] \\
\frac{\partial^2 \mathbf{v}}{\partial t^2} \cdot \mathbf{B}_0 &= 0
\end{aligned} \tag{3.5}$$

This treatment offers a clear demonstration of (linearly) decoupled waves for this specific case and provides confirmation that perturbations in $\hat{\boldsymbol{\theta}}$ will be associated with the Alfvén wave and perturbations in $\hat{\boldsymbol{\theta}} \times \mathbf{B}_0$ with the fast wave. Such a treatment in cylindrical polars has been used in previous studies of proper magnetic null points, for example Galsgaard et al. (2003) utilised a symmetric helical motions (in our terminology, perturbing in $\hat{\boldsymbol{\theta}}$), to study an Alfvén wave propagating about a proper, $\epsilon = 1$ null point. However, it is not obvious how this method would transfer to the more general improper null case.

3.2.3 System of orthogonal polarisation vectors: $\mathbf{A}$, $\mathbf{B}_0$ and $\mathbf{C} = \mathbf{A} \times \mathbf{B}_0$

The flux function/magnetic vector potential is defined such that $\mathbf{B} = \nabla \times \mathbf{A}$. Although vector potentials are not unique[1] we may choose a guauge $\mathbf{A}$ such that $\mathbf{A} \cdot \mathbf{B} = 0$ (in this case, this corresponds to the Coulomb gauge). We hypothesise that about potential null points the (linear) Alfvén wave is always associated with the flux function direction (which provides the invariant direction). For the $\epsilon = 1$ null, we find the flux function, and thus the special coordinate system, would be (in cylindrical polars):

$$\begin{aligned}
&\mathbf{B}_0 = [r, 0, -2z] \\
&\mathbf{A}_0 = [0, -rz, 0] \propto \hat{\boldsymbol{\theta}} \\
&\mathbf{C} = \left[2rz^2, 0, zr^2\right] \propto (\hat{\boldsymbol{\theta}} \times \mathbf{B}_0)
\end{aligned} \tag{3.6}$$

and we confirm that the vectors form an orthogonal set $\mathbf{A}_0 \cdot \mathbf{B}_0 = \mathbf{A}_0 \cdot \mathbf{C} = \mathbf{B}_0 \cdot \mathbf{C} = 0$. Thus, to generate and isolate a pure Alfvén mode, we consider perturbations in the $\hat{\mathbf{A}}_0$-direction only, and similarly for the pure fast wave, we must consider perturbations in the direction $\hat{\mathbf{C}}$, where

[1] If $\mathbf{A}$ is a vector potential satisfying $\mathbf{B} = \nabla \times \mathbf{A}$, then so is $\mathbf{A} + \nabla m$ where m is a differentiable scalar function.

$\mathbf{C} = \mathbf{A}_0 \times \mathbf{B}_0$. The system for $\epsilon = 1$ can be considered a special case of cylindrical polars that changes about the fan plane, and is sufficiently similar to be consistent with the decoupled linearised wave equations for the cylindrical polars (3.5). Figures 3.1 and 3.2 illustrates the vector fields for the $\epsilon = 1$ case.

By determining the flux function for general ϵ, we extend this to create an orthogonal, curvilinear coordinate system that is based on the equilibrium magnetic field ($\mathbf{B}_0$), the flux function ($\mathbf{A_0}$) and their cross product ($\mathbf{C} = \mathbf{A_0} \times \mathbf{B}_0$). These general vector fields are found to take the Cartesian form:

$$\begin{aligned}
\mathbf{B}_0 &= [x, \epsilon y, -(\epsilon+1)z] \\
\mathbf{A}_0 &= [zy, -\epsilon xz, (1-\epsilon)xy] \\
\mathbf{C} &= [C_x, C_y, C_z] \\
C_x &= x\left[\left(\epsilon^2-\epsilon\right)y^2 + \left(\epsilon^2+\epsilon\right)z^2\right] \\
C_y &= y\left[(1-\epsilon)x^2 + (\epsilon+1)z^2\right] \\
C_z &= \epsilon z\left(x^2+y^2\right)
\end{aligned} \tag{3.7}$$

with unit normals $\hat{\mathbf{B}}_0 = \mathbf{B}_0/|\mathbf{B}_0|$, $\hat{\mathbf{A}}_0 = \mathbf{A}_0/|\mathbf{A}_0|$ and $\hat{\mathbf{C}} = \mathbf{C}/|\mathbf{C}|$. Figure 3.3 shows the vector fields for the $\epsilon = 0.5$ case (cf. Figure 3.2). Note that on the line of the spine ($x = y = 0$) and the fan plane ($z = 0$), $\mathbf{A}_0 = \mathbf{C} = \mathbf{0}$ thus unit vectors cannot be defined. As such, this system of orthogonal polarisation vectors cannot be used to drive pure modes along the spine or fan, or distinguish the identity of these waves in such regions. This inability to differentiate between modes in such regions by way of polarisation is reflective of the physics in that there is a degeneracy between the fast and Alfvén modes along the spine and fan plane. Waves propagating along the spine or fieldlines in the fan plane are driven by tension only, as a transverse oscillation, and so along these particular fieldlines the fast mode is degenerate with the Alfvén mode.

This system of orthogonal polarisation vectors (equation 3.7) is at the heart of the work presented in this chapter. It is used in the following manner: Initially, it is employed to introduce a pure, linear, fast magnetoacoustic wave at a computational boundary by driving a velocity pulse in the direction $\hat{\mathbf{C}}$. Numerical experimentation (Sections 3.4 & 3.3.1) confirms that this approach successfully isolates the fast mode. The system is then used to seek evidence of linear and/or nonlinear coupling to the Alfvén mode, i.e. if we drive a pure fast wave ($\mathbf{v} \cdot \hat{\mathbf{C}} \neq 0, \mathbf{v} \cdot \hat{\mathbf{A}}_0 = 0$) does mode conversion/excitation occur? Do velocity components in the direction $\hat{\mathbf{A}}_0$ become manifest?

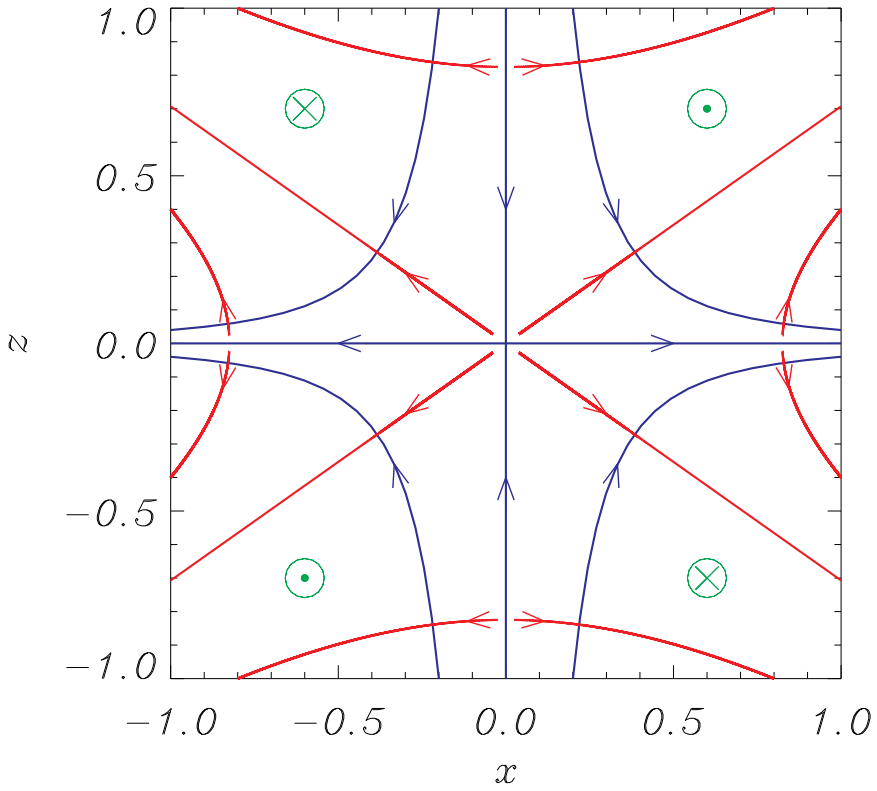

Figure 3.1: Fieldlines of magnetic induction $\mathbf{B}_0$ (blue) and the field $\mathbf{C}$ (red) perpendicular to both the magnetic induction and the flux function, in the case $\epsilon = 1$ for the $y = 0$ plane. Due to azimuthal symmetry other such planes have identical fieldline structure. The flux function $\mathbf{A}_0$ (green) in this case is azimuthal about the spine, running antiparallel to $\hat{\boldsymbol{\theta}}$ above the fan plane and parallel to $\hat{\boldsymbol{\theta}}$ below ($\odot$ corresponds to a vector directed towards the point of view, and $\otimes$ away). These vector fields are everywhere perpendicular, although $\hat{\mathbf{C}}$ and $\hat{\mathbf{A}}_0$ are undefined on the spine and fan plane. For a given fieldline other than those on the spine or fan plane, $\mathbf{C}$ and $\mathbf{A}_0$ form planes perpendicular to $\hat{\mathbf{B}}_0$ where $\hat{\mathbf{A}}_0$ delineates neighbouring fieldlines of like strength (constant B), and $\hat{\mathbf{C}}$ delineates those of variable strength. Thus, we can perturb across $\hat{\mathbf{A}}_0$ as a means of introducing tension without disturbing the pressure balance.

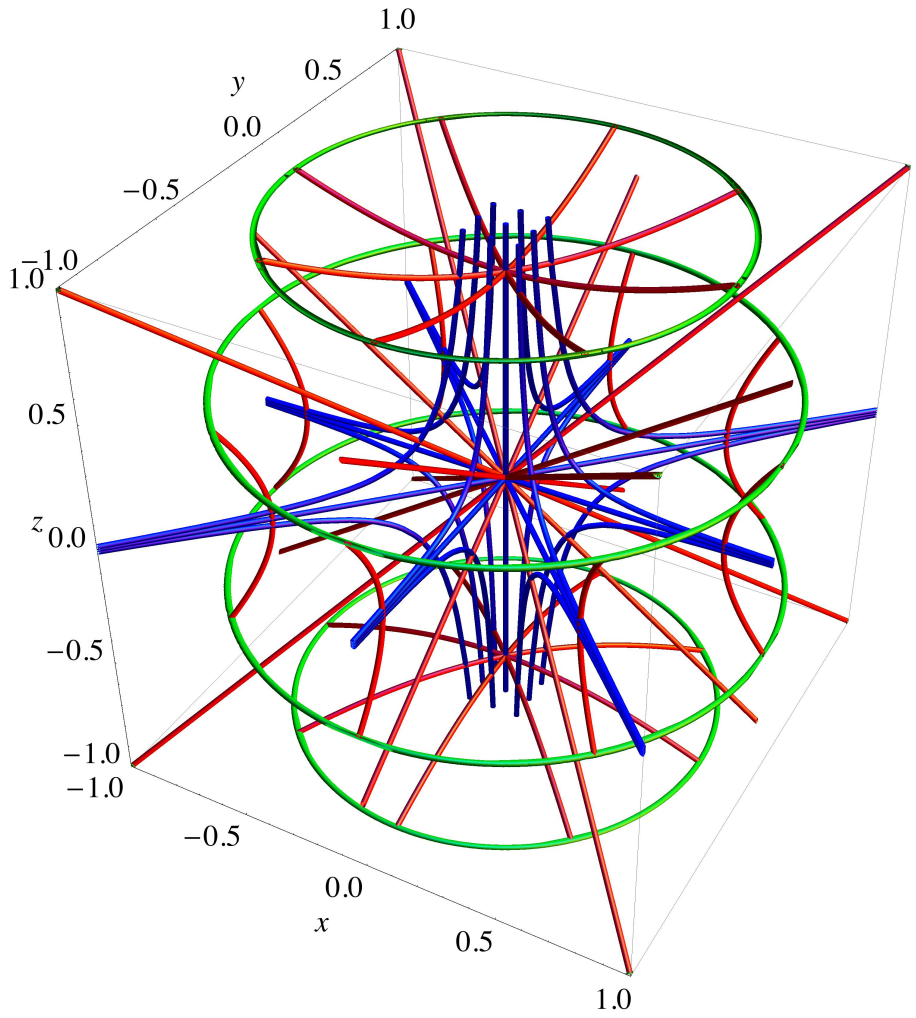

Figure 3.2: 3D perspectives of the system of orthogonal polarisation vectors for $\epsilon = 1$, with lines of force for $\mathbf{A}_0$ (green), $\mathbf{B}_0$ (blue) and $\mathbf{C}$ (red). Note that, apart from where it tends to the spine and fan, lines of force for $\mathbf{A}_0$ form closed loops (i.e., $\mathbf{A}_0$ is associated with torsional motion).

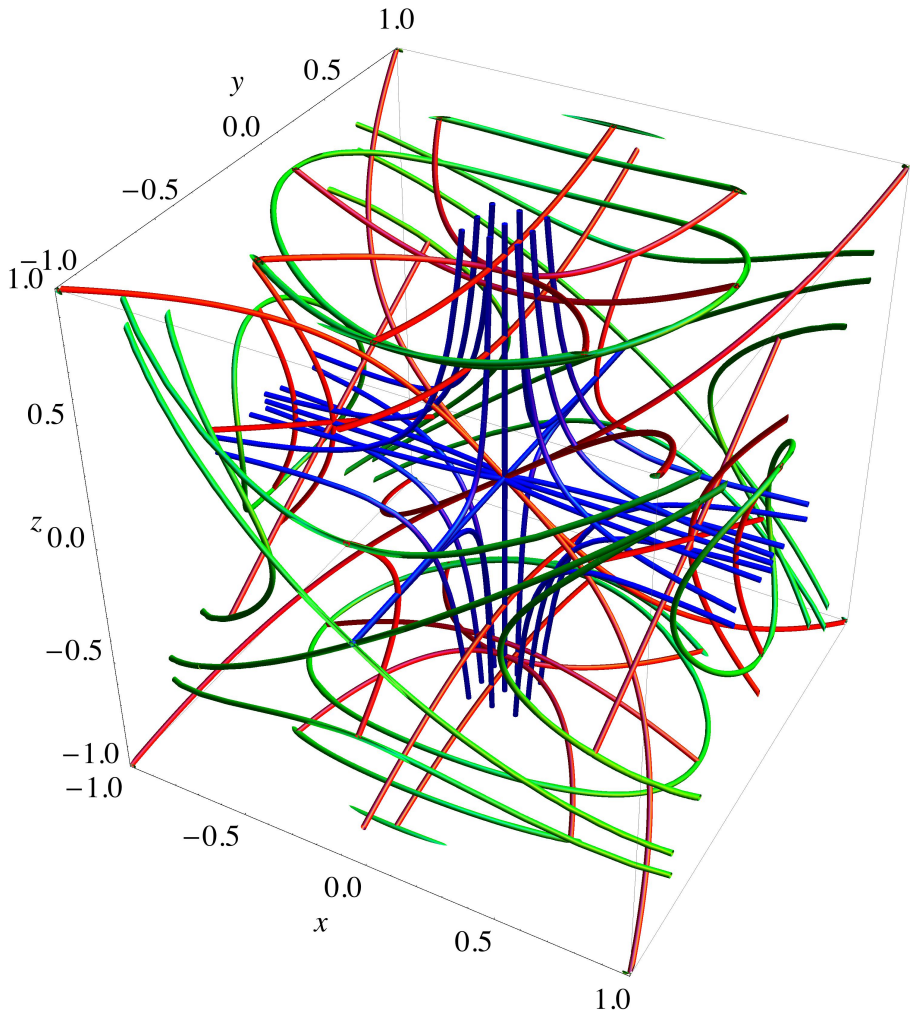

Figure 3.3: 3D perspectives of the system of orthogonal polarisation vectors for $\epsilon = 0.5$, with lines of force for $\mathbf{A}_0$ (green), $\mathbf{B}_0$ (blue) and $\mathbf{C}$ (red). Note that, apart from where it tends to the spine and fan, lines of force for $\mathbf{A}_0$ form closed loops (i.e., $\mathbf{A}_0$ is associated with torsional motion).

3.2.4 Numerical Solution

Nondimensionalised versions of the governing nonlinear MHD equations (3.2) are solved using the LARE3D numerical code (see Section 1.6) with magnetic equilibria corresponding to both proper and improper 3D null points. Each scenario introduces a pure, planar fast magnetoacoustic wave pulse along the upper z-boundary, by driving the following sinusoidal profile:

$$\mathbf{v}\cdot\hat{\mathbf{C}} = v_C = \alpha\sin(2\pi t), \quad \mathbf{v}\cdot\hat{\mathbf{A}}_0 = v_A = 0, \quad \mathbf{v}\cdot\hat{\mathbf{B}}_0 = v_B = 0 \quad \text{for} \quad 0 \leq t \leq 0.5 \quad (3.8)$$

Note that v_A, v_B, and v_C are velocity components in the directions of the coordinate system discussed in Section 3.2.3, and that v_A is *not* the Alfvén speed (which we denote c_A throughout this thesis). The other equlibrium simulation non-dimensionalised parameters are as follows; $\rho_0 = 1$, $p_0 = 0$ ($\beta = 0$), $\eta = 0$ and $\nu = 0$ (ideal, inviscid MHD) . Numerical tests determined that the amplitude $\alpha = 0.001$ was sufficiently small relative to other parameters to generate a linear wave[2] and for the rest of this chapter we set $\alpha = 0.001$. The other boundary conditions are set as zero-gradient conditions. The simulations utilise a uniform numerical grid with domain $x \in [-1,+1]$, $y \in [-1,+1]$, $z \in [-1,+2]$ and $720 \times 720 \times 1080$ grid points, giving a high effective resolution of $\delta x \approx \delta y \approx \delta z \approx 1/360$. The results presented focus into the region $x \in [-1,+1]$, $y \in [-1,+1]$, $z \in [-1,+1]$ i.e. a subset of the full numerical domain.

Since $\hat{\mathbf{C}}$ is undefined along the spine and the fan, driving v_C generates a planar wave with a small hole about the spine (for the top-boundary driven simulations) or a gap along the fan (for the side-driven simulations). This is essential to avoid the mode degeneracy on the spine and/or fan-plane fieldlines.

After the near-planar pulse is generated, a small trailing wake is also introduced due to dispersion (e.g. Uralov 2003). Such a wake does not impact upon the dynamics of the main/lead pulse.

3.2.5 WKB Approximation

Semi-analytical WKB approximations of fast waves about both proper and improper null points were previously considered by McLaughlin et al. (2008). Succinctly, the WKB method is an asymptotic series approximation for low-frequency wave forms and has previously proven useful in understanding and interpreting null point models[3]. According to their WKB solution, McLaughlin et al. (2008) find that fast mode rays propagate in a similar manner to that seen in 2D, namely in that they refract from regions of high-to-low Alfvén speed causing a wrapping effect about the null point, eventually accumulating in its vicinity. Different ray paths for fast

[2] although, as the code is fully nonlinear, we may see some weakly nonlinear effects

[3] More information regarding the WKB method can be found in Bender & Orszag (1978) and Tracy et al. (**?**)

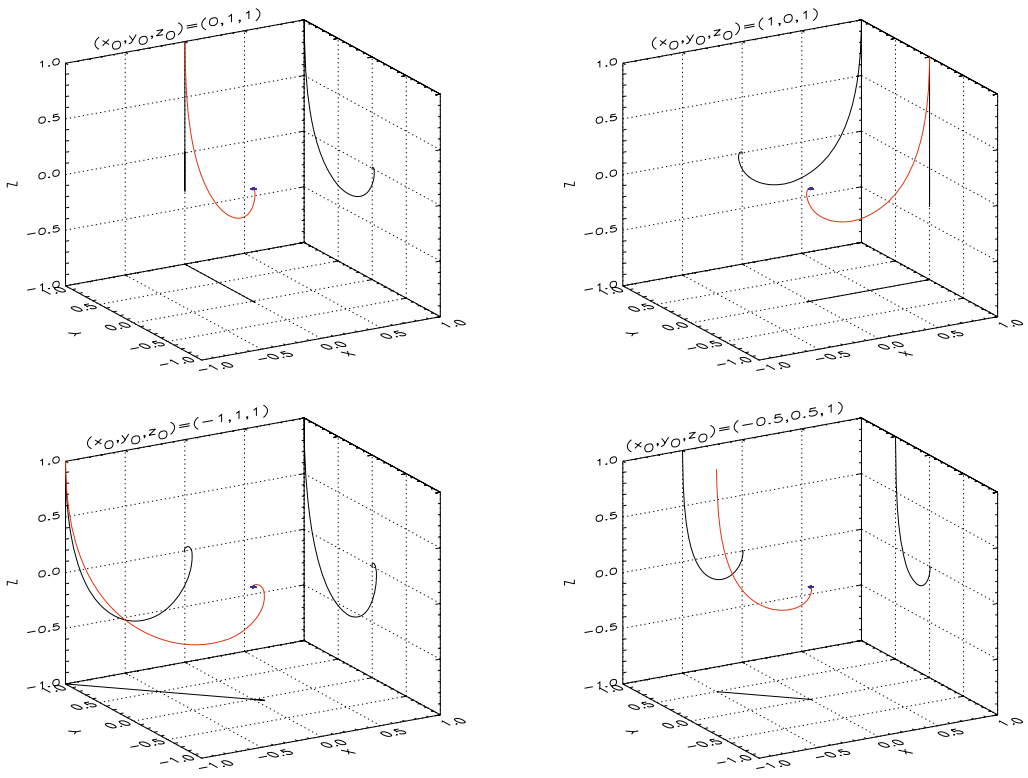

Figure 3.4: Ray paths originating in the $z = 1$ plane for solutions according to the fast wave WKB solution of McLaughlin et al. (2008) for the proper null point ($\epsilon = 1$). The red ray represents the 3D path, and the black curves indicate the xy, yz, and xz-projections of the ray into the respective planes. All rays eventually accumulate at the null point.

waves about the null are shown in Figures 3.4 and 3.5 for the $\epsilon = 1$ and $\epsilon = 0.5$ cases, where we see that different trajectories are taken for the same starting points due to different Alfvén speed profiles (c.f., Figure 3.8).

The WKB solution can be used to determine a position of a wave front by seeding many separate rays and then calculating a surfaces of constant phase (which correspond to the position of a front at a given time), as shown in Figure 3.6. Such solutions showing the expected location of the leading front of our driven pulses are presented in Sections 3.3 and 3.4 overlaying our numerical results.

The implementation of the WKB method as per McLaughlin et al. (2008) does not reveal information about the change in wave amplitudes, makes implicit ordering assumptions, and cannot capture any behaviour associated with mode coupling or conversion. It also cannot be used to determine nonlinear effects as it is a solution of the first-order, linearised MHD equations. As such, comparison to the WKB method serves a two-fold purpose: if the solutions disagree it indicates possible occurrences of mode coupling and other non-WKB effects or, alternatively, it indicates numerical inaccuracies. In addition, due to our special coordinate system being undefined on the

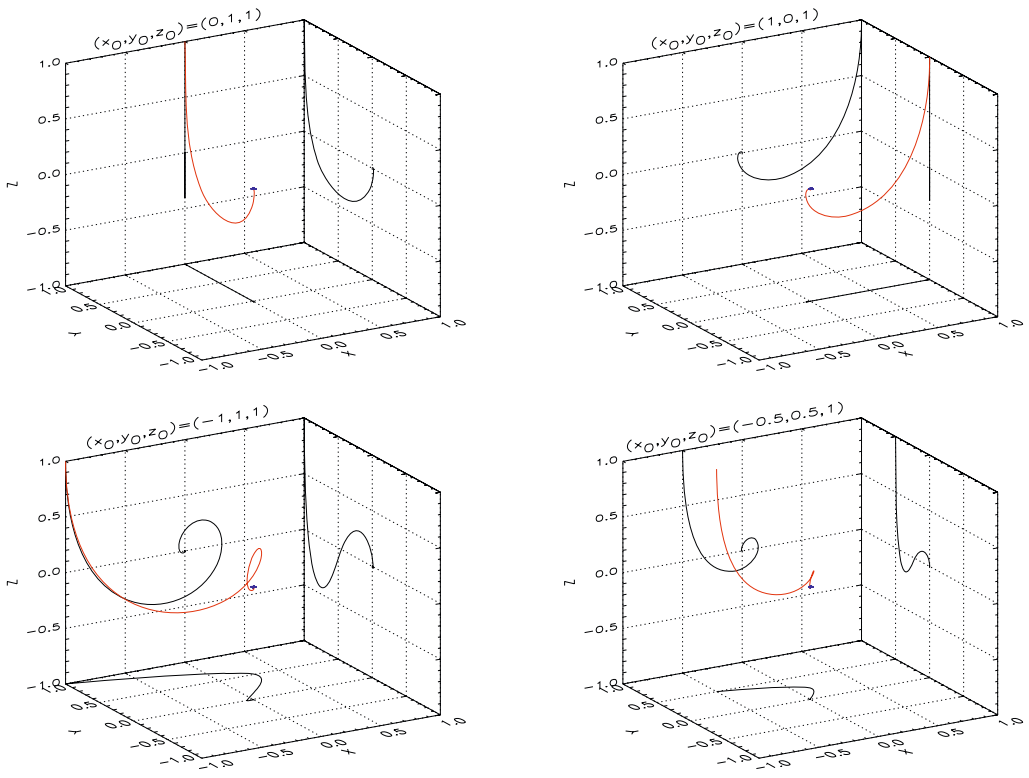

Figure 3.5: Ray paths originating in the $z = 1$ plane for solutions according to the fast wave WKB solution of McLaughlin et al. (2008) for the proper null point ($\epsilon = 0.5$). The red ray represents the 3D path, and the black curves indicate the xy, yz, and xz-projections of the ray into the respective planes. All rays eventually accumulate at the null point.

spine and fan, the near-planar waves presented in the numerical solutions have the aforementioned gap around the spine. However, the mathematical nature of the WKB solution allows one to avoid the question of whether it is possible to drive a pure mode on the spine or fan and simply determines which path a fluid element would take if it were possible. As such, discrepancies between the WKB solution and numerical solutions on the spine or fan plane are entirely to be expected and indicative of neither coupling nor numerical error.

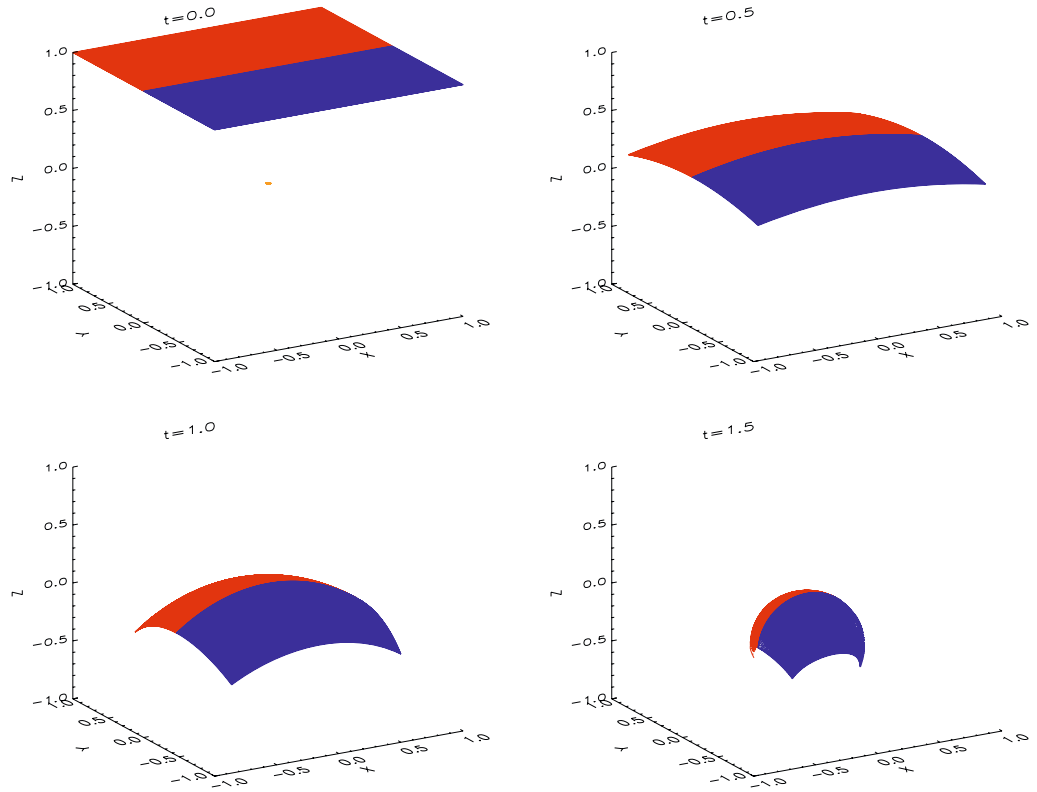

Figure 3.6: Surfaces of constant phase through time, showing the behaviour of the initially planar wavefront that starts at $z = 1$ and extends over the region $-1 \leq 1$, $-1 \leq 1$. From McLaughlin et al. (2008)

3.3 Proper Null, $\epsilon = 1$

Let us first consider the proper radial null point ($\epsilon = 1$) where a velocity pulse (equation 3.8) is driven in v_C along the top computational boundary (i.e. $z = 2$). The resultant propagation is seen in Figure 3.7. Figure 3.7 follows the wave in the $yz-$plane with $x = 0$, and since this wave remains azimuthally symmetric about the spine throughout, the panel captures all of the transient features of the wave in the domain.

The wave propagates towards the null point and *we observe a strong refraction effect which focuses the wave towards the null point*, i.e. all of the wave and thus wave energy eventually accumulate at this point. This refraction/wrapping effect has previously been identified as a key feature of the behaviour of the fast magnetoacoustic mode about 2D nulls (e.g. McLaughlin & Hood 2004) and is dictated by the Alfvén-speed profile around the null point, namely that the wave propagates from regions of high to low Alfvén speed. Here, the isosurfaces of Alfvén-speed profile (Figure 3.8) are spheroid shells that are azimuthally symmetric (explaining why the propagating wave maintains symmetry) and are of decreasing Alfvén-speed magnitude as one approaches the null

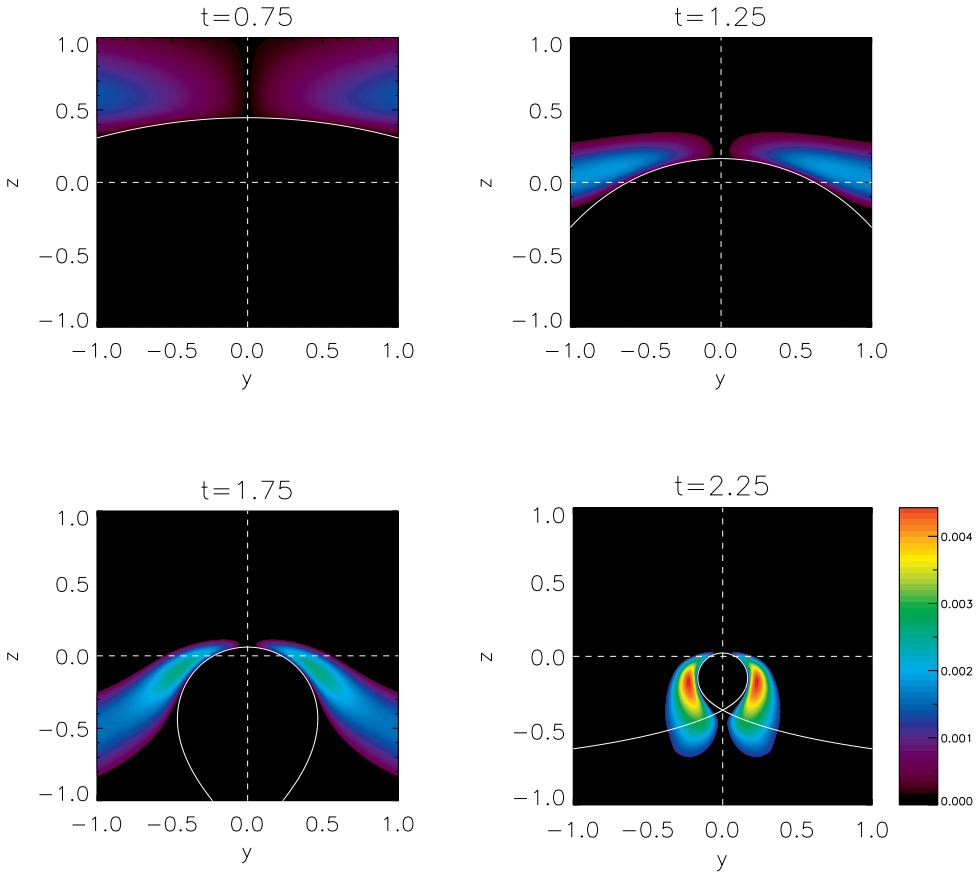

Figure 3.7: Contour plots illustrating the propagation of $|\mathbf{v}|$ about the null point. The white line illustrates the position of the leading edge of the wavefront predicted by the WKB solution, and is in good agreement with the numerical results (sufficiently far from the computational boundaries).

point.

The WKB solution for the leading edge of an infinitely planar fast wave starting at $z = 2$ is also shown in Figure 3.7 (in white). The agreement between the leading edge of the wave front observed in $|\mathbf{v}|$ and the WKB solution near the null point is good: the (numerical) wave experiences refraction along the same profile and at the same rate as prescribed by the analytical approximation. Towards the boundaries the numerical front increasingly lags behind the WKB front as time evolves: this is not a physical attribute of the fast wave but rather a consequence of the boundary conditions. However, this does not affect the key behaviour close to the null where the agreement between the two solutions is good. There is a further discrepancy where the WKB solution exists across the spine whereas the pulse does not. However, this is expected as we purposely did not drive any component along the spine due to the mode degeneracy discussed in Section 3.2.4. This agreement between the numerical solution and the WKB solution (which itself precludes mode coupling) suggests that the pulse is propagating only as the fast magnetoacoustic wave and thus no conversion to the Alfvén mode occurs. To verify this, we now utilise the special coordinate

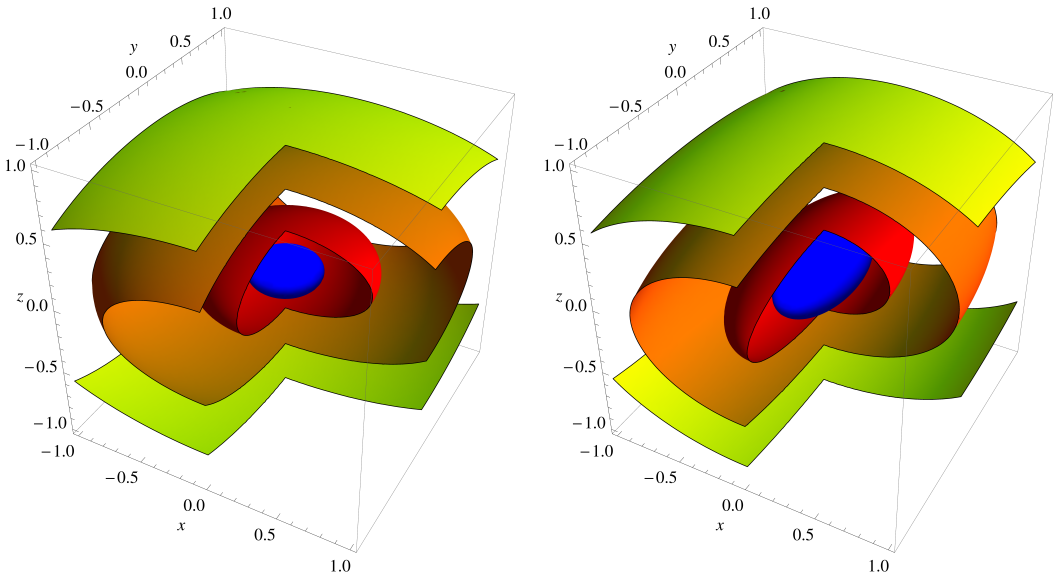

Figure 3.8: The Alfvén -speed profiles for the proper ($\epsilon = 1$, left) and improper null point ($\epsilon = 0.5$, right). The spheroid surfaces of constant c_A become increasingly prolate with greater degrees of fieldline eccentricity. Here the Alfvén speed varies $\propto |\mathbf{B}_0|$ as ρ_0 is taken as constant.

system to inspect the individual constituent modes of the pulse.

3.3.1 $\hat{\mathrm{C}}$: proxy for the fast mode

Figure 3.9 illustrates a typical comparison between contour plots of $|\mathbf{v}|$ and $|v_C|$; *viz.* the whole disturbance and the constituent fast mode. We find that the spatial extent, i.e. positions of the leading, middle and trailing wavefronts, of $|v_C|$ is spatially identical to that of $|\mathbf{v}|$ at any given time. As $|\mathbf{v}| = \sqrt{v_x^2 + v_y^2 + v_z^2} = \sqrt{v_A^2 + v_B^2 + v_C^2}$, we consider the quantity $\sqrt{|\mathbf{v}|^2 - v_C^2} = \sqrt{v_A^2 + v_B^2}$ and find that is non-zero and of order $\mathcal{O}(\alpha^2)$. As the difference between $|\mathbf{v}|$ and $|v_C|$ is non-zero, it is clear that nonlinear effects, possibly $\mathcal{O}(\alpha^2)$ mode conversion, are present but the two are linearly equivalent. Thus, we observe that the (linear) transient behaviour of the fast wave about a proper null point is be dominated by the refraction effect, focusing the pulse at the null point . We now investigate the other orthogonal directions.

3.3.2 $\hat{\mathbf{A}}_0$: proxy for the Alfvén mode

By considering $|v_A|$, we find that there is no velocity perturbation in this direction at any location or time in the simulation. Hence, no figure is presented, since $|v_A|$ is identically zero for all time. As detailed in Section 3.2.2, this velocity component is in the direction of the Alfvén wave, and

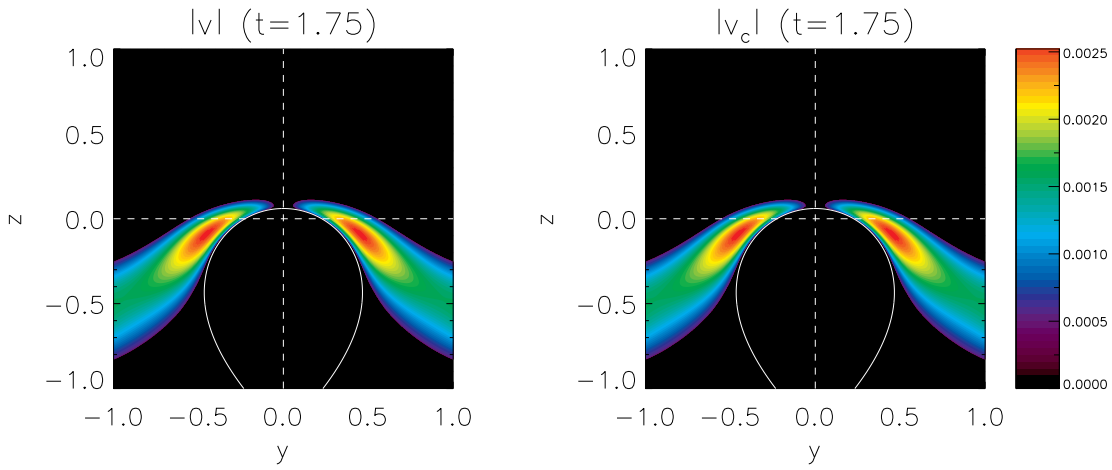

Figure 3.9: Comparison between $|\mathbf{v}|$ (left) and $|v_C|$ (right). The waves occupy the same spatial region and the difference between the magnitudes is of $\mathcal{O}(\alpha^2)$. Hence, we consider the two equivalent in the linear regime, but note the presence of a nonlinear effect which is investigated subsequently.

as such the results assert that no conversion of the fast mode to the Alfvén mode has occurred on either a linear or a nonlinear level.

3.3.3 $\hat{\mathrm{B}}_0$: proxy for the field-aligned motions

Figure 3.10 shows contour plots of $|v_B|$ (motions aligned with equilibrium magnetic field) over the same time scale as Figure 3.7. We see that there is a nonlinear disturbance of $\mathcal{O}(\alpha^2)$ that, bar a slight lag on the trailing edge, is confined to within the same spatial locations as the linear fast wave. The discrepancy of the trailing edge is due to the small trailing wake. We also confirm that the calculated value of $|v_B|$ is equivalent to the earlier computed quantity $\sqrt{|\mathbf{v}|^2 - v_C^2}$, which must be true given that we earlier found that $|v_A| = 0$ at all times (thus, we do not show a separate figure of $\sqrt{|\mathbf{v}|^2 - v_C^2}$).

The wave seen in Figure 3.10 is of a different geometry to that of the fast pulse (Figure 3.7) and splits into multiple peaks on the approach to the fan plane. During the evolution, we find that the disturbance of $\mathcal{O}(\alpha^2)$ is entirely sustained by and dependent upon the propagating fast pulse of $\mathcal{O}(\alpha)$, which acts as a *progenitor wave* that creates this *daughter disturbance* instantaneously as it propagates.

Thus, as the fast wave propagates about the proper null point, it causes small disturbances to the equilibrium (which can be thought of as both a force-free magnetic field and a convective/flow free fluid) as it passes. This effect is the subsequent field/fluid response (as a consequence of frozen flux the two are unsurprisingly connected) that settles to the initial configuration. Due to

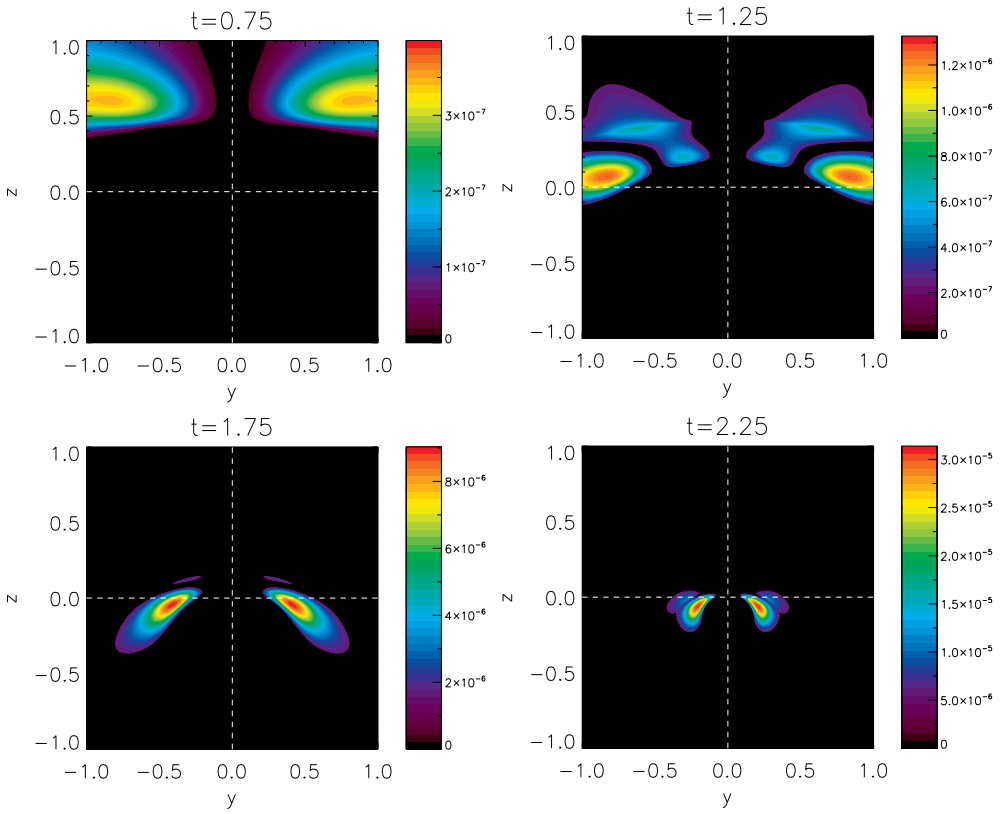

Figure 3.10: Contours of $|v_B|$. Each is shown relative to its own magnitude to enhance contrast, although this makes it difficult to study the evolution of the multiple peaked geometry. The disturbance is $\mathcal{O}(\alpha^2)$, i.e. is small compared to the wave in $|v_C|$ of $\mathcal{O}(\alpha)$.

this dependency on the propagating fast mode (it eventually returns to zero once the fast wave has passed an area, as opposed to being generated but then propagating independently) we have used the term *disturbance* when describing this effect as opposed to *wave* or *mode*. The effect responsible for the nonlinear disturbance is related to what has been called the *ponderomotive* effect in MHD literature (see e.g. Verwichte 1999; Verwichte et al. 1999; McLaughlin et al. 2011a), and is explored further in Chapter 4.

For $\epsilon = 1$ where there is no fast to Alfvén mode conversion, this nonlinear effect has no impact/feedback on coupling dynamics. However, the effect is reconsidered in Section 3.4 as a potential mechanism for mode conversion should $|\mathbf{v} \cdot \hat{\mathbf{A}}_0|$ be non-zero, i.e. $|\mathbf{v}_{\hat{\mathbf{B}}_0}|$ could act as a 'bridge' facilitating exchange of information between $|\mathbf{v} \cdot \hat{\mathbf{C}}|$ and $|\mathbf{v} \cdot \hat{\mathbf{A}}_0|$.

In summary, our numerical experiments have shown that *fast waves do not couple to the Alfvén mode in the vicinity of a proper 3D null point*. As such, the transient behaviour of such fast waves is found to be in good agreement with the results produced via the first-order WKB method (McLaughlin et al. 2008). Additionally, we find that the pure, linear fast waves generate a nonlin-

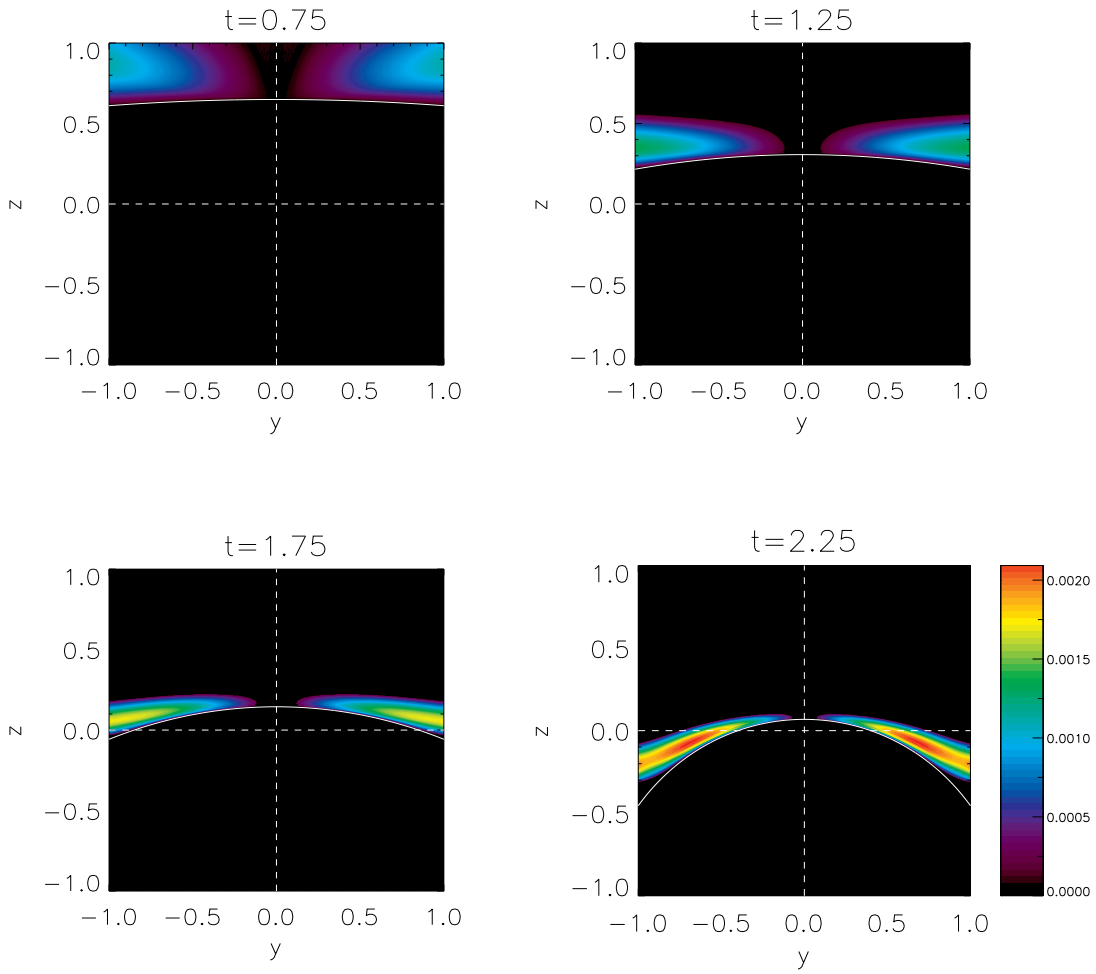

Figure 3.11: Contour plots illustrating the propagation of $|\mathbf{v}|$ about the improper ($\epsilon = 0.5$) 3D null point for the $x = 0$, yz-plane. The position of the lead wave front according to the WKB solution shown in white, which is in good agreement with the numerical results (sufficiently far from the boundary).

ear disturbance aligned with the equilibrium magnetic field.

3.4 Improper Null

We now investigate the behaviour of fast waves at improper 3D null points and consider the specific case of $\epsilon = 0.5$. As in Section 3.3, the aim of our simulations is to generate a pure, linear fast magnetoacoustic wave, observe its propagation, and determine if coupling to the Alfvén mode occurs. Unlike the proper *symmetric* null, it is not clear from analysis of the MHD equations as to whether decoupled wave modes are permitted about improper 3D nulls, because of the asymmetric magnetic topology. It is also unclear as to whether these possible coupling terms/effects

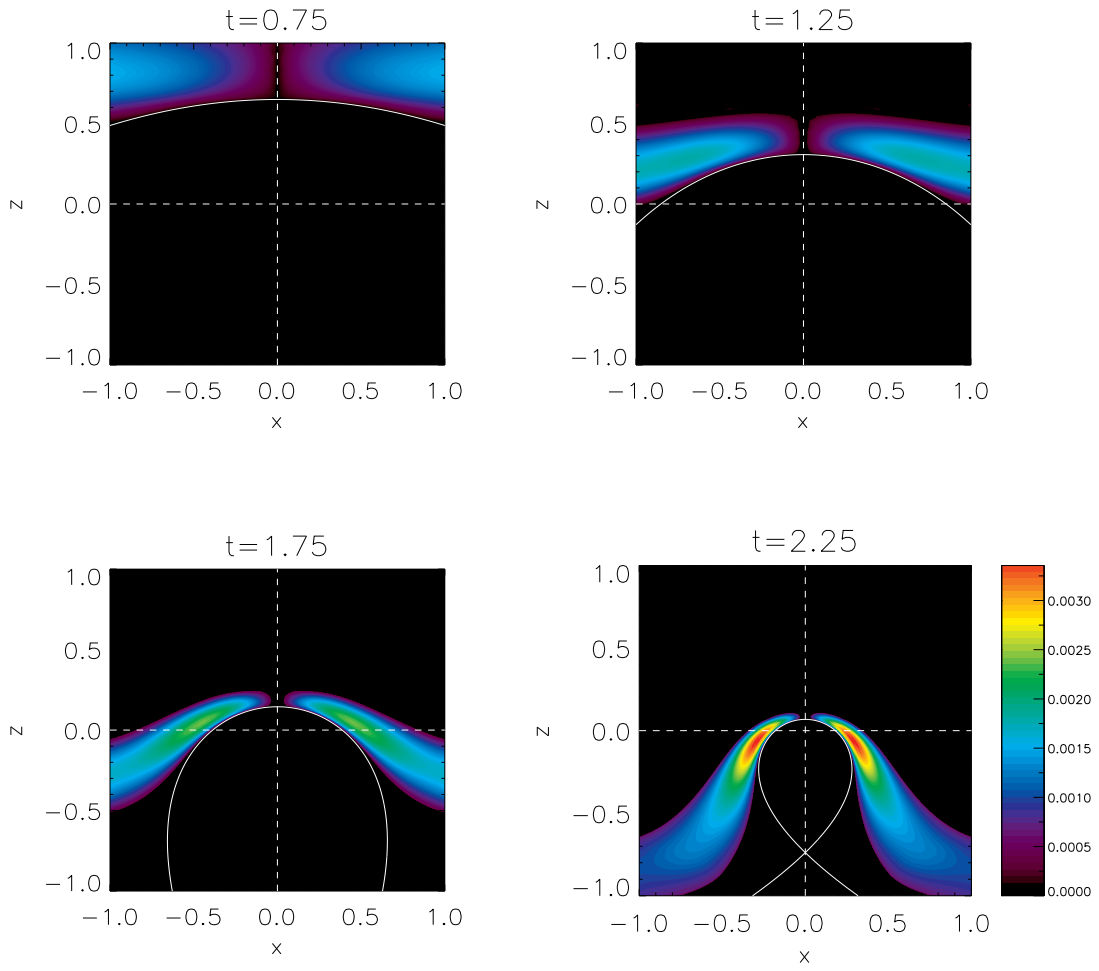

Figure 3.12: Contour plots illustrating the propagation of $|\mathbf{v}|$ about the improper 3D null point for the $y = 0$, xz-plane. The position of the lead wave front according to the WKB solution shown in white, which is in good agreement with the numerical results (sufficiently far from the boundary).

are linear or nonlinear and, generally, what the overall general effect of departing from azimuthal symmetry has on wave dynamics at a null point.

A fast magnetoacoustic wave is driven via v_C at the upper numerical boundary ($z = 2$) using boundary conditions (3.8). Figures 3.11 and 3.12 chart the propagation of the whole wave, $|\mathbf{v}|$, in the same manner as Figure 3.7. However, here the azimuthal symmetry is lost so we show the planes defined by both $x = 0$ and $y = 0$ respectively.

In Figure 3.11, we observe the wave in $|\mathbf{v}|$ propagates through the domain and experience a refraction effect, focused at the null, and that is weaker than the refraction seen in Figure 3.7 for the proper null. In Figure 3.12 ($y = 0$), this refraction effect is comparable to that seen in Figure 3.7. In previous models, refraction effects in MHD waves have been ascribed to gradients in the Alfvén-speed profile. For the improper null, the Alfvén-speed profile forms prolate spheroid

shells with the major axis in the fan plane. As such, the $x = 0$ plane (Figure 3.11) shows the wave propagating in the region with the 'gentlest' Alfvén-speed profile: $c_A^2 = \frac{1}{4}\left(y^2 + 9z^2\right)$ and the $y = 0$ plane (Figure 3.12) shows the wave propagating in the region with the strongest Alfvén-speed profile: $c_A^2 = \frac{1}{4}\left(4x^2 + 9z^2\right)$. This difference in Alfvén-speed profile entirely explains the difference in refraction effects seen in Figures 3.11 and 3.12, and is illustrated by Figure 3.8,.

Along both planes, the wave eventually accumulates at the null point. However, since the strength of the refraction varies and hence the time taken to accumulate at the null differs, we observe the wave in the $y = 0$ plane (Figure 3.12) wrap more rapidly in comparison to that of the $x = 0$ plane (Figure 3.11).

Hence, we have observed a fast magnetoacoustic wave that appears to accumulate only at the 3D null point, via a wave refraction effect entirely dependent on the Alfvén-speed profile. As before, the WKB solution for the leading edge of the pulse is shown in both Figures 3.11 and 3.12. Again, the WKB approximation gives good agreement with the leading edge of the numerical results, bar the expected mode degeneracy along the spine and the boundary effect observed in section 3.3. Hence, the simulation has successfully generated a pulse that conforms to our definition of a fast wave laid out in Section 3.2.2, and is supported by analytical WKB solutions for the fast wave.

Figure 3.13 is analogous to Figure 3.9, demonstrating typical comparisons between the whole disturbance $|\mathbf{v}|$ and the constituent fast mode $|v_C|$. Here, we see results analogous to that of the proper null in Section 3.3.1, i.e. $|v_C|$ corresponds spatially to that of $|\mathbf{v}|$ for both subfigures, furthering the assertion that the wave can be considered a *linear*, pure fast wave. Thus in our simulation evidence for any linear conversion of the fast wave is clearly absent, despite the fully 3D magnetic topology.

We now turn our attention to nonlinear coupling and perform further analysis of the simulation using our special coordinate system.

Figures 3.14 and 3.15 show the velocity component in $|v_B|$ over the same times as Figures 3.11 and 3.12. These field-aligned, nonlinear disturbances have the same features as their $\epsilon = 1$ counterparts considered in Section 3.3.3. Again, bar the small trailing-edge wake, the propagating disturbance seen in $|v_B|$ exists only within the spatial extent occupied by the progenitor wave (in $|v_C|$) and as such its propagation remains entirely dependent upon the fast wave throughout. This nonlinear disturbance is expected due to its presence in the $\epsilon = 1$ case, which can be thought of as a specific subset of general 3D improper nulls. Of course, should the Alfvén-mode component $|v_A|$ be nonzero, this nonlinear effect is potentially a mode-conversion mechanism. However, as in Section 3.3.2, we find the velocity component $|v_A|$ is permanently zero throughout the $\epsilon = 0.5$ simulations, indicating that a fast wave propagating about an improper 3D null does not generate an Alfvén wave due to either linear or nonlinear coupling.

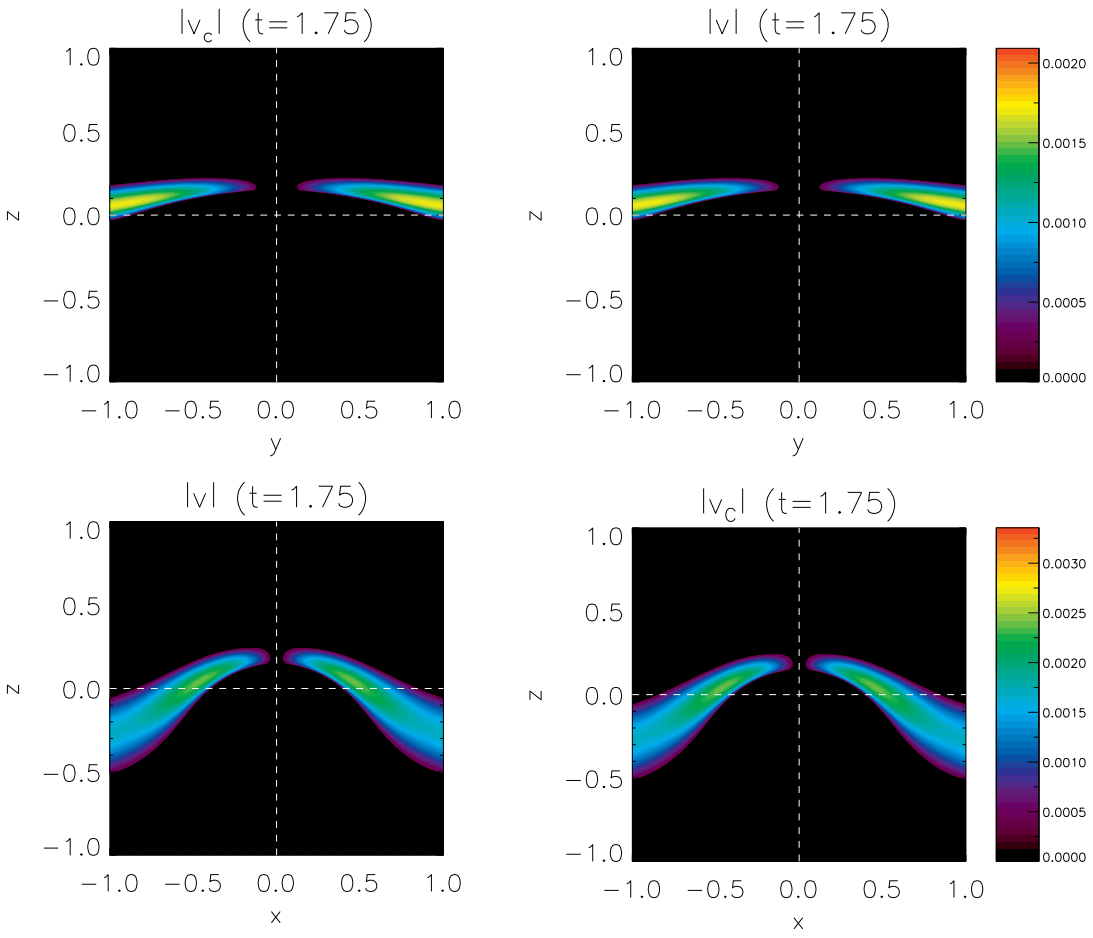

Figure 3.13: Comparison between $|\mathbf{v}|$ (left) and $|v_C|$ (right) for the $x = 0$ (upper) and $y = 0$ (lower) cuts of the improper null point. Throughout the simulation $\sqrt{|\mathbf{v}|^2 - |v_C|^2} \sim \mathcal{O}\left(\alpha^2\right)$ and so we conclude that in the linear regime, the pulse is purely a fast magnetoacoustic wave.

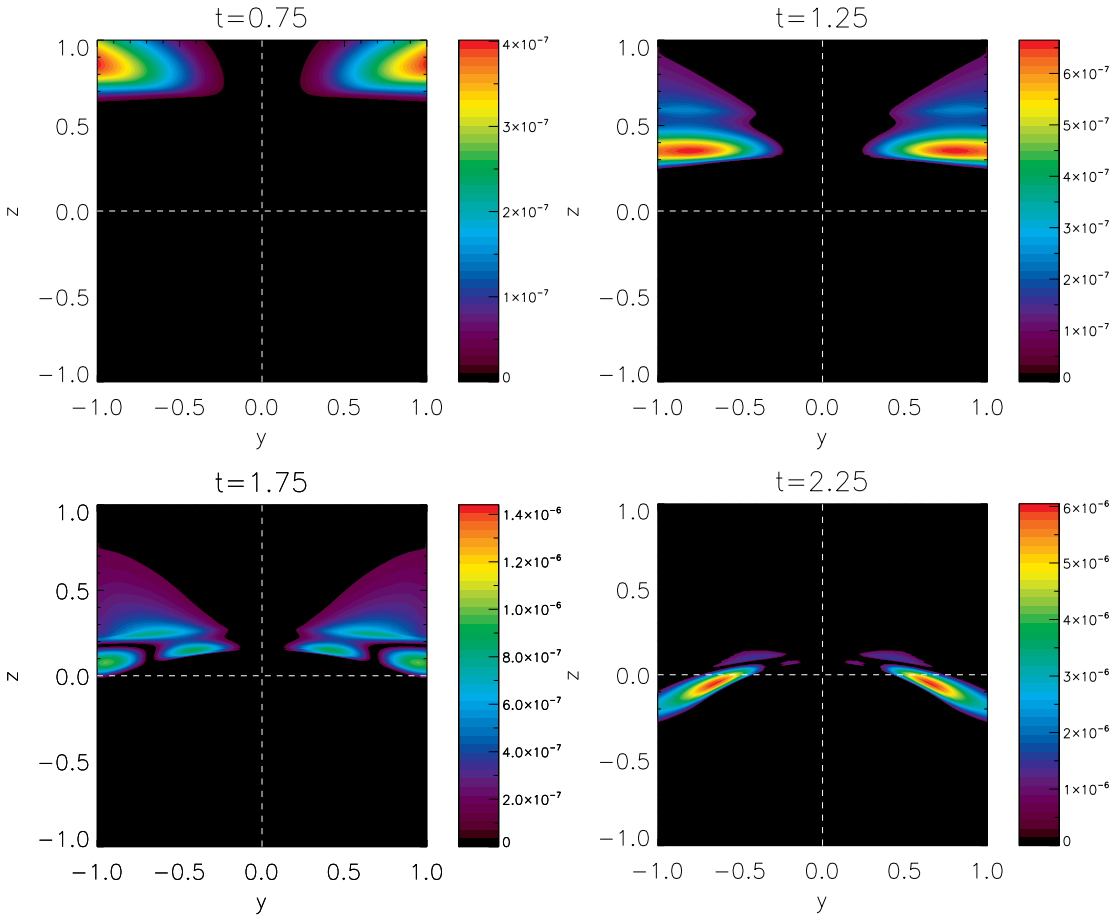

Figure 3.14: The nonlinear velocity component $|v_B|$ for the $x = 0$ cut of the improper null point: a small disturbance is created that mostly occupies the same space as $|v_C|$. As in Figure 3.10, each contour is scaled relevant to the amplitude at the specific times to enhance the contrast of the features.

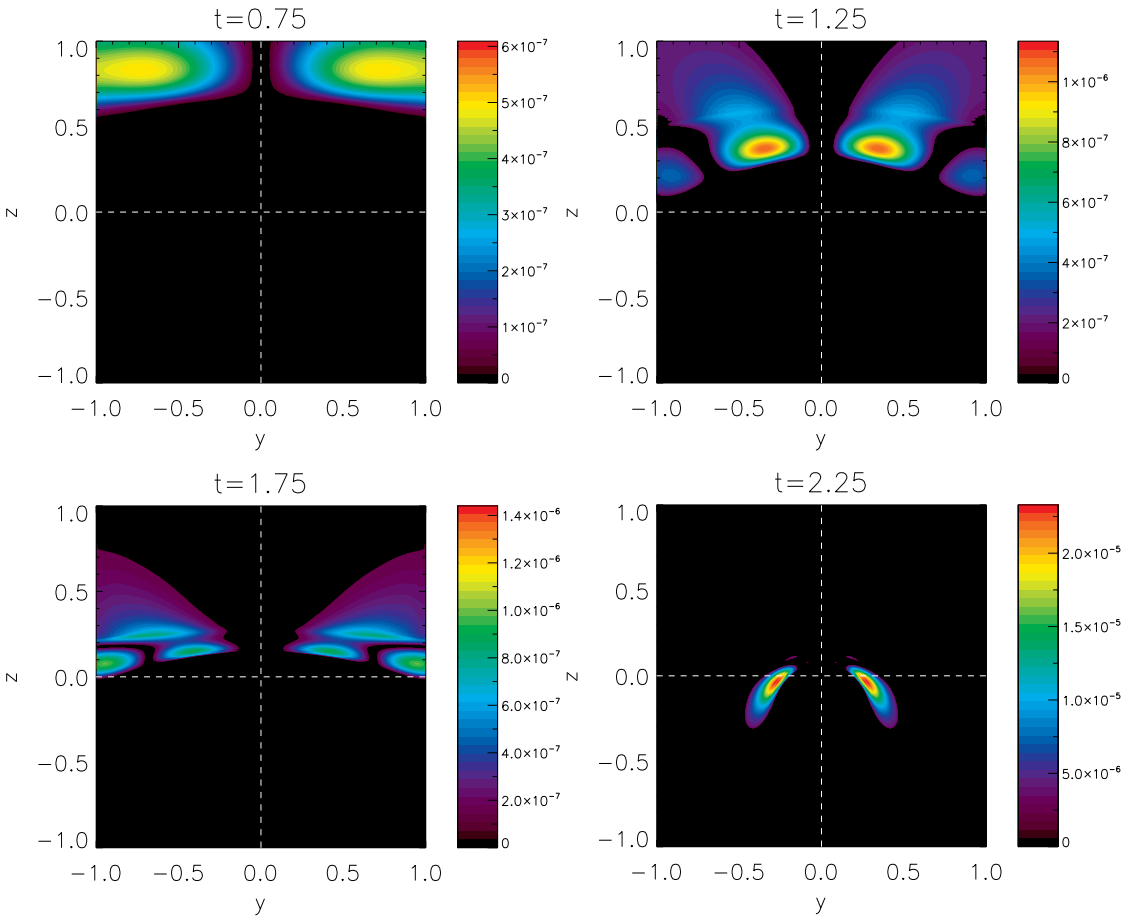

Figure 3.15: The nonlinear velocity component $|v_B|$ as per Figure 3.14 corresponding to the $y = 0$ cut.

One of the chief aims of the simulations in Section 3.4 was to look for evidence of MHD mode coupling about an improper null point. We have generated a pure fast magnetoacoustic wave that exhibits no mode coupling to the Alfvén mode at either a linear or nonlinear scale, but does generate and sustain a nonlinear disturbance aligned with the equilibrium field. Due to the absence of mode coupling, the key features of fast wave behaviour in the neighbourhood of improper nulls are fundamentally the same as that about proper nulls. That is to say, the fast wave propagation is entirely dictated by the Alfvén-speed profile, which causes a refraction effect around null points. Hence, the comparison between the results in Sections 3.3 and 3.4 reduce to a comparison of their differing Alfvén-speed profiles, which affect how rapidly the wave energy accumulates at the null point.

3.5 Conclusion

We have studied both the transient properties of fast magnetoacoustic waves and the nature of linear and nonlinear mode coupling in the vicinity of two potential 3D null points: the proper ($\epsilon = 1$) null, which can be treated as a 2.5D problem using cylindrical polars, and the fully 3D, improper ($\epsilon = 0.5$) null point. Regardless of the eccentricity, ϵ, of the null point studied, we find that:

- The observed fast wave exhibits no linear or nonlinear coupling to the Alfvén mode in the neighbourhood of a 3D null point.
- In this absence of coupling, the propagation of the fast wave is entirely dictated by the Alfvén-speed profile which about a 3D null point leads to a refraction effect, focusing all the wave energy at the null point itself.
- The propagating fast wave generates and sustains an instantaneous and dependent nonlinear field-aligned disturbance.

One of the chief aims of the simulations was to look for evidence of MHD mode coupling about improper null points. Unlike the azimuthally symmetric proper null, it was not clear from analysis of the MHD equations as to whether wave modes about improper 3D nulls are coupled due to the asymmetric magnetic topology, nor whether these coupling terms are linear or nonlinear, i.e. it was not clear what the overall general effect of departing from azimuthal symmetry would have on the wave dynamics. To address this we have generated a pure fast magnetoacoustic wave in the vicinity of 3D nulls and analysed its subsequent propagation. We find no evidence of conversion to, coupling with, or excitation of the Alfvén mode at either a linear or nonlinear scale about both the proper ($\epsilon = 1$) and improper null point ($\epsilon = 0.5$) for planar fast waves which initially lie parallel to the fan plane. Further experiments with the same driving for different eccentricities, namely $\epsilon = 0.25$ and $\epsilon = 0.75$ (values $\epsilon > 1$ have analogues in the range $0 < \epsilon < 1$, and $\epsilon = 0$ recovers the 2D null point), retain these results. Thus, we find that discrete, decoupled MHD wave modes are permitted about general potential null points, i.e. magnetic fieldline eccentricity does not necessarily facilitate fast to Alfvén mode conversion about 3D nulls.

Additionally we find that, in both numerical experiments, the fast-mode pulse generates and sustains a field-aligned disturbance in $|v_B|$. We find that this field-aligned disturbance is not self-sustaining: it is an instantaneous *daughter* disturbance resulting from the *progenitor* fast wave. It is evident that the disturbance in $|v_B|$ does not act as a mode-conversion mechanism in the cases considered here, since no signal is ever generated in $|v_A|$, and the disturbance has no feedback effect upon the main wave. Manifest at $\mathcal{O}\left(\alpha^2\right)$, this disturbance is caused by the nonlinear Lorentz force associated with the propagating fast wave.

Due to the absence of mode coupling, the key features of fast wave behaviour in the neighbourhood of the $\epsilon = 0.5$, improper null points are fundamentally the same as the behaviour in 2D, $\beta = 0$ null point studies (e.g. McLaughlin & Hood 2004), despite the inhomogeneous, fully 3D magnetic field. The difference between propagating fast waves about different potential null points is due *only* to the differing Alfvén-speed profiles. Thus, the propagation of the fast wave is found to be entirely dictated by such profiles, causing the refraction effect which, over time, focuses all of the wave energy at the null point. This is confirmed by our numerical simulations and supports the conclusions drawn from a 3D WKB approach in McLaughlin et al. (2008). Note, in the numerical simulations at large time, the pulse is so close to the null point that the resolution will eventually become inadequate. Nonetheless, in our simulations, over a finite, resolvable time the wave energy accumulates in a small spatial region around the null point, resulting in an exponential steepening of current-gradients, hence resistivity (taken as zero in our simulations) will eventually become non-negligible, resulting in ohmic heating of the local coronal plasma via resistive dissipation (a conclusion directly carried-over from 2D studies, see McLaughlin et al. 2011b). Thus, *we conclude that 3D null points are likely locations for preferential heating by passing fast magnetoacoustic waves.*

We cannot, however, assume the results presented here hold in the opposite case, namely a similar scenario for an initially pure Alfvén wave, follows suit. In fact, results of Galsgaard et al. (2003) report this may not be the case. Although this Chapter shows that, at 3D nulls, the transient behaviour of fast waves can be much like the 2D case, it is not clear whether this is so for Alfvén waves at 3D nulls. We will consider the case of the Alfvén wave at 3D null points in Chapter 6.

Finally, it is important to note that although we have found no evidence of mode conversion for this specific form of fast wave (namely, a pulse which comprises of initially planar wave fronts which are parallel to the fan) that this does not necessarily rule out the possibility of mode-conversion or resonant absorption effects for all fast wave geometries at 3D null points. In fact, new results show that the system of orthogonal polarisation vectors does not always successfully isolate different modes, and that locally Alfvén waves can have other polarisations other than v_A. These initial results are shown in Appendix A. The consequences of possible mode conversion effects for the deposition of energy at the null point versus energy escape via conversion to the Alfvén wave is discussed in Section 7.2. Thus, the work presented in this chapter has not fully addressed the question of mode conversion at 3D nulls but nonetheless is the first numerical simulation to show the main, qualitative features of fast waves at 3D nulls, their weakly nonlinear effects, and how these transient and nonlinear features vary with fieldline eccentricity.

Chapter 4

Ponderomotive Effects

The following chapter details research first reported in:

'On Ponderomotive Effects Induced by Alfvén Waves in Inhomogeneous 2.5D MHD Plasmas'

Thurgood & McLaughlin, Solar Physics, **228**, 205-222, 2013a

4.1 Introduction

Initial experiments into the behaviour of Alfvén waves at 3D nulls (i.e. the complimentary scenario to that presented in the previous chapter) indicated that nonlinear effects played a much more prominent role than in the fast wave case. In order to better understand this phenomenon, let us now take a detour from the topic of 3D wave-null interactions and consider how nonlinear MHD waves behave in general inhomogeneous media.

One important consequence of considering Alfvén wave propagation in an inhomogeneous medium is the concept of *phase mixing*. Simply put, when an Alfvén wave propagates through an inhomogeneous medium, oscillations on neighbouring fieldlines become out of phase as local Alfvén speeds on each fieldline differ. This process naturally creates transverse gradients in the wave across the background magnetic field, and acts as a (linear) dissipative mechanism of Alfvén wave energy, and hence is often considered as a potential mechanism of coronal heating (see, e.g., Heyvaerts & Priest 1983; Browning 1991; Narain & Ulmschneider 1990; 1996; Botha et al. 2000). Typically, such studies have considered an inhomogeneity in density (to permit a unidirectional field, which makes mathematics more tractable), however as this chapter will re-enforce, the process of phase mixing is more generally dependent on a non-uniform background Alfvén speed, i.e. is dependent on both density and magnetic field profiles, and is not restricted to cases of density inhomogeneity only.

There is a secondary consequence of these non-zero spatial gradients in the amplitude of a propagating MHD wave: nonlinear magnetic-pressure gradients and nonlinear magnetic tension (i.e. the nonlinear Lorentz force[1]) act upon the plasma. In the MHD context, these forces are often referred to as the *ponderomotive force*. Generally, a ponderomotive force is defined as a basic nonlinear force consisting of spatial gradients in a wave-field which has a non-vanishing effect when averaged over the period, however we note that the term has been used to refer to other forces (see Allan et al. 1991 and Verwichte 1999 for discussions of the term's historical usage). The concept also exists in areas of plasma physics other than MHD wave theory, for example in the study of laser-plasma interaction where the force causes self-focusing (e.g. Chen 1984) and channel formation (e.g. Boyd & Sanderson 2003). The ponderomotive force in the MHD waves context (i.e. the nonlinear Lorentz force arising in fluid equations of motion) has been formally discussed by Dewar (1970) and Webb et al. (2005). For a thorough discussion of the ponderomotive force in various contexts, and a demonstration of the equivalence of particle-orbit ponderomotive force, see Allan et al. (1991).

In our case (propagating MHD waves in inhomogeneous media; specifically nulls), the effects of such a force are primarily of interest in that it has the potential to facilitate nonlinear mode conversion, the result of which has consequences on energy transport and dissipation. In many previous studies of ponderomotive effects (e.g., in almost all of the forthcoming references), because such studies are concerned with phenomena due to propagating Alfvén waves, the authors use the term ponderomotive force to refer specifically to the nonlinear magnetic-pressure force (since Alfvén waves do not act on the medium via nonlinear magnetic tension, e.g. as shown in Section 4.3). However, as reported in Chapter 3 (and Thurgood & McLaughlin 2012), propagating magnetoacoustic waves have a similar action on the medium, but in that case this is due to both nonlinear magnetic tension and nonlinear magnetic pressure. To avoid ambiguity, in this chapter when referring to the force responsible for the investigated phenomena we avoid the term 'ponderomotive force' in favour of the more specific 'nonlinear magnetic-pressure gradient' or 'nonlinear magnetic tension' as appropriate. We use the term 'ponderomotive effect' to refer to the wider family of phenomena caused by the nonlinear Lorentz force of propagating MHD waves, and in this chapter we primarily consider the specific set of ponderomotive effects induced by propagating Alfvén waves. Outside of the coronal plasma context, ponderomotive effects of MHD waves have been investigated in magnetospheric physics (e.g. Rankin et al. 1994; Tikhonchuck et al. 1995; Allan & Manuel 1996) and as an acceleration mechanism in the solar wind (e.g. Stark et al. 1995). Within the context of coronal plasmas, ponderomotive effects were considered initially by Hollweg (1971) and later by Nakariakov et al. (1997), Verwichte (1999) and Verwichte et al. (1999), the last three of which are key references in this chapter.

[1] N.B. Strictly speaking, the Lorentz force is inherently nonlinear. In this context we specifically mean the nonlinear terms arising from the Lorentz force expanded in the perturbation $\mathbf{B} = \mathbf{B}_0 + \mathbf{b}$. Physically, these nonlinear terms are a consequence of the current and magnetic field of the perturbation itself, whereas the linear terms represent the response of the equilibrium field to its perturbation.

Verwichte (1999) and Verwichte et al. (1999) considered the nonlinear evolution of an Alfvén wave in a homogeneous 1.5D model. They found that the nonlinear magnetic-pressure gradient was responsible for two features of the resultant wave behaviour. Firstly, they found that the propagating Alfvén wave sustains a disturbance which is longitudinal to the background magnetic field, and caused no net perturbation to the plasma (since the average nonlinear magnetic pressure over the wave period was zero). They dubbed this feature a *ponderomotive wing*. Secondly, they found that the interaction between two crossing Alfvén waves gives rise to a non-zero net perturbation of plasma density. Hence, in warm plasmas, this *cross-ponderomotive effect* was identified as a potential mode conversion mechanism, as would certain combinations of pulse geometry and background inhomogeneity leading to non-zero longitudinal perturbations as the pulse propagates.

Nakariakov et al. (1997) considered the nonlinear excitation of the fast wave by a propagating Alfvén wave which undergoes phase mixing in a unidirectional field structured by a background density profile (hence, an inhomogeneous background Alfvén speed). They derive governing wave equations, then evaluate them at an initial instant where only a pure, linear Alfvén wave is perturbing the system to find that the nonlinear fast wave equation contains a source term dependent on transverse gradients in the Alfvén-wave amplitude, hence showing that nonlinear mode conversion is permitted in their scenario. This was then demonstrated in a numerical simulation, where an initial condition perturbs the medium to generate an Alfvén pulse with a profile $\propto \text{sech}^2(y)$ (where $\hat{\mathbf{B}} = \hat{\mathbf{y}}$). The pulse subsequently generates fast magnetoacoustic waves as the simulation evolves. They conclude that Alfvén waves not only heat directly via the phase mixing dissipation method as per Heyvaerts & Priest (1983) but also indirectly through nonlinear coupling to the fast wave, which is itself dissipative.

Botha et al. (2000) extended this work and found that the efficiency of the mode conversion is determined by the frequency and amplitude of the Alfvén wave, and by the gradient in the background Alfvén speed. Their work showed that the fast wave component eventually reached saturation, and concluded that (if the Alfvén-wave amplitude is high enough) the nonlinear mode conversion can be a significant sink of Alfvén-wave energy that otherwise would contribute to the linear phase mixing damping mechanisms as per Heyvaerts & Priest (1983). McLaughlin et al. (2011a) further extended the work into the visco-resistive case, where they found that the equilibrium density profile (and hence the location of heating) is significantly modified by the visco-resistive heating and the ponderomotive effects (i.e. drifting of the heating layer can occur).

In this chapter, we focus on the possibility of the nonlinear Lorentz force as an agent for mode conversion in the general 2.5D MHD scenario, and also consider how ponderomotive effects identified in 1.5D models carry over. To do so, we first extend the source term analysis of Nakariakov et al. (1997) to a MHD scenario which may be inhomogeneous in both magnetic induction and density (i.e. the background Alfvén speed is inhomogeneous; Nakariakov et al. 1997 consider

inhomogeneity in density, but not magnetic field). Then, we emulate the numerical experiment of Nakariakov et al. (1997) in light of our extended analysis to discuss previously unreported ponderomotive effects.

Thus, the chapter is presented as follows; in Section 4.2 we derive wave equations for a general 2.5D cold plasma, to determine the set of nonlinear interactions permitted between the MHD wave modes. In Section 4.3, we analyse nonlinear source terms forced by general Alfvén waves, and further consider the case for harmonic Alfvén waves in Sections 4.3.1 and 4.3.2 . In Section 4.4 we present results of the numerical experiment. Finally, we interpret our results and draw conclusions in Section 4.5.

4.2 MHD Wave Equations in a General, 2.5D $\beta = 0$ Medium

We first determine the role nonlinear terms of the MHD equations play in facilitating mode coupling in an ideal, 2.5D, $\beta = 0$ plasma permeated by a general, potential, magnetic field, which we take as $\mathbf{B}_0 = [B_x, B_y, 0]$ such that $\nabla \times \mathbf{B}_0 = \mathbf{0}$, with a background density $\rho_0 = \rho_0(x, y)$. We set $\partial/\partial z = 0$ throughout, i.e. take $\hat{\mathbf{z}}$ as the invariant direction. The governing, ideal, $\beta = 0$ nonlinear MHD equations are:

$$\begin{aligned} \rho\left[\frac{\partial \mathbf{v}}{\partial t} + (\mathbf{v}\cdot\nabla)\mathbf{v}\right] &= \left(\frac{\nabla\times\mathbf{B}}{\mu}\right)\times\mathbf{B} \\ \frac{\partial \mathbf{B}}{\partial t} &= \nabla\times(\mathbf{v}\times\mathbf{B}) \\ \frac{\partial \rho}{\partial t} &= -\nabla\cdot(\rho\mathbf{v}) \end{aligned} \tag{4.1}$$

where the standard MHD notation applies. Initially, the medium is flow-free ($\mathbf{v}_0 = \mathbf{0}$), and is perturbed by finite amplitude perturbations of the form $\mathbf{B} = \mathbf{B}_0 + \mathbf{b}(x, y, t)$, $\rho = \rho_0 + \rho_1(x, y, t)$, $\mathbf{v} = \mathbf{0} + \mathbf{v}_1(x, y, t)$. This yields:

$$\begin{aligned} \frac{\partial \mathbf{v}_1}{\partial t} - \frac{1}{\mu\rho_0}(\nabla\times\mathbf{b})\times\mathbf{B}_0 &= \frac{1}{\mu\rho_0}(\nabla\times\mathbf{b})\times\mathbf{b} - \frac{\rho_1}{\rho_0}\frac{\partial \mathbf{v}_1}{\partial t} - \left(1+\frac{\rho_1}{\rho_0}\right)(\mathbf{v}_1\cdot\nabla)\,\mathbf{v}_1 \\ \frac{\partial \mathbf{b}}{\partial t} - \nabla\times(\mathbf{v}_1\times\mathbf{B}_0) &= \nabla\times(\mathbf{v}_1\times\mathbf{b}) \\ \frac{\partial \rho_1}{\partial t} + \nabla\cdot(\rho_0\mathbf{v}_1) &= -\nabla\cdot(\rho_1\mathbf{v}_1) \end{aligned} \tag{4.2}$$

where the left-hand-side/right-hand-side governs the linear/nonlinear behaviour respectively.

We now decompose into xyz-components such that $\mathbf{v}_1 = (v_x, v_y, v_z)$ and $\mathbf{b} = (b_x, b_y, b_z)$, giving:

$$\begin{aligned}
\frac{\partial v_x}{\partial t} + \frac{B_y}{\mu\rho_0}\left(\frac{\partial b_y}{\partial x} - \frac{\partial b_x}{\partial y}\right) &= N_1 \\
\frac{\partial v_y}{\partial t} - \frac{B_x}{\mu\rho_0}\left(\frac{\partial b_y}{\partial x} - \frac{\partial b_x}{\partial y}\right) &= N_2 \\
\frac{\partial v_z}{\partial t} - \frac{1}{\mu\rho_0}\left(B_x\frac{\partial}{\partial x} + B_y\frac{\partial}{\partial y}\right) b_z &= N_3 \\
\frac{\partial b_x}{\partial t} - \frac{\partial}{\partial y}\left(v_x B_y - v_y B_x\right) &= N_4 \\
\frac{\partial b_y}{\partial t} + \frac{\partial}{\partial x}\left(v_x B_y - v_y B_x\right) &= N_5 \\
\frac{\partial b_z}{\partial t} - \left(B_x\frac{\partial}{\partial x} + B_y\frac{\partial}{\partial y}\right) v_z &= N_6 \\
\frac{\partial \rho_1}{\partial t} + \frac{\partial}{\partial x}\left(\rho_0 v_x\right) + \frac{\partial}{\partial y}\left(\rho_0 v_y\right) &= N_7
\end{aligned} \tag{4.3}$$

where the nonlinear components $N_1, \ldots, N_7$ are:

$$\begin{aligned}
N_1 &= \frac{1}{\mu\rho_0}\left[\left(b_y\frac{\partial b_x}{\partial y}\right) - \left(b_y\frac{\partial b_y}{\partial x} + b_z\frac{\partial b_z}{\partial x}\right)\right] \\
&- \frac{\rho_1}{\rho_0}\frac{\partial v_x}{\partial t} - \left(1 + \frac{\rho_1}{\rho_0}\right)\left(v_x\frac{\partial}{\partial x} + v_y\frac{\partial}{\partial y}\right) v_x \\
N_2 &= \frac{1}{\mu\rho_0}\left[\left(b_x\frac{\partial b_y}{\partial x}\right) - \left(b_x\frac{\partial b_x}{\partial y} + b_z\frac{\partial b_z}{\partial y}\right)\right] \\
&- \frac{\rho_1}{\rho_0}\frac{\partial v_y}{\partial t} - \left(1 + \frac{\rho_1}{\rho_0}\right)\left(v_x\frac{\partial}{\partial x} + v_y\frac{\partial}{\partial y}\right) v_y \\
N_3 &= \frac{1}{\mu\rho_0}\left(b_x\frac{\partial}{\partial x} + b_y\frac{\partial}{\partial y}\right) b_z \\
&- \frac{\rho_1}{\rho_0}\frac{\partial v_z}{\partial t} - \left(1 + \frac{\rho_1}{\rho_0}\right)\left(v_x\frac{\partial}{\partial x} + v_y\frac{\partial}{\partial y}\right) v_z \\
N_4 &= \frac{\partial}{\partial y}\left(v_x b_y - v_y b_x\right) \\
N_5 &= -\frac{\partial}{\partial x}\left(v_x b_y - v_y b_x\right) \\
N_6 &= \frac{\partial}{\partial x}\left(v_z b_x - v_x b_z\right) - \frac{\partial}{\partial y}\left(v_y b_z - v_z b_y\right) \\
N_7 &= -\rho_1\left(\frac{\partial v_x}{\partial x} + \frac{\partial v_y}{\partial y}\right) - \left(v_x\frac{\partial}{\partial x} + v_y\frac{\partial}{\partial y}\right)\rho_1
\end{aligned}$$

Note that the nonlinear Lorentz force in the momentum equation has been considered here in the alternative tension-pressure form

$$(\nabla \times \mathbf{b}) \times \mathbf{b} = (\mathbf{b} \cdot \nabla)\,\mathbf{b} - \frac{1}{2}\nabla\,(\mathbf{b} \cdot \mathbf{b})$$

so that the contributions of the different aspects may be compared. Here, $(\mathbf{b}\cdot\nabla)\,\mathbf{b}$ is the nonlinear magnetic tension and $\nabla\left(\mathbf{b}\cdot\mathbf{b}\right)/2$ is the nonlinear magnetic-pressure gradient.

We now seek (wave) equations governing the evolution of the permitted wave modes. To do so, we differentiate the momentum equation terms to link the system of equations. We then find the velocity components corresponding to the fast, slow and Alfvén wave by using the Cartesian equivalent of the coordinate system used in Chapter 3. In the 2.5D Cartesian analysis here the velocity components are $v_\perp = \mathbf{v}_1\cdot(\hat{\mathbf{z}}\times\mathbf{B}_0) = -B_y v_x + B_x v_y$ (fast), v_z (Alfvén), and $v_\parallel = \mathbf{v}_1\cdot\mathbf{B}_0 = B_x v_x + B_y v_y$ (longitudinal perturbations, where the slow mode is absent/static in $\beta = 0$). Hence, the governing equations are:

$$\left[\frac{\partial^2}{\partial t^2} - c_\mathrm{A}^2\left(\frac{\partial^2}{\partial x^2}+\frac{\partial^2}{\partial y^2}\right)\right] v_\perp = B_x\frac{\partial N_2}{\partial t} - B_y\frac{\partial N_1}{\partial t} + c_\mathrm{A}^2\left(\frac{\partial N_5}{\partial x} - \frac{\partial N_4}{\partial y}\right) \tag{4.4}$$

$$\left[\frac{\partial^2}{\partial t^2} - \frac{1}{\mu\rho_0}\left(B_x\frac{\partial}{\partial x}+B_y\frac{\partial}{\partial y}\right)^2\right] v_z = \frac{\partial N_3}{\partial t} + \frac{1}{\mu\rho_0}\left(B_x\frac{\partial}{\partial x}+B_y\frac{\partial}{\partial y}\right) N_6 \tag{4.5}$$

$$\frac{\partial^2}{\partial t^2}\, v_\parallel = B_x\frac{\partial N_1}{\partial t} + B_y\frac{\partial N_2}{\partial t} \tag{4.6}$$

where $c_\mathrm{A} = \sqrt{B_0^2/\mu\rho_0}$ is the background/equilibrium Alfvén speed that varies in the xy-plane, such that $c_\mathrm{A} = c_\mathrm{A}(x,y)$. Note that by setting the nonlinear terms of equations (4.4)–(4.6) to be zero (i.e. the right-hand-side) we revert to the linear regime, and can see that the linear, $\beta = 0$ fast waves and Alfvén waves are completely decoupled, and there are no disturbances along the magnetic field.

4.3 Source Term Analysis

We now consider conditions on the fluid variables that correspond to a pure, linear Alfvén wave at an early time before coupling or excitation effects have occurred. In this source term analysis, we take the other modes as absent to determine which terms of Equations (4.4)–(4.6) will act as sources of other modes of oscillation in the general MHD case (i.e. we focus terms that contribute to the acceleration of velocity components that are initially zero in the absence of the corresponding wave mode).

To do so, we take $v_z \neq 0$ and $b_z \neq 0$ with $v_x = v_y = b_x = b_y = \rho_1 = 0$ (and so $v_\perp = v_\parallel = 0$), as perturbations in the $\hat{\mathbf{z}}$-direction correspond linearly to a pure Alfvén wave (and the linear Alfvén wave does not perturb mass density). Note that this sets $N_i = 0$ for $i = 3,\ldots,7$, and simplifies N_1 and N_2. The wave equations (Equations 4.4–4.6) thus become:

$$\frac{\partial^2 v_\perp}{\partial t^2} = \frac{1}{\mu\rho_0}\frac{\partial}{\partial t}\left[b_z\left(B_y\frac{\partial}{\partial x} - B_x\frac{\partial}{\partial y}\right) b_z\right] \tag{4.7}$$

$$\left[\frac{\partial^2}{\partial t^2} - \frac{1}{\mu\rho_0}\left(B_x\frac{\partial}{\partial x} + B_y\frac{\partial}{\partial y}\right)^2\right] v_z = 0 \tag{4.8}$$

$$\frac{\partial^2 v_\parallel}{\partial t^2} = -\frac{1}{\mu\rho_0}\frac{\partial}{\partial t}\left[b_z\left(B_x\frac{\partial}{\partial x} + B_y\frac{\partial}{\partial y}\right)b_z\right] \tag{4.9}$$

again, the right-hand-side contains the nonlinear terms.

Here, we see that there is a source term associated with $v_\perp$, thus in this case it is possible that $\partial^2 v_\perp/\partial t^2 \neq 0$. Inspection reveals that Equation (4.7) can be rewritten as:

$$\frac{\partial^2 v_\perp}{\partial t^2} = -\frac{B_0}{\mu\rho_0}\frac{\partial}{\partial t}\left[\hat{\mathbf{z}}\times\hat{\mathbf{B}}_0\cdot\nabla\left(\frac{b_z^2}{2}\right)\right]. \tag{4.10}$$

Hence, the Alfvén wave can cause a nonlinear magnetic-pressure gradient to arise which in turn causes the excitation of fast magnetoacoustic waves, where gradients *transverse* to $\mathbf{B}_0$ are responsible. Note that the term $\hat{\mathbf{z}}\times\hat{\mathbf{B}}_0\cdot\nabla$ is the gradient (directional-derivative) in the unit-direction across fieldlines. This concurs with the analysis of Nakariakov et al. (1997), which considered nonlinear effects in a unidirectional field and found coupling terms associated with transverse gradients (note that if we specifically consider equations 4.4 and 4.5 for such a scenario, we recover their wave equations, see Appendix B). Hence, the Alfvén wave exerts a transverse, nonlinear magnetic-pressure gradient in any situation in which it assumes non-zero gradients across the magnetic field. However as highlighted by Verwichte (1999) the net perturbation will only be non-zero if the ponderomotive force averaged over a complete wave-period is non-zero.

Similarly, we find that the Alfvén wave can cause a nonlinear pressure gradient to arise which causes longitudinal perturbations to the equilibrium field. By rewriting Equation (4.9) as

$$\frac{\partial^2 v_\parallel}{\partial t^2} = -\frac{B_0}{\mu\rho_0}\frac{\partial}{\partial t}\left[\hat{\mathbf{B}}_0\cdot\nabla\left(\frac{b_z^2}{2}\right)\right] \tag{4.11}$$

we see that this is due to *longitudinal gradients* in the Alfvén wave amplitude, i.e. this is the longitudinal effect of nonlinear magnetic pressure.

We note that equations (4.10) and (4.11) can be integrated with respect to time to yield

$$\frac{\partial v_\perp}{\partial t} = -\frac{B_0}{\mu\rho_0}\,\hat{\mathbf{z}}\times\hat{\mathbf{B}}_0\cdot\nabla\left(\frac{b_z^2}{2}\right) = -\frac{B_0}{\mu\rho_0}\nabla_\perp\left(\frac{b_z^2}{2}\right) \tag{4.12}$$

$$\frac{\partial v_{\parallel}}{\partial t} = -\frac{\mathbf{B}_0}{\mu\rho_0}\cdot\nabla\left(\frac{b_z^2}{2}\right) = -\frac{B_0}{\mu\rho_0}\nabla_{\parallel}\left(\frac{b_z^2}{2}\right) \tag{4.13}$$

i.e., a familiar force equation ('$\mathbf{F} = \mathrm{m}\mathbf{a}$') dependent on the square of the amplitude of the Alfvén wave field, conforming to the general definition of a 'ponderomotive force' discussed earlier. Here, we have adopted the notation $\nabla_{\perp} \equiv \hat{\mathbf{z}} \times \hat{\mathbf{B}}_0 \cdot \nabla$ and $\nabla_{\parallel} \equiv \hat{\mathbf{B}}_0 \cdot \nabla$; these terms are the gradients across and along the equilibrium magnetic field in the xy-plane.

One can also perform a source term analysis for fluid variables corresponding to an initially pure fast wave. Doing so, we find that the ponderomotive effects of the propagating fast wave do not facilitate coupling to the Alfvén mode, *the fast wave does not interact with the Alfvén wave on any level, linear or nonlinear* in a 2.5D medium (see Appendix C). Hence, we further can conclude that ponderomotive conversion in $\beta = 0$ is a one-way process from the Alfvén to the fast magnetoacoustic mode.

4.3.1 Harmonic Alfvén Wave

To further investigate the nature of ponderomotive coupling, we reconsider the source terms of the fast wave and longitudinal equations when forced by a harmonic linear Alfvén wave of the form

$$v_z = A\cos\theta = \Re\left(Ae^{i\theta}\right) \quad , \quad \theta = \omega t - \mathbf{k}\cdot\mathbf{r} \quad , \quad b_z = S\left(x,y\right)v_z$$

where A is constant and $S(x,y)$ is a spatial scaling term between velocity and magnetic field perturbations that is associated with the background Alfvén speed (for a linear Alfvén wave, $\mathbf{b} = \pm\sqrt{\mu\rho_0}\mathbf{v}$). If we consider that linear Alfvén waves propagate along magnetic fieldlines only, then the direction of the unit wavevector must be $\hat{\mathbf{k}} = \hat{\mathbf{B}}_0$. We also can derive a dispersion relationship from Equation (4.8) (linear terms only) that links frequency, wave number and Alfvén speed: $c_{\mathrm{A}}^2 = \omega^2/k^2$. Thus, we can consider the wavevector to be $\mathbf{k} = k\hat{\mathbf{k}} = k\hat{\mathbf{B}}_0 = \omega\hat{\mathbf{B}}_0/c_{\mathrm{A}}$, hence the function $\theta = \omega\left(t - \hat{\mathbf{B}}_0\cdot\mathbf{r}/c_{\mathrm{A}}\right)$. Inserting the harmonic form of such a wave, the source terms driving the fast and longitudinal modes (Equations 4.7 and 4.9) become:

$$\frac{\partial^2 v_{\perp}}{\partial t^2} = \frac{A^2S^2}{\mu\rho_0}\frac{\omega^2}{c_{\mathrm{A}}^2}B_0\left[\left(\hat{\mathbf{B}}_0\cdot\mathbf{r}\right)\nabla_{\perp}\left(c_{\mathrm{A}}\right) - c_{\mathrm{A}}\nabla_{\perp}\left(\hat{\mathbf{B}}_0\cdot\mathbf{r}\right)\right]\cos 2\theta\,, \tag{4.14}$$

$$\frac{\partial^2 v_{\parallel}}{\partial t^2} = \frac{A^2S^2}{\mu\rho_0}\frac{\omega^2}{c_{\mathrm{A}}^2}B_0\left[\left(\hat{\mathbf{B}}_0\cdot\mathbf{r}\right)\nabla_{\parallel}\left(c_{\mathrm{A}}\right) - c_{\mathrm{A}}\nabla_{\parallel}\left(\hat{\mathbf{B}}_0\cdot\mathbf{r}\right)\right]\cos 2\theta\,. \tag{4.15}$$

where we have made the additional simplification of constant ρ_0 (i.e. we consider the specific case of inhomogeneity due to variation of the equilibrium magnetic field). Hence, Equations (4.14) and (4.15) govern the transverse and longitudinal perturbations forced via the action of a harmonic Alfvén wave.

The forced motion is driven at double the frequency ($\cos 2\theta$) and is of order $\mathcal{O}(A^2)$, i.e. key features of the ponderomotive effect previously reported in the literature (see e.g., Nakariakov et al. 1997; Botha et al. 2000; McLaughlin et al. 2011a). We find that perturbations to $v_\perp$ and $v_\parallel$ are dependent on two distinct classes of terms, one associated with gradients in the Alfvén-speed profile and the other with gradients in the geometry of the propagating pulse relative to the equilibrium magnetic field.

4.3.2 Instantaneous, Geometric Terms: $\nabla_\perp \left(\hat{\mathbf{B}}_0 \cdot \mathbf{r}\right)$ and $\nabla_\parallel \left(\hat{\mathbf{B}}_0 \cdot \mathbf{r}\right)$

It is known in 1.5D homogeneous MHD, for an Alfvén pulse propagating along a fieldline, that due to gradients in the wave intensity (i.e. ponderomotive effect) the leading flank acts to longitudinally-accelerate the plasma and the rear flank acts to longitudinally-decelerate the plasma. Thus the wave sustains a *cospatial, instantaneous perturbation* that is transported along the magnetic field which, depending on the specific pulse geometry, may or may not cause a non-zero (net) longitudinal perturbation as it passes through the medium (i.e. the 'ponderomotive wings' of Verwichte 1999). Regardless of whether a net perturbation to the plasma occurs, this *longitudinal daughter disturbance* is continually sustained by the propagating Alfvén wave and always remains cospatial to its *progenitor* (viz. the daughter occupies the same spatial region as the Alfvén wave). If we impose conditions equivalent to 1.5D homogeneous MHD (i.e. Equations 4.14 and 4.15 where $\nabla_\perp = 0$ and $\nabla_\parallel (c_\mathrm{A}) = 0$) only one driving term remains,

$$\frac{\partial^2 v_\parallel}{\partial t^2} \sim \nabla_\parallel \left(\hat{\mathbf{B}}_0 \cdot \mathbf{r}\right)$$

i.e. this term governs the longitudinal daughter disturbance.

Our equations indicate that, if we extend our consideration to the homogeneous 2.5D case (i.e. allow non-zero transverse gradients), a transverse equivalent to Verwichte's 1.5D ponderomotive wings, namely a *transverse daughter disturbance*, can exist when there are transverse gradients in the pulse profile across the equilibrium magnetic field, i.e.:

$$\frac{\partial^2 v_\perp}{\partial t^2} \sim \nabla_\perp \left(\hat{\mathbf{B}}_0 \cdot \mathbf{r}\right).$$

Such a profile, in homogeneous MHD, is imposed as an initial condition and would be maintained throughout, however in inhomogneous MHD a profile with transverse gradients can developss

naturally via phase mixing, i.e where the pulse enters a region with a transverse *Alfvén-speed profile*, thus assuming a pulse geometry with transverse gradients. Although in this analysis we have taken the equilibrium field as the source of inhomogeneity, we stress that such a transverse inhomogeneity of the Alfvén-speed profile (i.e. a phase mixing region) can be dependent on variable $\mathbf{B}_0$ and/or ρ_0.

4.3.3 Inhomogeneity Terms: $\nabla_\perp (c_\mathrm{A})$ and $\nabla_\parallel (c_\mathrm{A})$

Now permitting $\nabla(c_\mathrm{A}) \neq 0$ and considering 2.5D inhomogeneous MHD, our equations show the ponderomotive effects not only depend upon the instantaneous magnetic pressure perturbations of assumed pulse geometry discussed previously, but also upon magnetic pressure perturbations as the pulse geometry is altered from instant to instant (i.e. the full set of Equations 4.14 and 4.15). This term is thus the ponderomotive effect due to Alfvén-speed profile inhomogeneities, where its transverse manifestation (which can be thought of as a phase mixing term) excites fast waves, and the longitudinal manifestation excites longitudinal perturbations (which can be thought of as a longitudinal dispersion term). If the net longitudinal perturbation is non-zero, due to the absence of gas pressure gradients in $\beta = 0$ the perturbation will be static.

Thus, the analysis of Sections 4.3.1-4.3.3 shows that the harmonic Alfvén wave nonlinearly interacts with the medium via the longitudinal and transverse manifestations of two classes of ponderomotive effect, namely the geometric effect (cospatial, ponderomotive daughter disturbances) and the $\nabla(c_\mathrm{A})$ effect (ponderomotive acceleration due to inhomogeneous Alfvén-speed profile). Both may yield non-zero net perturbations of the medium, causing coupling to the longitudinal and transverse (fast magnetoacoustic) modes. As the two terms may interfere (constructively or destructively), the precise dynamics of ponderomotive mode conversion will vary on a case-by-case basis.

4.4 Numerical Demonstration

We now demonstrate the ponderomotive effects identified in Section 4.3 by considering simulations of a simple scenario; namely that of an initially uniform pulse propagating and separating in a unidirectional field stratified by a smooth, yet steep, transverse density profile (i.e. a transverse Alfvén-speed profile). Such a scenario was considered in Nakariakov et al. (1997) and we emulate their results to demonstrate features that they did not report upon. We solve the nondimensionalised, nonlinear MHD equations using LARE2D (See Section 1.6 for details of code and Section 3.2.1 for details of the nondimensionalisation procedure, noting that all quantities are nondimensional in this section) for the equilibrium magnetic field $\mathbf{B}_0 = \hat{\mathbf{y}}$ where the plasma is structured

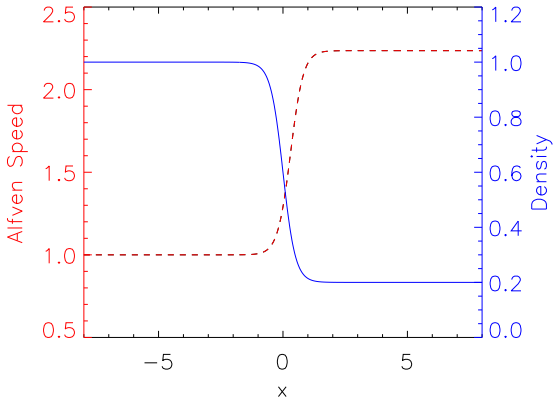

Figure 4.1: The Alfvén-speed profile c_{A} (red dashed line) and the density profile ρ_0 (blue solid line). There is steep, continuous, transverse gradient in Alfvén speeds (a phase mixing region) in the region $-1 < x < 1$.

by a density inhomogeneity of the form:

$$\rho_0 = \rho_0\left(x\right) = \frac{0.2 + e^{-4x}}{1.0 + e^{-4x}}$$

in the numerical domain $x, y \in [-8, +8]$ with a resolution of 1920^2 grid points for a cold plasma initially at rest ($\mathbf{v}_0 = \mathbf{0}$).

The resulting (nondimensionalised) Alfvén-speed profile, shown in Figure 4.1, is thus $c_{\mathrm{A}} \approx 1$ for $x < -1$, $c_{\mathrm{A}} \approx \sqrt{5}$ for $x > +1$, with a steep but continuous transition between the two limits in the region $-1 < x < 1$. In this scenario (due to the unidirectional field) the longitudinal direction here is simply $\hat{\mathbf{y}}$ and the transverse direction is $\hat{\mathbf{x}}$. Thus the transverse and longitudinal velocity components of the simulation (v_x and v_y) relate to the transverse and longitudinal velocity components in the previous analysis ($v_\perp$ and $v_\parallel$) such that $v_\perp = -B_y v_x + B_x v_y = -v_x$ and $v_\parallel = B_x v_x + B_y v_y = v_y$.

We perturb the system by imposing an initial condition of the form

$$v_z = 2A\mathrm{sech}^2\left(\frac{y}{a}\right)$$

with pulse-width parameter $a = 0.25$, which creates an Alfvén wave (with apex at $y = 0$) which separates into two oppositely-travelling pulses each with amplitude $A = 0.001$. The initial amplitude is taken to be small so that if a fast wave is nonlinearly generated, it will not disturb the equilibrium field through, e.g., shock wave formation. Simple reflecting boundary conditions are employed, thus the simulation is halted once the pulses reach the boundaries. Figure 4.2 shows the resulting separation and propagation of the Alfvén waves (seen in v_z). Throughout the simulation, the pulse geometry maintains its initial longitudinal ($\propto \mathrm{sech}^2 y$) and transverse ($= 0$) profiles

outside of the phase mixing region ($x < -1$ and $x > +1$). Within the region, due to phase mixing, the profiles change in time, with the creation of transverse gradients in pulse geometry which become increasingly steep as time progresses.

We now consider perturbations to the longitudinal velocity component v_y, shown in Figure 4.3. Here, we note two nonlinear features, which were not detailed in the original experiment of Nakariakov et al. (1997) (they did not consider longitudinal effects). The first is a disturbance that appears to propagate as the Alfvén waves (i.e. along the fieldlines at the Alfvén speed) yet is observed in the longitudinal velocity component. These are not independently propagating waves (in our $\beta = 0$ simulation there is no gas pressure to facilitate longitudinal oscillations) but instantaneous perturbations/disturbances that are sustained and carried by the propagating Alfvén waves in v_z, i.e. these are the *longitudinal daughter disturbances* identified in Section 4.3.2, and are associated with longitudinal gradients in the pulse geometry (for the harmonic Alfvén wave, this was of the form $\nabla_{\parallel} \hat{\mathbf{B}}_0 \cdot \mathbf{r}$). The longitudinal daughter disturbance sustained by the upwardly propagating Alfvén wave is of the same sign, whereas the daughter sustained by the downwardly propagating wave is the opposite to its progenitor. Their maximum amplitudes are $v_y = \pm 4.999 \times 10^{-7}$ respectively, which is of $\mathcal{O}\left(0.5A^2\right)$. We note that the amplitude of the longitudinal daughter is weaker by a factor of approximately $\sqrt{5}$ in the higher Alfvén speed region compared to its counterpart in the lower Alfvén speed region.

The second longitudinal ponderomotive effect is a static perturbation assuming the geometry of the initial pulse, which is also is of smaller amplitude in the higher Alfvén speed region. The fluid velocity is perturbed such that $v_y = \pm 3.031 \times 10^{-7}$ at $x = -8$ and $v_y = \pm 6.678 \times 10^{-8}$ at $x = +8$ (in the vicinity of $y = 0$), hence this perturbation is also weaker in the higher Alfvén speed region by a factor of approximately $\sqrt{5}$, i.e. the amplitude of the longitudinal perturbations is inversely proportional to c_{A}. The perturbation is accompanied by a stationary mass density enhancement (ρ_1), initially generated at the same order as the velocity perturbations (the same magnitude and inversely proportionality to c_{A}) then grows linearly in time during the simulation. These features are the 2.5D analogue of the cross-ponderomotive effect noted in the homogeneous 1.5D MHD study of Verwichte et al. (1999), a non-zero longitudinal plasma perturbation caused by crossing pulses (which corresponds to our initial condition).

Figure 4.4 shows the transverse velocity component v_x, which is the velocity component associated with the fast magnetoacoustic wave. As reported in Nakariakov et al. (1997), we find nonlinear disturbances in v_x are generated in the phase mixing region and propagate outwards from regions of high-to-low Alfvén speed, independently of the Alfvén wave, clear evidence that the Alfvén wave nonlinearly generates independently propagating fast magnetoacoustic waves as it undergoes phase mixing. Since the Alfvén wave is small, the fast wave saturates at a low amplitude ($v_x = -3.338 \times 10^{-7}$) relative to its progenitor, in agreement with Botha et al. (2000). Figure 4.4 also reveals a feature unreported by Nakariakov et al. (1997), namely that as the Alfvén

wave undergoes phase mixing, a transverse cospatial disturbance arises in the region, i.e. we can see the *transverse daughter disturbance*. This is most clearly visible when comparing the later panels of Figure 4.4 to the corresponding times on Figure 4.2 (to determine the region cospatial to the Alfvén wave).

Preliminary results of analytical approach to this problem is presented in Appendix D, where we attempt to determine the form of $v_{\parallel}$ and $v_{\perp}$ analytically from equations (4.12) and (4.13).

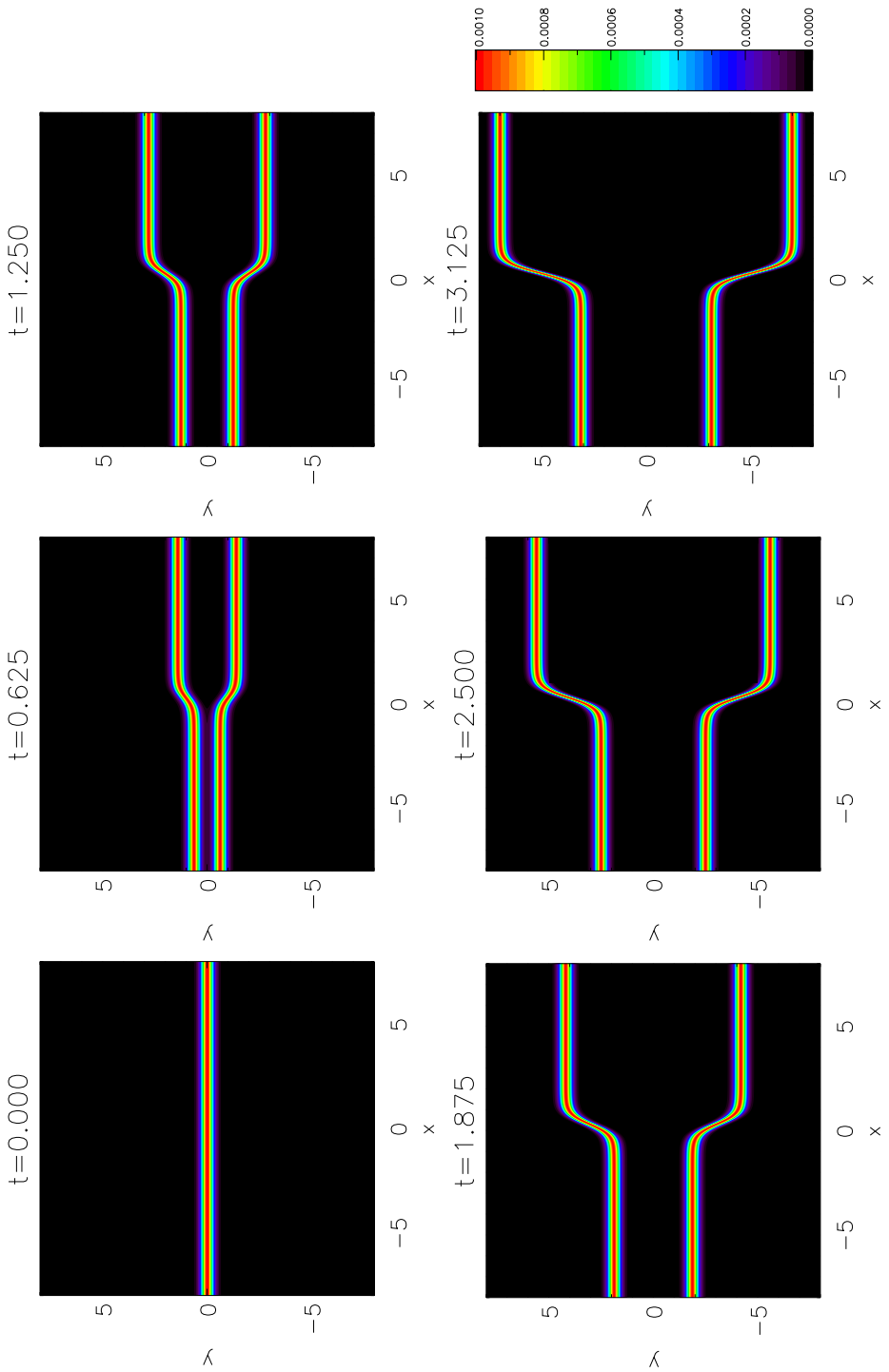

Figure 4.2: Contour plots of v_z, showing the propagation of the Alfvén wave, which undergoes phase mixing due to the transverse inhomogeneity in Alfvén-speed profile.

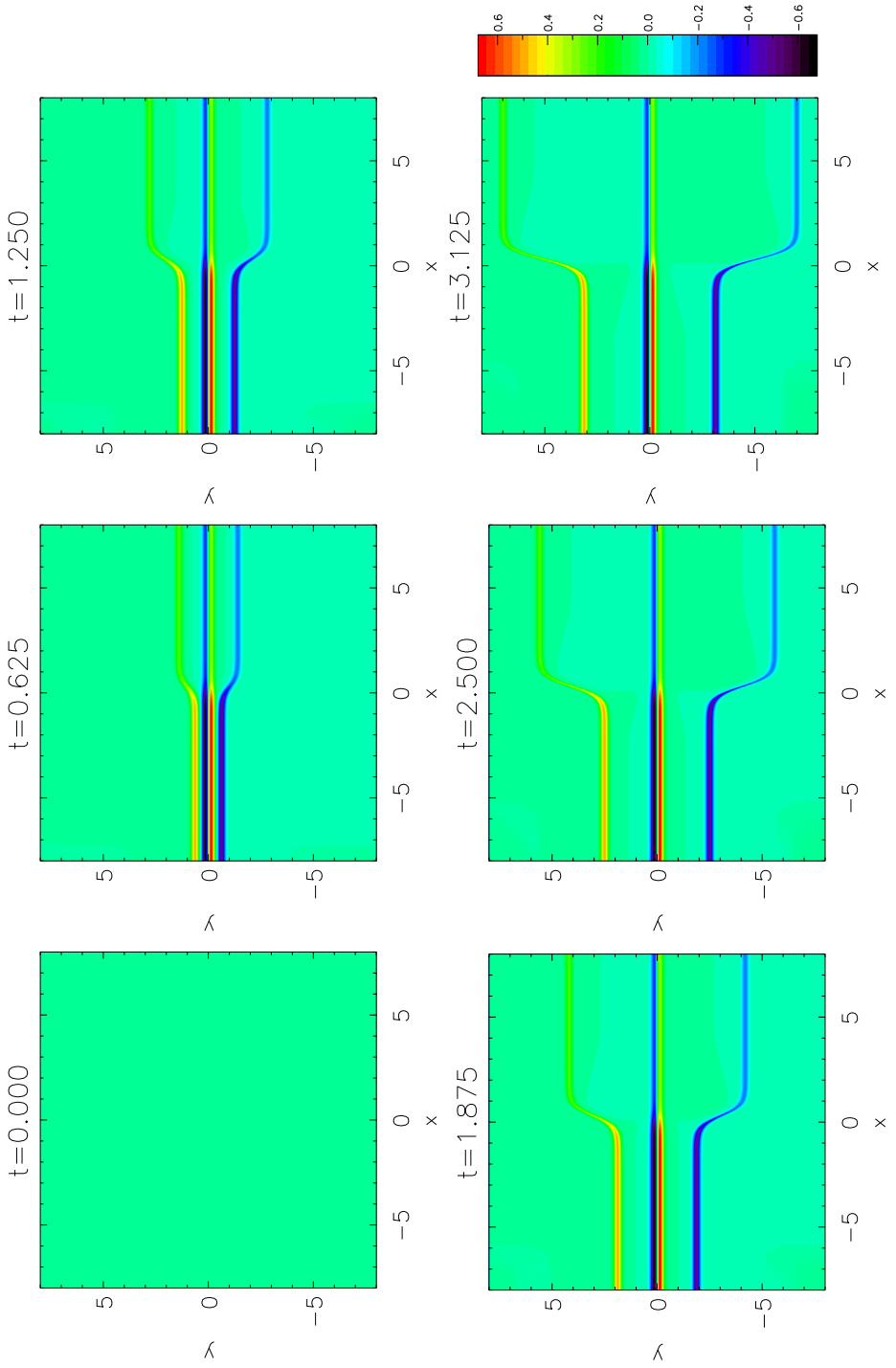

Figure 4.3: The longitudinal velocity component v_y for the same times as Figure 4.2. We find a nonlinear static perturbation localised at the initial position of the Alfvén pulse and nonlinear cospatial disturbances that are transported with the Alfvén waves. The colour bar is scaled by a factor of $\times 10^6$, i.e. by $\times A^2$.

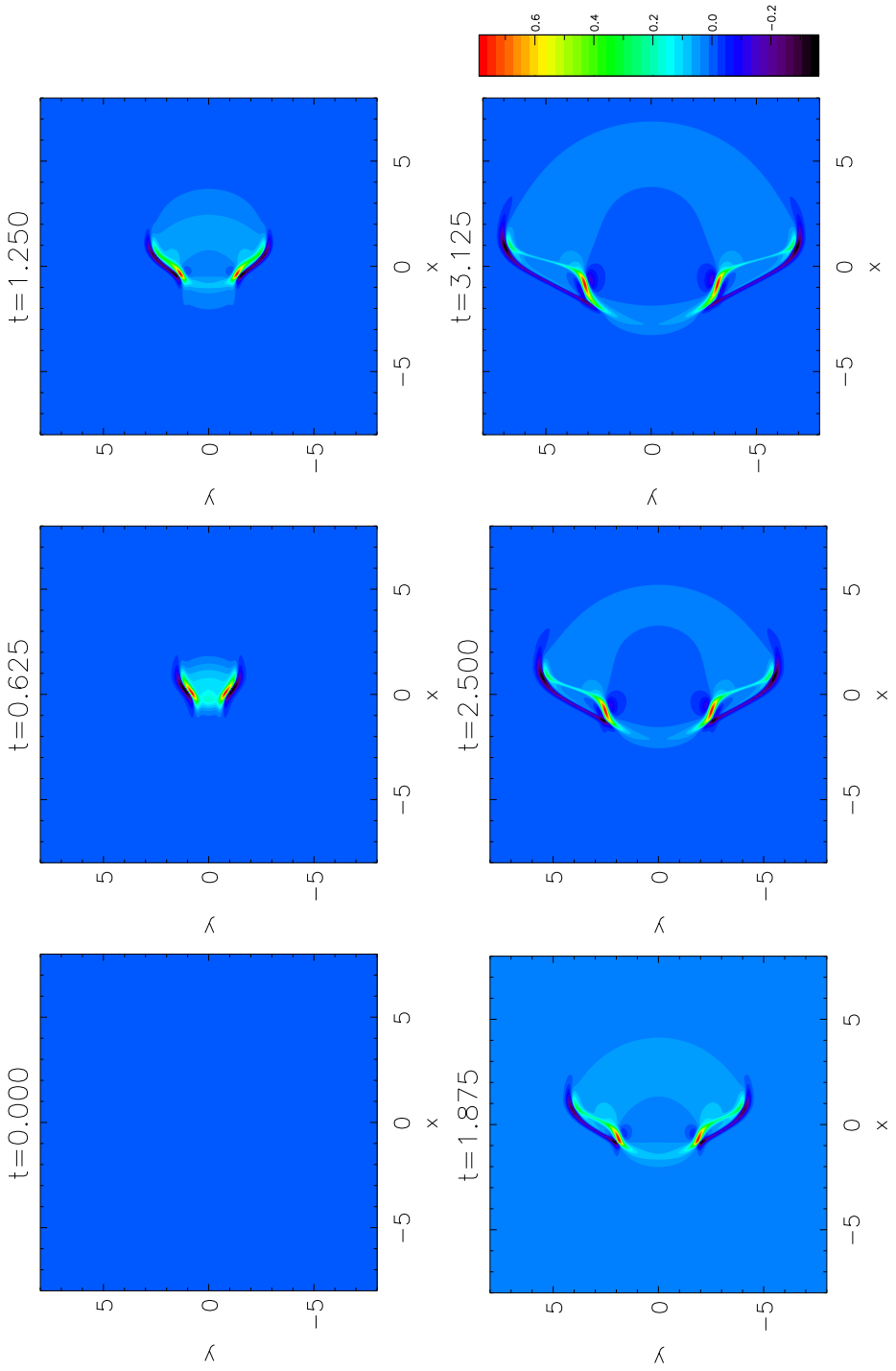

Figure 4.4: The transverse velocity component v_x for the same times as Figure 4.2. Propagating fast waves emanate from the phase mixing region. As the Alfvén wave undergoes phase mixing, independently propagating fast waves are generated and a cospatial transverse daughter disturbance develops. The colour bar is scaled by a factor of $\times 10^6$, i.e. by $\times A^2$.

4.5 Conclusion

In this chapter, we present two main results:

- The analysis and conclusions of Nakariakov et al. (1997) extend to the general 2.5D MHD case, such that the nonlinear magnetic pressure exerted by an Alfvén wave propagating through a region of variable Alfvén speed facilitates mode conversion from the Alfvén to magnetoacoustic modes in many MHD scenarios (to the fast mode via phase mixing and to the longitudinal mode via dispersion along fieldlines).

- The ponderomotive effect not only generates independently propagating magnetoacoustic waves but also longitudinal and transverse daughter disturbances, which remain cospatial and dependent upon the progenitor wave.

After deriving wave equations for a general MHD system (equations 4.4-4.6) with a translational invariance (i.e. non-rotational, $\partial/\partial z = 0$), the source term analysis of Section 4.3 demonstrates that the nonlinear magnetic-pressure gradients generated by a propagating Alfvén wave can facilitate mode conversion from the Alfvén to magnetoacoustic modes, providing that, the pulse assumes a geometry which yields a non-zero net force over the wave's period. A similar source term analysis for a propagating fast wave is presented in Appendix C, which confirms the additional result that the process is one-way (i.e. the nonlinear Lorentz force does not permit conversion from the fast magnetoacoustic to the Alfvén mode). This, of course, is entirely intuitive as pressure gradients (magnetic or otherwise) cannot act in the Alfvén wave direction, because it is impossible to have gradients in an invariant direction by definition.

In Section 4.3.1 we consider the terms forced by a harmonic Alfvén wave, and find that perturbations to $v_\perp$ and $v_\parallel$ are generated at double the frequency and at the square of the driving/initial amplitude, in agreement with previous results reported in the literature. Such a result is inevitable for ponderomotive effects, as the nonlinear magnetic-pressure gradient acts upon the square of b_z (and hence the square of v_z). The forced wave equations (Equations 4.14 and 4.15) are found to contain two distinct sets of terms, each with a longitudinal and transverse manifestation, that are:

- Geometric effects
  - (a) $\nabla_\parallel \left(\hat{\mathbf{B}}_0 \cdot \mathbf{r}\right)$ - Longitudinal daughter disturbances
  - (b) $\nabla_\perp \left(\hat{\mathbf{B}}_0 \cdot \mathbf{r}\right)$ - Transverse daughter disturbances
- $\nabla\left(c_\mathrm{A}\right)$ effects

(c) $\nabla_{\parallel}(c_{\mathrm{A}})$ - Perturbations due to longitudinal dispersion (viz. longitudinal stratification)

(d) $\nabla_{\perp}(c_{\mathrm{A}})$ - Perturbations due to phase mixing (viz. transverse stratification)

Reducing to homogeneous 1.5D MHD, we find that one term forcing longitudinal perturbations remains, corresponding to $\nabla_{\parallel}\left(\hat{\mathbf{B}}_0 \cdot \mathbf{r}\right)$ above, which is dependent on longitudinal gradients in a function of pulse geometry and background magnetic field. This term is responsible for the cospatial *ponderomotive wing* reported in Verwichte et al. (1999). Upon permitting a transverse direction (i.e. homogeneous 2.5D MHD), we find that a transverse analogue is permitted. Hence, to distinguish the two we refer to the longitudinal/transverse manifestations as the *longitudinal daughter disturbance* and *transverse daughter disturbance* respectively. When we further consider the inhomogeneous scenario and permit gradients in the Alfvén speed, a second class of forcing term is permitted, again with transverse and longitudinal manifestations, which accelerates the medium as the Alfvén wave passes through regions of inhomogeneity. The transverse manifestiation occurs where the Alfvén wave undergoes phase mixing (regions with transverse gradients in Alfvén speed) and the longitudinal manifestation occurs where longitudinal dispersion occurs (in regions with longitudinal gradients in Alfvén speed), where we stress that the Alfvén-speed profiles vary with $\mathbf{B}_0$ and ρ_0 (i.e., phase mixing can occur in regions of uniform density, if the magnetic field has transverse stratification, an important example for this thesis being magnetic null point configurations, see e.g., Fruit & Craig 2006).

To illustrate the phenomena implied by our analysis and interpretation of Sections 4.3–4.3.3, we considered numerical simulations of plasma with a unidirectional field structured by transverse density profile (the same scenario considered in Nakariakov et al. 1997). In addition to the results detailed in Nakariakov et al. (1997); namely, the generation of independently propagating fast waves, we find clear evidence for the existence of the longitudinal daughter disturbance, which remains cospatial to its progenitor throughout its transit. We note that the disturbance differs by a factor of $\sqrt{5}$ in the higher Alfvén speed region (relative to its amplitude in the lower Alfvén speed region). An explanation is found by reconsidering Equation (4.15) in the limit $x = -\infty$ and $x = +\infty$ for our scenario. Specifically, for the scenario there is no longitudinal dispersion ($\nabla_{\parallel} c_{\mathrm{A}} = 0$) and both the frequency and the longitudinal geometric gradient are identical at both extremes (thus we arbitrarily take $\omega = 1$ and $\nabla_{\parallel}\left(\hat{\mathbf{B}}_0 \cdot \mathbf{r}\right) = 1$ without loss of generality), and the scaling function is taken as $S^2 = \mu\rho_0$. The equation implies

$$\max\left(v_{\parallel}\right) \approx \frac{1}{2c_{\mathrm{A}}} v_z^2 \quad .$$

Given that in the simulation $c_{\mathrm{A}}(x = -\infty) = 1$, $c_{\mathrm{A}}(x = +\infty) = 5$ with the Alfvén wave amplitude $A = 0.001$ we find that $v_{\parallel}(x = -\infty) = 5.000 \times 10^{-7}$ and $v_{\parallel}(x = +\infty) = 2.236 \times 10^{-8}$ which is in excellent agreement with the reported amplitudes of the longitudinal daughter dis-

turbances in the homogeneous regions. Hence, the longitudinal daughter disturbances of Alfvén waves are generated with amplitude of $\mathcal{O}\left(A^2/2c_\mathrm{A}\right)$.

The simulations also reveal the transverse manifestation of the cospatial disturbance, the transverse daughter. This is observed to develop over time (initially, transverse gradients in pulse geometry zero) as the Alfvén wave undergoes phase mixing, remaining cospatial to the phase mixed part of the Alfvén wave. To our knowledge, this is the first time this phenomenon has been reported.

An additional effect noted in the simulation is that of the static perturbation at $y = 0$ that is manifest in the longitudinal, $\hat{\mathbf{y}}$-components of fluid variables (e.g. in v_y, Figure 4.3). We believe that this is the same cross-ponderomotive effect as reported in Verwichte et al. (1999), despite the fact that our scenario is inhomogeneous 2.5D as opposed to the homogeneous 1.5D analysis they perform. This is because (a) the cross-ponderomotive effect will not have any transverse action as Alfvén waves cannot separate in the transverse direction (and there is nothing to suggest such a phenomena in the simulation data), and (b) there is no inhomogeneity along the fieldlines, and hence dispersion terms ($\nabla_\parallel c_\mathrm{A}$) will not, in the specific case, impact upon the separation dynamics. As our simulation is inhomogeneous (with transverse stratification), it highlights that perturbations due to the cross-ponderomotive effect are (like the other ponderomotive effects observed) inversely proportional to the speed c_A. It is however likely that in general, dispersion during pulse crossings will yield a more complicated effect. For cases where propagating Alfvén wave pulses are likely to meet (e.g. recent simulations by Matsumoto & Suzuki 2012 report wave reflection due to the transition region and, subsequently, turbulent effects in the lower solar atmosphere) and the scenario is sufficiently nonlinear it would be necessary to investigate the ponderomotive effects on interaction between Alfvén waves further. We suggest that it would be necessary to integrate Equation (4.15) over a separation period of a general wave form on v_z (from which the form of b_z follows) that corresponds to the general solution satisfying the variable-speed 1.5D wave equation $u_{tt} = c(y)u_{yy}$ for travelling pulses from a Gaussian-like initial condition (i.e. a variable speed D'Alembert solution). Such an analytic solution can be found by transforming the variable speed wave equation to a constant coefficient Klein-Gordon equation, however the profile of the wave speed has to conform to various conditions (of which, our scenario in Section 4.4 does not satisfy). See Grimshaw et al. (2010) for a comprehensive overview of the homogenisation process.

During the separation of the pulse, we also note the generation of a stationary density enhancement, initially of $\mathcal{O}\left(A^2/2c_\mathrm{A}\right)$, that subsequently grows linearly in time. Again, this is in agreement with that reported by Verwichte et al. (1999). Linear density instabilities were shown to be a general feature of $\beta = 0$ MHD by Falle & Hartquist (2002). There, the authors analyse the eigenmodes of cold MHD and show that there is a *Jordan-mode instability*, associated with the absent/zero-speed slow waves, which causes such density enhancements. This instability is shown to arise when the parallel (i.e. slow) velocity component is not constant. The cross-ponderomotive

effect of a separating Alfvén wave (or two crossing Alfvén waves), as observed in our simulations, excites such a mode by acelerating the parallel velocity component by applying a (nonlinear) magnetic-pressure gradient.

Throughout the chapter we have considered the cold plasma regime. If the $\beta \neq 0$ MHD wave equations (Equations 4.4–4.6 if gas pressure gradients are permitted) are considered under the conditions for an initially pure Alfvén wave as per Section 4.3, we find that gas pressure gradients do not contribute, i.e. the $\beta \neq 0$ equivalents of the source terms derived in Equations (4.7)–(4.15) are unchanged, i.e. the way in which a passing Alfvén wave nonlinearly perturbs the medium is identical to that detailed in this chapter. Hence, where non-zero longitudinal perturbations of the medium occur (which are static in $\beta = 0$, e.g. the cross-ponderomotive perturbation in Figure 4.3), gas pressure gradients will subsequently arise to transport the disturbance longitudinally, i.e. slow magnetoacoustic waves will be generated. Thus, in $\beta \neq 0$, ponderomotive mode conversion is permitted between the Alfvén wave and *both* magnetoacoustic modes. In addition to the implications for mode conversion in an extension to a $\beta \neq 0$ regime, we note that the cross-ponderomotive effect, and subsequent excitation of a Jordan-mode instability, will still generate large density enhancements in low-β plasmas as per Falle & Hartquist (2002). Thus, crossing Alfvén waves will directly contribute to the creation of inhomogeneity in low-β plasmas, due to their cross-ponderomotive effects.

We conclude this chapter by highlighting that all of the analyses can be repeated with different types of 2.5D coordinate system. For instance, we could consider azimuthal invariance ($\partial/\partial\theta = 0$), or the system of orthogonal polarisation vectors presented in Chapter 3 ($\partial/\partial A = 0$) and yield the same results [2]. Given that invariance is intimately associated with true Alfvén waves as per Alfvén 1942 (see, e.g., Parker 1991 and Section 3.2.2), we believe our results and conclusions extend to any scenario in which an Alfvén wave (*a wave driven by magnetic tension only*) can exist. We have shown that a nonlinear Lorentz force of a propagating Alfvén wave can generate independently propagating fast and slow magnetoacoustic waves, dependent on the interplay between Alfén speed profile and pulse geometry (viz., the form of the daughter disturbances), which varies on a case by case basis. As the transient properties of the magnetoacoustic modes are fundamentally different to the Alfvén wave, such conversion facilitates the indirect transport and dissipation of (initially) Alfvén wave energy to plasma regions that are inaccessible in the linear MHD regime. In modelling wave behaviour in sufficiently nonlinear (solar) plasmas, the ponderomotive effects of propagating waves must be evaluated.

[2] Although, it would require determining what the vector calculus operators are in such a system and creating a fully-fledged 'coordinate system'

Chapter 5

Nonlinear Alfvén wave behaviour about 2D magnetic null points

The following chapter details research first reported in:

'Nonlinear Alfvén Wave Dynamics at a 2D Magnetic Null point: Ponderomotive Force'

Thurgood & McLaughlin, *Astronomy & Astrophysics*, **555**, A86, 2013b

5.1 Introduction

In the previous chapter, we have seen that Alfvén waves can nonlinearly excite fast magnetoacoustic waves as they propagate through inhomogeneous plasmas, and that the exact nature of such excitation varies on a case-by-case basis. Given that all classes of magnetic null point have inhomogeneous Alfvén-speed profiles, it is possible that the ponderomotive mode excitation could play a role in wave-null dynamics. The role of the ponderomotive force has not been considered in either the 2D or 3D cases, and as such we first investigate its role in the simpler 2D scenario.

Thus, in this chapter we address the question: *how does the weakly nonlinear Alfvén wave behave in the vicinity of a 2D null point?* To do so, we numerically solve the cold-plasma MHD equations to simulate the nonlinear wave dynamics at a null point where a pure linear Alfvén wave is driven at the boundary, i.e. initially we ensure there is no fast wave present. The chapter is structured as follows. In Section 5.2 we detail mathematical model and numerical set up. Then, we present the results of our simulations in Section 5.3. We discuss the nonlinear effects observed in our experiments in Section 5.4, and finally conclude in Section 5.5.

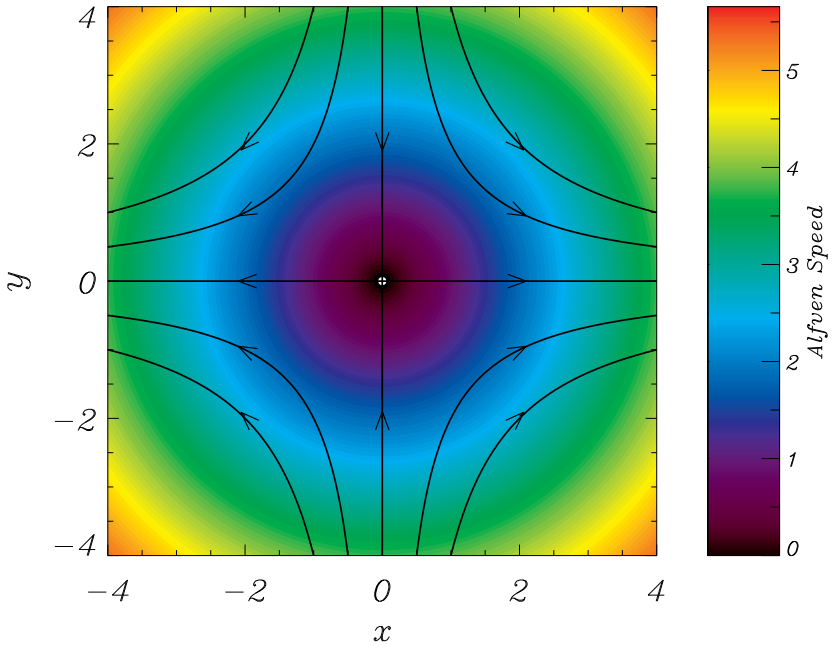

Figure 5.1: Indicative lines of the equilibrium magnetic field structure $\mathbf{B}_0$ (black lines) and contours of the Alfvén-speed profile $c_A = \sqrt{x^2 + y^2}$ (ρ_0 is constant).

5.2 Mathematical Model & Simulation Set-Up

As in the previous chapter's numerical simulation, we solve the full set of the nonlinear, nondimensionalised 2.5D ($\partial/\partial z = 0$) MHD equations using the LARE2D code. We consider a $\beta = 0$ plasma, with constant equilibrium density ρ_0, and an equilibrium magnetic field of the form

$$\mathbf{B}_0 = [x, -y, 0] \ . \tag{5.1}$$

Equation (5.1) corresponds to a 2D, potential null point with the null point itself at the origin, and the separatrices located at $x = 0$ and $y = 0$ (see Figure 5.1 and McLaughlin et al. 2011b). We drive a planar, sinusoidal pulse in v_z and b_z at the upper y-boundary to introduce a linear Alfvén wave as per the simulations in Chapter 4. To do so we drive

$$v_z(x, 4) = A \sin(2\pi t), \quad v_x = v_y = v_\perp = v_\parallel = 0, \quad \mathbf{b} = -\sqrt{\mu\rho_0}\,\mathbf{v} \tag{5.2}$$

for $0 \leq t \leq 0.5$, and we consider a driving amplitude $A = 0.001$. This amplitude is small with respect to the characteristic velocity of the nondimensionalisation used and thus we consider the weakly nonlinear scenario. Simple zero-gradient conditions are employed on the other boundaries, and the simulations are performed over the domain $x \in [-4, 4]$, $y \in [-4, 4]$ with 2400×2400 grid points.

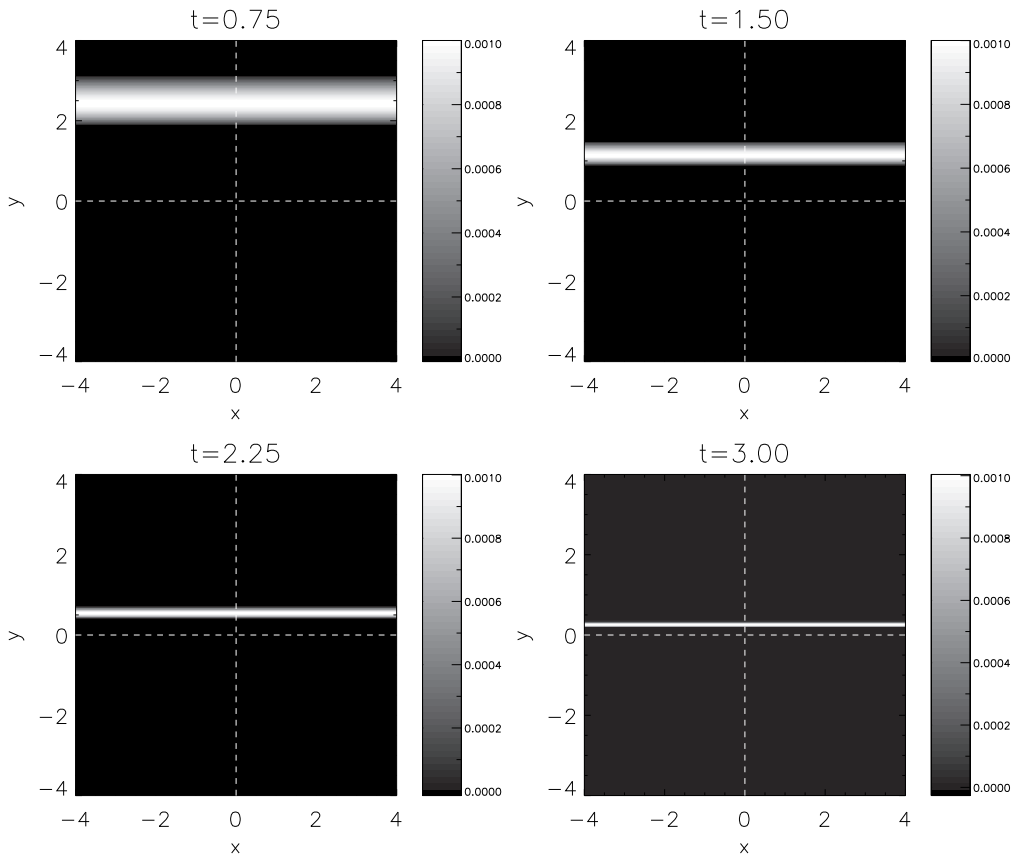

Figure 5.2: The evolution of v_z (the Alfvén wave) over time. The Alfvén wave propagates along fieldlines at the Alfvén speed, hence we see a narrowing planar pulse propagating towards the $y = 0$ separatrix (the separatrices are marked by dashed white lines).

5.3 Results

In Figure 5.2, we plot the propagating Alfvén wave in the velocity component v_z. We have also computed the b_z perturbation which shows a qualitatively identical result. It is known that the linear Alfvén wave propagates along the magnetic fieldlines at the Alfvén speed c_A (here $c_A = \sqrt{x^2 + y^2}$), causing spreading of pulses along fieldlines and is unable to cross the separatrices (McLaughlin & Hood 2004). Given that our driving imposes a planar profile, this spreading effect is not obvious in our simulation, instead we see the planar pulse that propagates towards the $y = 0$ separatrix at a speed which is equivalent to the Alfvén speed evaluated at $x = 0$. It cannot cross the separatrix, as $c_A|_{x=0} \to 0$ as $y \to 0$, and it accumulates nearby with ever increasing gradients, hence resistive dissipation will eventually become an important consideration (McLaughlin & Hood 2004). Thus, v_z *behaves as in the linear regime.*

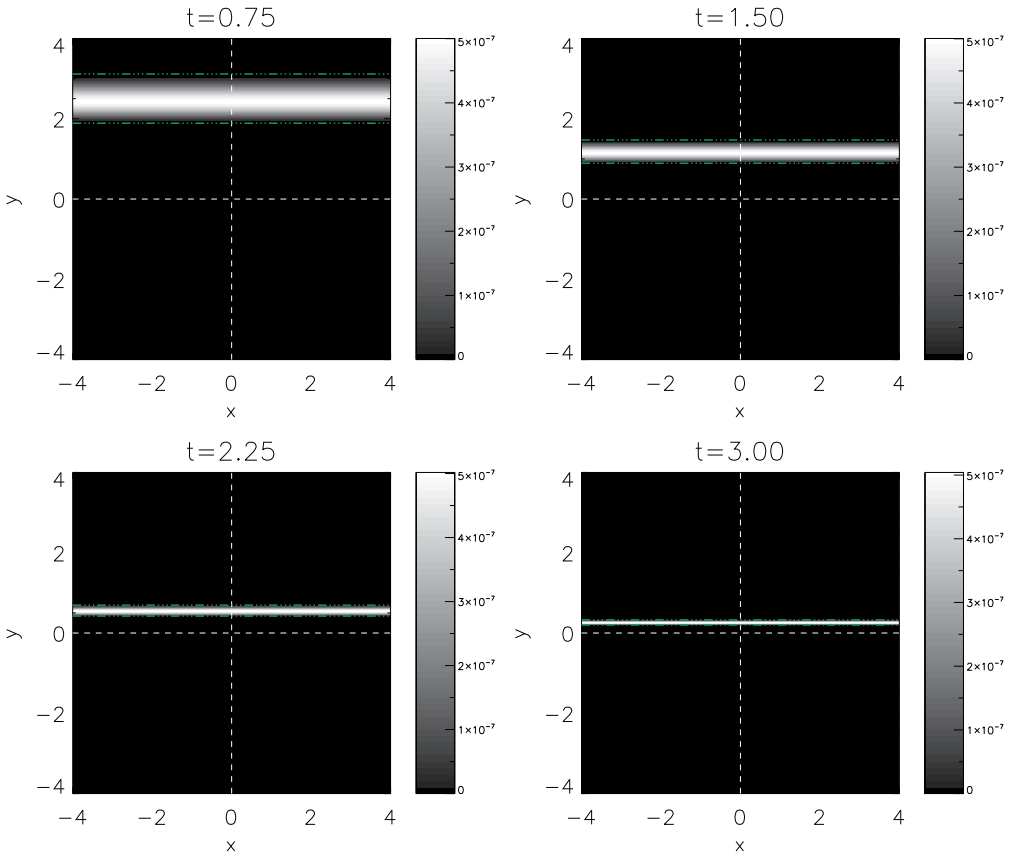

Figure 5.3: The longitudinal component $v_{\parallel}$ over time. We find that the ponderomotive force of the propagating Alfvén wave (position marked by green lines) sustains a cospatial disturbance in velocity along the background magnetic field. This *longitudinal daughter disturbance* is a ponderomotive effect which in this case does not facilitate any conversion to the slow mode.

We now consider the other orthogonal velocity components ($v_{\perp}$ and $v_{\parallel}$) which remain zero throughout linear simulations, to investigate possible nonlinear effects. We first consider the longitudinal velocity component $v_{\parallel}$, shown in Figure 5.3. Here, we find a nonlinear disturbance of $\mathcal{O}(0.5A^2 = 5 \times 10^{-7})$, which is cospatial to the Alfvén wave pulse in time (the front and rear position of the Alfvén pulse is marked by green lines). The pulse appears similar in profile to that of the Alfvén wave, however is more compressed and steeper, i.e. the profile is approximately that of a squared sine wave (see Figure 5.4), whereas v_z is sinusoidal. This disturbance is not an independently propagating wave (in $\beta = 0$ such motion is prohibited), but a direct consequence of the longitudinal component of the ponderomotive force, which is induced, sustained and carried by the propagating Alfvén wave. Thus, this is the specific manifestation of the *longitudinal daughter disturbance* (as discussed in Chapter 4 and Thurgood & McLaughlin 2013a) of the planar, nonlinear Alfvén wave at the 2D magnetic null point.

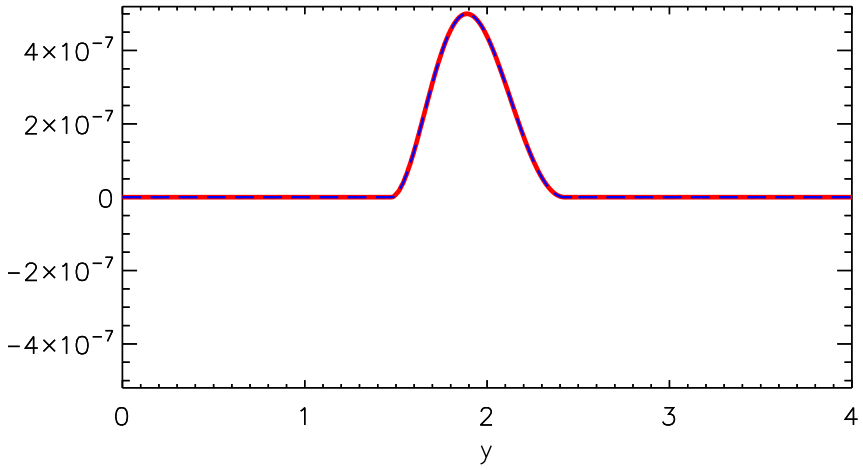

Figure 5.4: Cuts taken through $x = 0$ at $t = 1$ comparing $v_{\parallel}$ (blue) and $0.5v_z^2$ (red), showing that $v_{\parallel} = 0.5v_z^2$, which holds for all times $t > 0$ and different cuts through x. Thus, the daughter disturbance is generated with the form of a (half-period/cycle) square sine wave.

Now we consider the fast-mode velocity component $v_{\perp}$, shown in Figure 5.5, which consists of two features: a wave that propagates independently of the Alfvén wave and a cospatial disturbance, both nonlinear of order $\mathcal{O}(0.5A^2 = 5 \times 10^{-7})$. The independently propagating wave is generated during the driving stage of the simulation, and propagates with the transient characteristics of a linear fast wave at a single null point, namely that it undergoes refraction due to the Alfvén-speed profile, crosses the separatrices and accumulates at the null point. Hence, driving a linear Alfvén wave according to equation (5.2) *appears* to have nonlinearly excited a fast wave.

We also find a disturbance in $v_{\perp}$ which does not appear to correspond to a fast wave (qualitatively, in terms of transient behaviour), and is cospatial to the Alfvén wave pulse (again, the position of which is shown by the green envelope in Figure 5.5). This is the *transverse daughter disturbance*, detailed for general MHD in the previous chapter. This disturbance is not an independently propagating wave. Within the cospatial region, the disturbance becomes increasingly focused towards the separatrix and ultimately to the vicinity of the null point. The profile of $v_{\perp}$ further away from the separatrix, where the intensification occurs, is shown in Figure 5.6. We further discuss the nature of the observed behaviour of $v_{\perp}$ in the next section.

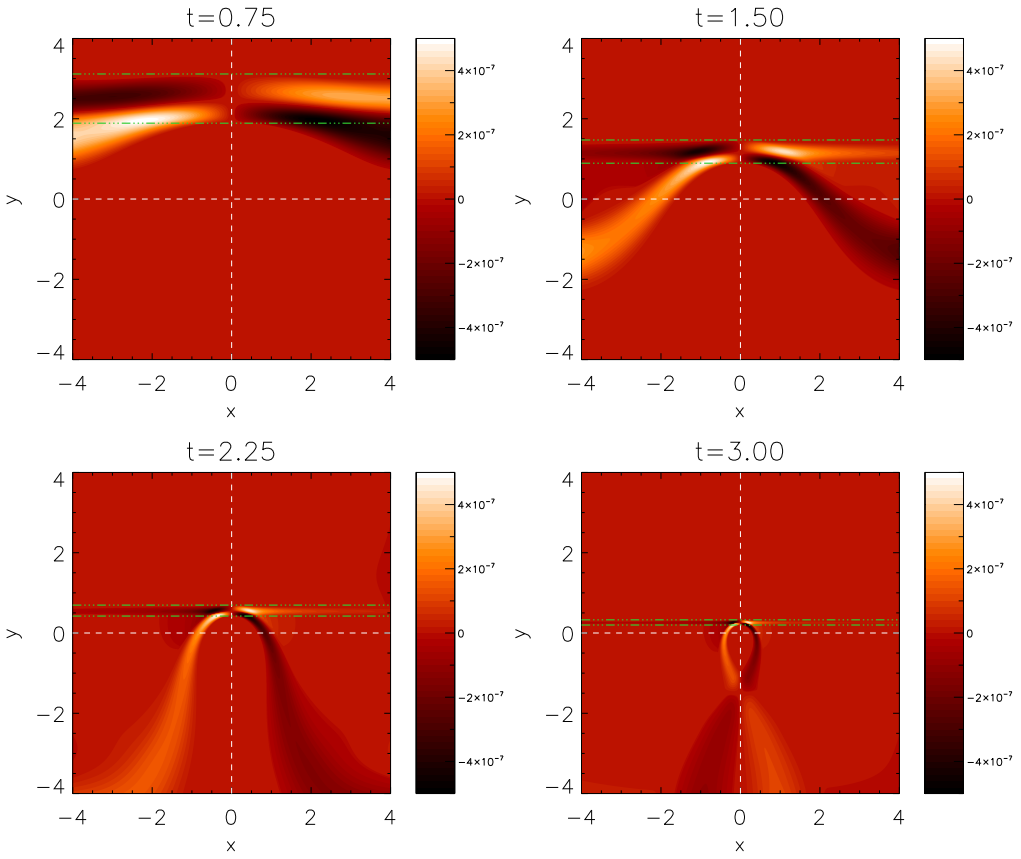

Figure 5.5: The evolution of $v_\perp$ over time. We find two pronounced nonlinear effects: a transverse daughter disturbance which is cospatial to the Alfvén wave (indicated by dashed green lines) and an independently propagating fast wave.

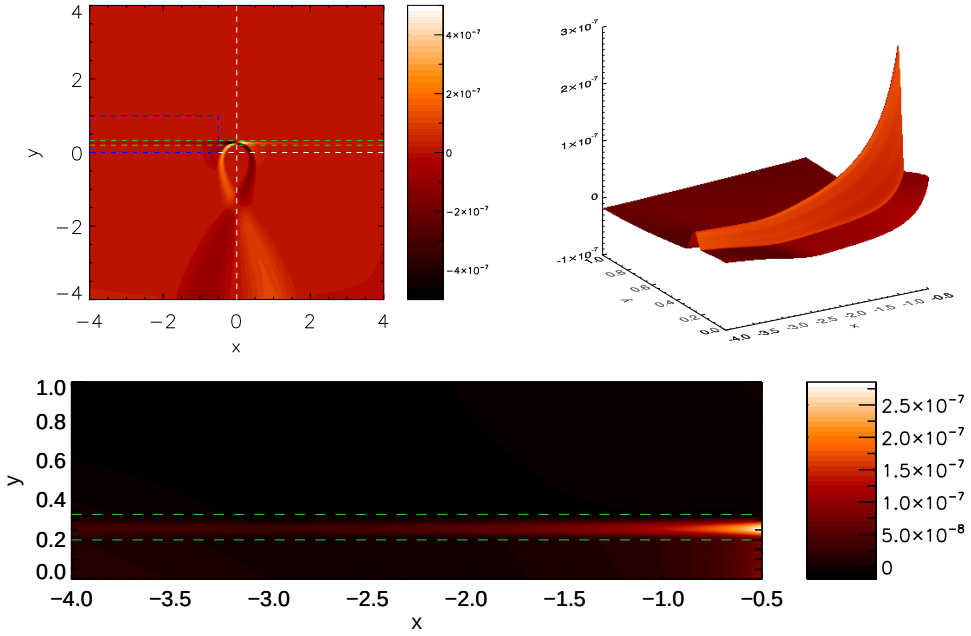

Figure 5.6: The transverse daughter disturbance away from the separatrix at $t = 3$. *Top Left*: Context image showing $v_\perp$ over the whole domain, with the sub-region indicated by the blue-dashed box. *Top Right:* Shaded surface of $v_\perp$ in the sub-region. *Bottom:* Contour of $v_\perp$ in the sub-region. We see that the transverse daughter disturbance exists in all regions co-spatial to the Alfvén wave, and that it is characterised by a planar profile that intensifies towards the separatrix at $x = 0$.

5.4 Exploring the Nonlinear Effects

Due to the choice of small driving amplitude A, v_z behaves as in the linear regime (Figure 5.2). Whilst the choice of a low driving amplitude makes the nonlinear effects small, it is nonetheless sufficient to demonstrate in what ways the (shock-free) nonlinear system differs from the linear, in particular its interaction with the transverse and longitudinal fluid variables and between differing modes of oscillation. Here we see two types of nonlinear effects which are absent in the linear study of McLaughlin & Hood (2004), both of which are generated or sustained at $\mathcal{O}(A^2/2)$: daughter disturbances and independently propagating fast waves.

5.4.1 Daughter disturbances

As discussed previously, where the action of the force of the leading pulse edge is consistently nullified by the trailing edge, disturbances arise in the transverse and longitudinal fluid-variables that do not excite independently propagating wave motions but remain confined to a region cospatial to the Alfvén wave (the *ponderomotive envelope*). In the simulations, we observe disturbances in $v_\perp$ and $v_\parallel$ which develop immediately and remain cospatial to the wave observed in v_z throughout the simulations, which we have identified as such disturbances in the previous section.

In Section 5.2 we found that the spatial distribution of these two disturbances differs. The longitudinal daughter ($v_\parallel$) varies only in $\hat{\mathbf{y}}$ with a profile that goes as half of the square of v_z (see Figure 5.4). However, the transverse daughter ($v_\perp$) not only $\hat{\mathbf{y}}$ but also in $\hat{\mathbf{x}}$, with an intensification effect such that it appears to become increasingly focused towards the $x = 0$ separatrix as time evolves. In this section we further explore these two effects by considering the ponderomotive force of the Alfvén wave as it propagates.

The ponderomotive force equations (4.12) and (4.13) derived in Section 4 apply directly to this scenario, and thus at any given instant the ponderomotive force of an Alfvén wave manifest in $\hat{\mathbf{z}}$ across and along the field $\mathbf{B}_0 = [x, -y, 0]$ is

$$\frac{\partial v_\perp}{\partial t} = -\frac{B_0}{\mu\rho_0}\nabla_\perp\left(\frac{b_z^2}{2}\right) \longrightarrow F_\perp = -\frac{1}{\mu\rho_0}\left(y\frac{\partial}{\partial x} + x\frac{\partial}{\partial y}\right)\frac{b_z^2}{2} \tag{5.3}$$

$$\frac{\partial v_\parallel}{\partial t} = -\frac{B_0}{\mu\rho_0}\nabla_\parallel\left(\frac{b_z^2}{2}\right) \longrightarrow F_\parallel = -\frac{1}{\mu\rho_0}\left(x\frac{\partial}{\partial x} - y\frac{\partial}{\partial y}\right)\frac{b_z^2}{2} \quad . \tag{5.4}$$

Note that, because the Alfvén wave remains planar in $\hat{\mathbf{x}}$ throughout $\partial b_z^2/\partial x = 0$ and thus these

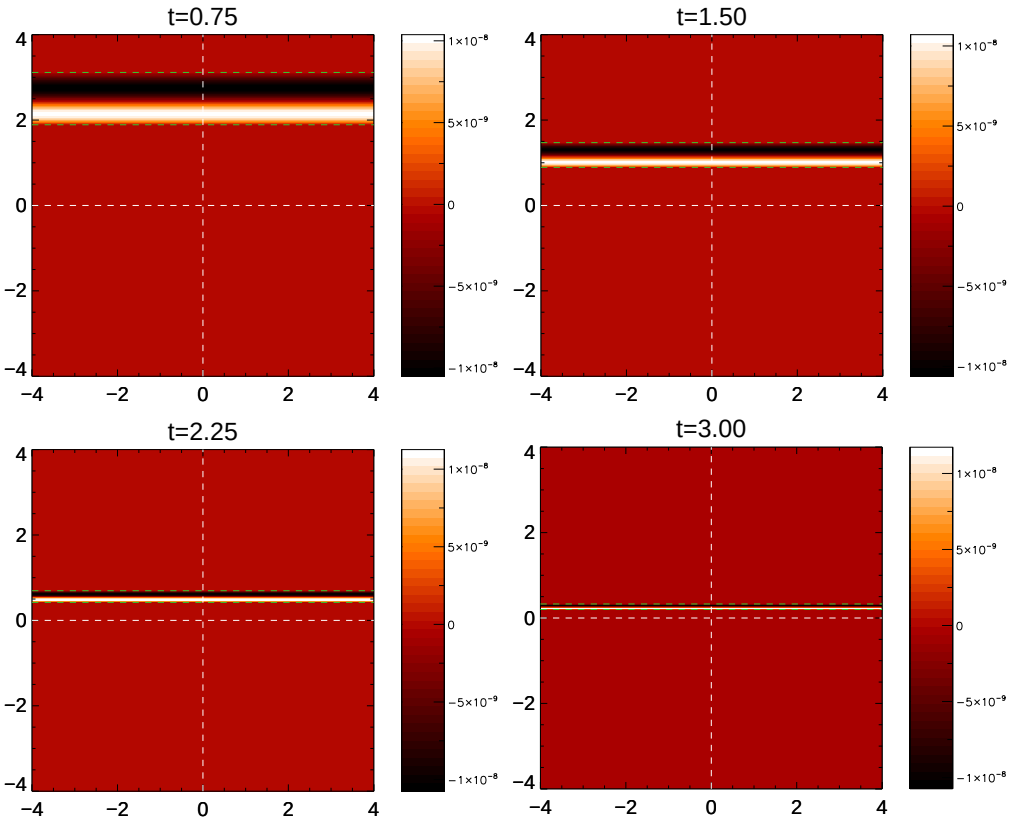

Figure 5.7: The evolution of $F_{\|}$ over time. The force has a profile such that cancels itself over the Alfvén waves path, and shows no sign of intensification as gradients increase.

equations further simplify (NB: this was also checked through direct calculation). The evolution of perpendicular and parallel ponderomotive forces during the simulation are shown in Figures 5.7 and 5.8.

Our interpretation of the signal in $v_{\|}$ as due to the action of the longitudinal ponderomotive force of the leading pulse edge which is subsequently nullified by the trailing edge is verified in Figure 5.7, where we find the required such a profile at all times. Interestingly, there is no intensification of $F_{\|}$ (and thus $v_{\|}$) as the pulse approaches the $y = 0$ separatrix despite the fact that the gradients in b_z with respect to y are increasing. This is because the product of y in Equation (5.4) balances the gradient which grows as y^{-1} (this growth rate was determined for linear Alfvén waves analytically by McLaughlin & Hood (2004); the lengthy derivation is not repeated here for brevity).

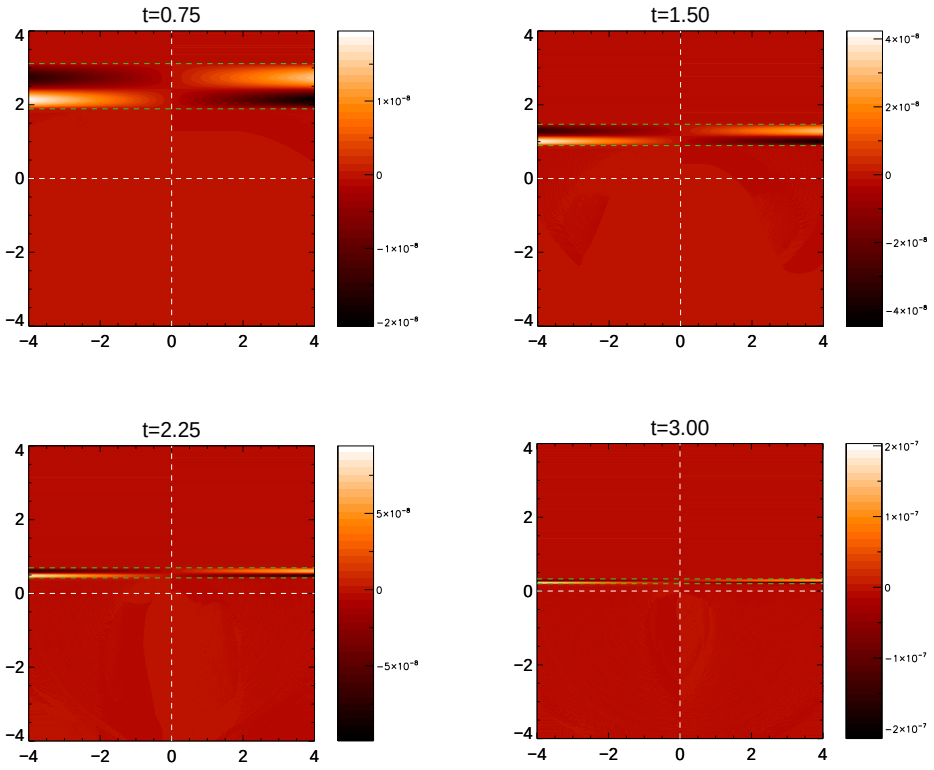

Figure 5.8: The evolution of $F_\perp$ over time. Again, its profile in the y-direction is such that it effects are cancelled over the path.

In Figure 5.8 we consider the transverse ponderomotive force $F_\perp$ and again find a profile which is again consistent with subsequent acelleration and deceleration of $v_\perp$ as the Alfvén wave propagates in y. We find that $F_\perp$ is is greater with increasing $|x|$ (this is necessary, on the $x = 0$ separatrix itself there are no cross-field gradients, which increase with x). This profile proportional to x is maintained throughout however it undergoes appreciable intensification of $F_\perp$ as time evolves due to the Alfvén waves increasing gradients. A possible explination for the observed focusing of $v_\perp$ in the vicinity of the $x = 0$ separatrix which intensifies with time (see Figure 5.5) is that the $F_\perp$ acts as an applied pressure gradient to accelerate fluid within the ponderomotive envelope (cospatial region) towards $x = 0$. Hence, the observed signals in $v_\perp$ and $v_\parallel$ are consistent with our interpretation of them as ponderomotive effects, specifically transverse and longitudinal daughter disturbances.

5.4.2 Independently propagating fast wave

In Section 5.2 we have also seen that a wave in $v_\perp$ is generated during the driving phase ($0 \leq t < 0.5$). This wave subsequently propagates with all of the transient features of a linear fast magnetoacoustic wave (refracting about the Alfvén-speed profile and accumulating at the null point). As the nonlinear magnetic pressure is the only facilitator of coupling between v_z and $v_\perp$ in cold, 2.5D MHD systems, the generation of such a wave is due to the exertion of a transverse ponderomotive force (equation 5.3) such that the net force over the period is non-zero. After the driving phase, no further excitation of fast waves occurs, thus the net ponderomotive force must be zero (and thus is only manifest in the aforementioned daughters). Hence, after this driving period, gradients in the trailing edge nullify the fluid acceleration caused by the gradients in the leading edge.

The value of the net ponderomotive force can only change if the pulse geometry is altered. This requires a change in the Alfvén speed. Here, gradients in the Alfvén speed are non-zero

$$\nabla_\perp c_A = \frac{1}{B_0}\frac{2xy}{\sqrt{x^2+y^2}} \quad , \quad \nabla_\parallel c_A = \frac{1}{B_0}\frac{x^2-y^2}{\sqrt{x^2+y^2}}$$

generally permitting such changes in the pulse geometry (i.e. our system is inhomogeneous). However since we impose a planar profile, the effective speed of the wave is $c_A|_{x=0} = y$, and its derivative in the direction of propagation is constant. Thus, as the Alfvén wave propagates its geometry is not altered such that there should be a change from a non-zero to zero net ponderomotive force.

This raises the question that, since the net force *cannot change*, why do we observe the generation of fast waves only during the driving phase, rather than continuously? There are two possible explanations

(i) Physical Effect: The net force is initially non-zero and remains so, i.e. there is a physical mechanism which suppresses the further generation of independently propagating fast waves.

(ii) Mathematical Artefact: The net force is actually zero, thus no ponderomotive excitation of the fast mode should occur. The excitation of the fast wave is a consequence of linearly driving a nonlinear system.

Physical Effect

If the net-force of the wave is always non-zero, in the absence of continuous fast wave generation a mechanism must act to oppose further wave excitation. Botha et al. (2000) considered the case of a harmonic Alfvén wave propagating in a homogeneous field stratified by a transverse

density profile. They reported that the transverse gradients caused the nonlinear excitation of fast waves. However, these waves eventually saturated and did not continue to develop in time. This saturation was also later reported to occur for pulse-type Alfvén waves in the same equilibrium set-up by Tsiklauri et al. (2001). Botha et al. (2000) proposed that the saturation occurs due to wave interference between the generated fast waves. It is possible that in our system a level of saturation sufficient to oppose further mode conversion is reached so rapidly that only a single independent fast wave is generated.

Mathematical Artefact

Alternatively, if the net ponderomotive force is zero throughout, then the independent fast wave has been introduced as a mathematical consequence of our driving condition. We have used the driving condition (5.2) so we can directly compare our nonlinear experiment to the linear results of McLaughlin & Hood (2004). However, in nonlinear MHD, driving the $\hat{\mathbf{z}}$-components of the fluid variables and holding the transverse and longitudinal components at zero corresponds to an Alfvén wave with no instantaneous ponderomotive force. The driven Alfvén wave subsequently enters an inhomogeneous region which 'instantly' alters the pulse profile and contributes to the nonlinear magnetic-pressure perturbation, unopposed by other factors (which are specified as zero). Thus a non-zero ponderomotive force acts *across* the field, resulting in the fast wave, and *along* the field, resulting in a static longitudinal perturbation, as $\beta = 0$ (this static perturbation is subsequently removed by our boundary post-driving boundary conditions, hence absent from our discussion in Section 5.2).

If this is indeed the case, then physically boundary condition (5.2) is inappropriate as it corresponds to an incoming wave with no ponderomotive daughters, and hence no ponderomotive force. At the bare minimum, longitudinal daughters are present for Alfvén wave pulses in straight-field, homogeneous MHD (see Verwichte et al. 1999). From the perspective of wave-stability the driving conditions used are entirely appropriate in the linear regime, as they correspond to a pure linear Alfvén wave (i.e. a wave driven solely by magnetic tension, as per Alfvén 1942) that does not interact with other modes of oscillation (see Parker 1991). This can be be confirmed by considering the linear governing wave equation in the $v_{\parallel}, v_{\perp}, v_z$ coordinate system, which yields three separate and decoupled equations for invariant, transverse and longitudinal variables, i.e. for the Alfvén, fast and (absent) slow modes of oscillation. As perturbations in $\hat{\mathbf{z}}$ do not elicit responses in other directions in the linear regime, such a wave could be considered *linearly stable.* However, in the full nonlinear system, disturbances to v_z do not exist independently to perturbations in $v_{\perp}$ and $v_{\parallel}$ due to the action of the ponderomotive force. The driving conditions still successfully introduce an Alfvén wave (in the nonlinear regime the motion of an Alfvén wave is still primarily due to linear magnetic tension), yet specify values of transverse and longitudinal fluid variables that are inconsistent with those specified by the equations for a single Alfvén wave (these values should

correspond to those implied by equations 5.3 and 5.4).

In the absence of a physical saturation mechanism such as that described in Section 5.4.2, the independent fast wave is a consequence of linearly driving a nonlinear system; the solution is consistent with the equations, which introduce a small fast wave via what could be called a *boundary-ponderomotive effect*.

5.5 Conclusion

In this chapter we have addressed the question, *how does the weakly nonlinear Alfvén wave behave in the vicinity of a 2D null point?* The null point topology (5.1) and equilibrium variables considered are identical to those considered in the linear study of McLaughlin & Hood (2004), as is the method for introducing the Alfvén wave (i.e. driving the $\hat{\mathbf{z}}$-components of the fluid variables). Thus, we can directly compare the behaviour of the waves in the linear and nonlinear regimes. Our three main results are that

(i) In v_z, the wave propagates along fieldlines at the background Alfvén speed, c_A, accumulating at the separatrices. The wave does not steepen to form a shock (hence, we refer to our choice of A as low amplitude or weakly-nonlinear).

(ii) The Alfvén wave sustains cospatial, nonlinear disturbances that have transverse ($v_\perp$, Figure 5.5) and longitudinal ($v_\parallel$, Figure 5.3) manifestations - phenomena not reported before in null point simulations.

(iii) During the driving phase, a wave develops in $v_\perp$ and subsequently propagates independently of the Alfvén wave. It propagates with the transient properties of a linear fast wave, crossing separatrices and accumulating at the null point.

We find that in the low-amplitude limit of the nonlinear solution the majority of the Alfvén wave cannot cross separatrices as in the linear solution of McLaughlin & Hood (2004). However, we find two key results not seen in the linear case - the wave sustains cospatial daughter disturbances and that an independently propagating fast wave is generated via ponderomotive mode excitation (although it is unclear whether the fast wave excitation is physical or imposed by the driving condition).

The longitudinal daughter, sustained by the Alfvén wave, has no real impact upon the medium. The transverse daughter appears to be focused towards the $x = 0$ separatrix, and thus the null

point as the Alfvén wave carries it towards $y = 0$. Since the amplitude here is small, such an effect has little impact on energy transport and dissipation in the vicinity of the null, however the effect has the potential to be significant for larger amplitude Alfvén waves.

A key feature of linear 2D nulls is that the Alfvén wave and magnetoacoustic modes are decoupled, and that Alfvén wave energy accumulates along the separatrices and not at the null. However, in the nonlinear case we observe the ponderomotive excitation of a fast magnetoacoustic wave which refracts around, and eventually accumulates at, the null point. Thus, unlike in 2D, some of the Alfvén wave's energy is focused at the null point by the fast wave, however the physicality of this effect is currently uncertain (see Section 7.2).

After the initial generation of the fast magnetoacoustic wave, we note that no further magnetoacoustic waves are generated, despite the fact that the pulse is travelling through an inhomogeneous region - undergoing longitudinal dispersion ($\nabla_{\parallel} c_A \neq 0$) and phase mixing ($\nabla_{\perp} c_A \neq 0$). The analysis of Thurgood & McLaughlin (2013a) demonstrated that when a pulse propagates through an inhomogeneous medium, nonlinear mode excitation can occur, but that it is dependent on the specific scenario (e.g., the phase-mixing experiment of Nakariakov et al. 1997). Since no conversion occurs in our experiment after the initial excitation, ∇c_A in the vicinity of our 2D null point must not be sufficiently inhomogeneous to further excite magnetoacoustic waves from the planar Alfvén wave considered.

Chapter 6

Alfvén wave behaviour about 3D magnetic null points

The following chapter details research first reported in:

'3D Alfvén wave behaviour about proper and improper magnetic null points'

Thurgood & McLaughlin, Astronomy & Astrophysics, **558**, A127, 2013c

6.1 Introduction

As it stands, the question of how MHD waves behave in the neighbourhood of 3D potential magnetic null points is only partially answered. In Chapter 3, we determined how the fast wave behaves at proper and improper nulls. In this chapter, we consider the complementary scenario and investigate the dynamics of the Alfvén wave about 3D null points of varying eccentricity. We seek to determine the general properties of the Alfvén wave at such nulls, investigate the sensitivity with respect to eccentricity, and investigate possible mode conversion and excitation in the vicinity.

We proceed follows: in Section 6.2 we outline the methods used to model the scenario; in Section 6.3 we detail the results at the proper (6.3.1) and improper (6.3.2) null points. Finally, in Section 6.4 we present our conclusions.

6.2 Mathematical Model

We model the behaviour of the Alfvén wave at 3D null points similar to the case of the 3D fast wave simulations in Chapter 3, again considering magnetic equilibria corresponding to both proper and improper 3D null points ($\epsilon = 1$ and $\epsilon = 0.5$, see Section 6.3.1 and Section 6.3.2 respectively). In each scenario we introduce an Alfvén wave at the upper z-boundary, by driving the following:

$$\mathbf{v}\cdot\hat{\mathbf{A}}_0 = v_A = \alpha F(t)G(r) \quad , \quad \mathbf{v}\cdot\hat{\mathbf{B}}_0 = v_B = 0 \quad , \quad \mathbf{v}\cdot\hat{\mathbf{C}} = v_C = 0 \tag{6.1}$$

$$F(t) = \sin(2\pi t) \quad , \quad G(r) = \frac{20}{9}\frac{r}{r_0}\left[1-\left(\frac{r}{r_0}\right)^4\right]^2 \quad , \quad r = \sqrt{x^2+y^2}$$

for $0 \leq t \leq 0.5$, $0 \leq r \leq r_0$, with driving amplitude $\alpha = 0.001$ (we consider the weakly-nonlinear case). The factor $20/9$ normalises function $G(r)$ such that the maxima/minima in the range is ± 1. We choose $r_0 = 0.25$. The other boundary conditions are set as zero-gradient conditions. The simulations utilise a uniform numerical grid with domain $x \in [-3, 3]$, $y \in [-3, 3]$, $z \in [-1, 2]$ with $960\times960\times720$ grid points. The results presented focus on the region $x \in [-2, 2]$, $y \in [-2, 2]$, $z \in [-1, 2]$, i.e. a subset of the full numerical domain. The experiment ends just prior to the first instance of waves reaching the side boundaries (to ensure boundary reflection is not an issue).

6.3 Numerical Results

6.3.1 Proper Null, $\epsilon = 1$

Let us first consider the proper, radial null point ($\epsilon = 1$) where an Alfvén wave is introduced along the top boundary ($z = 2$) by driving v_A according to equation (6.1). The resultant propagation of the Alfvén wave is shown in Figure 6.1. Figure 6.1 follows the Alfvén wave in the xz-plane with $y = 0$, which is manifest in the velocity perturbation in the invariant direction $\hat{\mathbf{A}}_0$ (NB: the corresponding field-perturbation $\mathbf{b}\cdot\hat{\mathbf{A}}_0$ is qualitatively the same). Since the pulse remains azimuthally symmetric about the spine ($x = y = 0$) throughout, the figure captures all of the transient features of the wave in the whole domain.

The pulse propagates at the local Alfvén speed $c_A = \sqrt{x^2+y^2+4z^2}$ along the magnetic field-lines on which it is driven. The pulse is confined to the fieldlines throughout and does not propagate across the field (as is characteristic of an Alfvén wave). The pulse therefore initially propagates down towards the null point, propagating primarily in the z-direction (i.e. moving nearly parallel to the spine, e.g., $t = 0.75$, $t = 1.25$). Subsequently, it begins to spread radially outward (from the spine) and ultimately tends towards propagating primarily radially outwards (i.e.,

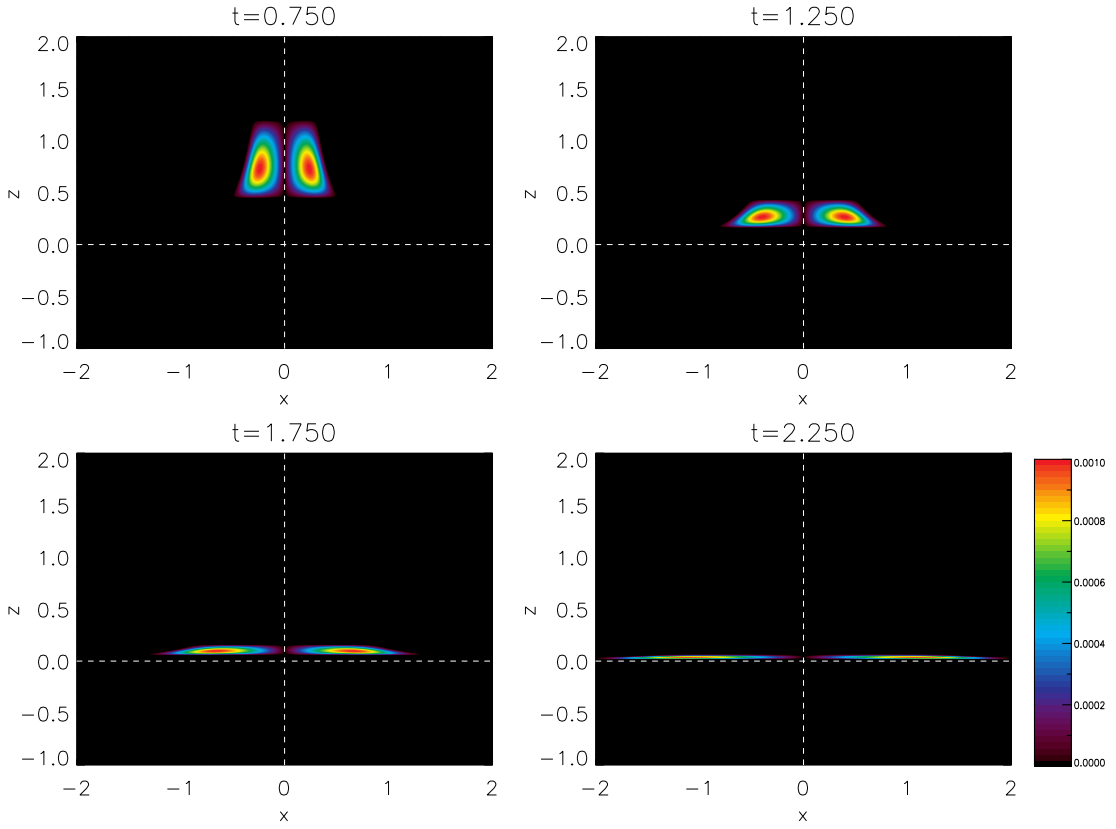

Figure 6.1: The evolution of the Alfvén wave pulse at the proper null point, observed in $|v_A|$, in the xz-plane with $y = 0$. Due to the azimuthal symmetry, the corresponding figures for other planes which intersect the spine-line $x = y = 0$ are identical. The dotted white lines indicate the position of the spine line and fan plane.

mostly moving parallel to the fan-plane, e.g., $t = 1.75$, $t = 2.25$). From a 3D perspective, driving according to equation (6.1) has introduced a toroidal pulse which undergoes isotropic dilation as it propagates down towards the fan. It propagates in the $\hat{z}$-direction at speed $c_A(0, 0, z) = 2z$ and dilates uniformly as magnetic fieldlines diverge from the spine. It accumulates near the fan-plane ($c_A(0, 0, z) \to 0$) where gradients in the pulse become increasingly steep and consequently, strong currents build. Eventually resistivity becomes non-negligible, in agreement with previous wave-null studies (e.g., Galsgaard et al. 2003; McLaughlin & Hood 2004), indicating that the fan-plane is a likely region for (wave-driven) heating events.

We now consider fluid-velocity perturbations in the other orthogonal directions $\hat{\mathbf{B}}_0$ and $\hat{\mathbf{C}}$. All perturbations to variables in the $\hat{\mathbf{B}}_0$- and $\hat{\mathbf{C}}$-directions are of $\mathcal{O}(\alpha^2)$ and smaller, indicating that behaviour detailed in the following paragraphs is nonlinear and that the Alfvén wave is linearly decoupled from the magnetoacoustic waves.

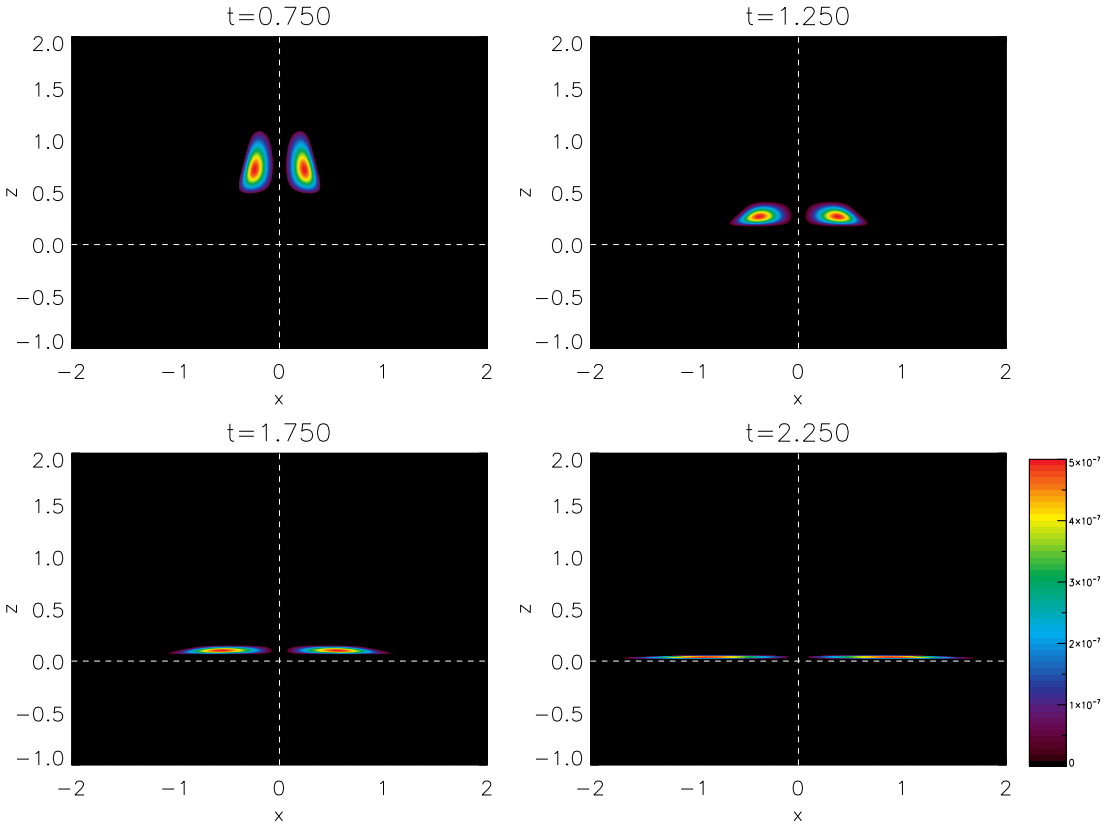

Figure 6.2: The evolution of $|v_B|$ at the proper null, which shows a *longitudinal daughter disturbance*. It is nonlinear and everywhere cospatial to the Alfvén wave. It arises due to the action of the Alfvén wave's ponderomotive force, which carries the disturbance along its path as it propagates. The daughter disturbance does not impact upon the medium as it passes through.

Figure 6.2 shows the field-aligned perturbations in $|v_B|$, where we find a nonlinear $\mathcal{O}(\alpha^2/2)$ disturbance that is everywhere cospatial to the Alfvén wave in v_A. As in previous chapters, the disturbance in $|v_B|$ is not an independently propagating wave (as $\beta = 0$), and is rather a daughter disturbance which we have identified both as a general feature (Chapter 4) and at 2D nulls (Chapter 5). We do not observe the development of static perturbations to the longitudinal velocity. This indicates that nonlinear excitation of slow waves does not occur, again in agreement with the 2D results (in $\beta = 0$, the slow mode has zero-speed and hence is manifest as a static, unstable perturbation, see Falle & Hartquist 2002). The form of the nonlinear force of the field-perturbation along the direction of the field, $\mathbf{B}_0 \cdot \nabla(b^2)$, is also shown in Figure 6.4.

In Figure 6.3 we report the velocity component in the $\hat{\mathbf{C}}$-direction, which in $\beta = 0$ is associated with fast magnetoacoustic waves and *transverse daughter disturbances* (cross-field equivalents to the ponderomotive effect manifest in $|v_B|$). During the driving phase, we observe the nonlinear generation of a multiple-lobed pulse of $\mathcal{O}(\alpha^2/2)$, which subsequently propagates *independently of the Alfvén wave*. The pulse travels towards the null point, across fieldlines at speed c_A (thus

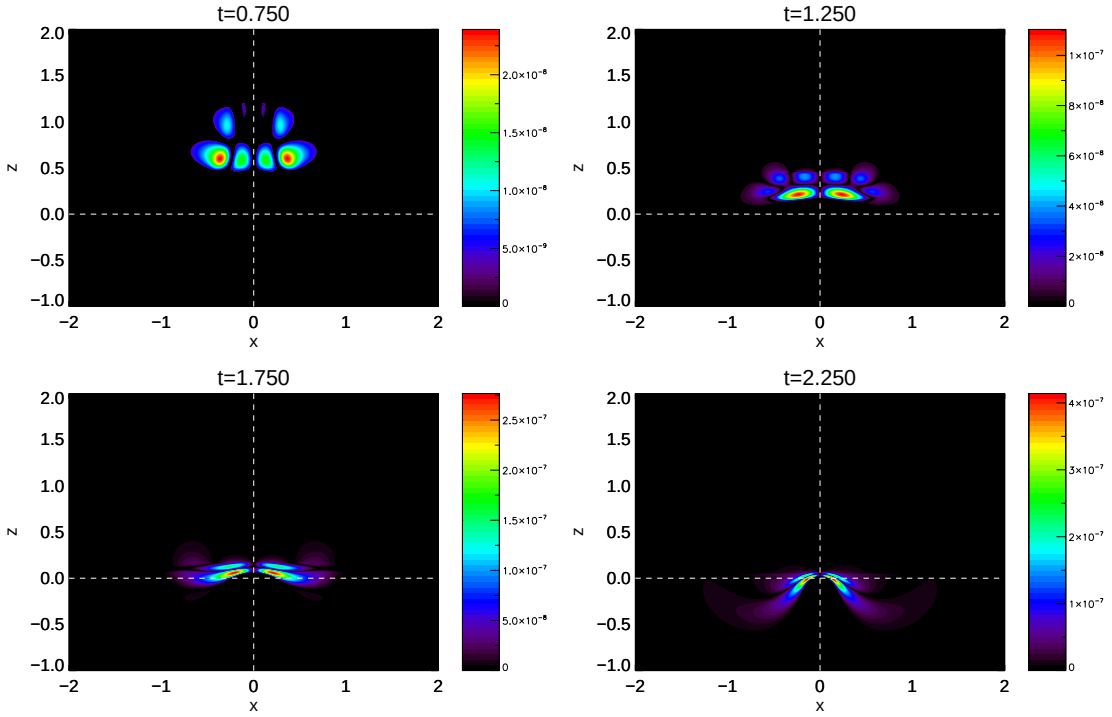

Figure 6.3: The evolution of $|v_C|$ at the proper null, in which we see an independently propagating wave, which generated during the driving phase and is of nonlinear magnitude. It refracts along the Alfvén-speed profile, crosses the fan plane and accumulates at the null.

slowing on the approach to the null), crossing the fan and wrapping about the null point. Crucially, this wave crosses the fan plane (which is forbidden for the Alfvén wave). This refraction along the Alfvén-speed profile and accumulation at the null point has been documented as the typical feature of propagating fast magnetoacoustic waves at both 2D and 3D null points. After the driving phase, we find that there is no further excitation of fast magnetoacoustic waves.

This independently propagating fast wave is excited nonlinearly either by the process of ponderomotive mode excitation or the driving itself. Although the 3D proper null has cross-field inhomogeneity throughout, we only observe the generation of fast waves during the driving phase and do not observe further excitation, exactly as in the 2D case (Chapter 5). The possible explanations are the same as those outlined in Section 5.4.2, namely that:

- The net ponderomotive force is non-zero, and acts to excite fast waves. However, after the initial driving period, a physical mechanism arises to suppress the further generation of fast waves.
- The net ponderomotive force is zero throughout and no excitation of fast waves should occur. The excitation observed is an artefact due to driving at the boundary, which effectively specifies a non-physical ponderomotive force during the driving phase. If this is the case,

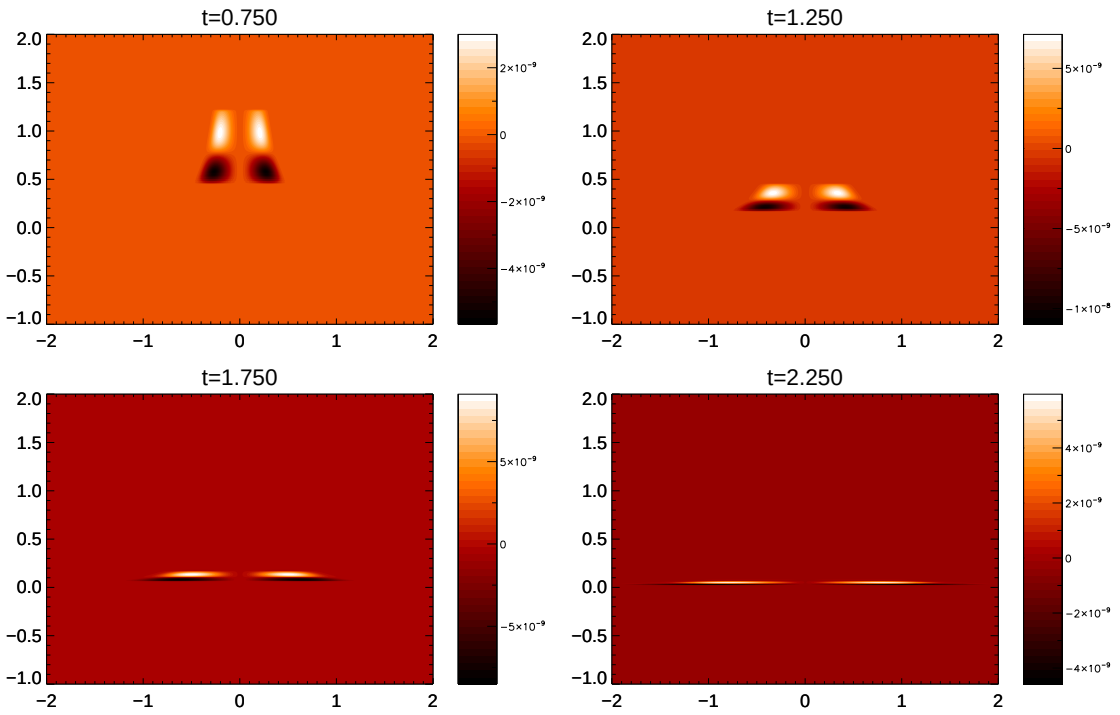

Figure 6.4: Contours of the gradients in the field-perturbation along the direction of the field for the proper null, $\mathbf{B}_0 \cdot \nabla(b^2)$.

then the wave is a mathematical artefact as opposed to a physical effect.

As the 2D and 3D results agree, we refer the reader to Section 5.4 for a further discussion of the possible explanations outlined above.

Finally, we do not clearly observe any cospatial disturbances manifest in $\hat{\mathbf{C}}$ (transverse daughter disturbances). Such a manifestation of the ponderomotive force is expected as the Alfvén wave assumes transverse gradients in the amplitude as shown in Figure 6.5 which shows $\mathbf{C}_0 \cdot \nabla(b^2)$. This has also been seen, for example, in the 2D null case (cf. Figure 5.5). As such, it is currently inconclusive as to whether the transverse daughter occurs in this situation,. It is possible that the transverse daughter cannot be distinguished as initially it is obscured by the fast wave, and at later times (when the Alfvén and fast waves are sufficiently separated) the configuration of the pulse is such that gradients across fieldlines rend the ponderomotive force exerted too small to observe at $\mathcal{O}(\alpha^2/2)$ scales.

6.3.2 Improper Null, $\epsilon = 0.5$

We now repeat the experiment and drive v_A as per equation 6.1 about an improper null point of eccentricity $\epsilon = 0.5$. Here, the null is not azimuthally symmetric and fieldlines are predominantly

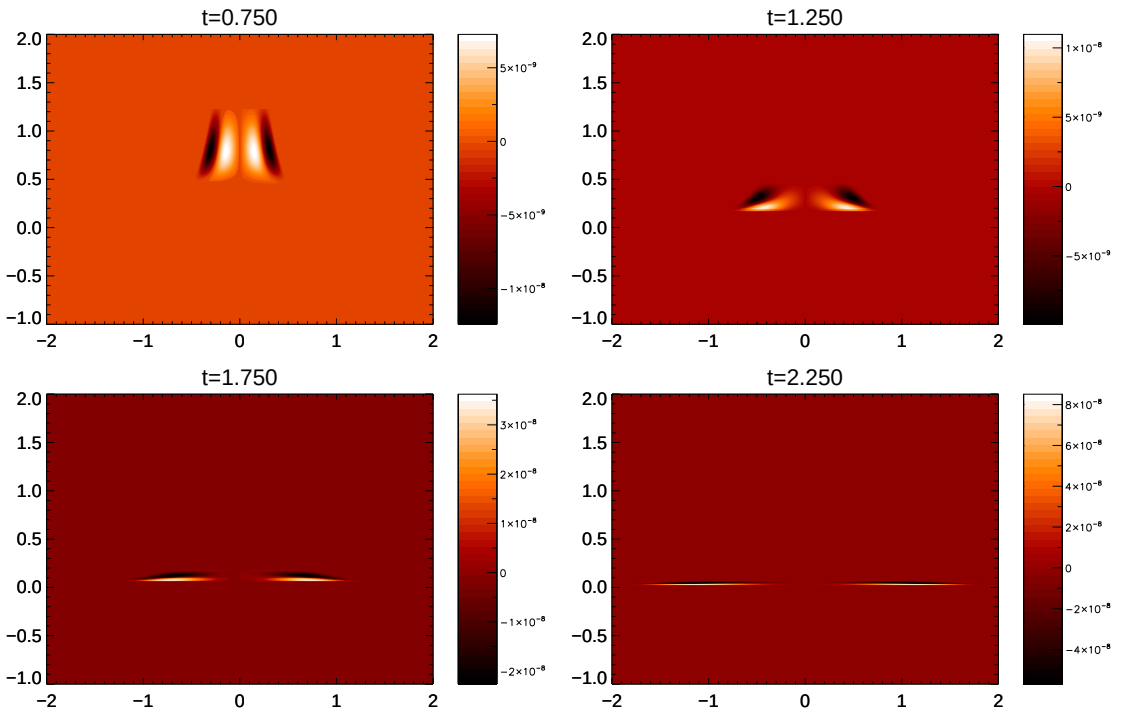

Figure 6.5: Contours of the gradients in the field-perturbation across the direction of the field for the proper null, $\mathbf{C}_0 \cdot \nabla(b^2)$.

aligned parallel to the x-axis (see Figure 1.8). Again, we separately consider velocity in the $\hat{\mathbf{A}}_0$-, $\hat{\mathbf{B}}_0$-,and $\hat{\mathbf{C}}$-directions to isolate different modes of oscillation and disturbances.

Figure 6.6 shows the propagation of the Alfvén wave, manifest in v_A. Since the azimuthal symmetry is lost for $\epsilon \neq 1$, we show the figure in the planes defined by $x = 0$ and $y = 0$ (the right and left panels, respectively). As in Section 6.3.1, the pulse initially propagates down towards the null point, and is stretched as fieldlines diverge from the spine. Unlike in the proper-null case, the 'spreading' effect is realised more rapidly in the $y = 0$ plane than the $x = 0$ plane. From a 3D perspective the dilation of the toroidal pulse is now anisiotropic, and the pulse which is initially a uniform, ring-shaped torus becomes prolate at later times, due to preferential stretching in the $\hat{\mathbf{x}}$-direction (where fieldlines diverge at the greatest rate). The non-uniformity of the dilation corresponds to the non-azimuthally symmetric manner in which fieldlines diverge from running parallel to the spine line when $\epsilon = 0.5$ (see the right panel, Figure 1.8). Thus, as at the proper null, throughout the simulation (i.e., not just in these planes) the Alfvén wave propagates along fieldlines at the local Alfvén speed, and the difference between nulls of different epsilon ϵ is manifest in the differing rates of divergence in the $x = 0$ and $y = 0$ planes.

Let us now consider the other directions $\hat{\mathbf{B}}_0$ and $\hat{\mathbf{C}}$. As per Section 6.3.1, we observe no linear disturbances to fluid-variables in these directions. Thus, the eccentricity of the null and departure

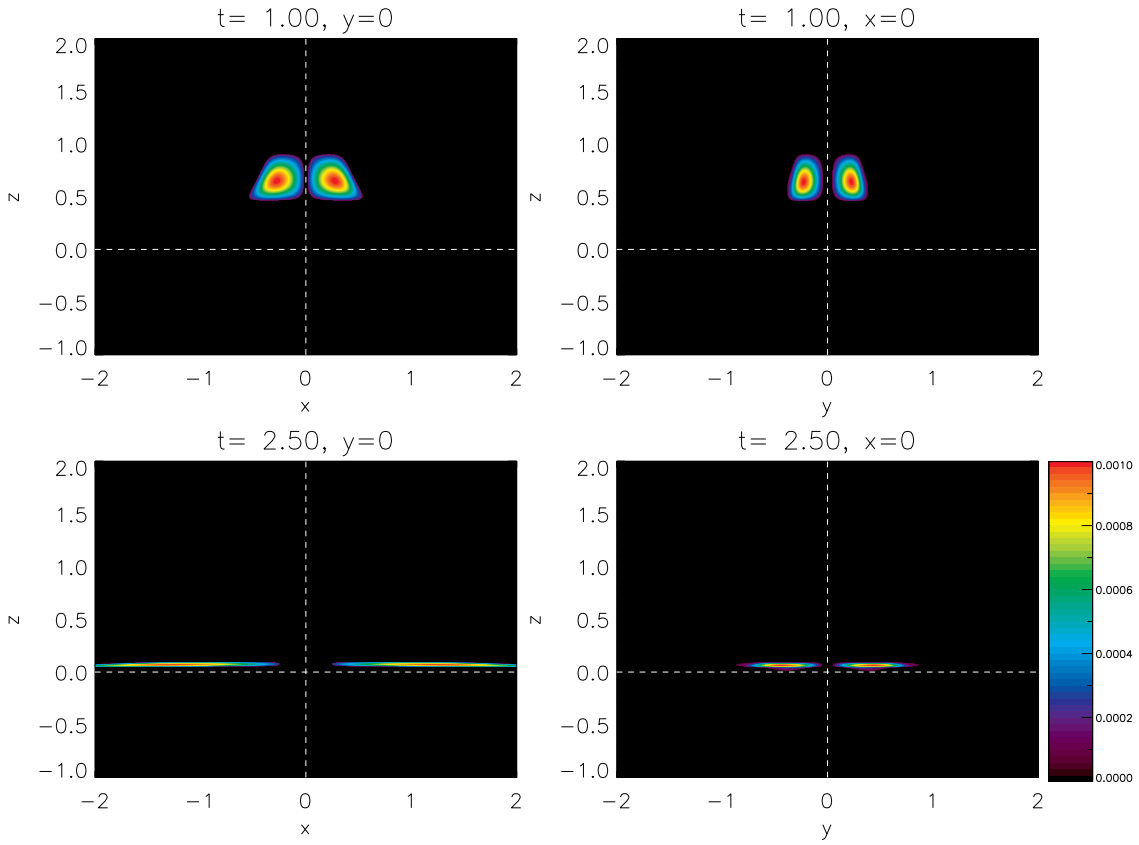

Figure 6.6: The Alfvén wave, here shown in $|v_A|$, for the improper null $\epsilon = 0.5$. As azimuthal symmetry is broken, we show two planes $y = 0$ and $x = 0$ (left and right columns respectively). Note that that the pulse spreads at different rates in the different planes.

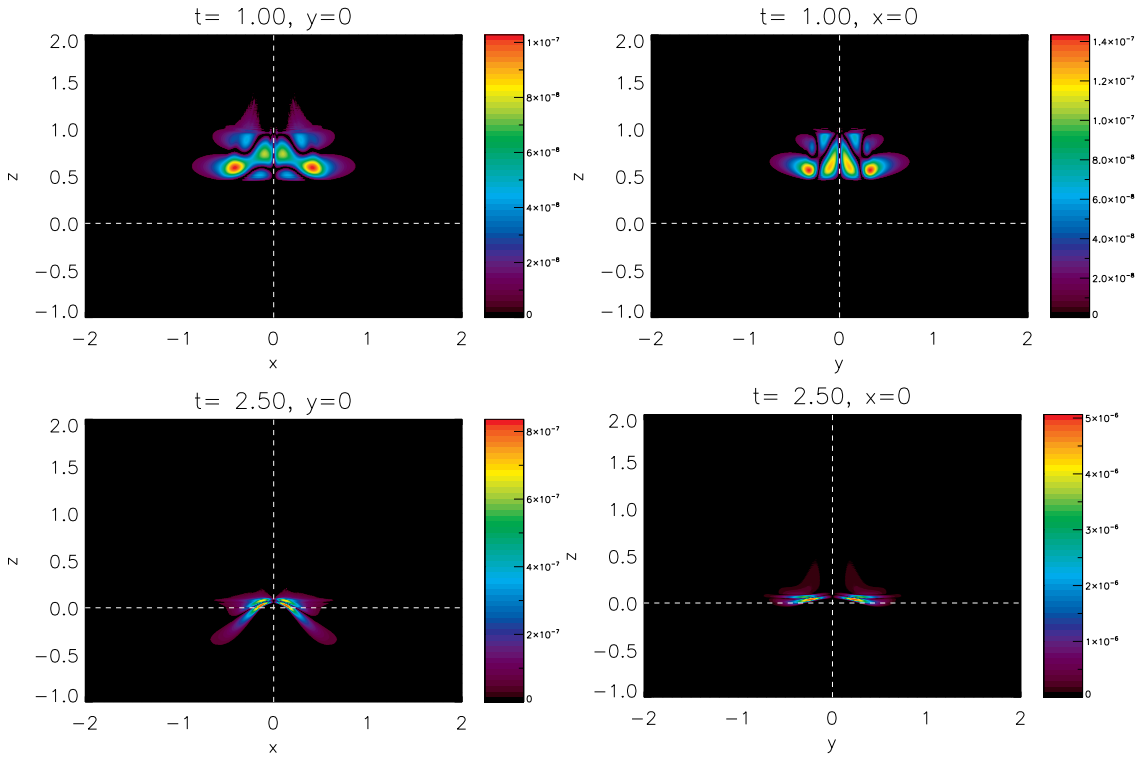

Figure 6.7: The evolution of $|v_C|$ at the improper null $\epsilon = 0.5$. An independently propagating fast magnetoacoustic wave is generated during the driving phase. Again, as azimuthal symmetry is lost we show two planes to demonstrate the different rates of refraction.

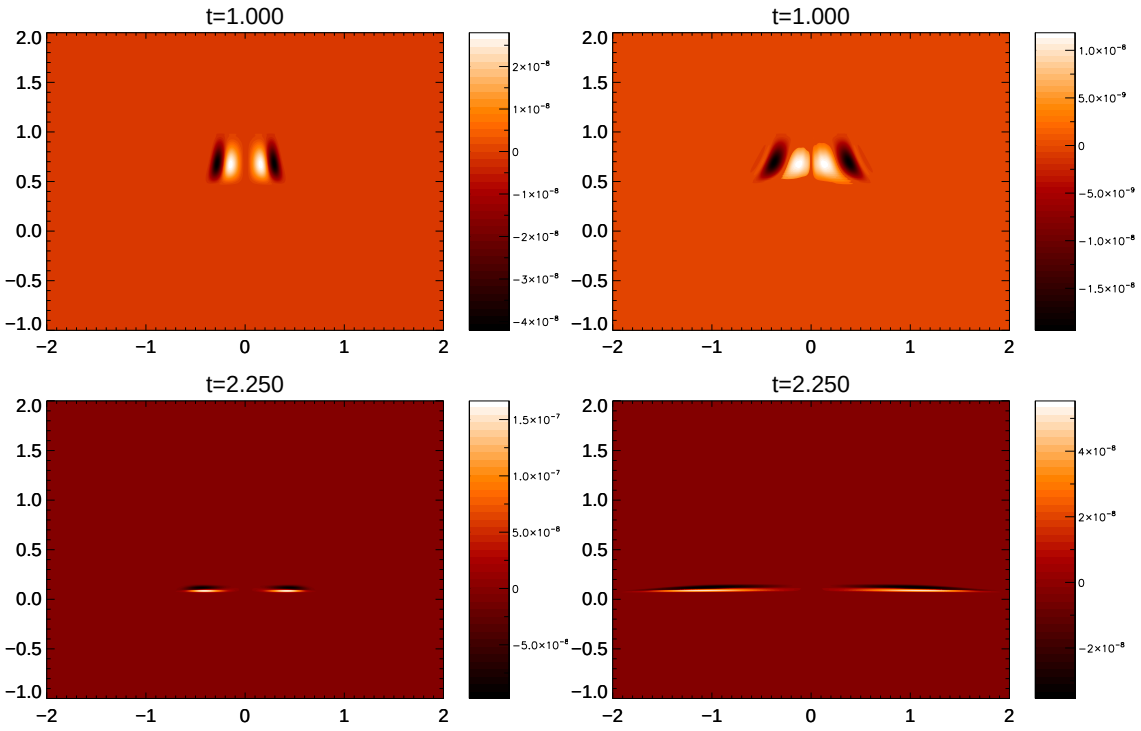

Figure 6.8: Contours of the gradients in the field-perturbation across the direction of the field for the improper null, $\mathbf{C}_0 \cdot \nabla(b^2)$.

from azimuthal symmetry does not facilitate any linear, geometric interaction between differing wave modes. The fluid-velocity $|v_C|$ is shown in Figure 6.7. We see an independently propagating wave nonlinearly generated which propagates towards the null, crosses fieldlines and the fan, and wraps about the null point. The rate of refraction is again dependent on the Alfvén-speed profile, and therefore the refraction effect is weaker in the $x = 0$ plane (right panel) than the $y = 0$ plane (left panel), corresponding to the relative steepness of the Alfvén-speed profile (see Chapter 3). There is no further generation of independently propagating waves after the driving phase, as reported for the proper null case. No daughter-type disturbances are clearly observed in $|v_C|$, as per Section 6.3.1, although there are gradients in the field-perturbation aligned with $\hat{\mathbf{C}}$ as shown in Figure 6.8.

The Alfvén wave was also found to be accompanied by a longitudinal daughter disturbance, manifest in in the $\hat{\mathbf{B}}_0$-direction as per that detailed in Section 6.3.1, which is of $\mathcal{O}(\alpha^2/2)$ and is everywhere cospatial to the Alfvén wave (hence we have not included an extra figure). The field-aligned gradients in the magnetic field perturbation responsible are shown in Figure 6.9. As in the case of the proper null, no static disturbances (indicators of slow wave excitation) are observed in any of the components.

We also considered intermediate values of $0 < \epsilon < 1$ and found qualitatively identical results.

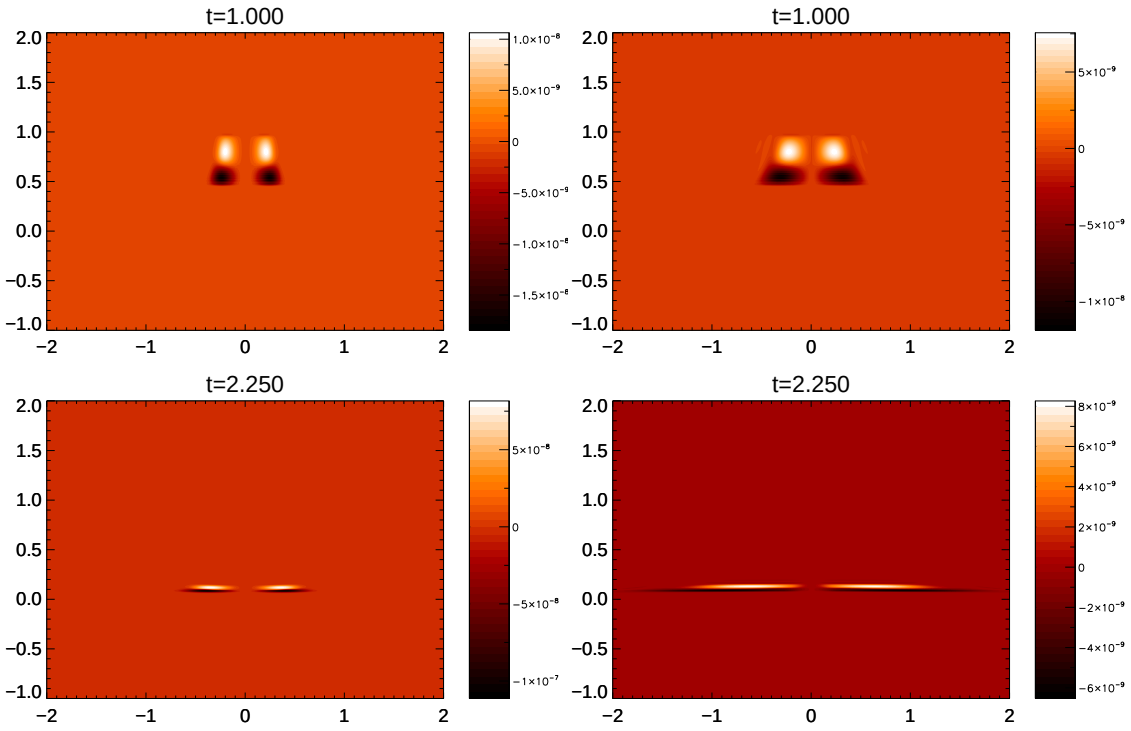

Figure 6.9: Contours of the gradients in the field-perturbation across the direction of the field for the improper null, $\mathbf{B}_0 \cdot \nabla(b^2)$.

Wave behaviour about null points of different eccentricity only differs in that Alfvén waves spread throughout the region according to the differing rates of fieldline divergences, and any fast waves excited refract at differing rates according to the differing Alfvén-speed profiles. Crucially, different ϵ do not cause differing nonlinear effects. In all cases excitation of the fast wave occurs only during the driving phase and no subsequent conversion occurs.

6.4 Conclusion

We have studied the behaviour of the Alfvén wave, and associated nonlinear effects, in the vicinity of both proper ($\epsilon = 1$) and improper ($\epsilon = 0.5$) 3D magnetic null points. Independent of eccentricity, we find that:

1. The Alfvén wave is confined to fieldlines, spreading radially outward as fieldlines diverge, and eventually assumes steep gradients as it nears the fan-plane, causing current accumulation.

2. The Alfvén wave continuously sustains a longitudinal daughter disturbance, due to its pon-

deromotive force directed along the equilibrium magnetic field $\hat{\mathbf{B}}_0$.

3. During the driving phase, independently propagating fast waves are introduced to the simulation. Subsequently, no further excitation of fast waves occurs.

The Alfvén wave behaves in its characteristic manner - it is confined to fieldlines and travels at the Alfvén speed, without exception. Here, where toroidal Alfvén wave pulses are driven about the spine, this results in an dilation/stretching of the torus as the fieldlines diverge from the spine. When Alfvén waves are driven in forms such as that prescribed by equation (6.1) at null points of differing eccentricity, the *only* difference in the transient behaviour is the manner in which the wave-pulse expands, which is entirely dependent on the topological eccentricity parameter ϵ, which determines the degree of dilation anisotropy.

This transient behaviour is wholly consistent with analytical predictions made by the 3D WKB approximation (McLaughlin et al. 2008), and the proper null results reported by Galsgaard et al. (2003), and is an intuitive extension of the 2D results to 3D. As with the separatricies in the 2D models, in 3D the fan-surface is a location where current accumulates due to propagating Alfvén waves and is thus a possible location of preferential, ohmic heating.

Nonlinearly, we also find that the theory of Alfvén waves at 2D magnetic null points (Chapter 5) carries over to the 3D case. Namely, in the manifestation of the daughter disturbances and the excitation of fast waves only during the driving phase. As in the 2D case, it is unclear whether the excitation of the fast wave is a physical effect or an artefact of the driving. The possibilities are fully discussed in Chapter 5 and Thurgood & McLaughlin (2013b, section 4.2).

Overall, in the case of Alfvén waves at proper nulls, we find that changing ϵ only has minor, qualitative effects on the transient behaviour and that it does not change the nature of the nonlinear effects. Despite the eccentricity and inhomogeneity, the wave retains its primary characteristic, that is, it is driven by magnetic tension only, and is a therefore a *true* Alfvén wave as per Alfvén (1942). As an Alfvén wave must perturb fluid variables across the field without causing a (linear) magnetic pressure gradient to arise, in the absence of translational invariance Alfvén waves *are always torsional* and cannot be shear. In this case we have considered the 3D Alfvén wave arising from twisting along surfaces of $\hat{\mathbf{A}}_0$, i.e, a toroidal pulse centred about the spine, however it is important to note that other torsional fieldline perturbations could facilitate Alfvén waves (see, e.g., Section 7.2 and Appendix A). As 3D Alfvén waves are necessarily torsional any effects noted in 2D wave-null modelling which are geometry-specific (e.g., many 2D models consider planar Alfvén waves only) will not necessarily extend to 3D in as straightforward a manner as we have found for the cases considered in this chapter.

Chapter 7

Summary and Further Work

There are no limits. There are plateaus, but you must not stay there; you must go beyond them.

— Bruce Lee (1940 - 1973)

7.1 Summary

At the start of this thesis, we discussed how previous work on 2D wave-null interactions implicated null points as coronal features which act as sites for localised and preferential heating, mode-conversion and wave-driven reconnection events (Sections 1.1 & 2.1). We stressed that as real coronal nulls are 3D, and as such completely topologically distinct to their 2D counterparts, it was important to develop a theory of 3D wave-null interactions and evaluate the extent to which such conclusions carried over from the 2D to 3D case.

To that end, in Section 2.2 we outlined more specific questions, namely:

- What are the key, transient features of different MHD waves in the vicinity of 3D nulls?
- What role does fieldline eccentricity play? How does transient wave behaviour differ at proper and improper nulls?
- What role does the inhomogeneity of the magnetic topology play? Do the waves correspond to their homogeneous, unidirectional field counterparts? What is the nature of their coupling?

To begin to develop a theory of 3D wave-null interaction, and to answer the above questions, in this thesis we have focused on the behaviour of waves at the most fundamental class of 3D null; the

$\beta = 0$ potential null point. By developing a method for isolating different modes about 3D nulls and simulating the behaviour of MHD waves at such nulls (Chapters 3 & 6), further investigating the theory of nonlinear waves in inhomogeneous media (Chapter 4) and extending 2D wave-null theory (Chapter 5), we can now begin to answer these questions.

Let us now review the key results of this thesis:

Transient Features

- **Fast Waves:** propagate according to the Alfvén-speed profile along and across the fieldlines, refracting and accumulating at the null point. Different ϵ simply alters the rate of refraction (due to steeper/gentler gradients in the Alfvén-speed profiles). Independent of eccentricity, the fast wave eventually accumulates at the null point itself.
- **Alfvén Waves:** are confined to fieldlines, travelling at c_A, and thus pulses approaching from above the fan exhibit a 'spreading' effect as fieldlines diverge, typically accumulating near the fan plane. Different parameters ϵ simply change the preferential direction on the pulse spreading, due to the manner in which fieldlines diverge from the spine.
- As in 2D, this accumulation and focusing of wave energy leads to large gradients and small length scales, rending resistivity important and leading to localised ohmic heating at the null (fast wave) and of the fan (Alfvén wave).

Coupling

- We find no evidence of linear interaction between the different modes in the cases considered where we vary fieldline eccentricity; i.e. the departure from azimuthal symmetry does not itself facilitate mode conversion and completely (linearly) decoupled modes can exist about 3D nulls.

Nonlinear Effects

- In the vicinity of nulls, the Alfvén wave sustains nonlinear, compressive disturbances (i.e. daughters or wings) due to the inhomogeneity of the medium giving rise to ponderomotive force acting along (*longitudinal* daughters) and across (*transverse daughters*) the background magnetic field. For higher amplitude Alfvén waves, such compressive motion could enhance the dissipative properties of the wave in the vicinity of the null.
- We find evidence of ponderomotive excitation of fast waves as Alfvén waves enter the vicinity of the null. However, this occurs only in the driving stages, rather than a continuous process of excitation as the Alfvén wave propagates throughout the inhomogeneous region.

- Although such behaviour could be consistent with the general theory of ponderomotive effects (Chapter 4) if some saturation mechanism exists, it is currently unclear whether nonlinear mode excitation of fast waves at nulls is physical. The fact that it occurs during the driving stage raises the possibility of an artificial origin, i.e. the observed Alfvén-to-fast conversion may be a 'mathematical artifact'.

At the outset of this thesis, the basic features of MHD wave behaviour in the vicinity of 3D magnetic null points were unknown, and it was a completely open question as to whether the results and implications of the 2D literature applied to the 3D case. Now, the key features of the 3D wave-null system are known, as detailed above. We can conclude that, barring some subtle differences, *the key features of 2D theory carries over in an intuitive way*, and as such the 2D conclusion that coronal null points are likely locations of localised heating holds in 3D as well.

7.2 Further Work

The results of this thesis show that the interaction between waves and realistic 3D nulls can have important consequences for coronal physics and other MHD-plasma regimes (previously this had only been inferred from 2D models), and it is clear that further study of 3D wave-null systems has merit. In this thesis we have restricted our attention to the most fundamental class of 3D null, the potential null, so as to focus on the key question of how the 3D geometry affects wave behaviour without extraneous physical effects confusing the results. Having answered such questions, it is now appropriate to systematically consider additional physical effects, building up to more realistic solar model. In the author's opinion, several extensions to our models are required and will be the subject of future investigation. Here, I will now outline these research avenues.

$\beta = 1$ Layer

This study has utilised the $\beta = 0$ approximation to intentionally prohibit the introduction of the slow mode and restrict attention to the behaviour of the fast and Alfvén waves, so as to understand the most fundamental 3D null system. However, it is important to highlight that sufficiently close to the null point, as magnetic induction drops off, there will be a region where sound speed and Alfvén speed become comparable; identified by Bogdan et al. (2003) as the *magnetic canopy*, viz. the $\beta = 1$ layer. McLaughlin & Hood (2006b) extended their cold 2D model to account for this effect, and found that in the vicinity of the layer some of the fast mode energy is (linearly) converted to the slow mode and thus can escape the vicinity of the null, reducing the overall effectiveness of the localised ohmic heating (although, this can still be significant). Since realistic 3D null points must contain such a region (where $c_S = c_A$), such effects would also be present.

Although is possible that, as we have found in the cold case, the 2D theory carries over quite well, this is currently just a prediction and must be given proper consideration.

Consideration of Nonpotential Configurations

This thesis has considered MHD wave behaviour about proper and improper potential null points. However, solar nulls are unlikely to be current-free (potential), as is found to be the case in various field extrapolations (e.g., Valori et al. 2012, Sun et al. 2012). As discussed in Section 1.5.2, nonpotential nulls are more topologically complicated and asymmetric than the potential class where the fan plane may be skewed with respect to the spine, and fieldlines may be twisted (spiral nulls). Currently, it is unclear to what extent the potential null results will hold in the case of nonpotential null points; they represent further complications of the fieldline geometry, but are otherwise topologically equivalent, i.e. the difference between 3D potential and nonpotential nulls is not as great as the difference between 2D and 3D nulls.

It may well be expected that the fast wave will refract about the Alfvén-speed profile (regardless of fieldline structure) as in Chapter 3, viz. as the fast wave can propagate across fieldlines, actual fieldline geometry is less important than the profile of the total magnetic induction. However the increased asymmetry could possibly complicate the Alfvén wave dynamics at such nulls. Additionally, the greater inhomogeneity may increase the efficiency of any ponderomotive mode excitation. Since nulls in the solar atmosphere will be nonpotential, the further extension of 3D wave-null theory from potential to nonpotential cases is an important outstanding question and should be addressed in future research.

3D Oscillatory Reconnection

At 2D null points, in significantly nonlinear regimes, it has been shown that incoming large amplitude fast waves can steepen to form fast oblique shock waves. These shocks act to heat the vicinity of the null point directly and to deform the local magnetic field such that periodic reconnection events occur (McLaughlin et al. 2009; Gruszecki et al. 2011; McLaughlin et al. 2012; Threlfall et al. 2012). This process, known as *oscillatory reconnection*, provides a natural mechanism for the impulsive excitation of dynamic magnetic reconnection events due to propagating MHD waves. The resultant reconnection has been (theoretically) shown to make significant heating contributions in the locality.

However, again we meet the problem that 2D nulls are neither 3D nor are they physical. Although we now understand the basic theory of fast wave propagation at 3D nulls, which turns out to be similar to the 2D case, reconnection mechanisms are well known to be *significantly different* in

3D (see, e.g., Priest & Pontin 2009; Pontin 2012). Thus at this stage we cannot assume or infer anything about the nature of 3D oscillatory connection, however we are now well placed to begin to study it as a system thanks to the work presented in this thesis. Given the potential for impulsive reconnection processes to play a significant role in atmospheric heating, the study of wave-driven 3D reconnection at nulls is imperative.

Resonant Absorption

Resonant absorption is an important process in solar physics, which has been shown to facilitate (linear) fast-to-Alfvén mode conversion in inhomogeneous MHD (see e.g., Ionson 1978; 1982; 1983; Hollweg 1981; Rae & Roberts 1982; Ruderman & Roberts 2002, Cally & Hansen 2011; Goossens et al. 2011; Hansen & Cally 2012). As such, we may have expected resonant-absorption-type mode conversion to occur in the vicinity of our null points. However, in Chapter 3 we found no evidence suggesting mode conversion of any sort occurred about the null point. Does this mean that resonant absorption is completely prohibited in the vicinity of nulls? The answer is currently unclear; one possibility is that our election of driver implicitly prohibits the process, rather than that the inhomogeneity of the field configuration does not allow for it.

A recent series of studies by Cally & Andries (2010) and Hanson & Cally (2011) lends some insight. In an attempt to show that resonant absorption is equivalent to parallel developments in seemingly unconnected mode-conversion theories, these authors investigate the coupling between the fast magnetoacoustic and Alfvén modes by using a Generalised Ray Theory (GRT) analysis (Tracy et al. 2003; Schunker & Cally 2006) for the simplest 3D, transversely inhomogeneous MHD problem. Specifically, they consider the case of a constant unidirectional field $\mathbf{B}_0 = B_0\hat{\mathbf{z}}$, with an arbitrary density profile in the x-direction of a cold plasma. Pulses are considered as bundles of WKB-like rays, which reflect off the Alfvén speed profile at a turning point (which corresponds to the resonant line/layer). During this reflection, mode-conversion or resonant absorption occurs (they suggest 'mode conversion' as the appropriate terminology for where energy is able to escape from the region as an Alfvén wave, and 'resonant absorption' when the Alfvén wave is trapped, leading to localised energy build-up).

The efficiency of the process is found to be dependent on an angle of attack at the point of resonance in the xy-plane, and (crucially for our purposes) that no such process occurs when the incoming fast wave is propagating only in x (i.e., $k_x \neq 0$, $k_y = 0$). Although the authors do not comment as such, this highlights the basic mechanical nature of the process; *such mode conversion occurs when magnetoacoustic waves reflect/refract in such a manner as to rotate the plasma in the transverse plane*. The resulting, torsional perturbation of the plasma facilitates the presence of a tension-driven wave with zero (net) magnetic pressure, and thus an Alfvén wave is born. This mechanism is illustrated in Figures 7.1 and 7.2.

The fast wave considered in Chapter 3 at no point rotates in the transverse plane (viz., the 'AC-plane' in the language of our coordinate system), and as such no conversion can occur. This absence of torsion can be clearly be seen in the corresponding WKB ray paths for such a pulse illustrated in McLaughlin et al. (2008) (see, e.g., their Figure 3). With hindsight, it seems that the system of orthogonal polarisation vectors has in a sense been overly successful in isolating the fast mode; the cases to which it applies happen to be those where mode conversion/resonant absorption does not occur and thus it cannot be used to study resonant-type conversion at the null, as demonstrated in Appendix A. Although the approach in Chapter 3 is indeed successful in investigating the key transient features and nonlinear effects, a slightly different approach will be needed to investigate the possibility of resonant-type conversion at 3D nulls. Numerical approaches could involve other, more generalised choices of initial condition where the requirements for resonant absorption may be met. Alternatively, extending the GRT approach to nulls may prove fruitful (if tractable). Aside from the immediate interest in wave-null interactions, it would also be interesting to study such a system as an example of resonant absorption in an unusual configuration (the vast majority of resonant absorption literature focuses on flux tubes/ coronal loop models, recent examples include Terradas et al. 2010; Pascoe et al. 2010; 2011; 2012; 2013; Ruderman & Terradas 2013; Hood et al. 2013).

Thus, we have not completely answered the questions regarding the nature of mode conversion at 3D nulls, although we have demonstrated that it is possible for the completely decoupled, 'classic' waves to exist despite the complicated topology and discerned their properties and behaviour. If fast-to-Alfvén mode conversion can occur, the key consequence would be that the (otherwise trapped) fast-wave energy could escape from the vicinity of the null by conversion to outwardly-directed Alfvén waves, reducing the overall heating effects focused at the null and along the fan. Assuming straight-field models provide a reasonable estimate for curvilinear fields, the work of Cally & Andries (2010) indicates that the efficiency of resonant absorption/mode conversion could be as great as 50%, depending on angle of attack at turning points. As such, this is an important direction for future work in wave-null theory.

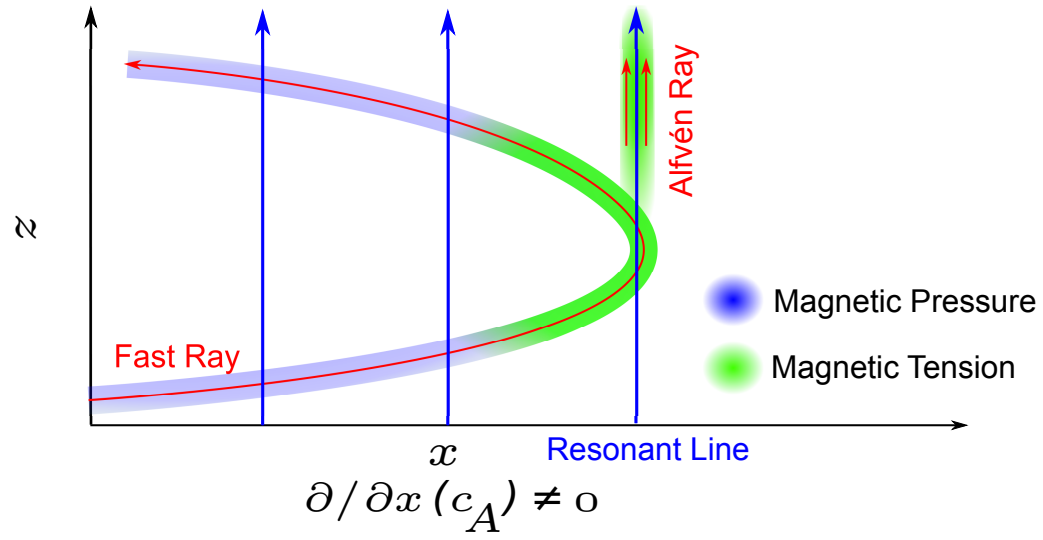

(a)

Figure 7.1: Cartoon based on the set-up of Cally & Andries (2010), showing the projection of the mode conversion process in the xz-plane. A fast wave, which is initially propagating against the Alfvén speed profile (low-to-high) reflects at a turning point/resonance into the high-to-low speed fast waveguide. Provided that the fast wave is also propagating in the transverse plane during the reflection ($k_y \neq 0$), clearly identifiable, unambiguous Alfvén waves are generated. See also, e.g., their supplementary movie.

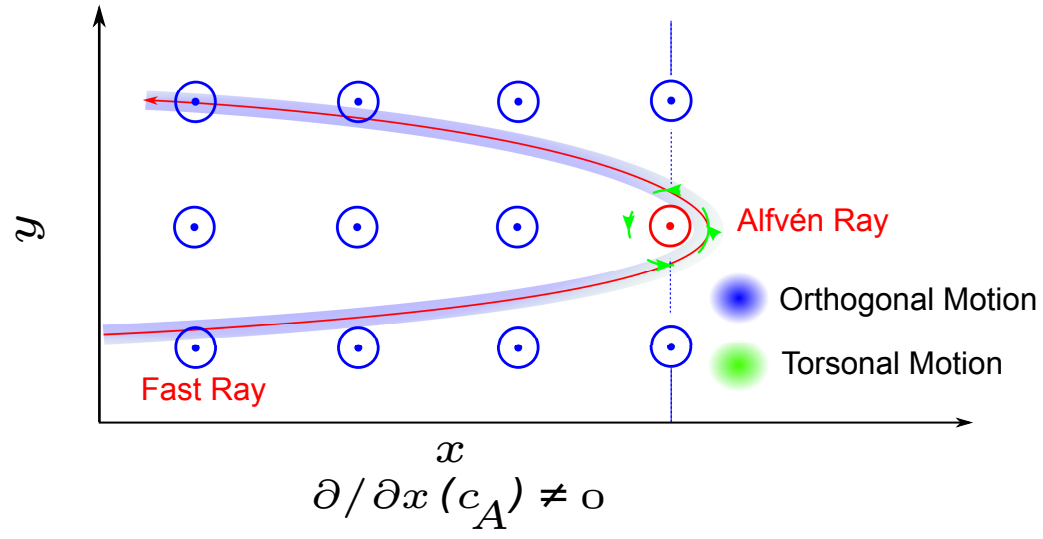

(a)

Figure 7.2: The same cartoon as Figure 7.1 for a projection in the xy-plane. As we have discussed extensively, an Alfvén wave requires some mechanism which nullifies magnetic pressure (so that it is driven by tension only). Since the fast wave is reflected in the xy-plane (transverse plane), the plasma is rotated creating an 'invariant perturbation' which prohibits pressure gradients (much like rotating along surfaces of $\mathbf{A}$ in Chapter 6). There is a direct correspondence between the vortex generated (via the angle of attack and parameters relative to the c_A-profile) and the efficiency of the conversion mechanism (see, e.g., Figure 2 of Cally & Andries 2010)

Nonlinear Driving

For reasons of tractability, initial/boundary conditions in fully nonlinear MHD simulations typically correspond to linear solutions (e.g., variables on a boundary may be driven in a manner that corresponds to a linear Alfvén wave). As discussed at length in Section 5.4.2, there is a possibility in such cases observed ponderomotive excitation of waves may be a mathematical consequence of the driving mechanism, rather than a physical effect.

Although not yet verified (and hence kept apart from the main text and conclusions), it is the authors suspicion that if an initial condition fails to correctly specify the ponderomotive force of a wave (e.g., $v_\perp$ and $v_\parallel$ are inappropriately taken as zero) the medium responds by nonlinearly introducing magnetoacoustic waves. If the intention of the initial/driving condition was to introduce a pure mode of oscillation (as opposed to represent generic impulses or driving), these magnetoacoustic waves are not physically realistic and care should be taken to ensure that such waves are not interpreted as part of the physics and do not go on to further influence the system.

As such approaches to numerical simulations are now common, it is important to consider this possibility and, if it is the case, make the community aware of the potential pit-falls that could lead to mis-interpreted results. Preliminary investigations into this 'boundary-ponderomotive effect' are detailed in Appendix E.

7.3 Closing Remarks

The experiments, analyses, and deductions presented in this thesis have lead to an understanding of the fundamental aspects of three-dimensional MHD wave-null interaction theory. We have found that the main results from existing 2D work do indeed carry over to 3D magnetic null points. From a solar physics perspective, these results indicate that 3D nulls are likely locations for preferential wave heating in the corona. From an MHD theory perspective, we also have gleamed valuable insights into the nature of wave behaviour in non-standard, inhomogeneous magnetic topologies. At the time of writing, several important outstanding questions remain within the topic of MHD wave behaviour at magnetic null points. Thanks to the work presented in this thesis, we are now more suitability equipped to tackle these problems for realistic, physical, 3D geometries.

Appendix A

Side-driven pulse

(Section 3)

In Section 3 we presented the first numerical experiments to consider the behaviour of the fast magnetohydrodynamic wave about fully 3D null points. The primary goal was to establish the key transient aspects of the fast mode, and how this is effected by differing fieldline eccentricities. We were also interested in possible mode-conversion or excitation facilitated by three dimensional, inhomogeneous or nonlinear mechanisms. For the specific case of a fast pulse consisting of planar fronts which are initially parallel to the fan plane (the *'top-driven'* case), we found no evidence of coupling to the Alfvén mode.

However, it does not necessarily follow that coupling is prohibited for all cases. If we consider the discussion in Section 7.2, and Figures 7.1 and 7.2, we see that the basic mechanical nature of the mode-conversion process is that mode conversion occurs when magnetoacoustic waves reflect/refract in such a manner as to rotate the plasma in the plane transverse to fieldlines. One possible candidate that may meet the necessary conditions for mode conversion is a planar fast wave that is initially perpendicular to the fan plane (*'side-driven'*); WKB solutions for rays incident from the side suggest that side-driven pulses will refract azimuthally to some extent (see Figure A.1). Thus, it is reasonable to expect that a side-driven planar fast wave may satisfy mode-conversion conditions. In this section we present a brief summary of the side-driven numerical simulations, the results of which *could be* interpreted as evidence of fast to Alfvén mode-conversion occurring at 3D null points.

The experiment is constructed as per Section 3 except that we instead drive v_C on the lower x-boundary such that

$$\mathbf{v}\cdot\hat{\mathbf{C}} = \begin{cases} +\alpha \sin 2\pi t, & \text{if } z > 0 \\ -\alpha \sin 2\pi t, & \text{if } z < 0 \end{cases} \tag{A.1}$$

and we also drive $v_y = -\alpha \sin 2\pi t$ on the fan itself ($z = 0$). By driving in opposite signs of $\mathbf{C}$ either side of the fan plane we can match the expected polarisation of the fast wave across the fan (i.e., take $v_y = -\alpha \sin 2\pi t$) and avoid any issues associated with $\mathbf{C} = \mathbf{0}$ on the fan (i.e., as opposed to driving in say, $+\hat{\mathbf{C}}$ and allowing a gap in the pulse along the fan itself).

We show the evolution of $|\mathbf{v}|$, $|\mathbf{v}_C|$ and $|\mathbf{v}_A|$ throughout the simulation as viewed in the $y = 0$, $y = 1/3$ and $y = 1/2$ planes (Figures A.2, A.3 and A.4 respectively). We do not show $\mathbf{v}_B$ as it is always much smaller than the linear order (here, we are interested in linear mode conversion). Additionally, Figures A.5, A.6 and A.7 show $|v_x|$, $|v_y|$ and $|v_z|$ for the same slices. In $|\mathbf{v}|$ we see that the pulse or pulses resulting from the driving are qualitatively consistent with aspects of both fast wave behaviour (motion across field-lines and refraction around the null) and also Alfvén wave behaviour (motion along the fieldlines and accumulation near separatricies). These multi- or mixed-mode qualities are also seen in the transverse velocity components $|\mathbf{v}_C|$ and $|\mathbf{v}_A|$, which indicates that the polarisation vectors $\hat{\mathbf{C}}$ and $\hat{\mathbf{A}}$ do not correspond to the polarisation of the fast and Alfvén waves in this case and thus cannot always be used to distinguish between different modes of oscillation at null points.

In the absence of a means to distinguish between different modes and determine the rates and locations of energy exchange we cannot conclude whether these simulations are in fact evidence of mode conversion or if it is the case that both modes are excited by the driving. This simple experiment highlights the limitations of an approach based on a system of orthogonal polarisation vectors and shows that the question of mode-conversion at 3D nulls is still open. As discussed in Section 7.2, due to the breakdown of the coordinate system it is likely that an analytical approach in the vein of Cally & Andries (2010) and Hanson & Cally (2011) may prove to be the most informative approach in future investigations.

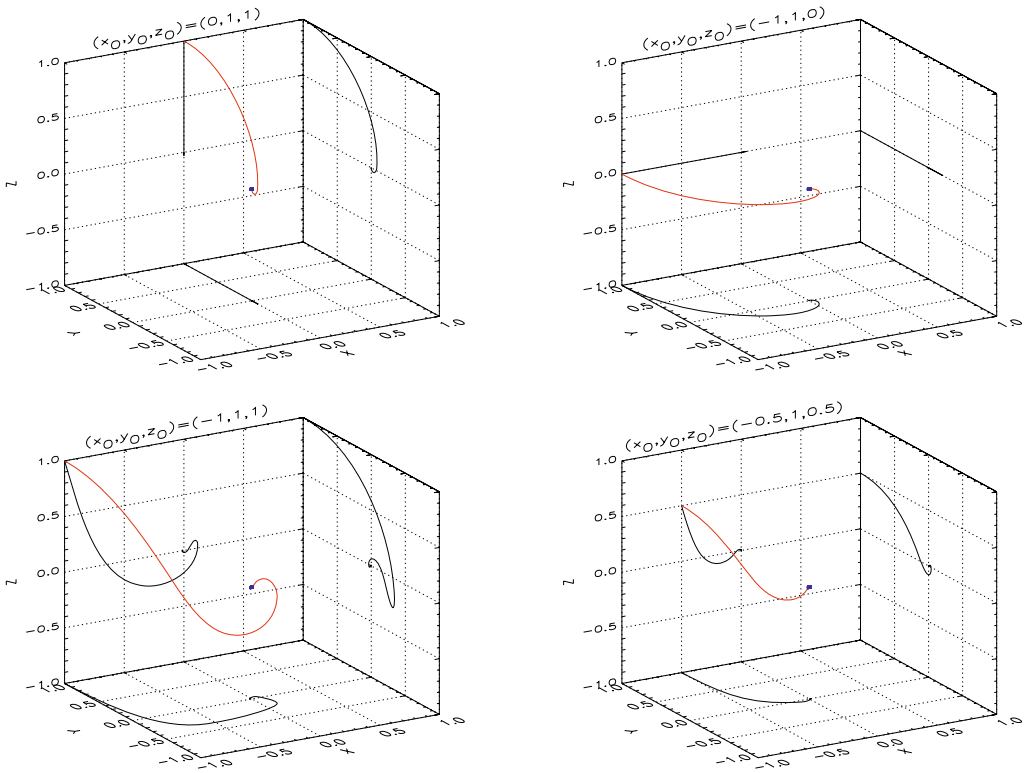

Figure A.1: Ray paths originating in the $y = 1$ plane for solutions according to the fast wave WKB solution of McLaughlin et al. (2008) for the proper null point ($\epsilon = 1$). The red ray represents the 3D path, and the black curves indicate the xy, yz, and xz-projections of the ray into the respective planes. We see that some of the rays refract azimuthally.

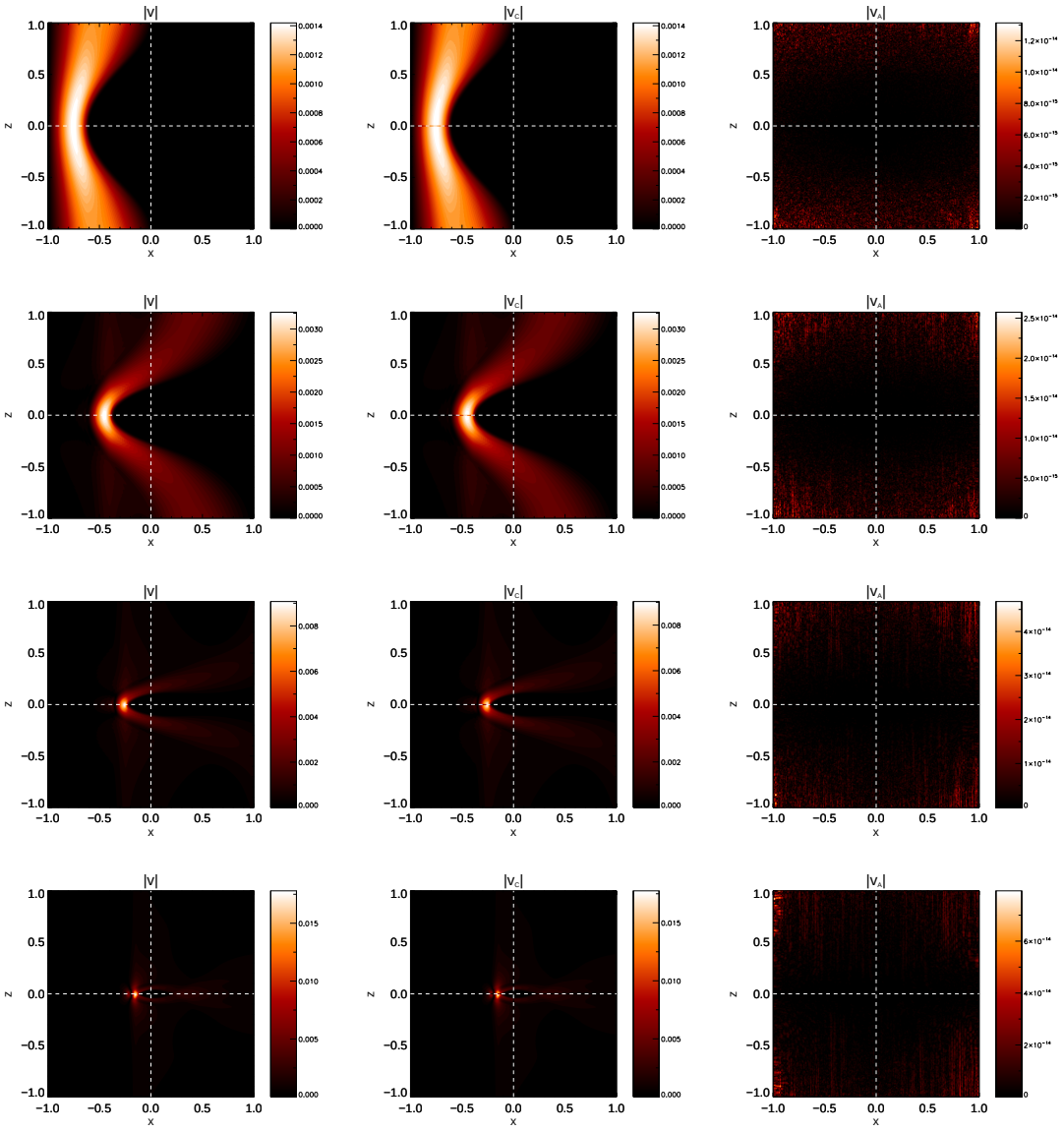

Figure A.2: The evolution of $|\mathbf{v}|$, $|\mathbf{v}_C|$ and $|\mathbf{v}_A|$ in the $y = 0$ plane (time evolves from top to bottom). Here $\mathbf{v}_A$ is effectively zero, however, on careful inspection we note that the $|\mathbf{v}|$ and $|\mathbf{v}_C|$ show signals that are consistent with both Alfvén wave and fast wave propagation.

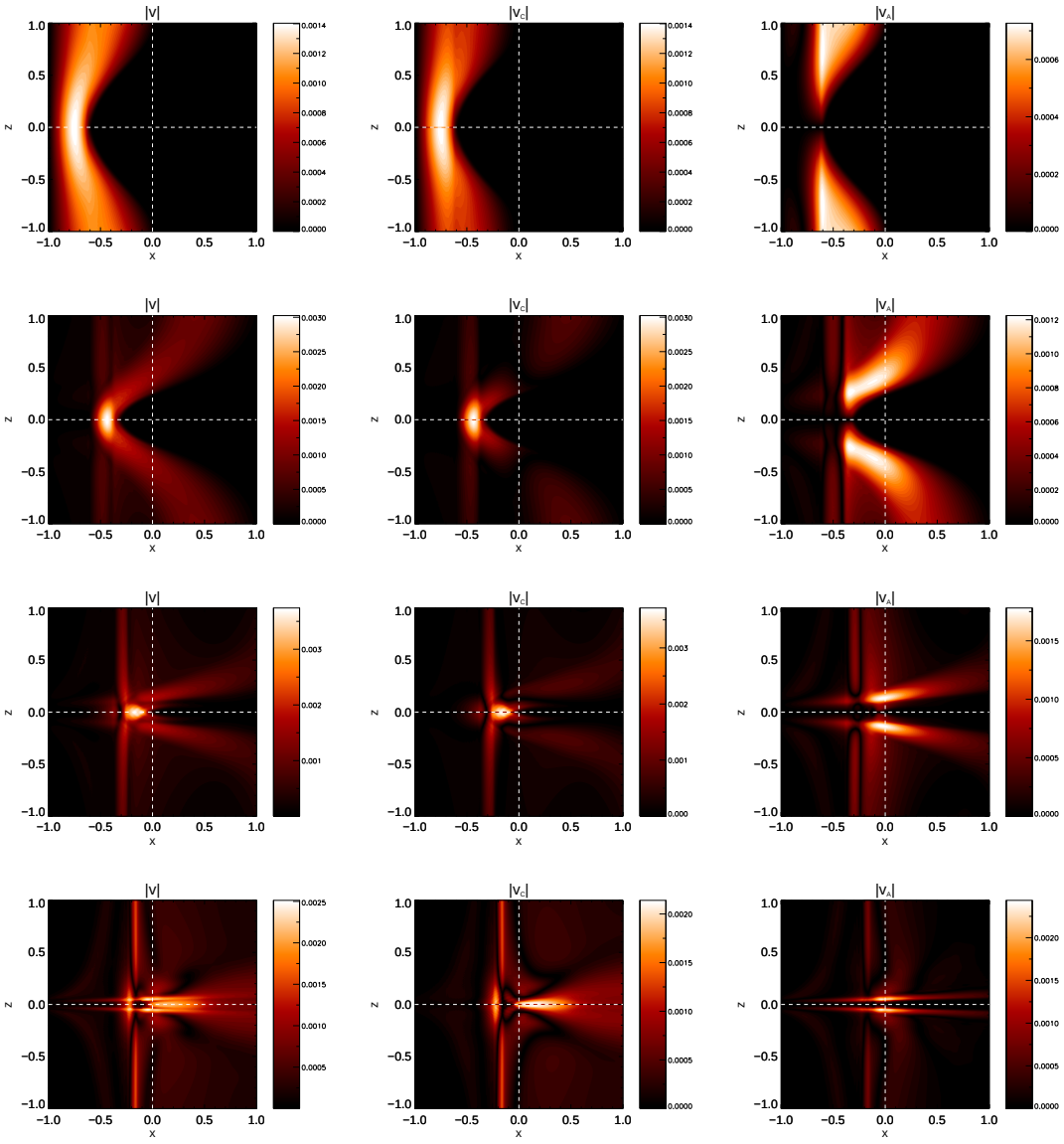

Figure A.3: As Figure A.2 but for the $y = 1/3$ plane. In all components we see signs of multi-mode behaviour (thus, note that v_C and v_A fail to isolate single modes of oscillation).

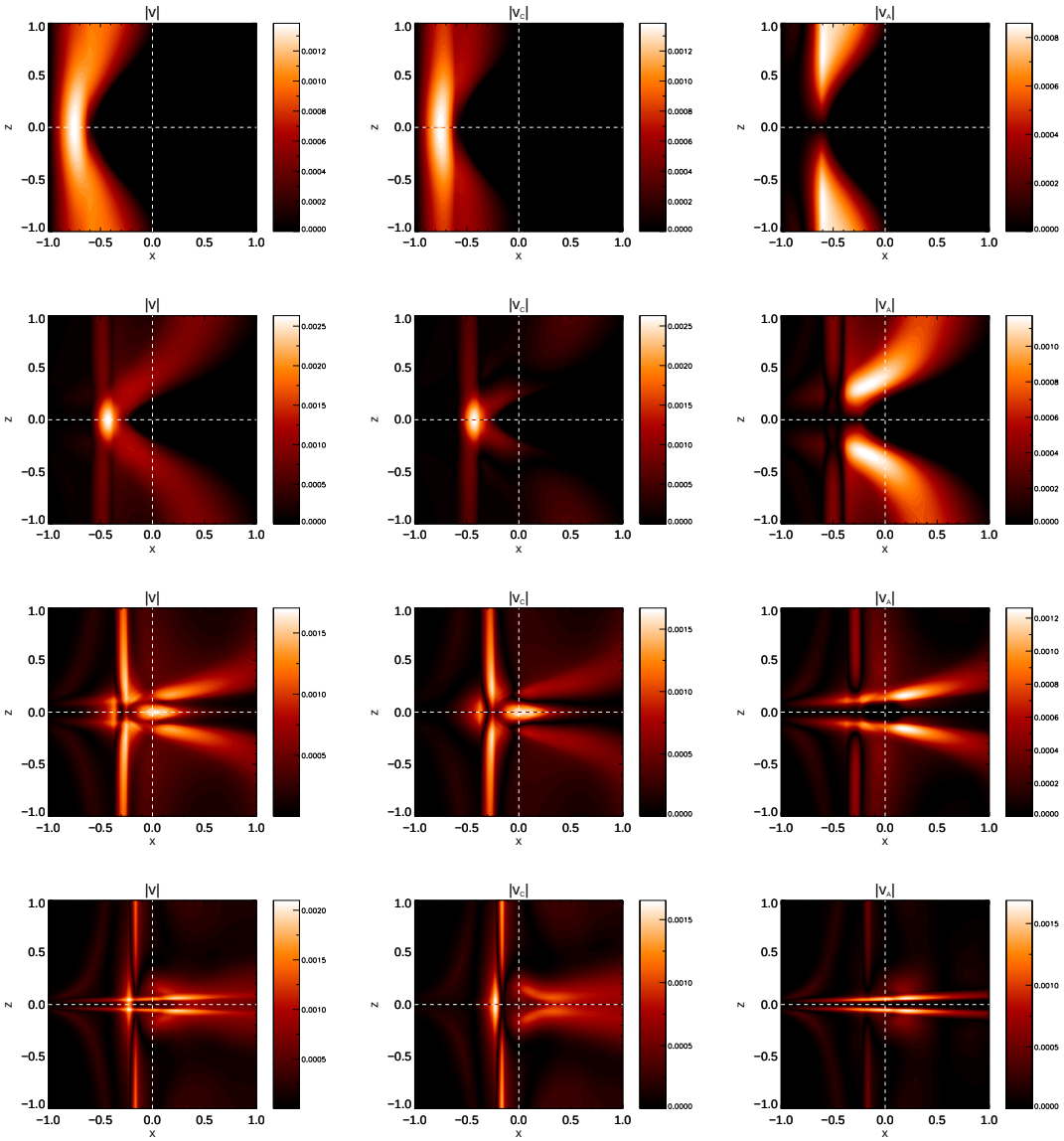

Figure A.4: As Figures A.2 and A.3 for the $y = 1/2$ plane.

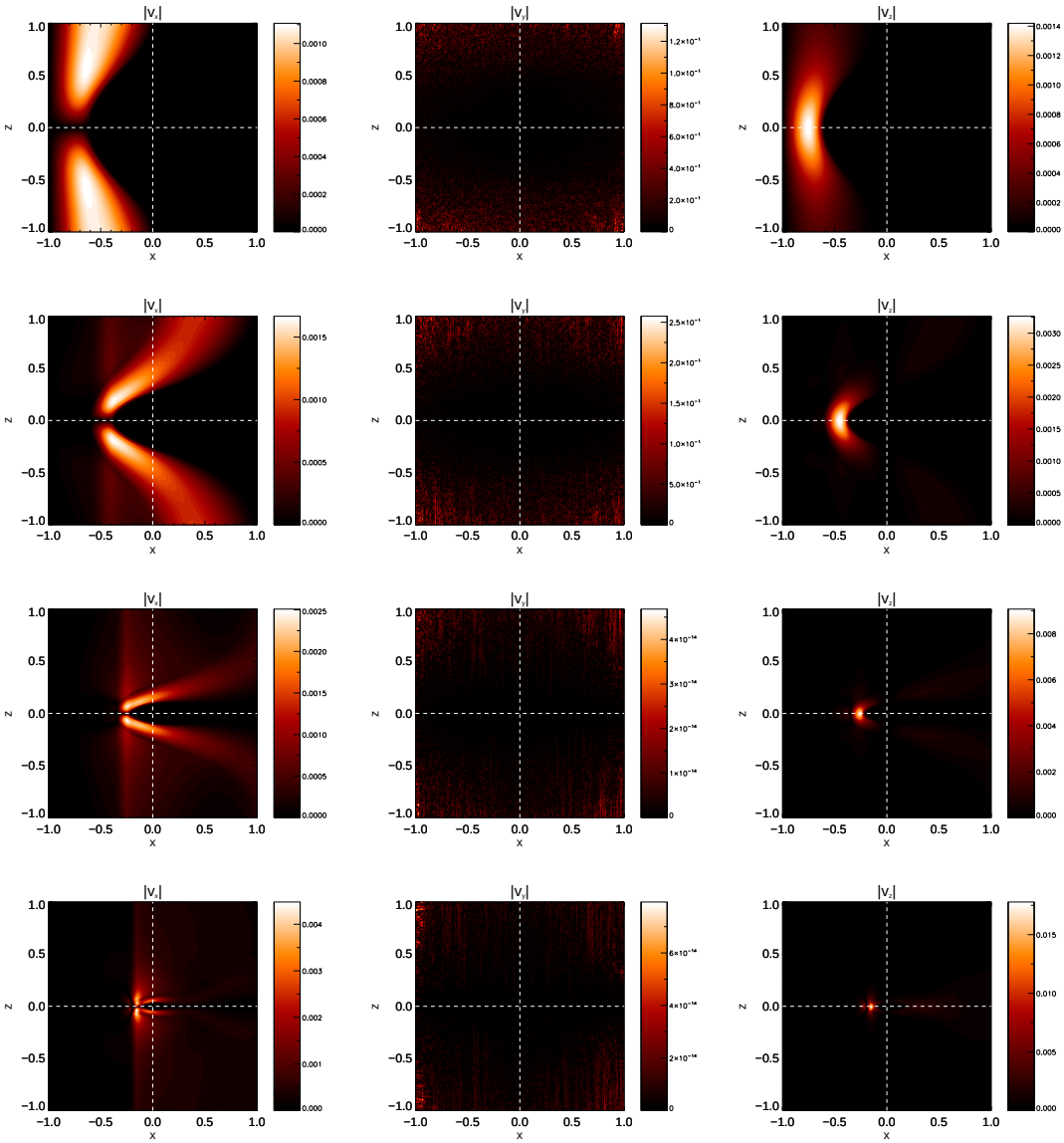

Figure A.5: Cartesian velocity components in the $y = 0$ plane.

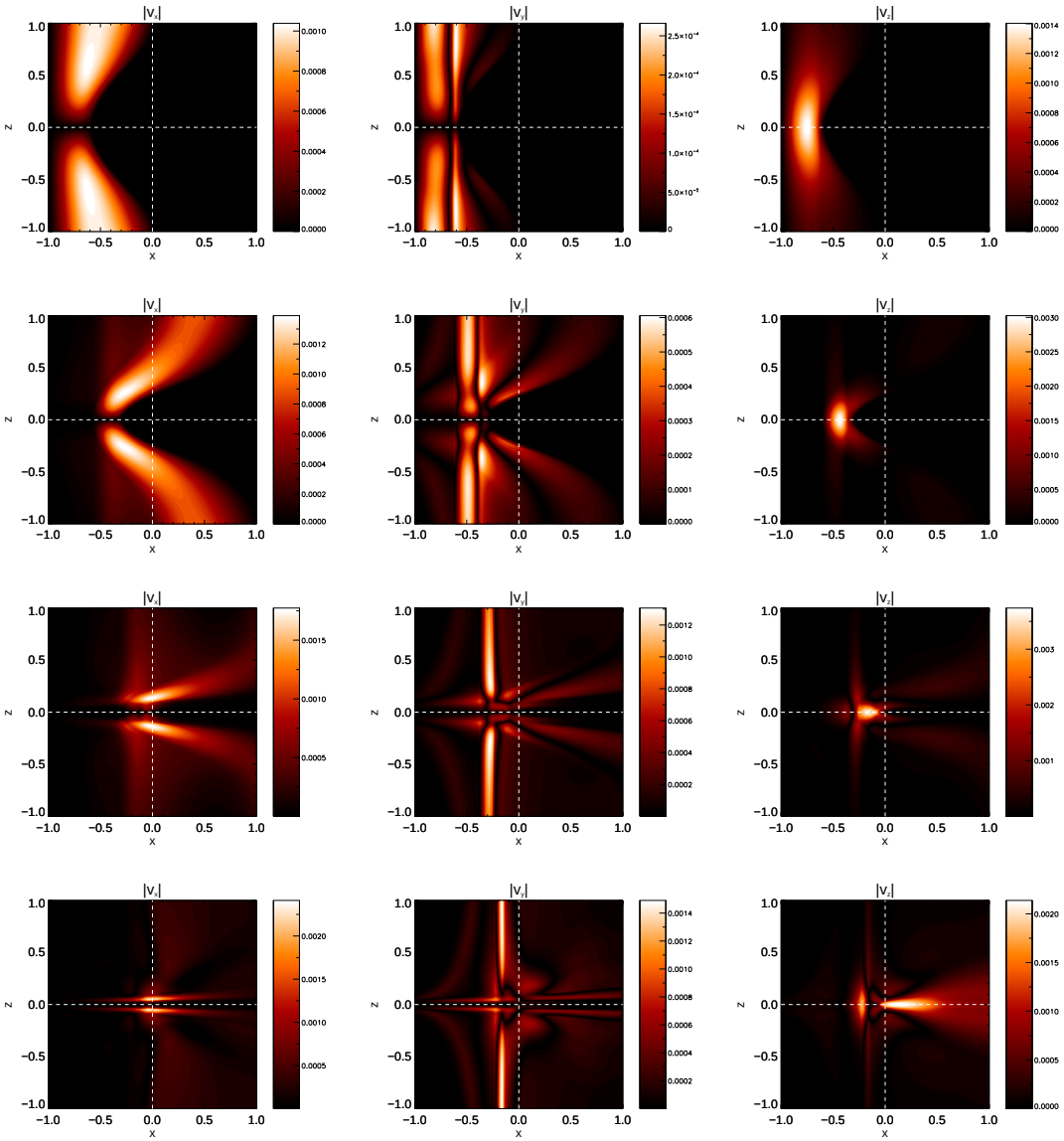

Figure A.6: Cartesian velocity components in the $y = 1/3$ plane.

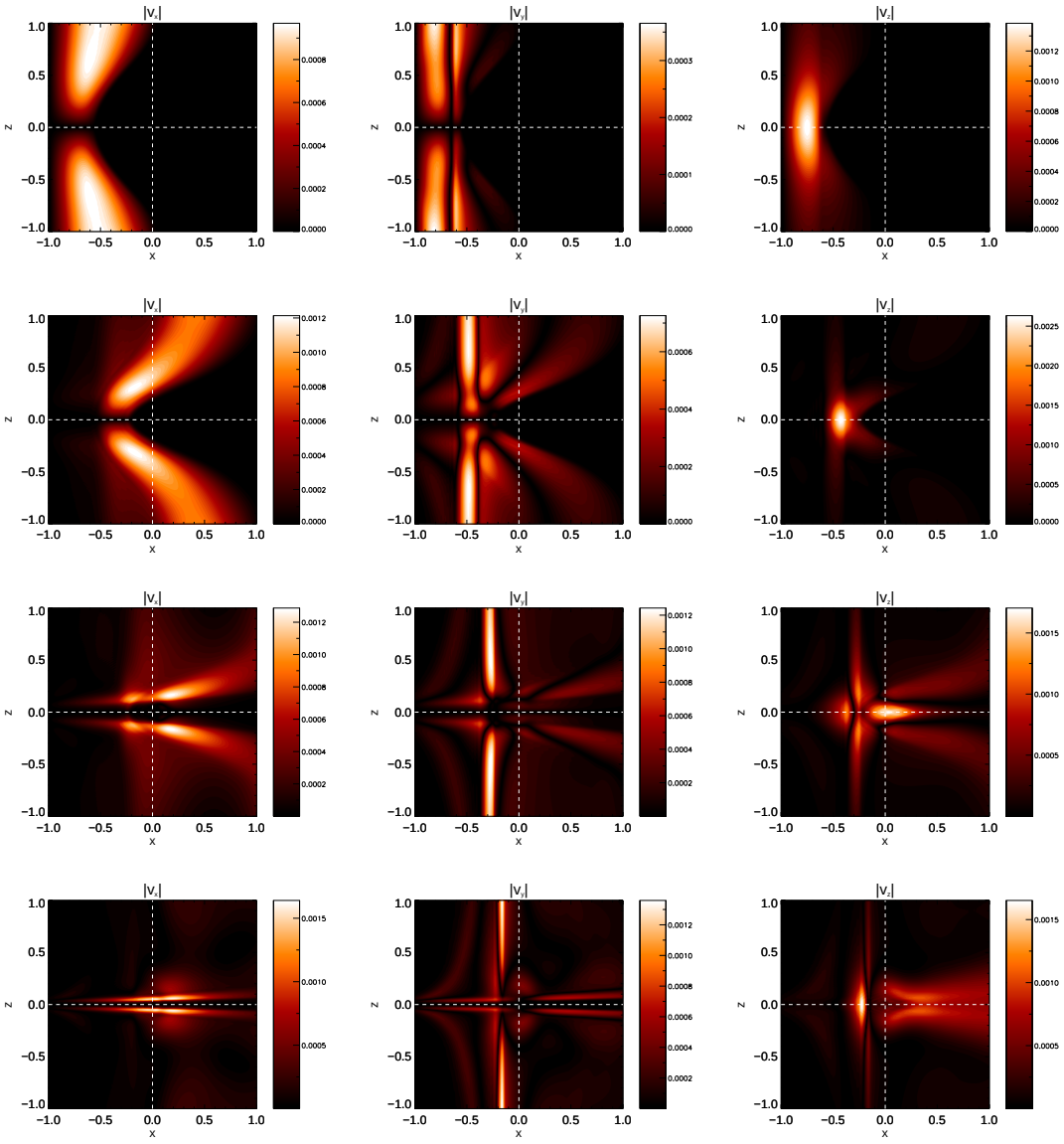

Figure A.7: Cartesian velocity components in the $y = 1/2$ plane.

Appendix B

Recovery of Wave Equations for a Medium with a Homogeneous Magnetic Field and a Transverse Density Profile (Nakariakov et al. 1997)

(Section 4.3)

Here we demonstrate that our general wave equations for 2.5D MHD (Equations 4.4 and 4.5) reduce to those considered in the case of Nakariakov et al. (1997), which considered a unidirectional homogeneous magnetic field structured by a transverse density profile. To do so, we take the field as constant in $\hat{\mathbf{y}}$, *i.e.* $\mathbf{B}_0 = B_0\hat{\mathbf{y}}$, $B_x = 0$, and $B_y = B_0$ and consider density as a function transverse to the field, *i.e.* $\rho_0 = \rho_0(x)$. Thus, the Alfvén and fast wave equations (Equations 4.4 and 4.5) become

$$\left[\frac{\partial^2}{\partial t^2} - c_{\rm A}^2(x)\frac{\partial^2}{\partial y^2}\right] v_z = \frac{\partial N_3}{\partial t} + \frac{B_0}{\mu\rho_0(x)}\frac{\partial N_6}{\partial y} \tag{B.1}$$

$$\left[\frac{\partial^2}{\partial t^2} - c_{\rm A}^2\left(\frac{\partial^2}{\partial x^2} + \frac{\partial^2}{\partial y^2}\right)\right] v_\perp = -B_0\frac{\partial N_1}{\partial t} - c_{\rm A}^2(x)\frac{\partial N_4}{\partial y} + c_{\rm A}^2(x)\frac{\partial N_5}{\partial x}\,. \tag{B.2}$$

The Alfvén wave equation (Equation B.1) is only superficially different from the equation governing the Alfvén wave in Nakariakov et al. (1997), which (in their notation) is

$$\left[\frac{\partial^2}{\partial t^2} - c_{\rm A}^2(x)\frac{\partial^2}{\partial z^2}\right] v_y = \frac{1}{\rho_0(x)}\left(\frac{\partial N_2}{\partial t} + \frac{B_0}{4\pi}\frac{\partial N_5}{\partial z}\right) \tag{B.3}$$

where the apparent difference is due to

- The analysis of Nakariakov et al. (1997) considered $\hat{\mathbf{y}}$ as the invariant direction, hence v_y corresponds to the Alfvén wave (as opposed to v_z in this paper as $\hat{\mathbf{z}}$ is invariant). Additionally, $\partial/\partial y$ corresponds to $\partial/\partial z$ in this paper and Nakariakov et al. (1997) respectively.

- Hence, the nonlinear terms have a different ordering; their N_1, N_2, N_3, N_4, N_5, N_6, N_7 corresponds to our N_1, N_3, N_2, N_4, N_6, N_5, N_7 respectively.
- The nonlinear terms originating in the equation of motion (N_1, N_2, N_3) are not exactly identical. They differ by a factor of ρ_0^{-1} (we divided through the equation of motion by ρ_0 to group it with the nonlinear terms, they left it with the linear terms, e.g., our N_1 is equal to their N_1/ρ_0).
- Nakariakov et al. (1997) use cgs units, as opposed to SI in this thesis.

The fast wave equation of Nakariakov et al. (1997) is

$$\left[\frac{\partial^2}{\partial t^2} - c_{\mathrm{A}}^2(x)\left(\frac{\partial^2}{\partial x^2} + \frac{\partial^2}{\partial y^2}\right)\right] v_x = \frac{1}{\rho_0(x)}\left(\frac{\partial N_1}{\partial t} + \frac{B_0}{4\pi}\frac{\partial N_4}{\partial z} - \frac{B_0}{4\pi}\frac{\partial N_6}{\partial x}\right). \tag{B.4}$$

The above only differs from our fast wave equation as per the aforementioned superficial differences. Additionally, the nonlinear terms (right hand side) differ by a factor of $-B_0$. The explanation is simple- in this case $v_\perp = \mathbf{v}_1 \cdot \hat{\mathbf{z}} \times \mathbf{B}_0 = -B_0 v_x$. Both correspond to a transverse perturbation of the field in this scenario and hence wave equations on either describe the evolution of the Alfvén wave; in a homogeneous field it is simpler to use v_x, for an inhomogeneous field $v_\perp$ is required. Expressing $v_\perp$ in terms of v_x and simplifying reduces our fast wave equation (Equation B.2) to the comparable form

$$\left[\frac{\partial^2}{\partial t^2} - c_{\mathrm{A}}^2(x)\left(\frac{\partial^2}{\partial x^2} + \frac{\partial^2}{\partial y^2}\right)\right] v_x = \frac{\partial N_1}{\partial t} + \frac{B_0}{\mu\rho_0(x)}\frac{\partial N_4}{\partial y} - \frac{B_0}{\mu\rho_0(x)}\frac{\partial N_5}{\partial x}. \tag{B.5}$$

Appendix C

Nonlinear Effects of a Propagating Fast Wave

(Section 4.3)

In Section 4.3 we performed a source-term analysis to consider the nonlinear effects caused by a propagating Alfvén wave. Here, we perform a similar analysis to consider some of the nonlinear effects of a propagating fast magnetoacoustic wave.

We can set $v_z = 0$ and $b_z = 0$ and place restrictions on v_x, v_y, b_x, and b_y that correspond to $v_\parallel = b_\parallel = 0$, $v_\perp \neq 0$, $b_\perp \neq 0$ and $\rho_1 \neq 0$ to consider the ponderomotive effects caused by a fast wave, yielding:

$$\left[\frac{\partial^2}{\partial t^2} - c_{\rm A}^2\left(\frac{\partial^2}{\partial x^2} + \frac{\partial^2}{\partial y^2}\right)\right] v_\perp = B_x\frac{\partial N_2}{\partial t} - B_y\frac{\partial N_1}{\partial t} + c_{\rm A}^2\left(\frac{\partial N_5}{\partial x} - \frac{\partial N_4}{\partial y}\right) \neq 0 \quad \text{(C.1)}$$

$$\frac{\partial^2 v_z}{\partial t^2} = 0 \quad \text{(C.2)}$$

$$\begin{aligned}\frac{\partial^2 v_\parallel}{\partial t^2} &= \frac{1}{\mu\rho_0}\frac{\partial}{\partial t}\left\{B_x b_y\left[\left(\frac{\partial b_x}{\partial y}\right)_{\rm T} - \left(\frac{\partial b_y}{\partial x}\right)_{\rm P}\right] + B_y b_x\left[\left(\frac{\partial b_y}{\partial x}\right)_{\rm T} - \left(\frac{\partial b_x}{\partial y}\right)_{\rm P}\right]\right\} \\ &= \frac{B}{\mu\rho_0}\frac{\partial}{\partial t}\left[b_\perp\left(\frac{\partial b_x}{\partial y} - \frac{\partial b_y}{\partial x}\right)\right] \quad \text{(C.3)}\end{aligned}$$

where subscripts $\rm T$ and $\rm P$ indicate whether a term is contributed by magnetic tension or magnetic pressure respectively, and $b_\perp = \mathbf{b}\cdot\hat{\mathbf{z}}\times\hat{\mathbf{B}}_0$ is the transverse perturbation of the magnetic field. The key result here is that *Equation (C.2) shows that the fast wave does not interact with the Alfvén wave on any level; linear or nonlinear in a 2.5D medium.*

However, Equation (C.3) contains source terms, thus a propagating fast wave does cause nonlinear field-aligned disturbances that will cause, in certain circumstances, nonlinear Lorentz force coupling (via both nonlinear magnetic pressure/ponderomotive force and nonlinear magnetic tension). Departing from the $\beta = 0$ case, these source terms remain,

i.e. the magnetoacoustic modes are coupled linearly by gas-pressure gradients, and nonlinearly by the Lorentz force.

Equation (C.1) shows that such an initial fast wave undergoes self interaction. In this case, this is due to a combination of nonlinear Lorentz force, convective acceleration (contained within N_1 and N_2 which are permitted to be non-zero) and nonlinear induction (N_4 and N_5). Interestingly, the nonlinear induction term can be rewritten as

$$c_{\mathrm{A}}^2 \left(\frac{\partial N_5}{\partial x} - \frac{\partial N_4}{\partial y} \right) = -c_{\mathrm{A}}^2 \left(\frac{\partial^2}{\partial x^2} + \frac{\partial^2}{\partial y^2} \right) \mathbf{v} \cdot \hat{\mathbf{z}} \times \mathbf{b}$$

i.e. the nonlinear induction term is effectively of the same form as that of the linear motion due to velocity perturbations across the equilibrium field, however is instead motion due to perturbations across the induced magnetic field (though at the equilibrium, not induced, Alfvén speed).

Finally, we note that although there are no slow waves in the $\beta = 0$ case, the nonlinear source term due to the Lorentz force acting upon the Alfvén wave (the right hand side of Equation (C.2)) would remain unchanged for $\beta \neq 0$. This source term remains zero if an Alfvén wave is initially absent. Thus, the nonlinear Lorentz force does not facilitate slow to Alfvén mode conversion either. Hence, the analysis shows that for any 2.5D MHD scenario that that there is a one-way, nonlinear mode conversion mechanism between the Alfvén and (both) magnetoacoustic modes, that will become manifest when a phase mixed/ dispersive Alfvén wave (via propagating in the vicinity of an inhomogeneous Alfvén-speed profile) assumes a geometry that exerts a non-zero average force over its period perturbing along and across the magnetic field.

Appendix D

Analytical Description of Section 4.4

Here we present *preliminary* results which aim to analytically describe the nonlinear effects arising due to the ponderomotive force in the phase-mixing simulations presented in Section 4.4 and Nakariakov et al. (1997).

We wish to evaluate the ponderomotive effects of the individual pulses (i.e., away from the separation region) and so take the form of v_z and b_z to be given as

$$v_z = AF\left(\frac{y \pm c_A\left(x\right)t}{a}\right) \qquad b_z = \pm\sqrt{\mu\rho_0}\, v_z \tag{D.1}$$

which corresponds to an arbitrary pulse of form F that propagates parallel or antiparallel to the field without (i.e., it is rigidly translated without self-moderation or dissipation). We proceed by attempting to solve equations (4.12) and (4.13), i.e.,

$$\frac{\partial v_\perp}{\partial t} = -\frac{1}{\mu\rho_0}\nabla_\perp\left(\frac{b_z^2}{2}\right) \tag{D.2}$$

$$\frac{\partial v_\parallel}{\partial t} = -\frac{1}{\mu\rho_0}\nabla_\parallel\left(\frac{b_z^2}{2}\right) \tag{D.3}$$

for the given form of b_z. We first evaluate the longitudinal effects (here, $v_\parallel = v_y$) before proceeding to the transverse effects (here, $v_\perp = v_x$)

Longitudinal Effects

The longitudinal effect of the ponderomotive force can be easily determined as follows, noting that ρ_0 and c_A do not vary along the field

$$\frac{\partial v_\parallel}{\partial t} = -\frac{A^2}{2}\nabla_\parallel\left(F^2\right)$$

$$
\begin{aligned}
&= -\frac{A^2}{2} 2FF' \nabla_{\parallel} \left(\frac{y \pm c_A(x)\, t}{a} \right) \\
&= -\frac{A^2}{2} 2FF' \frac{1}{a} \\
&= \mp \frac{A^2}{2c_A} \frac{\partial F^2}{\partial t} \\
v_{\parallel} &= \mp \frac{A^2}{2c_A} F^2 \,, \qquad \text{(D.4)}
\end{aligned}
$$

where we note

$$
\frac{a}{c_A} \frac{\partial F^2}{\partial t} = \pm 2FF' \qquad \text{(D.5)}
$$

Equation D.4 is exactly as that calculated of the 1.5D, homogeneous case (c.f. equation E.9), where it is opposite-signed (to v_z) for anti-parallel propagation and same-signed for parallel propagation (along the magnetic field).

Transverse Effects

Here, we proceed similarly

$$
\begin{aligned}
\frac{\partial v_{\perp}}{\partial t} &= -\frac{1}{\mu\rho_0} \nabla_{\perp} \left(\frac{b_z^2}{2} \right) \\
&= -\frac{A^2}{2\rho_0} \nabla_{\perp} \left(\rho_0 F^2 \right) \\
&= -\frac{A^2}{2\rho_0} \left[\rho_0 \nabla_{\perp} \left(F^2 \right) + F^2 \nabla_{\perp} \left(\rho_0 \right) \right] \\
&= -\frac{A^2}{2\rho_0} \left[\rho_0 2FF' \nabla_{\perp} \left(y \pm c_A(x)\, t \right) + F^2 \nabla_{\perp} \left(\rho_0 \right) \right] \\
&= -\frac{A^2}{2\rho_0} \left[\pm \rho_0 2FF' \nabla_{\perp} \left(c_A \right) t + F^2 \nabla_{\perp} \left(\rho_0 \right) \right] \\
&= -\frac{A^2}{2\rho_0} \left[\frac{\rho_0}{c_A} \frac{\partial F^2}{\partial t} \nabla_{\perp} \left(c_A \right) t + F^2 \nabla_{\perp} \left(\rho_0 \right) \right] \\
v_{\perp} &= -\frac{A^2}{2\rho_0} \left[\frac{\rho_0}{c_A} \nabla_{\perp} \left(c_A \right) \int_0^t \frac{\partial F^2}{\partial t} t \, \mathrm{d}t + \nabla_{\perp} \left(\rho_0 \right) \int_0^t F^2 \, \mathrm{d}t \right] \\
&= -\frac{A^2}{2\rho_0} \left[\frac{\rho_0}{c_A} \nabla_{\perp} \left(c_A \right) \left\{ F^2 t - \int_0^t F^2 \, \mathrm{d}t \right\} + \nabla_{\perp} \left(\rho_0 \right) \int_0^t F^2 \, \mathrm{d}t \right] \\
&= -\frac{A^2}{2\rho_0} \left[-\frac{1}{2} \nabla_{\perp} \left(\rho_0 \right) \left\{ F^2 t - \int_0^t F^2 \, \mathrm{d}t \right\} + \nabla_{\perp} \left(\rho_0 \right) \int_0^t F^2 \, \mathrm{d}t \right] .
\end{aligned}
$$

Thus

$$v_\perp = +\frac{A^2}{4\rho_0}\nabla_\perp(\rho_0)\left[F^2 t - 3\int_0^t F^2\,\mathrm{d}t\right], \tag{D.6}$$

where we exploited

$$\nabla_\perp(c_A) = -\frac{c_A}{2\rho_0}\nabla_\perp(\rho_0) \tag{D.7}$$

which is consistent with cases where $\nabla_\perp(B_0) = 0$ such as Section. 4.4.

Comparison to Numerical Solutions

Here, we compare forms of $v_\perp$ and $v_\parallel$ derived in the above way to nonlinear numerical results from LARE2D. For clarity, we actually consider a simplified case of the nonlinear phasemixing experiment. The equilibrium variables for $\rho_0 = \rho_0(x)$ and $\mathbf{B}_0$ are as per Section 4.4 with the initial conditions

$$b_z = A\mathrm{sech}^2(y/a) \quad v_z = -b_z/\sqrt{\mu\rho_0} \tag{D.8}$$

which corresponds to a pulse that propagates in the positive direction of the field (due to opposite signs) which initially has no transverse gradients (and hence, cross-field ponderomotive force). This difference in the initial variation of b_z across the field will mean that equations (D.4) and (D.6) are modified slightly. The explicit specification of both the field and velocity perturbation is also a simplification of that in Section 4.4 in that the crossing/separation of two oppositely directed pulses is avoided. We also specify its longitudinal daughter disturbance at $t = 0$

$$v_\parallel = v_y = +\frac{v_z^2}{2c_A}, \tag{D.9}$$

and the associated density enhancement[1]

$$\begin{aligned}\frac{\partial\rho_1}{\partial t} &= -\rho_0\frac{\partial}{\partial y}v_y \\ &= -\rho_0\frac{\partial}{\partial y}\frac{A^2F^2}{2\mu\rho_0 c_A} \\ &= -\rho_0\frac{A^2}{2\mu\rho_0 c_A}\left(\frac{2FF'}{a}\right)\end{aligned}$$

[1] see Appendix E for further details of calculating the density enhancement

$$
\begin{aligned}
&= +\rho_0 \frac{A^2}{2\mu\rho_0 c_A}\left(\frac{1}{c_A}\frac{\partial F^2}{\partial t}\right) \\
\rho_1 &= +\rho_0 \frac{A^2}{2\mu\rho_0 c_A}\left(\frac{1}{c_A}\int \frac{\partial F^2}{\partial t} dt\right) \\
&= +\frac{\rho_0}{c_A}\frac{A^2 F^2}{2\mu\rho_0 c_A} \\
&= +\frac{\rho_0}{c_A^2} v_z^2 \,. \qquad \text{(D.10)}
\end{aligned}
$$

For these modified initial conditions, the calculated form of $v_\perp$ is as follows

$$
\begin{aligned}
\frac{\partial v_\perp}{\partial t} &= -\frac{1}{\mu\rho_0}\nabla_\perp\left(\frac{b_z^2}{2}\right) \\
&= -\frac{A^2}{2\mu\rho_0}\nabla_\perp\left(F^2\right) \\
&= -\frac{A^2}{2\mu\rho_0}\left[2FF'\nabla_\perp\left(\frac{y - c_A(x)\,t}{a}\right)\right] \\
&= \frac{A^2}{2\mu\rho_0}\left[\nabla_\perp\left(c_A\right) 2FF'\frac{t}{a}\right] \\
&= -\frac{A^2}{2\mu\rho_0 c_A}\nabla_\perp\left(c_A\right)\frac{\partial F^2}{\partial t} t \\
v_x = v_\perp &= -\frac{A^2}{2\mu\rho_0 c_A}\nabla_\perp\left(c_A\right)\left[F^2 t - \int_0^t F^2 dt\right] \qquad \text{(D.11)}
\end{aligned}
$$

where, as $F = \mathrm{sech}^2$, the integral is

$$
\int_0^t F^2 \mathrm{d}t = -\frac{a}{3c_A}\left[(2+F)\tanh\left(\frac{y - c_A t}{a}\right)\right]_0^t . \qquad \text{(D.12)}
$$

The simulation evolves as expected, with the Alfvén wave undergoing phase mixing as it propagates, with its manifestation in b_z and v_z shown in Figure D.1. Here, we can clearly see that initially there is no transverse nonlinear magnetic pressure, as b_z is uniform at $t = 0$.

Figure D.2 shows a comparison of the nonlinear daughter disturbance present in the simulation with equation D.9, which shows excellent agreement everywhere, bar a slight, static disturbance at the initial position. Likewise, D.3 compares the analytical and numerical solution for the density perturbation ρ_1, where id depicts ρ_1 along the y-direction at positions $x = -5, 0, 5$ (regions of lower constant Alfvén speed, phase-mixing, and higher constant Alfvén speed). The numerical and analytical forms disagree in two cases.

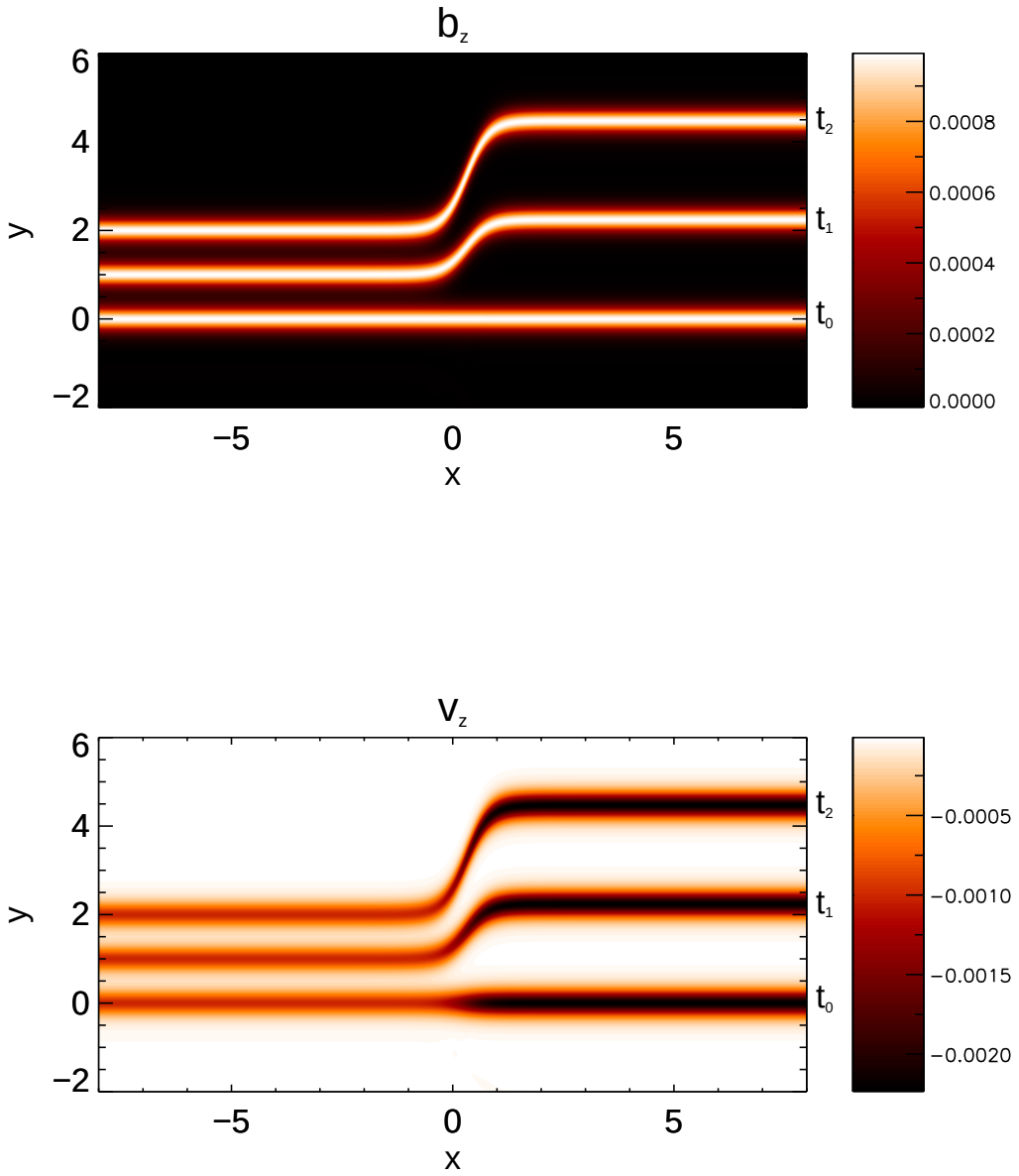

Figure D.1: Contours showing the evolution of the Alfvén wave in b_z and v_z for times $t_0 = 0$, $t_1 = 1.0$ and $t_2 = 2.0$ (the figure shows a superposition of v_z or b_z for the three times.) Due to the variable Alfvén speed, the pulse undergoes phase mixing and develops transverse gradients in the region of inhomogeneity.

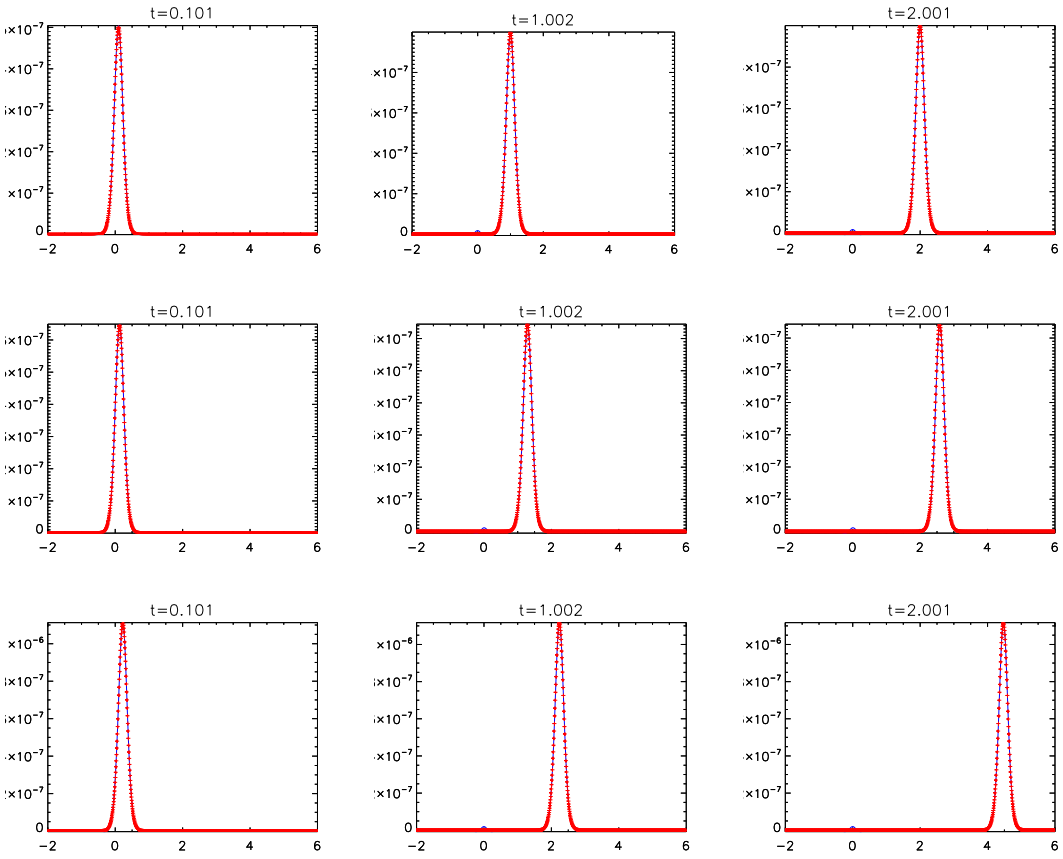

Figure D.2: Comparison of the numerical (blue) and analytical solution (red crosses) for the longitudinal daughter disturbance v (v_y) for $x = -5$ (top), $x = 0$ (center) and $x = 5$ (bottom). Bar a small perturbation associated with the initial condition near $y = 0$, the agreement is excellent everywhere.

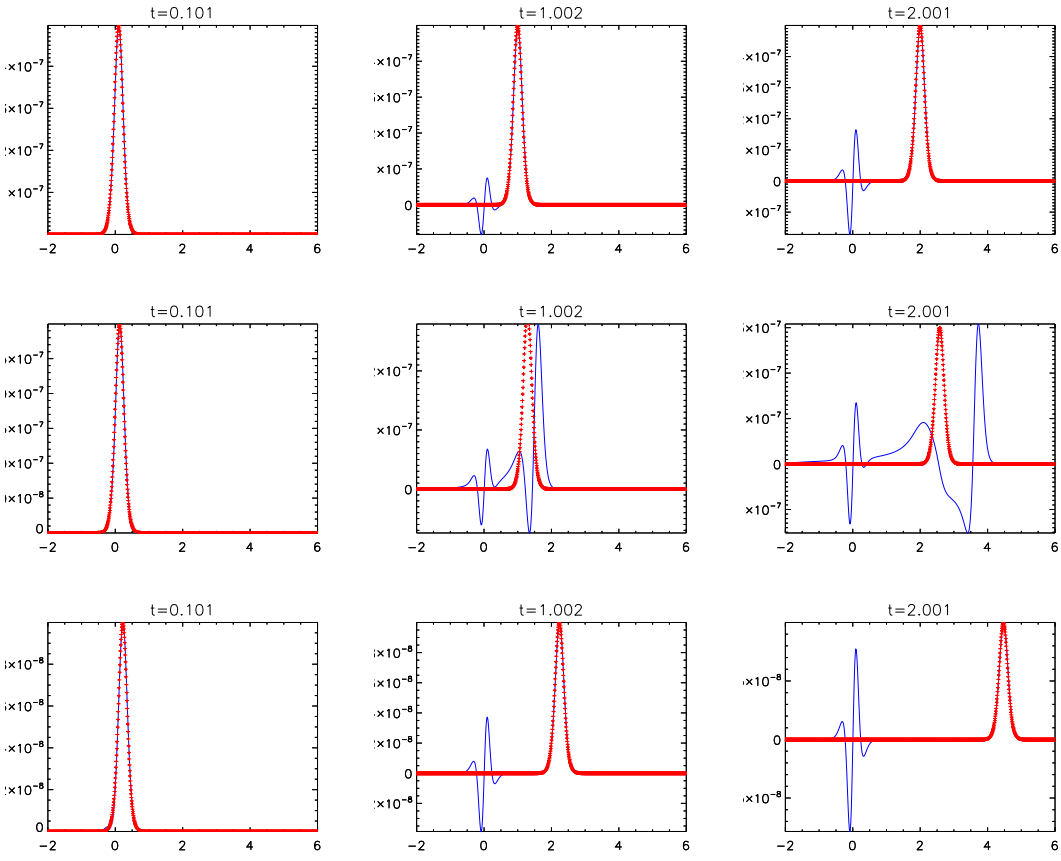

Figure D.3: Comparison of the numerical (blue) and analytical solution (red crosses) for ρ_1 for $x = -5$ (top), $x = 0$ (center) and $x = 5$ (bottom). After $t = 0$, a density instability develops at the initialisation site as a consequence of the initial conditions. Discounting the instability, away from the phase mixing regions the agreement is excellent. In regions of phasemixing, the given form of ρ_1 is inadequate as it does not account for contributions from the v_x components that arise due to the cross-field ponderomotive force.

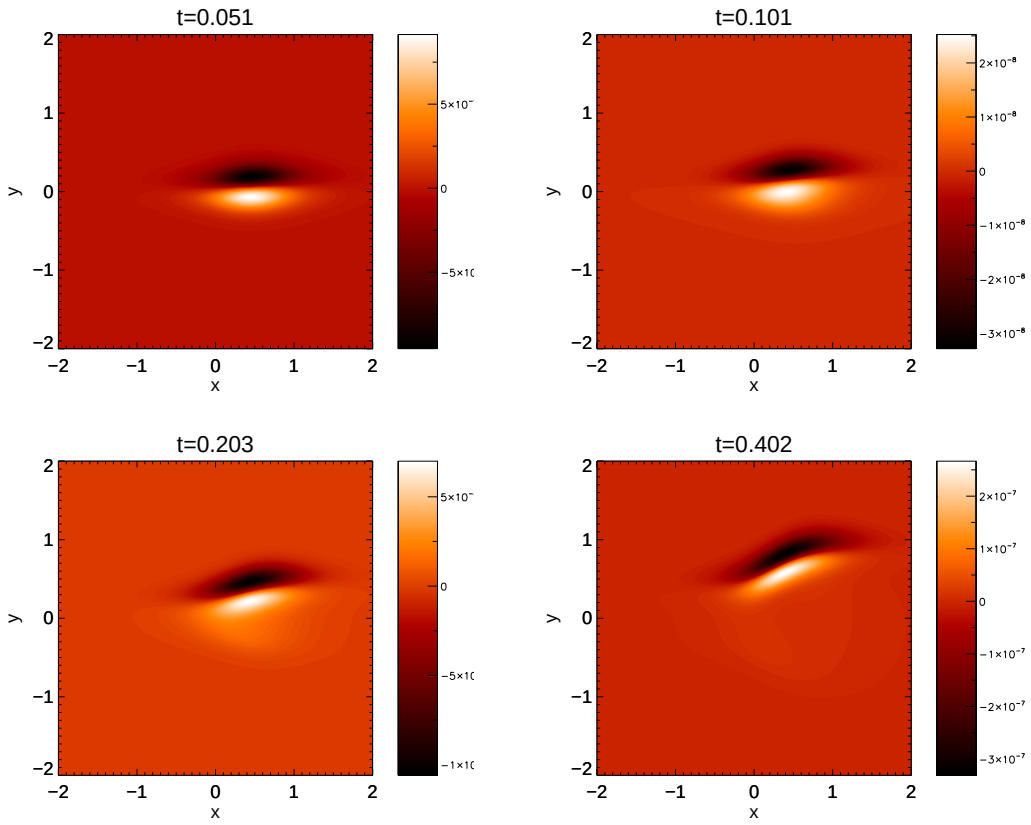

Figure D.4: Contours of the transverse velocity compoent v_x from the numerical solution.

Firstly, a density instability develops at the initialisation site. This instability does not impact on the main dynamics of the Alfvén wave and is associated with the static disturbance in v_y (the nature of this instability is explored in Appendix E). In the phase mixing region ($x = 0$), the form of ρ_1 is not adequately described by equation D.9 as it does not account for contributions due to v_x (fast waves/ transverse ponderomotive effects). Otherwise, the two agree outside of the phase mixing regions. The derived form of $v_{\parallel}$ (and ρ_1 away from regions where v_x arises) is expected to hold until late times where the cubic self-moderation of the Alfvén wave occurs.

Figure D.4 shows the evolution of v_x ($v_\perp$) according to the numerical solution and Figure D.5 shows the evolution according to equation (D.11). On visual inspection, we see that despite initial similarities that the analytical and numerical solutions begin to deviate after relatively short times. At later times still as shown in Figure (D.6), we see that the analytical solution completely breaks down and fails to adequately describe v_x even in the cospatial region (outside of the cospatial region, signals in v_x could be those of fast waves). There are two obvious discrepancies, firstly the 'accumulation' term (that involving a hyperbolic tangent function) of equation (D.11) leads to a smearing effect

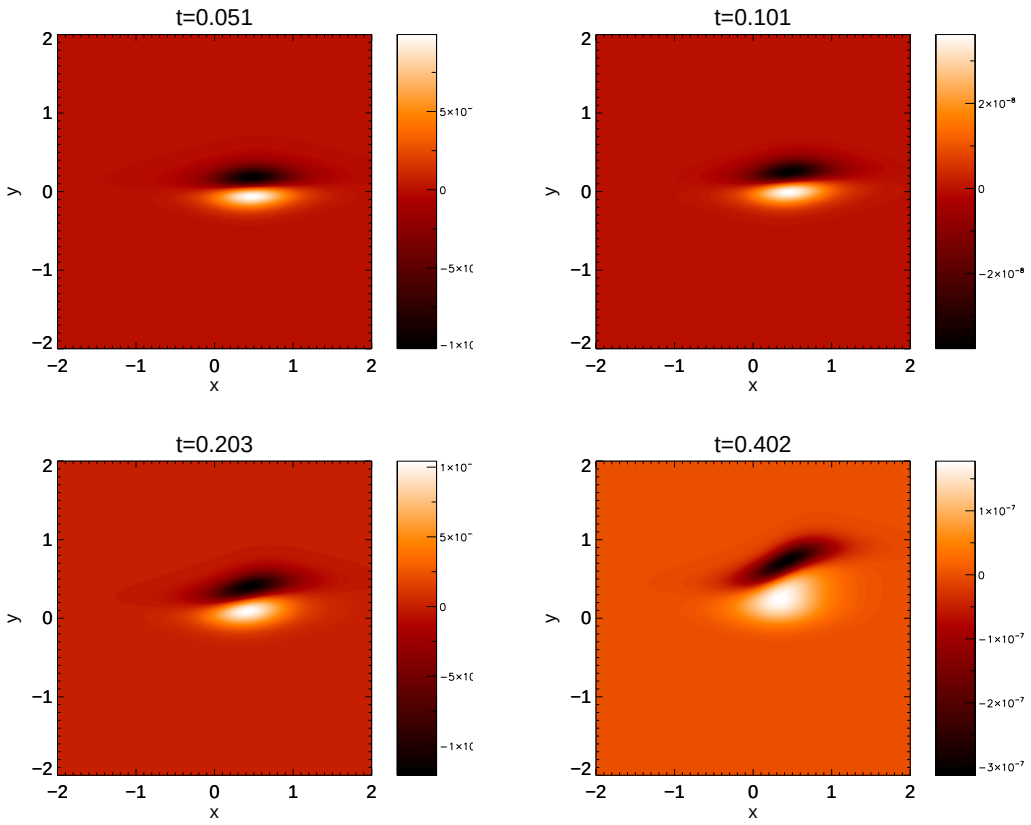

Figure D.5: Contours of the transverse velocity component v_x from the analytical solution. Note the increasing disagreement with Figure D.4 as time evolves.

along the pulses path. Secondly the secular growth term $F^2 t$ suggests continuous linear growth in time with maxima at the region of largest gradient (due to its product with $\nabla_\perp c_A$), however at $t = 2$ for the numerical solution we see that at later times the maxima is concentrated around the boundaries of the inhomogeneous regions. The growth rate of the maximum absolute value of v_x according to the analytical form and the simulations is shown in Figure D.7.

We can compare the analytical and numerical solution for v_x in more detail by considering cuts in the y-direction. We consider slices at $x = -1, 0, 1$, i.e. the boundaries and center of the inhomogeneous region, which are shown in figures D.8, D.9 and D.10 respectively. We see good agreement only at early times, and that at varying times for differing x (but no more than around $t = 0.1$) the solutions begin to disagree where we see a discrepancy in both geometry and amplitude.

Thus, we have found that the longitudinal effects due the ponderomotive force can be well described by simply solving a simple force equation consisting of only the source term

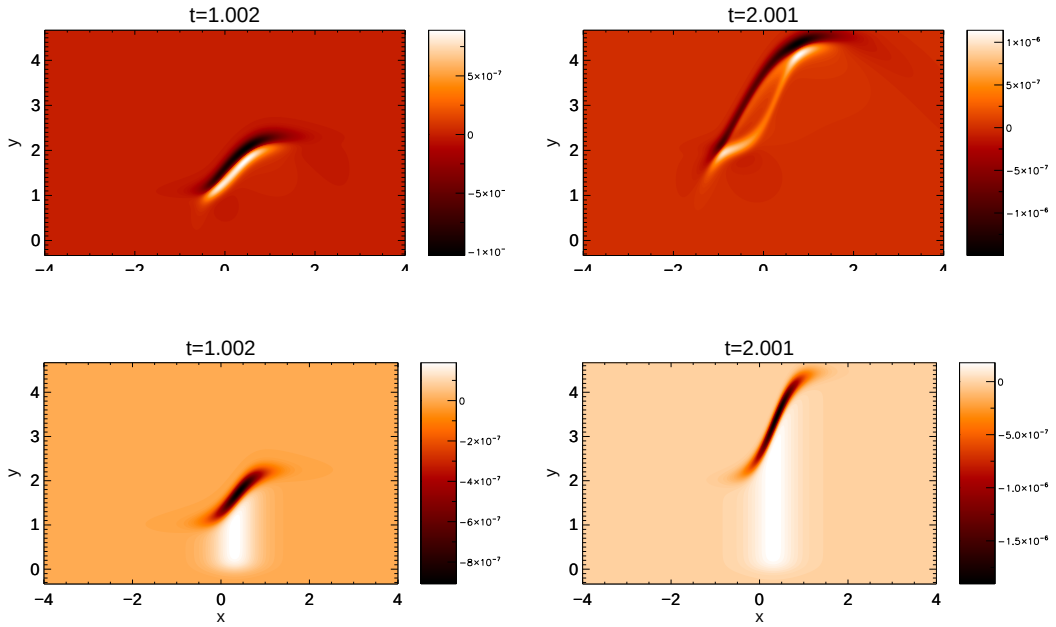

Figure D.6: Contours showing the comparison of numerical (top) and analytical (bottom) v_x at later times. Note the qualitative and quantitative differences.

due to nonlinear magnetic pressure for all times. We also find that the same approach for the transverse effects is only accurate for a short time as the transverse gradients develop.

After this short time, competing terms arise in the equation of motion. The equations (D.1) and (D.3) on which these analytical solutions are derived arise in a 'source-term' analysis whereby the assumption of $v_{\parallel} = v_{\perp} = 0$ suppresses other terms in the equation of motion. This is valid for all times for the longitudinal case, as in $\beta = 0$, the nonlinear magnetic pressure is the only term acting along the field in the equation of motion. However, for $v_{\perp}$, this can only be valid for times near the initialisation as once $v_{\perp} \neq 0$ competing terms from the equation of motion arise (i.e., the perturbation is not only accelerated and decelerated by the ponderomotive force, but can also be propagated as a fast wave). Thus, the precise form of the transverse daughter (the signal in $v_{\perp}$ which is not free to propagate away from the Alfvén wave) is more complicated than in the longitudinal case; it form is not only dependent on the subsequent acceleration and deceleration due of the ponderomotive force along an Alfvén wave's path, but is also dependent the propagation of excited v_x during the Alfvén wave's passage within the cospatial region. In a sense, the transverse daughter disturbances can be thought of as *trapped fast waves*.

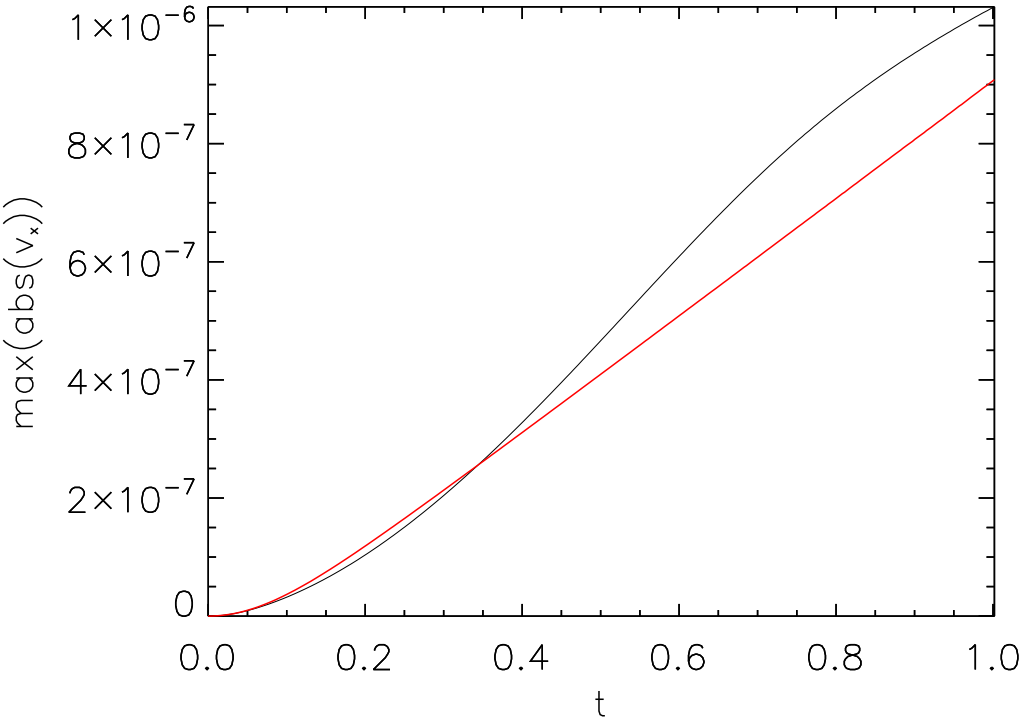

Figure D.7: The growth rate of the greatest perturbation of the transverse velocity component for the analytical (red) and numerical solution (black).

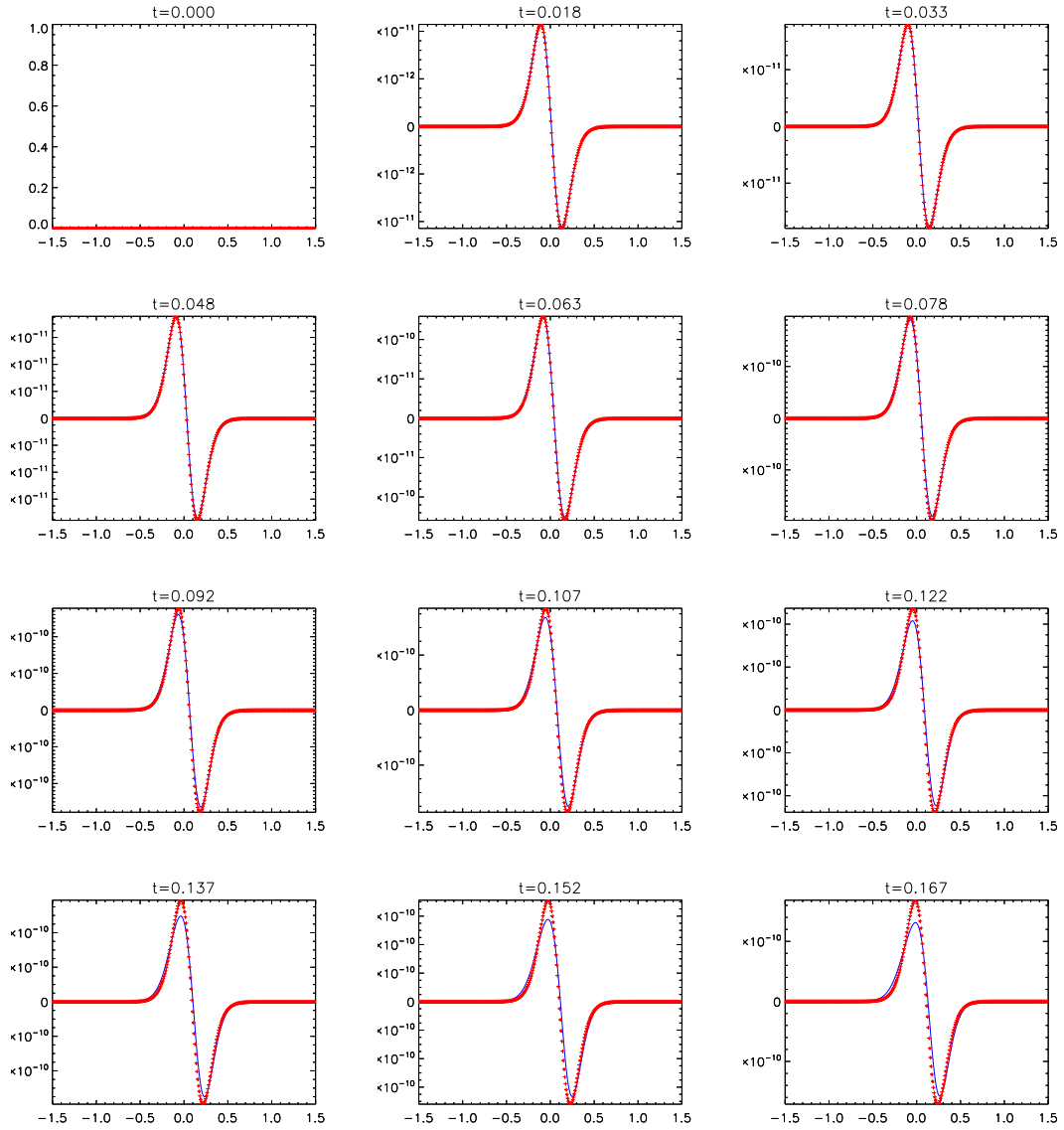

Figure D.8: A comparison of the analytical (blue) and numerical (red crosses) form of v_x near the lower boundary of the phasemixing region ($x = -1$). The two agree only during the initial stages of the development of v_x.

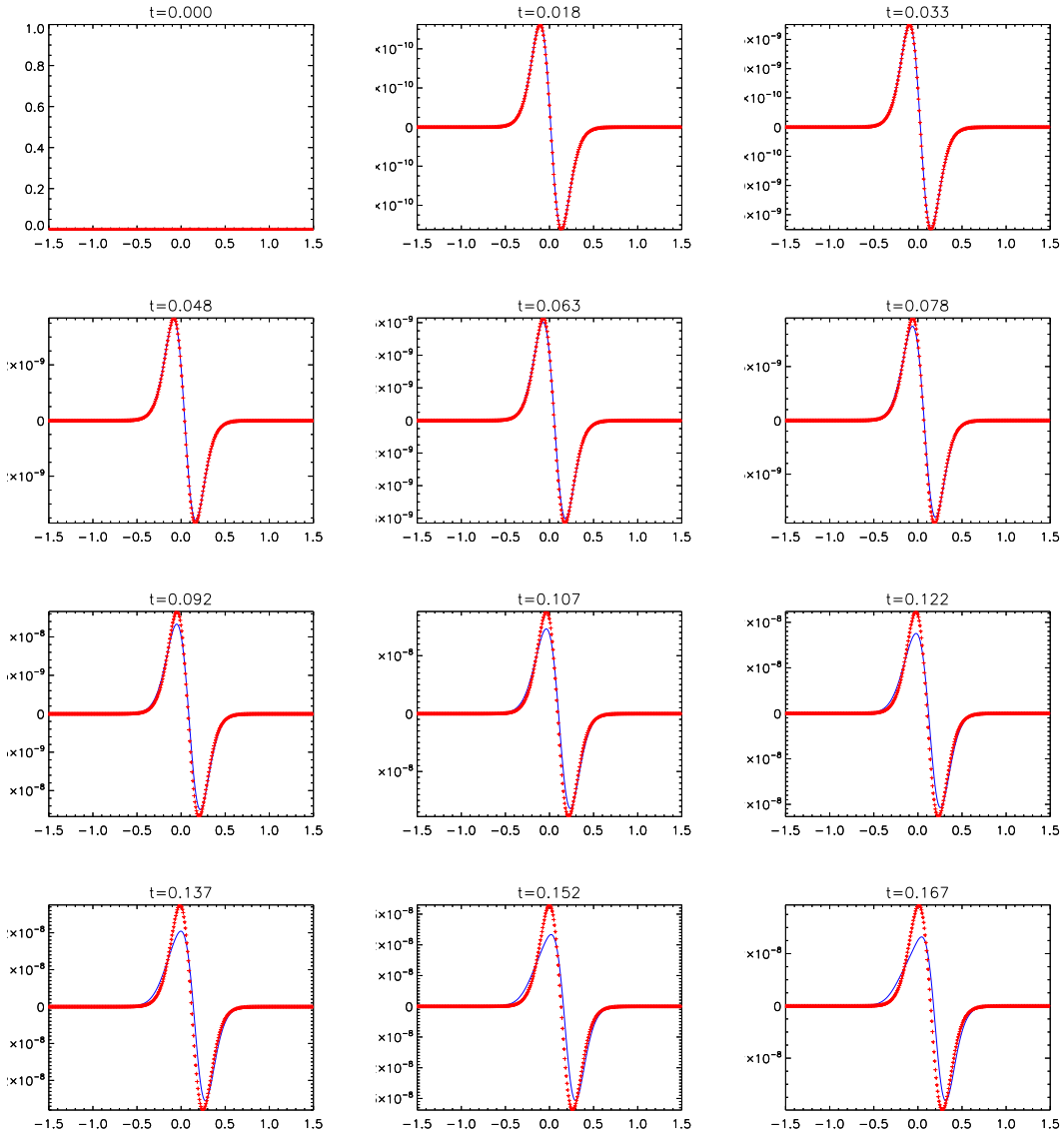

Figure D.9: A comparison of the analytical (blue) and numerical (red crosses) form of v_x near the center of the phasemixing region ($x = 0$). The two agree only during the initial stages of the development of v_x.

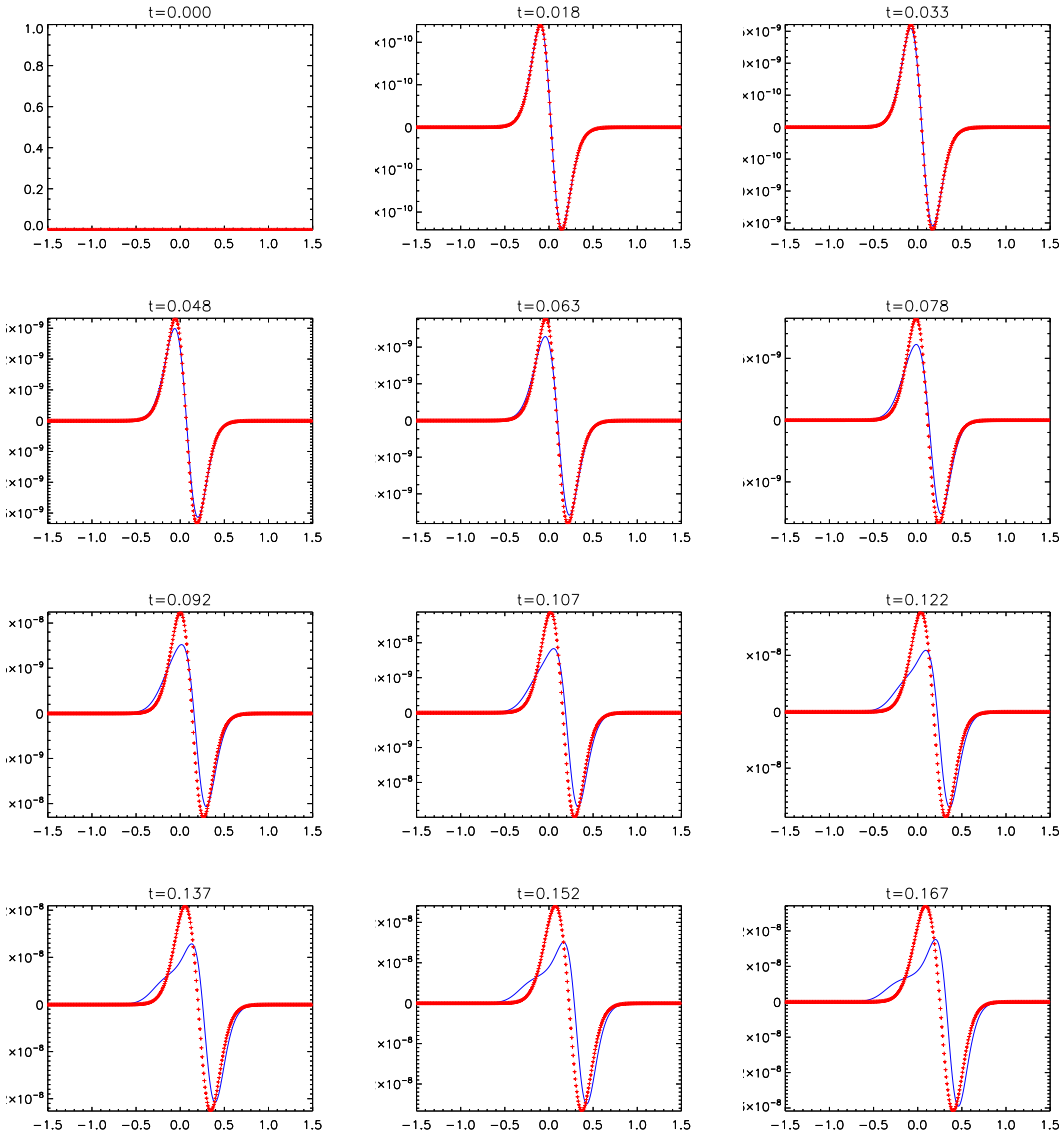

Figure D.10: A comparison of the analytical (blue) and numerical (red crosses) form of v_x near the upper boundary of the phasemixing region ($x = 1$). The two agree only during the initial stages of the development of v_x.

Appendix E

Nonlinear Driving Errors

(Section 7.2)

Here we consider a simple experiment that demonstrates some consequences of failing to correctly specify the ponderomotive force associated with an Alfvén wave. It is part of a preliminary investigation, and is included here to better develop the ideas discussed under Nonlinear Driving Errors in Section 7.2. Future readers beware, these ideas are still and results are still formative!

Let us consider homogeneous, 1.5D $\beta = 0$ MHD. Our governing equations are thus that of Chapter 4, with the additional simplification that equilibrium variables are constant and we prohibit transverse gradients and variables (which is arbitrarily taken as the x-direction, i.e. here $\mathbf{B}_0 = B_0\hat{\mathbf{y}}$, thus $v_\perp = v_x$ and $v_\parallel = v_y$). The governing equations (4.2) reduce to

$$\frac{\partial v_y}{\partial t} = N_2 \tag{E.1}$$

$$\frac{\partial v_z}{\partial t} - \frac{B_y}{\mu\rho_0}\frac{\partial b_z}{\partial y} = N_3 \tag{E.2}$$

$$\frac{\partial b_y}{\partial t} = N_5 \tag{E.3}$$

$$\frac{\partial b_z}{\partial t} - B_y\frac{\partial v_z}{\partial y} = N_6 \tag{E.4}$$

$$\frac{\partial \rho_1}{\partial t} + \rho_0\frac{\partial v_y}{\partial y} = N_7 \tag{E.5}$$

where the nonlinear components $N_1, \ldots, N_7$ are similarly simplified. If v_z is given at some order $\mathcal{O}(\alpha)$ where $\alpha \ll 1$, we can determine the other variables correct to the second order. Let us take v_z to initially be some function

$$v_z(t_0) = A\,F\left(\frac{y}{a}\right) \tag{E.6}$$

where a controls the pulse-width, A is a constant associated with maximum amplitude and F is a general function that determines the shape of the pulse, such as a Gaussian. Given that an Alfvén wave always travels along fieldlines at the local Alfvén speed, and the Alfvén-speed profile is homogeneous, and that self-moderation of the pulse occurs at higher-orders, $\mathcal{O}(\alpha^3)$, it follows that

$$v_z = A\,F\left(\frac{y \pm c_A t}{a}\right) \tag{E.7}$$

is correct to the second order. The choice of $\pm$ determines whether the wave propagates parallel or antiparallel to the field. The corresponding perturbation in b_z easily follows from (E.4)

$$\begin{aligned} b_z &= B_y \frac{\partial}{\partial y}\int v_z dt \\ &= \pm\frac{B_y}{c_A} v_z \\ &= \pm\sqrt{\mu\rho_0}\, v_z \end{aligned} \tag{E.8}$$

which is a standard, general result for Alfvén waves in the absence of dispersion. Next, we determine v_y from (E.1) which can be recast as

$$\begin{aligned} v_y &= \frac{1}{2\mu\rho_0}\frac{\partial}{\partial y}\int b_z^2\, dt \\ &= \frac{1}{2}\frac{\partial}{\partial y}\int v_z^2\, dt \\ &= \pm\frac{1}{2c_A} v_z^2 \quad . \end{aligned} \tag{E.9}$$

Now we determine ρ_1 from (E.1)

$$\begin{aligned} \rho_1 &= -\rho_0 \frac{\partial}{\partial y}\int v_y\, dt \\ &= \pm\frac{\rho_0}{2c_A}\frac{\partial}{\partial y}\int v_z^2\, dt \\ &= +\frac{\rho_0}{2c_A^2} v_z^2 \quad . \end{aligned} \tag{E.10}$$

Finally, inspecting (E.3) indicates that b_y remains zero throughout. Thus, we have

$$\begin{aligned} v_z &= A\,F\left(\frac{y + c_A t}{a}\right) \\ b_z &= \pm\sqrt{\mu\rho_0}\, v_z \end{aligned}$$

$$\begin{aligned} v_y &= \pm\frac{1}{2c_A}v_z^2 \\ b_y &= 0 \\ \rho_1 &= +\frac{\rho_0}{2c_A^2}v_z^2 \quad . \end{aligned} \tag{E.11}$$

These values have been shown to be valid up to a later time where modification of the Alfvén wave becomes important and our form of v_z is no longer valid (Verwichte 1999). We will now consider 3 simulations with initial conditions based on equations (E.11) to serve as an illustration accompanying the argument given in Section 7.2.

Splitting pulse

First, we demonstrate the validity of the expressions (E.11) . Let us consider the initial condition

$$\begin{aligned} v_z &= 2A\,\mathrm{Sech}^2\left(\frac{y}{a}\right) \\ b_z &= 0 \\ v_y &= 0 \\ b_y &= 0 \\ \rho_1 &= 0 \end{aligned} \tag{E.12}$$

where a is a parameter associated with the broadness of the pulse, taken to give a steep, Gaussian-like profile (see the t_0 panels of Figure E.1 for an illustration of the initial conditions). Physically, this corresponds linearly to an overlay of two oppositely travelling pulses of amplitude A, which leads to the cancellation of the b_z component and daughter in v_y. The compressive part, ρ_1, should however be non-zero. A is chosen as small so that, in effect, the assumed $2\mathrm{nd}$ order form v_z used in deriving (E.11) is valid for all time considered.

The evolution of the fluid-variables according to a simulation is shown in Figure (E.1). At the linear level (v_z and b_z), we see the pulses cleanly separate into the left- and right-bound Alfvén waves, and the $\pm$ relationship between v_z and b_z is clearly illustrated. Non-linearly, we examine the fluid-variables which are non-zero (v_y and ρ_1). We see that the ponderomotive wing/longitudnal daughter, manifest in both v_y and ρ_1, which travels with the main, linear pulse. We also see the development of a density instability at the location of the crossing, which grows with time. This instability, due to longitudinal acceleration of a cold fluid by a cross-ponderomotive effect (Verwichte et al. 1999), is the Jordan Mode Instability discussed by Fall & Hartquist (2002). There also sits a centralised, static

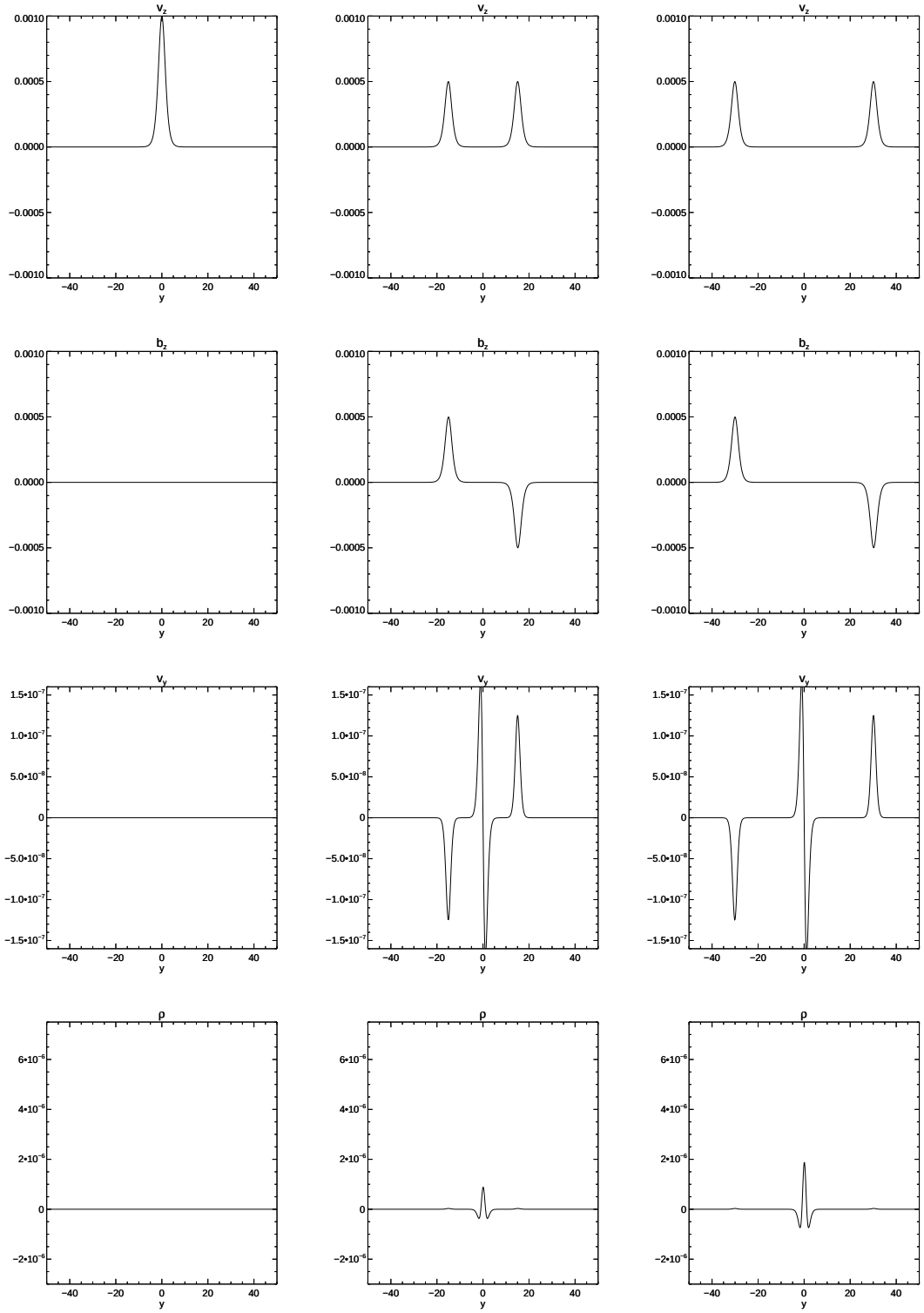

Figure E.1: Fluid variables at t_0, t_1 and t_3 (left-to-right) for the evolution of initial conditions (E.12). *Top Row:* The pulse splits into the left- and right-bound wave, manifest in v_z; 2^{nd} Row: Corresponding b_z perturbation; showing the $\pm$ relationship for the left- and right-bound waves; 3^{rd} Row: The longitudinal daughter in v_y; *Bottom Row:* The density perturbation, with the moving disturbance corresponding to the longitudinal daughter, and a centralised instability due to the cross-ponderomotive force. Plots for b_y are not shown, $b_y = 0$ throughout.

perturbation in v_y associated with the instability and the incorrect choice of $\rho_1(t_0) = 0$. Thus, the behaviour is similar to that seen in longitudinal aspects of our simulations in Chapter 4

After the separation, but before the time where the Alfvén wave becomes nonlinearly modified, we can compare our analytical expressions (E.11) to the numerical results for the left- and right-bound waves. We see excellent agreement, confirming our confidence in their viability and derivation. We will now isolate a single pulse, and experiment with different nonlinear initial conditions to illustrate possible nonlinear driving errors.

Single pulse, first order specification

Now let us consider the initial condition

$$\begin{aligned} v_z &= A\,\mathrm{Sech}^2\left(\frac{y}{a}\right) \\ b_z &= +\sqrt{\mu\rho_0}v_z \\ v_y &= 0 \\ b_y &= 0 \\ \rho_1 &= 0 \end{aligned} \tag{E.13}$$

This choice is highly analogous to the approach in Chapters 5 and 6 (but for the 1.5D case); we are trying to generate an Alfvén wave only, but have not specified nonlinear terms. *Viz.* we haven't given it any ponderomotive force, or rather, we have implicitly specified something that negates the effects of the Alfvén wave's ponderomotive force at the initial time.

We see in Figure E.2 that immediately after initialisation, the simulation "catches up" and the wave develops the appropriate daughter/wing manifest in v_y and ρ_1, which corresponds to equations (E.11) and the behaviour seen for the splitting pulse. However, we see a density instability form at the location of the initial condition. Falle and Hartquist (2002) show that such an instability occurs when v_y is accelerated in a cold plasma. However, in this scenario[1] there should be no such motion; the net ponderomotive force is zero[2], and, there is no interaction between two crossing Alfvén waves.

Given that our 'intention' was to introduce only an Alfvén wave, we can conclude the initial condition has been unsuccessful and is inappropriate; a slow wave (nonpropagating)

[1] Or rather, in the physical/intended case which it models.
[2] This can be calculated from E.11, and is evident in the post-separation times in Figure E.1.

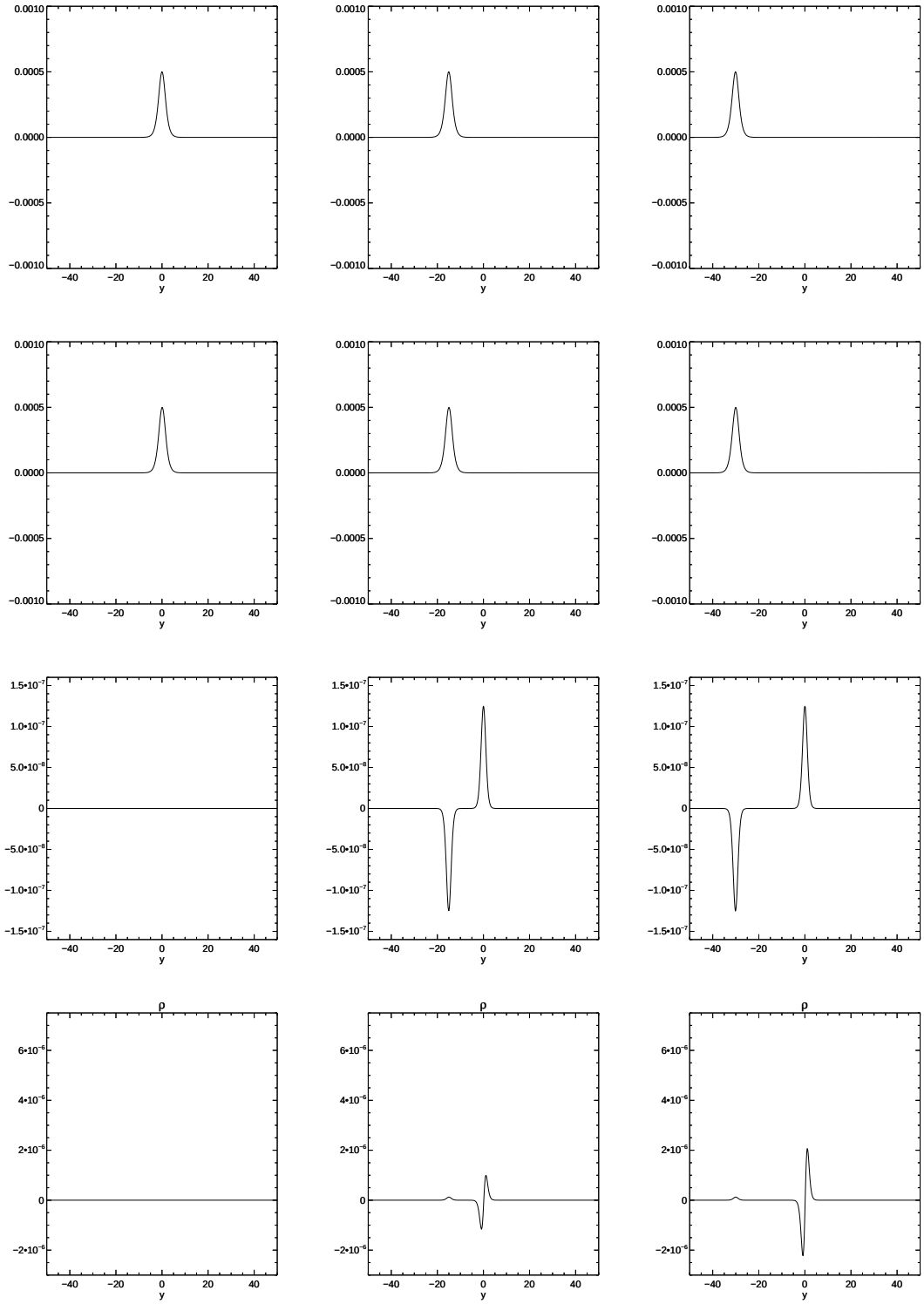

Figure E.2: Fluid variables at t_0, t_1 and t_3 (left-to-right) for the evolution of initial conditions (E.13). *Top Row:* The pulse no longer splits, and simply propagates as the left-bound wave, here manifest in v_z; 2^{nd} Row: Corresponding b_z perturbation; showing that the field-perturbation is the same sign for left-bound wave; 3^{rd} Row: The longitudinal daughter in v_y is seen, as is a static perturbation at the initial point which indicates the excitation of the slow mode; *Bottom Row:* The density perturbation, with the left-ward moving disturbance corresponding to the longitudinal daughter, there is also a centralised instability. However, in this case no-crossing effects have acted to drive it. It is a direct consequence of failing to specify the nonlinear terms.

has been excited. Thus, we must be careful to note that such an initial condition will act to nonlinearly excite a slow wave, which in the $\beta = 0$ case causes an instability, and in the $\beta \neq 0$ introduces a propagating wave which could proceed to interfere in unintended ways with the system.

Single pulse, second order specification

We now specify all terms according to (E.11)

$$\begin{aligned} v_z &= 2A\, e^{\left(-\frac{y}{a}\right)} \\ b_z &= +\sqrt{\mu\rho_0}v_z \\ v_y &= -\frac{1}{2c_A}v_z^2 \\ b_y &= 0 \\ \rho_1 &= +\frac{\rho_0}{2c_A^2}v_z^2 \end{aligned} \tag{E.14}$$

In this case, we find that the behaviour is much better[3]; in Figure (E.3) we see that there is a propagating Alfvén wave with the correct associated nonlinear effects, and no slow wave or instability has been initiated.

Conclusion

These simple experiments show even in 1.5D, homogeneous MHD that there is some sensitivity to the nonlinear terms associated with a propagating Alfvén wave, and that failure to properly consider them can introduce an erroneous slow magnetoacoustic wave/instability.

So far, it has proven difficult to illustrate the effect with the inclusion of the transverse direction (i.e., with the erroneous excitation of fast waves), however it is not too much of a leap to believe that such an effect is easily possible. Thus, although in the main text (Chapters 5 and 6) we have discussed multiple possibilities explaining the nonlinear excitation of the fast wave during the driving stages (for reasons of rigour); it seems very likely that it is indeed a nonlinear driving effect, as discussed in Section 5.4.2.

[3]It is nearly perfect, but there is actually a third order error which instigates the instability, which will eventually grow to be large. However, it is not visible at the amplitude and time scales considered in Figure (E.3)

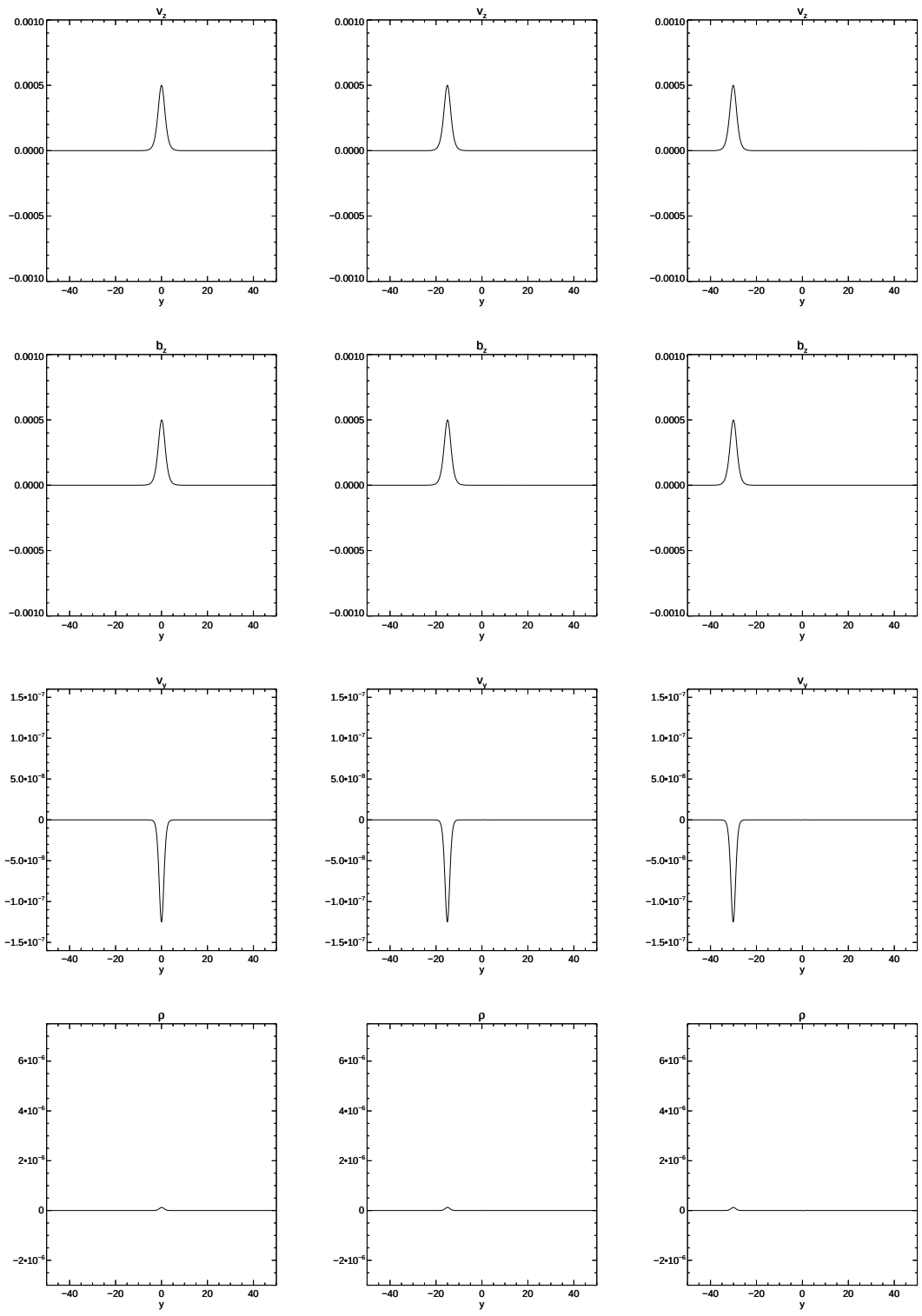

Figure E.3: As the previous figures for initial conditions (E.14). We now see the main Alfvén wave, plus its nonlinear daughter disturbance. By properly considering the nonlinear terms, the errors are removed.

Bibliography

Alfvén, H. (1942). *Nature*, 150:405–406.

Allan, W. and Manuel, J. R. (1996). *Annales Geophysicae*, 14:893–905.

Allan, W., Poulter, E. M., and Manuel, J. R. (1991). *J. Geophys. Res.*, 96:11461.

Antiochos, S. K. (1998). *ApJ*, 502:L181.

Antiochos, S. K., DeVore, C. R., and Klimchuk, J. A. (1999). *ApJ*, 510:485–493.

Arber, T. D., Longbottom, A. W., Gerrard, C. L., and Milne, A. M. (2001). *Journal of Computational Physics*, 171:151–181.

Aschwanden, M. J. (2004). *Physics of the Solar Corona. An Introduction*. Praxis Publishing Ltd.

Bender, C. M. and Orszag, S. A. (1978).

Benson, D. J. (1992). *Comput. Methods Appl. Mech. Eng.*, 99(2-3):235–394.

Beveridge, C., Priest, E. R., and Brown, D. S. (2002). *Sol. Phys.*, 209:333–347.

Bogdan, T. J., Carlsson, M., Hansteen, V. H., McMurry, A., Rosenthal, C. S., Johnson, M., Petty-Powell, S., Zita, E. J., Stein, R. F., McIntosh, S. W., and Nordlund, A. (2003). *ApJ*, 599:626–660.

Botha, G. J. J., Arber, T. D., Nakariakov, V. M., and Keenan, F. P. (2000). *A&A*, 363:1186–1194.

Boyd, T. and Sanderson, J. (2003). Cambridge University Press.

Brown, D. S. and Priest, E. R. (2001). *A&A*, 367:339–346.

Browning, P. K. (1991). *Plasma Physics and Controlled Fusion*, 33:539–571.

Bulanov, S. V. and Syrovatskii, S. I. (1980). *Fizika Plazmy*, 6:1205–1218.

Cally, P. S. and Andries, J. (2010). *Sol. Phys.*, 266:17–38.

Cally, P. S. and Hansen, S. C. (2011). *ApJ*, 738:119.

Chen, F. (1984). Number v. 1. Springer.

Close, R. M., Parnell, C. E., and Priest, E. R. (2004). *Sol. Phys.*, 225:21–46.

Craig, I. J. and Watson, P. G. (1992). *ApJ*, 393:385–395.

Craig, I. J. D. and McClymont, A. N. (1991). *ApJ*, 371:L41–L44.

Craig, I. J. D. and McClymont, A. N. (1993). *ApJ*, 405:207–215.

De Moortel, I. (2005). *Royal Society of London Philosophical Transactions Series A*, 363:2743–2760.

De Moortel, I., Ireland, J., and Walsh, R. W. (2000). *A&A*, 355:L23–L26.

De Pontieu, B., McIntosh, S. W., Carlsson, M., Hansteen, V. H., Tarbell, T. D., Schrijver, C. J., Title, A. M., Shine, R. A., Tsuneta, S., Katsukawa, Y., Ichimoto, K., Suematsu, Y., Shimizu, T., and Nagata, S. (2007). *Science*, 318:1574–.

Deforest, C. E. and Gurman, J. B. (1998). *ApJ*, 501:L217.

Dewar, R. L. (1970). *Physics of Fluids*, 13:2710–2720.

Edwin, P. M. and Roberts, B. (1983). *Sol. Phys.*, 88:179–191.

Erdélyi, R. and Fedun, V. (2007). *Science*, 318:1572–.

Evans, C. R. and Hawley, J. F. (1988). *ApJ*, 332:659–677.

Falle, S. A. E. G. and Hartquist, T. W. (2002). *MNRAS*, 329:195–203.

Friedrichs, K. (1957). *Nonlinear Wave Motion in Magneto-hydrodynamics*. Los Alamos Scientific Laboratory of the University of California.

Fruit, G. and Craig, I. J. D. (2006). *A&A*, 448:753–761.

Galsgaard, K. and Pontin, D. I. (2011a). *A&A*, 529:A20.

Galsgaard, K. and Pontin, D. I. (2011b). *A&A*, 534:A2.

Galsgaard, K., Priest, E. R., and Titov, V. S. (2003). *J. Geophys. Res.*, 108.

Gary, G. A. (2001). *Sol. Phys.*, 203:71–86.

Goedbloed, J. P. H. and Poedts, S. (2004).

Goossens, M., Andries, J., Soler, R., Van Doorsselaere, T., Arregui, I., and Terradas, J. (2012). *ApJ*, 753:111.

Goossens, M., Erdélyi, R., and Ruderman, M. S. (2011). *Space Sci. Rev.*, 158:289–338.

Goossens, M., Terradas, J., Andries, J., Arregui, I., and Ballester, J. L. (2009). *A&A*, 503:213–223.

Grimshaw, R., Pelinovsky, D., and Pelinovsky, E. (2010). *Wave Motion*, 99:496–507.

Gruszecki, M., Vasheghani Farahani, S., Nakariakov, V. M., and Arber, T. D. (2011). *A&A*, 531:A63.

Gurnett, D. and Bhattacharjee, A. (2005). *Introduction to Plasma Physics: With Space and Laboratory Applications*. Cambridge University Press.

Hahn, M. and Savin, D. W. (2013). *ApJ*, 776:78.

Hansen, S. C. and Cally, P. S. (2012). *ApJ*, 751.

Hanson, C. S. and Cally, P. S. (2011). *Sol. Phys.*, 269:105–110.

Hassam, A. B. (1992). *ApJ*, 399:159–163.

Hassam, A. B. and Lambert, R. P. (1996). *ApJ*, 472:832.

Heyvaerts, J. and Priest, E. R. (1983). *A&A*, 117:220–234.

Hollweg, J. V. (1981). *Sol. Phys.*, 70:25–66.

Hood, A. W., Ruderman, M., Pascoe, D. J., De Moortel, I., Terradas, J., and Wright, A. N. (2013). *A&A*, 551:A39.

Ionson, J. A. (1978). *ApJ*, 226:650–673.

Ionson, J. A. (1982). *ApJ*, 254:318–334.

Ionson, J. A. (1983). *ApJ*, 271:778–792.

Lang, K. R. (2001). *The Cambridge Encyclopedia of the Sun*.

Longcope, D. W. and Parnell, C. E. (2009). *Sol. Phys.*, 254:51–75.

Matsumoto, T. and Suzuki, T. K. (2012). *ApJ*, 749:8.

McDougall, A. M. D. and Hood, A. W. (2007). *Sol. Phys.*, 246:259–271.

McLaughlin, J. A., De Moortel, I., and Hood, A. W. (2011a). *A&A*, 527:A149.

McLaughlin, J. A., De Moortel, I., Hood, A. W., and Brady, C. S. (2009). *A&A*, 493:227–240.

McLaughlin, J. A., Ferguson, J. S. L., and Hood, A. W. (2008). *Sol. Phys.*, 251:563–587.

McLaughlin, J. A. and Hood, A. W. (2004). *A&A*, 420:1129–1140.

McLaughlin, J. A. and Hood, A. W. (2005). *A&A*, 435:313–325.

McLaughlin, J. A. and Hood, A. W. (2006a). *A&A*, 452:603–613.

McLaughlin, J. A. and Hood, A. W. (2006b). *A&A*, 459:641–649.

McLaughlin, J. A., Hood, A. W., and De Moortel, I. (2011b). *Space Sci. Rev.*, 158:205–236.

McLaughlin, J. A., Thurgood, J. O., and MacTaggart, D. (2012). *A&A*, 548:A98.

Morton, R. J. and McLaughlin, J. A. (2013). *A&A*, 553:L10.

Morton, R. J., Verth, G., McLaughlin, J. A., and Erdélyi, R. (2012). *ApJ*, 744:5.

Nakariakov, V. M., Ofman, L., Deluca, E. E., Roberts, B., and Davila, J. M. (1999). *Science*, 285:862–864.

Nakariakov, V. M., Roberts, B., and Murawski, K. (1997). *Sol. Phys.*, 175:93–105.

Nakariakov, V. M. and Verwicte, E. O. (2005). *Liv. Rev. Sol. Phys.*, 2:3.

Narain, U. and Ulmschneider, P. (1996). *Space Sci. Rev.*, 75:453–509.

Ofman, L., Morrison, P. J., and Steinolfson, R. S. (1993). *ApJ*, 417:748.

Ofman, L., Romoli, M., Poletto, G., Noci, G., and Kohl, J. L. (1997). *ApJ*, 491:L111.

Ofman, L. and Wang, T. J. (2008). *A&A*, 482:L9–L12.

Parker, E. N. (1991). *ApJ*, 376:355–363.

Parnell, C. E., Smith, J. M., Neukirch, T., and Priest, E. R. (1996). *Physics of Plasmas*, 3:759–770.

Pascoe, D. J., Hood, A. W., de Moortel, I., and Wright, A. N. (2012). *A&A*, 539:A37.

Pascoe, D. J., Hood, A. W., De Moortel, I., and Wright, A. N. (2013). *A&A*, 551:A40.

Pascoe, D. J., Wright, A. N., and De Moortel, I. (2010). *ApJ*, 711:990–996.

Pascoe, D. J., Wright, A. N., and De Moortel, I. (2011). *ApJ*, 731:73.

Pontin, D. I. (2012). *Royal Society of London Philosophical Transactions Series A*, 370:3169–3192.

Pontin, D. I., Bhattacharjee, A., and Galsgaard, K. (2007). *Physics of Plasmas*, 14(5):052106.

Pontin, D. I. and Galsgaard, K. (2007). *Journal of Geophysical Research (Space Physics)*, 112:3103.

Priest, E. and Forbes, T. (2000).

Priest, E. R. (1982). *Solar magneto-hydrodynamics*.

Priest, E. R. and Pontin, D. I. (2009). *Physics of Plasmas*, 16(12):122101.

Priest, E. R. and Titov, V. S. (1996). *Royal Society of London Philosophical Transactions Series A*, 354:2951–2992.

Rae, I. C. and Roberts, B. (1982). *MNRAS*, 201:1171–1182.

Rankin, R., Frycz, P., Tikhonchuk, V. T., and Samson, J. C. (1994). *J. Geophys. Res.*, 99:21291–21302.

Régnier, S., Parnell, C. E., and Haynes, A. L. (2008). *A&A*, 484:L47–L50.

Ruderman, M. S. and Erdélyi, R. (2009). *Space Sci. Rev.*, 149:199–228.

Ruderman, M. S. and Roberts, B. (2002). *ApJ*, 577:475–486.

Ruderman, M. S. and Terradas, J. (2013). *A&A*, 555:A27.

Schmieder, B., Mandrini, C., Dmoulin, P., Aulanier, G., Li, H., and Berlicki, A. (2007). *Advances in Space Research*, 39(12):1840 – 1846.

Schnack, D. (2009). *Lectures in Magnetohydrodynamics: With an Appendix on Extended MHD*. Lecture Notes in Physics. Springer.

Schunker, H. and Cally, P. S. (2006). *MNRAS*, 372:551–564.

Sousa, S. G. and Cunha, M. S. (2008). *MNRAS*, 386:531–542.

Stark, B. A., Musielak, Z. E., and Suess, S. T. (1995). In *Solar Wind Eight*, page 66.

Steinolfson, R. S., Ofman, L., and Morrison, P. J. (1995). *AGU*, 86:189.

Strogatz, S. H. (1994). *Nonlinear Dynamics And Chaos: With Applications To Physics, Biology, Chemistry, And Engineering (Studies in Nonlinearity)*. Studies in nonlinearity.

Perseus Books Group.

Sun, X., Hoeksema, J. T., Liu, Y., Chen, Q., and Hayashi, K. (2012). *ApJ*, 757:149.

Terradas, J., Goossens, M., and Verth, G. (2010). *A&A*, 524:A23.

Threlfall, J., Parnell, C. E., De Moortel, I., McClements, K. G., and Arber, T. D. (2012). *A&A*, 544:A24.

Thurgood, J. O. and McLaughlin, J. A. (2012). *A&A*, 545:A9.

Thurgood, J. O. and McLaughlin, J. A. (2013a). *Sol. Phys.*, 288:205–222.

Thurgood, J. O. and McLaughlin, J. A. (2013b). *A&A*, 555:A86.

Thurgood, J. O. and McLaughlin, J. A. (2013c). *A&A*, 558:A127.

Tikhonchuk, V. T., Rankin, R., Frycz, P., and Samson, J. C. (1995). *Phys. Plasmas*, 2:501–515.

Tomczyk, S., McIntosh, S. W., Keil, S. L., Judge, P. G., Schad, T., Seeley, D. H., and Edmondson, J. (2007). *Science*, 317:1192–.

Tracy, E. R., Kaufman, A. N., and Brizard, A. J. (2003). *Physics of Plasmas*, 10:2147–2154.

Tsiklauri, D., Arber, T. D., and Nakariakov, V. M. (2001). *A&A*, 379:1098–1105.

Ulmschneider, P. and Narain, U. (1990). In Priest, E. R. and Krishan, V., editors, *Basic Plasma Processes on the Sun*, volume 142 of *IAU Symposium*, page 97.

Uralov, A. M. (2003). *Astronomy Letters*, 29:486–493.

Valori, G., Green, L. M., Démoulin, P., Vargas Domínguez, S., van Driel-Gesztelyi, L., Wallace, A., Baker, D., and Fuhrmann, M. (2012). *Sol. Phys.*, 278:73–97.

Van Doorsselaere, T., Nakariakov, V. M., and Verwichte, E. (2008). *ApJ*, 676:L73–L75.

Verwichte, E. (1999). PhD thesis, The Open University.

Verwichte, E., Nakariakov, V. M., and Longbottom, A. W. (1999). *Journal of Plasma Physics*, 62:219–232.

Webb, G. M., Zank, G. P., Kaghashvili, E. K., and Ratkiewicz, R. E. (2005). *Journal of Plasma Physics*, 71:811–857.